17 April 2009 | $10

Science

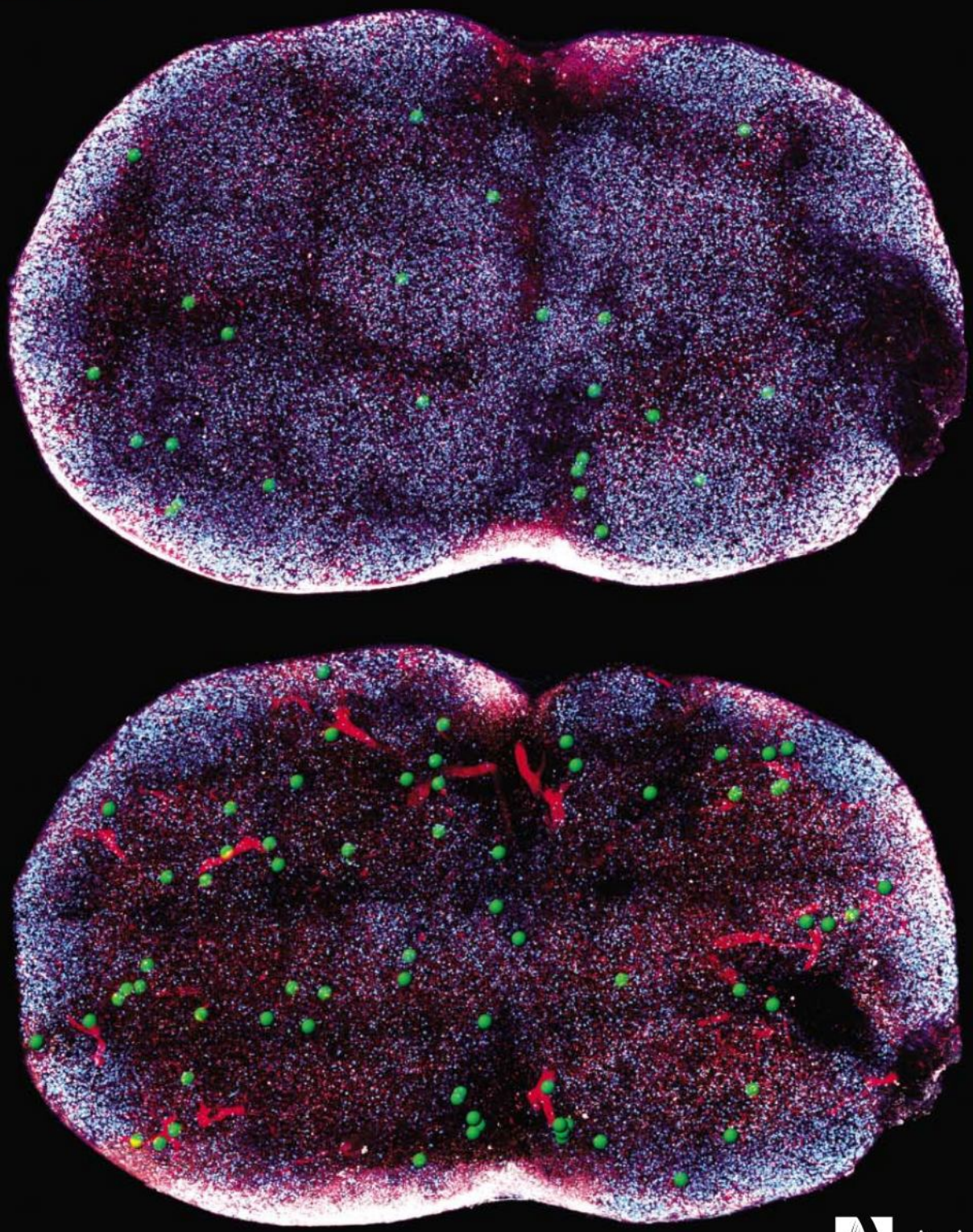

AAAS

Nontraditional Careers:
Opportunities Away From the Bench
Webinar

Want to learn more about exciting and rewarding careers outside of academic/industrial research? Join us for a round-table discussion that will look at the various career options open to scientists across different sectors, strategies you can use to find a nonresearch career, and the future of the scientific work force in nontraditional careers.

Join our panel of experts in a **FREE** live discussion, . Register to participate.

Questions can be submitted live to the panel during the webinar or in advance via e-mail provided with registration.

To register, visit **www.sciencecareers.org/webinar**

Webinar will be available on demand after the event for viewing anytime.

Tuesday
April 28, 2009
12 noon Eastern;
9 am Pacific;
4 pm GMT

Participating Experts:

Dr. Lori Conlan
Director of Postdoc Services,
Office of Intramural Training and Education
National Institutes of Health

Pearl Freier
President
Cambridge BioPartners

Dr. Marion Müller
Director, DFG Office North America
Deutsche Forschungsgemeinschaft
(German Research Foundation)

Richard Weibl
Director, Center for Careers in Science and Technology
American Association for the Advancement of Science

Produced by the
Science/AAAS Business Office.

Science Careers
From the journal *Science* AAAS


Look Closer.

Mapping your pathway to discovery.

Move beyond the boundaries of the known. Built on the solid Sigma foundation of quality and reliability, our cell biology portfolio is backed by a universe of experience, knowledge and biological data.

- 12,000+ Antibodies
- Highly Validated Prestige Antibodies® Powered by Atlas Antibodies
- New Precisio™ Active Human Kinases
- 3,000+ Bioactive Small Molecules
- LOPAC™ Libraries of Pharmacologically Active Compounds
- Navigate by Gene, Disease, Tissue or Pathway via Your Favorite Gene Powered by Ingenuity

Your Favorite Gene SEARCH Powered By INGENUITY

For a closer look at cell biology content you can count on visit ***sigma.com/cellbiology***

SIGMA Life Science

Our Innovation, Your Research — Shaping the Future of Life Science

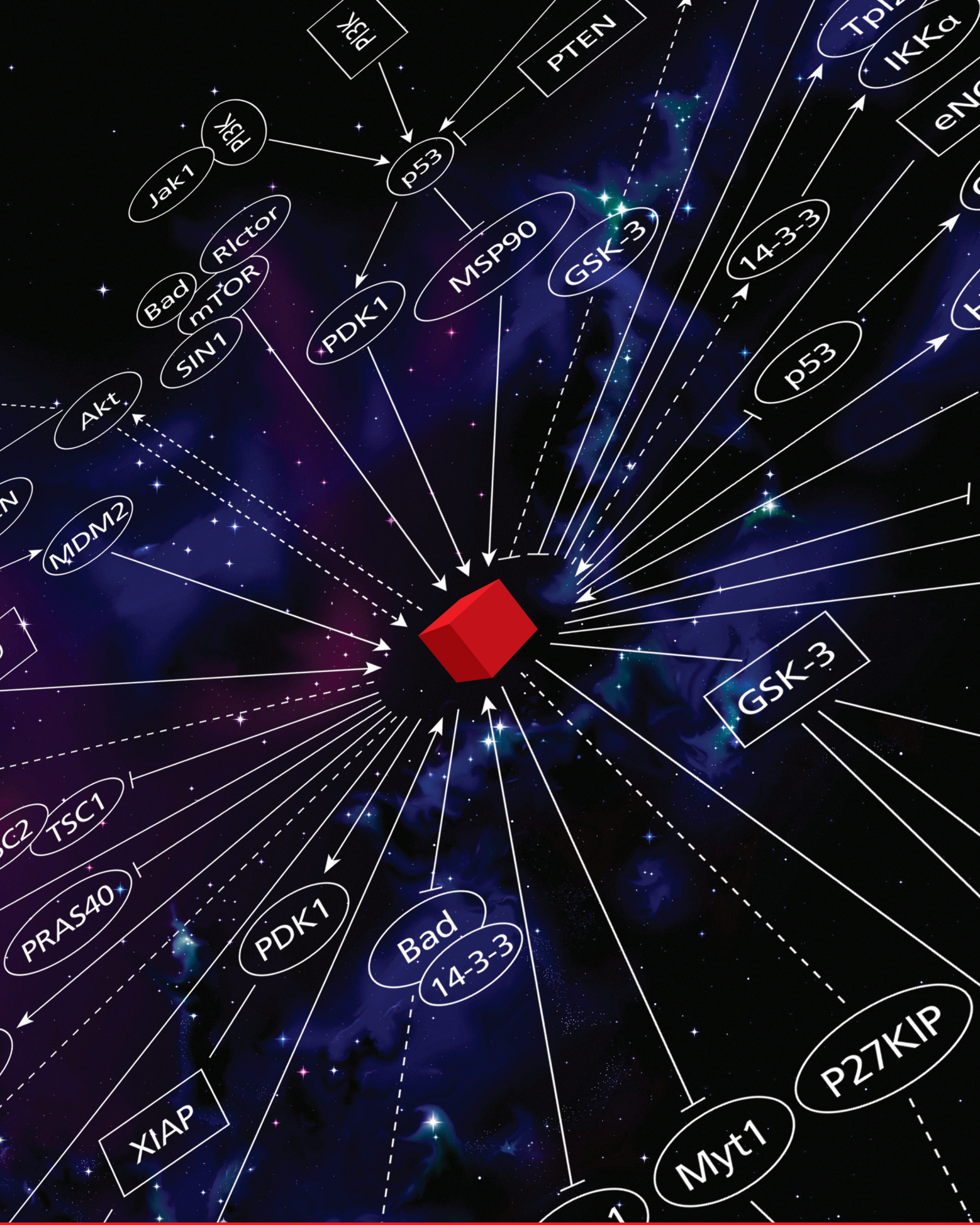
PI3K
PTEN
PI3K
Jak1
p53
Rictor
Bad
mTOR
SIN1
PDK1
MSP90
GSK-3
14-3-3
p53
Akt
MDM2
GSK-3
TSC1
PRAS40
PDK1
Bad
14-3-3
XIAP
Myt1
P27KIP

WHAT'S Next™

New Reprogramming Sets. Reliable.

Now you can generate iPS cell colonies from terminally differentiated cells with viral-delivered transcription factors that have been proven to reprogram.

Reprogramming Set One
Stemgent™ DOX Inducible Mouse TF Lentivirus Set
Introducing the first in a broad line of reprogramming reagents…the Stemgent™ DOX Inducible Mouse TF (Transcription Factor) Lentivirus Set. This set was developed to bring fast, easy reprogramming to every lab. It contains four concentrated lentiviral stocks, expressing Oct4, Sox2, Klf4, and c-Myc, shown to reprogram terminally differentiated mouse cells into induced pluripotent stem (iPS) cells.

Reprogramming Set Two
Stemgent™ Human TF Lentivirus Set
If you reprogram human cells, the Stemgent™ Human TF Lentivirus Set was made for you. The four transcription factors constitutively expressed by the viral vectors are Oct4, Sox2, Lin28, and Nanog. Tested and proven to reprogram terminally differentiated human cells, this set and its complete protocol are available now.

Supporting Application Notes
Application notes for both of these sets are available at www.stemgent.com/nat6. These notes provide all the information necessary to achieve your desired results on a consistent basis.

These new reagent sets broaden access to breakthrough cellular reprogramming by standardizing seminal experiments for reliably reproducible results.

Breakthrough Fundamentals
Reprogramming is the process by which cells are manipulated from a terminally differentiated state to a pluripotent state, down a new pathway, or directly from one differentiated state to another. And it's understood that reprogramming will completely revolutionize biological research.

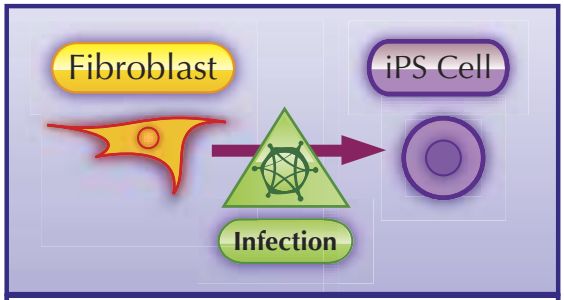

Viral-mediated reprogramming leads to generation of iPS cells from differentiated fibroblasts.

We've Reprogrammed the Stem Cell Reagent Field
Stemgent creates ready access to cellular reprogramming research materials, methods and experiments. Whatever your level of expertise, you will find everything you need for reprogramming in Stemgent's comprehensive line of reprogramming reagents: from individual components such as small molecules to complete "experiment-in-a-box" kits.

CERTIFIED TO CTR REPROGRAM

Qualified and Available Now
These new Stemgent sets have been proven by leading scientists and qualified in Stemgent laboratories. Stemgent stem cell scientists support you every step of the way and have been trained in leading stem cell laboratories.

Complete Support
For the application notes and more information, simply call Stemgent and ask for a scientist in our Reprogramming Group. We have been trained in leading stem cell laboratories. We have proven these sets in our own hands. And we are here to support you at every step.

Brambrink T., Foreman R., Welstead G.G., Lengner C.J., Wernig M., Suh H., and Jaenisch R. (2008) Sequential Expression of Pluripotency Markers during Direct Reprogramming of Mouse Somatic Cells. Cell Stem Cell 2, 151–159.

Proven. Built on Seminal Research.

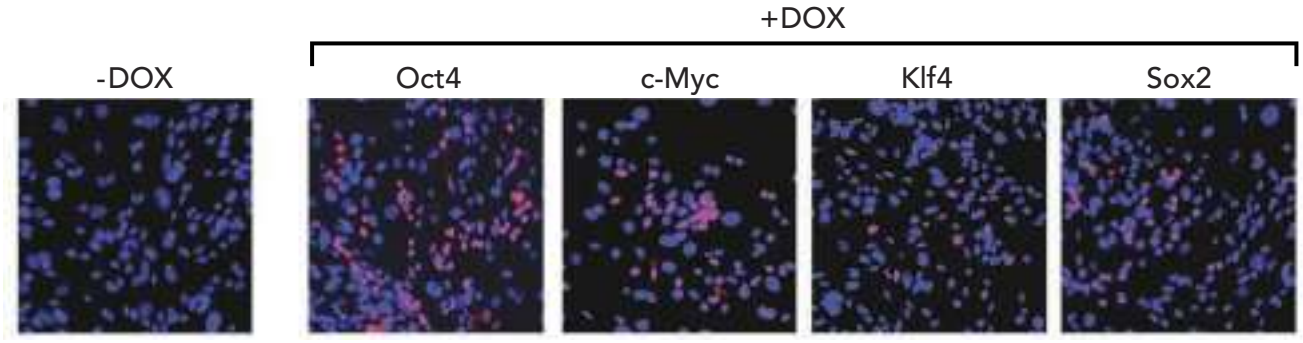

Figure 1. Immunocytochemistry (ICC) analysis 48 hours post-Doxycycline (DOX) induction. Nanog-GFP/rtTA mouse embryonic fibroblasts (MEFs) were transduced with each of four lentiviruses. The Nanog-GFP/rtTA MEFs contain the GFP gene knocked in at the Nanog locus as well as a reverse tetracycline transcriptional activator (rtTA) expression cassette, required for DOX inducible expression. Far left panel (-DOX) is a representative negative control for expression of the four transcription factors without DOX induction. Correctly expressed transcription factors were confirmed by corresponding antibodies (shown in red) stained with DAPI to visualize nuclei.

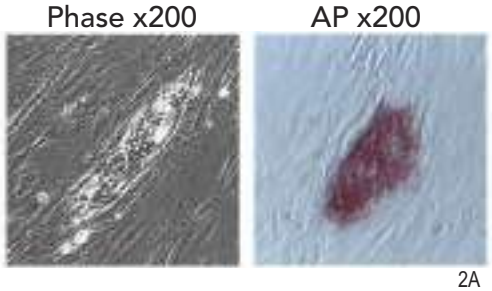

2A

Figure 2. Analysis of iPS colonies generated. Nanog-GFP/rtTA MEFs were transduced with four viruses carrying Oct2, Sox2, Klf4, and c-Myc cDNA. Expression of the four transcription factors was induced by adding DOX to initiate the reprogramming process. GFP expression reflects the endogenous Nanog expression level, monitoring pluripotency. Emergent colonies were manually isolated and passaged for further characterization.
[A] Phase contrast microscopy and alkaline phosphatase (AP) staining of an induced pluripotent stem (iPS) cell colony.
[B] Pluripotency marker analysis: Left panel – phase contrast overlay with GFP reprogramming reporter expression. Middle panel – ICC staining for pluripotency markers (Nanog, Oct4, and SSEA1.) Right panel – DAPI staining to visualize nuclei.

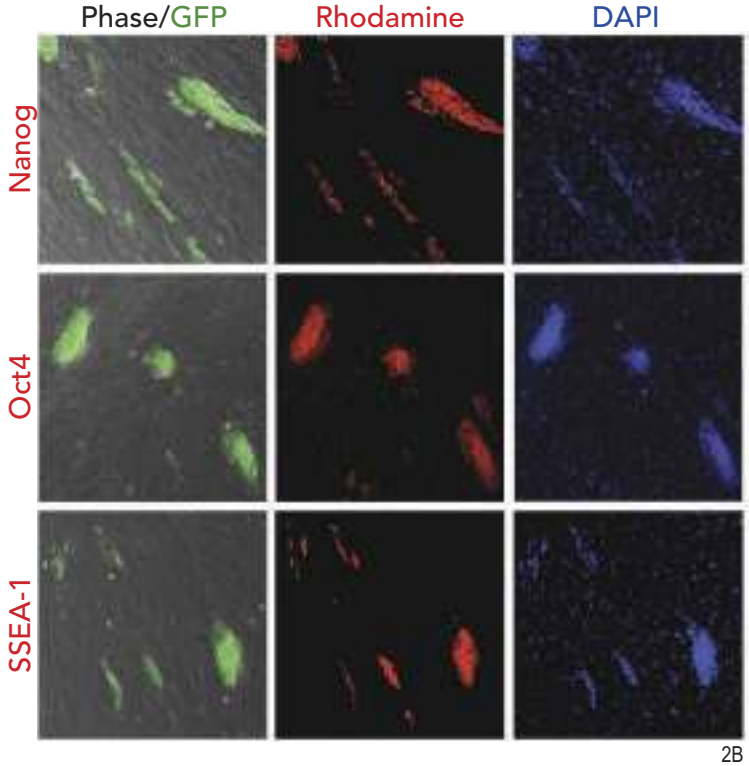

2B

Our Mission

Our mission is to bring you the newest proven reagents and tools from the best and brightest stem cell scientists and laboratories. Come to www.stemgent.com/nat6 for more information. Or call 877-228-9783 (toll-free) or +1-617-245-0098 (international).

STEMGENT™

REPROGRAMMING THE REAGENT™

BOSTON | www.stemgent.com/nat6 | SAN DIEGO

Biacore systems

from inspiration ...to publication

Highest quality, information-rich interaction data from Biacore™ systems deepen your understanding of molecular mechanisms and interaction pathways and enable you to add function to structure.

Select the perfect solution for your application and draw conclusions with confidence – from the company that continues to set the standard for label-free protein interaction analysis.

For further information or register to have one of our scientific experts contact you, please visit **www.gelifesciences.com/biacore-science**

Biacore T100
unmatched performance

Biacore X100
ready to run research system

Biacore Flexchip
array-based comparative profiling

imagination at work

EDITORIAL

NEWS OF THE WEEK

NEWS FOCUS

LETTERS

BOOKS *ET AL.*

POLICY FORUM

PERSPECTIVES

REVIEW

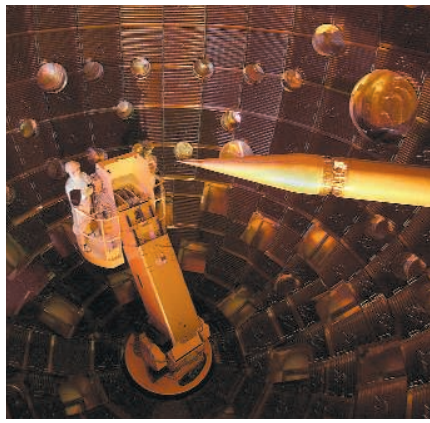

page 326

page 338

BREVIA

CONTENTS continued >>

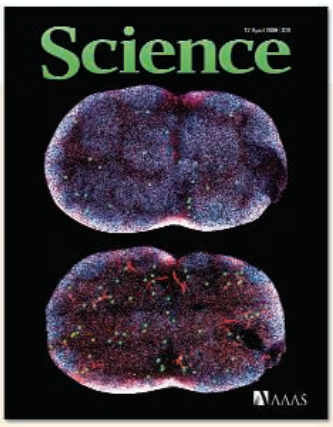

COVER

Multiphoton laser scanning images showing cortical (top) and medullary (bottom) portions of a mouse inguinal lymph node. Green spheres represent dendritic cell precursors 5 hours after transfer from bone marrow; B cell follicles are shown in blue; blood vessels and T cells are in red. During development, these precursors migrate through the blood to lymphoid tissues where they divide and disperse into the dendritic cell network. See page 392.

Image: Gabriel Victora and Tanja Schwickert, the Nussenzweig Laboratory, Rockefeller University

DEPARTMENTS

Epigenetics sample and assay technologies by QIAGEN

Trust in methylation analysis

Rely on QIAGEN epigenetics sample and assay technologies for:

- **DNA purification**
- **Bisulfite conversion**
- **Whole bisulfitome amplification**
- **Methylation-specific PCR**
- **Methylation detection and quantification with Pyrosequencing**

Making improvements in life possible — www.qiagen.com

QIAGEN®

Sample & Assay Technologies

ADNAEpigeneticsQ0309S1WW

RESEARCH ARTICLE

REPORTS

CONTENTS continued >>

page 339

page 397

page 403

Published by AAAS

What makes you happy?
How about Western blots in 55 minutes without equipment?

Put a smile on your face and your research with the chemiluminescent Thermo Scientific Pierce Fast Western Blot Kit 55-minute Western blot procedure.

- Fast – all the sensitivity you need in a fraction of the time; save 3-4 hours per blot over traditional blotting methods
- Convenient – no expensive hardware or extra bench space needed; eliminates membrane clogging issues
- Economical – costs about the same as a classical Western blot
- Easy – optimized kit includes all reagents except primary antibody
- Versatile – kits work with both rabbit and mouse primary antibodies

Visit *www.thermo.com/fastwest*

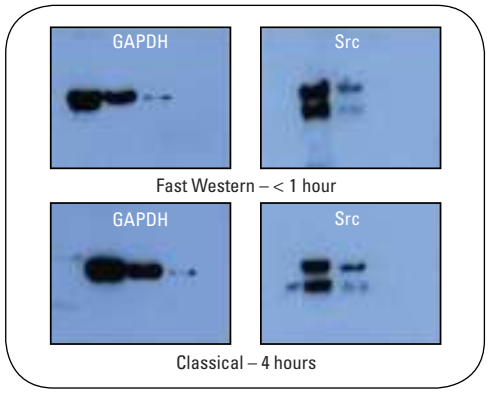

The sensitivity you need in less time with no expensive hardware.

Target proteins were probed using a classical Western blot procedure (3-4 hours) and the Fast Western Blot Kit procedure (55 minutes).

Moving science forward

Thermo SCIENTIFIC

Part of Thermo Fisher Scientific

SCIENCEONLINE

SCIENCEXPRESS
www.sciencexpress.org

Proteasomal Regulation of the Hypoxic Response Modulates Aging in *C. elegans*
R. Mehta et al.

Induction of the hypoxic response in a worm slows aging and enhances resistance to proteotoxicity.
10.1126/science.1173507

A Functional Role for Transposases in a Large Eukaryotic Genome
M. Nowacki et al.

The ciliate *Oxytricha* expresses transposase genes to influence thousands of DNA rearrangements required for proper development.
10.1126/science.1170023

The Nuclear DNA Base 5-Hydroxymethylcytosine Is Present in Purkinje Neurons and the Brain
S. Kriaucionis and N. Heintz

The genome of mammals contains appreciable amounts of a previously undescribed modified DNA base.
10.1126/science.1169786

Conversion of 5-Methylcytosine to 5-Hydroxymethylcytosine in Mammalian DNA by MLL Partner TET1
M. Tahiliani et al.

Methylated C bases, an important epigenetic mark in genomic DNA, can be enzymatically converted to 5-hydroxymethylcytosine.
10.1126/science.1170116

TECHNICALCOMMENTS

Comment on "Atmospheric Hydroxyl Radical Production from Electronically Excited NO_2 and H_2O"
S. Carr et al.

full text at www.sciencemag.org/cgi/content/full/324/5925/336b

Response to Comment on "Atmospheric Hydroxyl Radical Production from Electronically Excited NO_2 and H_2O"
S. Li et al.

full text at www.sciencemag.org/cgi/content/full/324/5925/336c

SCIENCENOW
www.sciencenow.org
Highlights From Our Daily News Coverage

Our Ancestors Were No Swingers
Study suggests early humans were poor climbers.

Blasting for Ice on Mars
Ongoing impacts are revealing what may be remnants of an ancient ice age.

What You See Is What You Feel
Sense of touch shapes our visual perception, a new study shows.

SCIENCESIGNALING
www.sciencesignaling.org
The Signal Transduction Knowledge Environment

EDITORIAL GUIDE: The Protein Dynamics of Cell Signaling
W. Wong and N. R. Gough

Changes in the conformation, binding partners, or localization of signaling proteins affect the flow of information through signaling cascades.

RESEARCH ARTICLE: Mechanical Signals Trigger Myosin II Redistribution and Mesoderm Invagination in *Drosophila* Embryos
P.-A. Pouille et al.

Mesoderm invagination during gastrulation is controlled by mechanical cues that promote Fog signaling and redistribution of a motor protein.

PERSPECTIVE: Arrestin Times for Developing Antipsychotics and β-Blockers
M. D. Houslay

Conformation determines G protein–independent signaling through β-arrestins.

PERSPECTIVE: HIV Infection of T Cells—Actin-In and Actin-Out
Y. Liu et al.

The coordinated activities of various actin-binding proteins facilitate entry of HIV into T cells.

MEETING REPORT: Visualizing Immune System Complexity
M. L. Dustin

From individual molecules to cells in animals, imaging has brought incredible insight to immunology.

PRESENTATION: Molecular Origin and Functional Consequences of Digital Signaling and Hysteresis During Ras Activation in Lymphocytes
A. K. Chakraborty et al.

Simulations, theory, and experiments reveal a potential molecular mechanism for digital signaling and short-term molecular memory in lymphocytes.

SCIENCECAREERS
www.sciencecareers.org/career_magazine
Free Career Resources for Scientists

Tooling Up: The Business Development Career Track
D. Jensen

Ph.D. scientists working in business development scout for new technologies and plan new initiatives.

In the Trenches: Science for Humanitarian Aid
R. Mejia

Humanitarian relief organizations need scientists to work in regions experiencing wars or natural disasters.

From the Archives: The Academic Scientists' Toolkit
J. Austin

Today's faculty must know research but must also have all the skills of a manager.

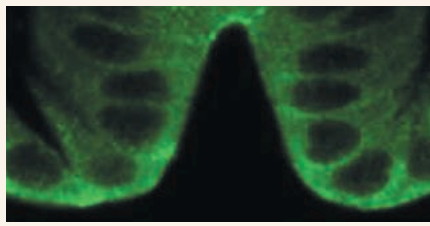

SCIENCESIGNALING
Invagination of the mesoderm.

SCIENCE ONLINE FEATURE
www.sciencemag.org/sciext/gonzoscientist/

THE GONZO SCIENTIST: The Science Dance Match-Up Challenge
Can you match the winning dances from the 2009 AAAS/*Science* Dance Contest with the science that inspired them?

SCIENCEPODCAST
www.sciencemag.org/multimedia/podcast
Free Weekly Show

Download the 17 April *Science* Podcast to hear about improving minority student performance, laser fusion at the National Ignition Facility, and more.

ORIGINSBLOG
blogs.sciencemag.org/origins
A History of Beginnings

SCIENCEINSIDER
blogs.sciencemag.org/scienceinsider
Science Policy News and Analysis

SCIENCE (ISSN 0036-8075) is published weekly on Friday, except the last week in December, by the American Association for the Advancement of Science, 1200 New York Avenue, NW, Washington, DC 20005. Periodicals Mail postage (publication No. 484460) paid at Washington, DC, and additional mailing offices. The title SCIENCE is a registered trademark of the AAAS. Domestic individual membership and subscription (51 issues): $146 ($74 allocated to subscription). Domestic institutional subscription (51 issues): $835; Foreign postage extra: Mexico, Caribbean (surface mail) $55; other countries (air assist delivery) $85. First class, airmail, student, and emeritus rates on request. Canadian rates with GST available upon request, GST #1254 88122. Publications Mail Agreement Number 1069624. **Printed in the U.S.A.**

Change of address: Allow 4 weeks, giving old and new addresses and 8-digit account number. **Postmaster:** Send change of address to AAAS, P.O. Box 96178, Washington, DC 20090–6178. **Single-copy sales:** $10.00 current issue, $15.00 back issue prepaid includes surface postage; bulk rates on request. **Authorization to photocopy** material for internal or personal use under circumstances not falling within the fair use provisions of the Copyright Act is granted by AAAS to libraries and other users registered with the Copyright Clearance Center (CCC) Transactional Reporting Service, provided that $20.00 per article is paid directly to CCC, 222 Rosewood Drive, Danvers, MA 01923. The identification code for *Science* is 0036-8075. *Science* is indexed in the *Reader's Guide to Periodical Literature* and in several specialized indexes.

AAAS
ADVANCING SCIENCE, SERVING SOCIETY

Published by AAAS

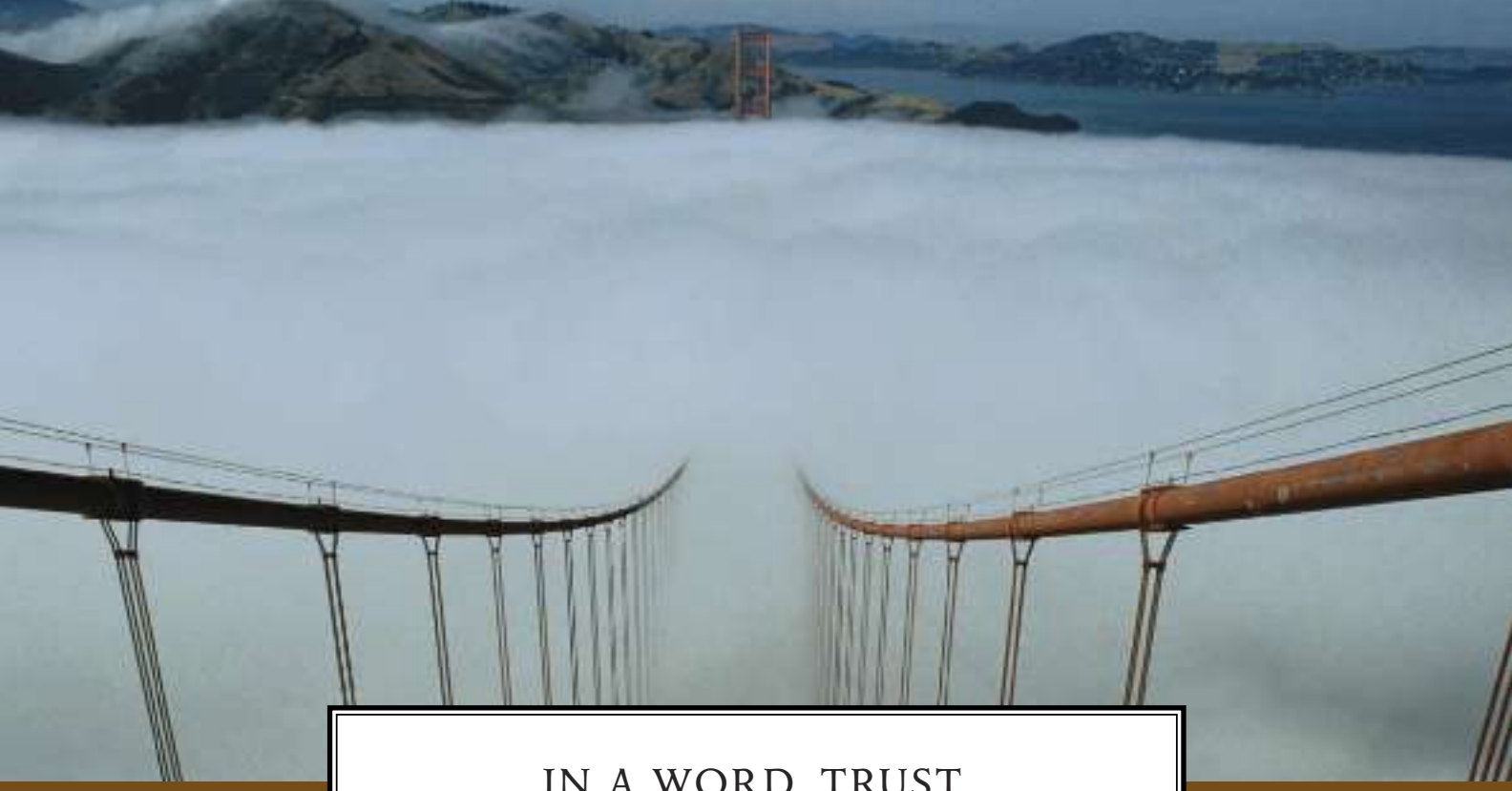

IN A WORD, TRUST.

T4 DNA Ligase

New England Biolabs is dedicated to providing our customers with guaranteed enzyme performance. Our recombinant T4 DNA Ligase is the most extensively used ligase for cloning experiments and other applications, including sample preparation and next generation sequencing. It is available at exceptional value, and an even greater value when purchased in large quantities for high throughput technologies. For cohesive, blunt, simple or complex reactions, make T4 DNA Ligase from NEB your first choice.

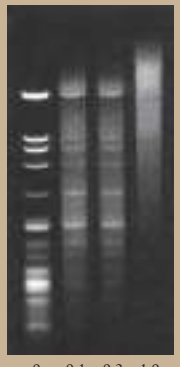

Ligation of blunt-ended HaeIII fragments of Lambda DNA using various amounts of T4 DNA Ligase (400,000 cohesive end units/ml) in a 20 µl reaction volume. Reactions were incubated for 30 minutes at 16°C.

Ligation of HindIII fragments (4-base overhang) of Lambda DNA using 1 cohesive end unit (1µl of 1:400 dilution) of T4 DNA Ligase. Reactions were incubated at 25°C.

Advantages:

Quality - Highly pure enzyme with no lot-to-lot variation

Convenience - Choose original T4 DNA Ligase or the Quick Ligation Kit to meet the demands of a variety of reaction conditions

Flexibility - Active at room temperature or 16°C; reaction times run from 5 minutes to overnight

Robustness - Active in a variety of reaction buffers

T4 DNA Ligase* [R]
Regular Concentration **M0202S/L**
For standard cloning reactions

High Concentration **M0202T/M**
For large or difficult constructs

Quick Ligation™ Kit* [R] **M2200S/L**
For ligation of cohesive or blunt-end DNA fragments in 5 minutes at room temperature

[R] = Recombinant
*NEB ligase products are BSA-free

For more information regarding customization and OEM opportunities, please contact **oem@neb.com**

New England Biolabs, Inc. is an ISO 9001 certified company

NEW ENGLAND BioLabs® Inc.
enabling technologies in the life sciences

<< Past as Prelude

The Sahel region of West Africa suffered terribly from a severe drought during the 1970s to the 1990s. Because of the disastrous social, economic, and environmental impacts of the drought, it is important to predict how common such droughts may be in the future, which raises the question of how often they may have occurred in the past. **Shanahan *et al.*** (p. 377) present a 3000-year-long record from two West African lakes, whose volumes and geochemistries are sensitive to regional rainfall. Severe, protracted droughts, lasting from decades to centuries, have occurred repeatedly in West Africa over the past few millennia. These results provide a strong incentive to develop better plans for adapting to and mitigating the consequences of the future dry periods expected to occur in a warming climate.

CREDITS (TOP TO BOTTOM): TIMOTHY M. SHANAHAN/UNIVERSITY OF TEXAS AND JONATHAN T. OVERPECK/UNIVERSITY OF ARIZONA; JEREMY LEVY/UNIVERSITY OF PITTSBURGH

How Does Deep Brain Stimulation Work?

Deep brain stimulation is used for the treatment of Parkinson's disease when traditional neurotransmitter replacement with L-DOPA fails. However, we do not understand how deep brain stimulation works. **Gradinaru *et al.*** (p. 354, published online 19 March) used light-sensitive neuronal modulators driven by cell type–specific promoters together with an implantable optical stimulator to drive or inhibit distinct circuit elements in the brains of Parkinsonian rodents. Surprisingly, neither increasing nor decreasing activity in excitatory neurons of the subthalamic nucleus was sufficient by itself to affect motor symptoms. Instead, direct selective high-frequency stimulation of afferent axons projecting to the subthalamic nucleus yielded robust, consistent, and reversible therapeutic results.

Four-Legged and Fishy

The emergence of four-legged creatures and the colonization of land by vertebrates were key events in evolution. Fossils of the Devonian tetrapods *Ichthyostega* and *Acanthostega* have revealed insights into the locomotory patterns of these early land animals. **Callier *et al.*** (p. 364; see the Perspective by **Friedman**) now compare two series of humeri (upper arm bones) from these genera, assumed to belong to individuals at different growth stages. While the growth of the humerus of *Acanthostega* shows no indication of a major functional change during life, that of *Ichthyostega* shows marked differences between juvenile and adult individuals. This suggests that *Ichthyostega* had a more pronounced aquatic lifestyle when young than when adult. This result is at odds with character analyses for early tetrapods, which show *Acanthostega* as the most aquatic tetrapod known from complete skeletons. Thus, *Ichthyostega* may occupy a deeper position in the evolutionary tree than the more aquatic and seemingly more fishlike *Acanthostega.*

Controllable Domain Patterning

Most semiconductor devices are built on a platform of silicon coated with a thin layer of silicon oxide. In fact, it is difficult to avoid the oxide overlayer because silicon readily oxidizes and it can also steal oxygen from any oxide layers that are deposited on top of bare silicon. Using molecular-beam epitaxy, **Warusawithana *et al.*** (p. 367) managed to grow strontium titanate ($SrTiO_3$) onto a silicon substrate. As the film thickness increased, the $SrTiO_3$ showed a transition from being mostly commensurate with the underlying silicon to being a fully relaxed structure. Thinner, strained films showed ferroelectric behavior and could be patterned with domains of either polarity.

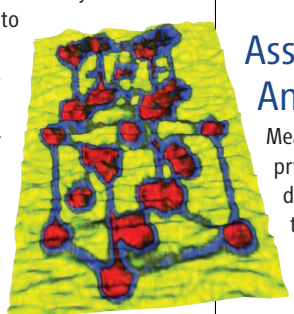

The Clock Strikes Itself

Fermionic particles such as electrons and certain atoms cannot occupy the same space if they are in the same quantum-mechanical state. This property has inspired atomic clock designs based around fermion ensembles, which should boost signal strength through the presence of multiple absorbing atoms without suffering from collisional broadening. **Campbell *et al.*** (p. 360) show, however, that the act of probing an ultracold sample of fermionic strontium atoms gives rise to density-dependent frequency shifts consistent with collisions. This phenomenon may be due to a small degree of inhomogeneity in the interaction of the laser pulse with the atom ensemble, which confers slight distinctions on the states of neighboring atoms and so allows them to interact.

Assessing Asteroid Anomalies

Measurements of isotopic abundances of primitive solar system materials reveal deviations in the stable isotope compositions of some elements compared to those of Earth. These isotope anomalies have been interpreted as signs of imperfect mixing of presolar materials following the collapse of the molecular cloud that formed the solar system. **Trinquier *et al.*** (p. 374) report high-precision measurements of titanium isotopic compositions of a variety of meteorites and objects within them, showing that inner solar system planets and asteroids exhibit correlated anomalies in two titanium isotopes that are produced by different stellar processes. Thus, the protosolar molecular cloud was, in fact, homogenized by the time the oldest dated solar system's solids formed, and other isotope anomalies were created within the solar system by a secondary process.

Continued on page 311

Published by AAAS

www.roche-applied-science.com

xCELLigence

RTCA DP Instrument

Everyone,

Discover what you've been missing!

The RTCA DP Instrument's 16-well E-Plate. Unique gold microelectrodes cover approximately 80% of each well bottom, maximizing sensitivity. Cell activity is monitored by measuring impedance across the electrodes. Well characteristics (size, shape, volume) are identical to those of the E-Plate 96 used with the RTCA SP and MP Instruments.

Available Soon:

Cell Invasion and Migration analysis with the **RTCA DP Instrument!**

Now you have even more choices to monitor your cells. The new **RTCA DP Instrument** is the latest addition to the **xCELLigence Real-Time Cellular Analysis** portfolio, offering additional throughput, format, and pricing options to meet your workflow needs.

- **Monitor cell response in real time with highly sensitive, label-free analysis.**
- **Generate data continuously from up to three 16-well E-Plates independently or in parallel.**
- **Perform a broad range of applications to assess short-term and long-term cellular effects.**

Go beyond end-point analysis. Focus your research with the **xCELLigence System** – now with expanded versatility.

View updated product information, Application Notes, and more at ***www.xcelligence.roche.com***

ACEA Biosciences Inc.

Roche Diagnostics
Roche Applied Science
Indianapolis, Indiana

Roche

Continued from page 309

Immune Cell Origins

In the immune system, dendritic cells, monocytes, and macrophages are critical for the inflammatory response to pathogens. Although these cell types arise from a common hematopoietic precursor, they are functionally diverse, and the developmental relationships between these subsets and where they develop have not been fully delineated in vivo. **Liu *et al.*** (p. 392, published online 12 March; see the cover) elucidate the precursor-progeny relationship between mouse conventional dendritic cells, plasmacytoid dendritic cells, and monocytes. Conventional dendritic cells arise in the bone marrow and traffic to the peripheral lymphoid organs, where further differentiation and expansion occurs.

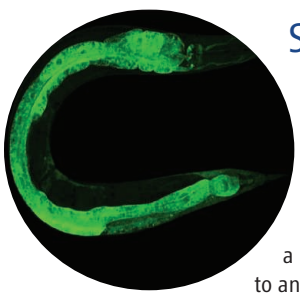

Suffocating Worms

Lack of oxygen rapidly leads to the demise of most animals. **Menuz *et al.*** (p. 381; see the Perspective by **Crowder**) conducted a screen for mutants of the worm *Caenorhabditis elegans* that are particularly sensitive to the effects of anoxia. The gene *Hyl-2*, which encodes a ceramide synthase, is a member of a family of genes that influence life span in yeast. Worms have another gene, *hyl-1*, that also encodes a related ceramide synthase, whose mutants are instead more resistant to anoxia than normal animals. The two ceramide synthases have different specificities for fatty acyl chains, with HYL-2 preferentially producing ceramide molecules with shorter fatty acyl chains. Thus, the abundance of particular ceramides can influence cell survival mechanisms.

Rusty Glacier

Blood Falls at the snout of an Antarctic glacier marks the discharge of an iron-rich subglacial water pocket. **Mikucki *et al.*** (p. 397) now show that the water pocket is ancient seawater that was trapped some 1.5 to 4 million years ago under the advancing Taylor Glacier. The water is anoxic, cryogenically concentrated, loaded with Fe-II, and has no evidence of sulfide. The isotopic composition of the oxygen in the sulfate indicates that reduction of sulfate to sulfite is occurring by microbially coupled sulfur and iron cycles driven by adenosine 5′-phosphosulfate reductase and probably originating in an organic source of sulfur. This system offers a clear example of how a microbial system can survive for an extended period without photosynthesis or nutrients from an external source.

Think Positive

Positive feedback cycles can generate a self-perpetuating pattern of behavior. When the outcome is detrimental, however, these cycles can make it difficult for subjects to escape being drawn further into repetitively negative thinking. **Cohen *et al.*** (p. 400) performed a multiyear field experiment in which three cohorts of 7th-grade students were given seemingly gentle interventions—a brief writing assignment on personal values—several times throughout their 7th- and 8th-grade school years. Poorly performing African American students who had been assigned to write about self-affirmation displayed significantly smaller declines in their grades than those who had written about someone else's values; the intervention had no effect on the grade trends of highly performing African American or European American students. The intervention appeared to help to prevent the poorly performing group from falling into a cycle of negativity.

Understanding Within Reach

Mirror neurons are thought to enable the understanding of the actions of others, possibly by internally simulating observed actions. Now **Caggiano *et al.*** (p. 403) report that, in monkeys, mirror neurons might have a much broader cognitive role. The visual responses of mirror neurons were recorded while the experimenter was executing motor acts either within the monkey's reaching distance (peripersonal space) or out of reach (extrapersonal space). About half of the recorded mirror neurons exhibited spatial selectivity and discharged only when the observed action was executed in the monkey's peripersonal space or only when it was executed in the monkey's extrapersonal space. Although completely unimportant for ''understanding'' the observed action, the relative distance between observer and observed action plays a fundamental role in selecting possible subsequent behavioral responses. Thus, the role of mirror neurons is not limited to understanding actions, but encodes observed motor acts in terms of the monkey's own potential behavior.

CREDIT: MENUZ *ET AL.*

PCR Products

Switch to Superior High Fidelity PCR

PrimeSTAR®

Top Five Reasons to Switch to PrimeSTAR®:

- **Higher Accuracy:** A strong exonuclease activity results in an extremely low error rate, with only 15 errors per 480,000 bp on a GC-rich template.
- **Higher Efficiency:** Higher than *Taq* Polymerase.
- **Robust Amplifications:** A single PCR cycling protocol can be used to amplify products of varying sizes.
- **Greater Specificity:** The antibody mediated Hot Start formulation prevents false initiation events during reaction assembly.
- **Excellent with GC-Rich Targets:** Robust performance with GC-rich templates using the GC buffer formulation.

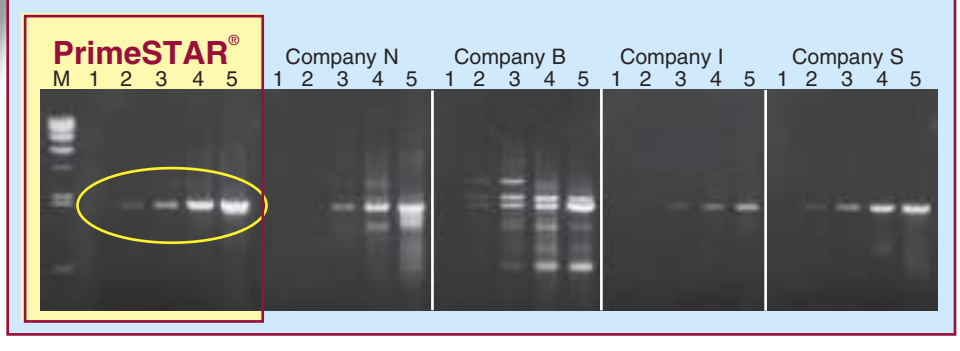

Amplification Efficiency of a 2 kb Human Genomic DNA Fragment (DCLRE1A)**.** Excellent sensitivity and yield are observed when amplifying with PrimeSTAR®. Quantities: Lane1: 0 ng (dH_2O), Lane 2: 100 pg, Lane 3: 1 ng, Lane 4: 10 ng, Lane 5: 100 ng.

TaKaRa

For more information
www.takara-bio.com

Japan:
Takara Bio Inc.
+81 77 543 7247
www.takara-bio.com

USA:
Takara Bio USA
A Division of Clontech Laboratories, Inc
888-251-6618
www.takarabiousa.com

Europe:
Takara Bio Europe S.A.S.
+33 1 3904 6880
www.takara-bio.eu

China:
Takara Biotechnology (Dalian) Co., Ltd.
+86 411 8764 1681
www.takara.com.cn

Korea:
Takara Korea Biomedical Inc.
+82 2 2081 2525
www.takara.co.kr

Alan I. Leshner is the chief executive officer of the American Association for the Advancement of Science and executive publisher of *Science*.

Accountability and Transparency

THERE IS GREAT EXCITEMENT IN THE U.S. SCIENTIFIC COMMUNITY ACCOMPANYING THE ARRIVAL of the new president and his views on the role of science in society. Many people feel that the climate for science has turned 180 degrees. Science has gone from seeming at times to be disregarded or treated as unimportant or even annoying, to again being recognized as central to every major issue of modern life, with superb appointments being made to science leadership positions in government.

Great opportunities come with this increased national commitment, but so do great expectations and responsibilities. Others have recently written on this page about some of them. There is no question that we will need many more people to expand their roles as "scientist citizens" and participate in the policy-making process, contributing in ways in which they have not been asked to do for many years. There also are increased responsibilities associated with the recent boost to science from the U.S. economic stimulus package, the American Recovery and Reinvestment Act (ARRA).

ARRA commits $21.5 billion in additional funding for science and technology programs over the next 2 years, administered through virtually all of the federal science agencies. This funding largesse comes with increased requirements and responsibilities for the scientific community. Because this money must be spent on an unusually short timetable, a substantial portion from the science agencies, including the National Institutes of Health and National Science Foundation (NSF), will be spent on proposals that have already been approved. However, many additional programs are also being developed, with requests for proposals being released every week. These requests will trigger new research and infrastructure development proposals that will have to be evaluated rapidly. The agencies can only do this with enormous help from the scientific community as reviewers and advisory panel members. Scientists have an obligation to step up and participate in these additional review processes, giving this service an even higher priority than in the past. If they don't, of course, the possible outcomes could be grim: Mediocre or irrelevant projects could inadvertently be funded, or even worse, the entire funding system could stall, and that could threaten future support for science. Thus, the success of the U.S. science funding system depends on full participation in the process by the entire science community.

In addition, President Obama has declared that his administration and its programs will be characterized by increased openness, transparency, and accountability. In this spirit, scientists will have to do a much better job of sharing both the results and the implications of their work with members of the broader public, particularly with policy-makers, to make clear what they do, why they do it, and how it will benefit society.

A recent Important Notice from NSF states that new reporting responsibilities will accompany any ARRA funds. This could be hard to implement because many outcomes are difficult to quantify, and the metrics that can be used differ among the categories of research: basic, translational, and applied. But, as a 1999 report from the U.S. National Academies pointed out, the quality and outcomes of research can be responsibly evaluated.* Although there seems to be a dearth of agreed-upon formal measures of outcome for scientific activities, NSF has a relatively new program called the Science of Science and Innovation Policy that is intended to develop metrics for some of the outcomes, impacts, and implications of science. It may take a while to see the products of this new line of research, but they should be helpful in the longer term in this new climate of accountability and transparency for science.

The confidence expressed by both the Obama administration and the U.S. Congress, and the tremendous infusion of public funds, are great boons to the scientific enterprise and its ability to serve society. The accompanying demand for increased levels of participation, accountability, and transparency from scientists seems an appropriate price to pay.

– Alan I. Leshner

10.1126/science.1174215

*www.nap.edu/catalog/6416.html.

Published by AAAS

MILLIPORE™

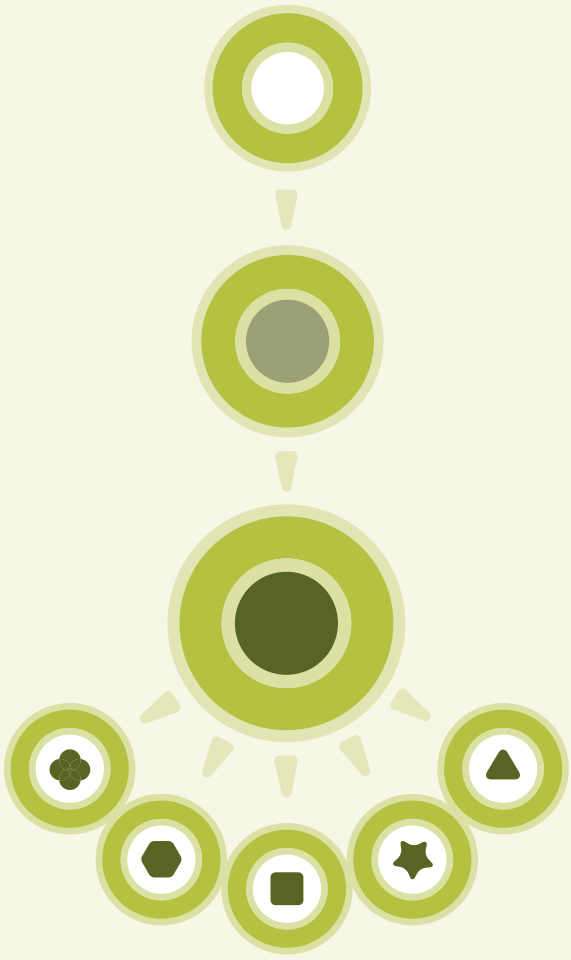

CELL BIOLOGY
CELL SIGNALING
DRUG DISCOVERY
IMMUNODETECTION
LAB WATER
PROTEIN BIOMARKERS
STEM CELL RESEARCH

NEXT GENERATION?

Give rise to controlled differentiation.

We stand with you in our investment in and commitment to stem cell research. By combining Upstate® and Chemicon® products and services with our years of experience supporting Life Science research, we successfully partner with the world's leading scientists to develop proven solutions for human and murine, adult and embryonic stem cell research.

ADVANCING LIFE SCIENCE TOGETHER™

Visit www.millipore.com/stem_cells for more information on this and other ways Millipore supports Life Science research.

THE EXPERTISE OF
CHEMICON® & UPSTATE®
IS NOW A PART OF MILLIPORE

PALEONTOLOGY

Tracks in the Sand

Animals evolved the ability to breathe air and then colonized the land in the Silurian period about 430 million years ago; however, curious tracks preserved by Cambrian microbial mats sitting atop mudflats and dunes seem to imply that arthropods or other animals ventured ashore before then. Hagadorn and Seilacher provide considered thoughts about who made these tracks and how. The tracks show a distinctive tail trace and other marks suggesting that the animals scurried along via the synchronous action of pairs of legs. The tracks, and in particular the tail trace, imply that the animal carried only a small shell, in contrast to, for example, the capacious shell used by a modern-day hermit crab. The authors suggest that an early chelicerate—possibly a eurypterid (sea scorpion)—used a mollusk shell to protect its gills and to keep them hydrated; a larger shell would not have been necessary as there were no other land predators yet. — BH

Geology **37**, 295 (2009).

CELL BIOLOGY

One for You, Two for Me

Asymmetric cell division, wherein the daughter cell receives an unequal set of contents from the dividing mother cell, drives the formation of the many and diverse cell lineages that populate multicellular organisms. The single-celled yeast *Saccharomyces cerevisiae* also undergoes asymmetric cell divisions to produce so-called mother and daughter cells, but as this occurs at every cell division, there are no obviously distinct cell lineages formed, as is true for many unicellular organisms. However, a closer look at the way yeast proteins are segregated during meiosis reveals a rather different outcome.

Thorpe *et al.* have fluorescently tagged a number of proteins from the kinetochore (the molecular machine that links the chromosomes to the spindle in dividing cells and thus ensures their proper segregation) and find that they segregate asymmetrically at the first meiotic division, forming the haploid spore, and also in subsequent divisions, so that they are preferentially retained in the mother cell lineage derived from the spore. These same proteins are symmetrically distributed between other dividing "cell types," and other proteins that are not part of the kinetochore do not show a similar asymmetry. The unequal segregation of the kinetochores may allow for the non-random segregation of sister chromatids, which would thereby maintain an "immortal" DNA strand, or of the centromeric DNA to which the kinetochores bind, which could drive the evolution of the centromeres. — GR

Proc. Natl. Acad. Sci. U.S.A. **106**, 10.1073/pnas.0811248106 (2009).

PHYSICS

Colliding Light Beams

Under normal conditions, photons don't interact with each other very much. For instance, the light beams from two laser pointers pass through each other without trouble. Ramping up the power of the beams, however, changes that somewhat standoffish behavior. High-powered-laser beams can form self-focusing filaments in air that propagate without dispersion. These light bullets or light sabers are finding use in a diverse range of applications from triggering lightning to remote spectroscopic sampling. Finding ways of controlling propagation on the wing rather than tinkering with the laser on the ground would offer much more flexibility.

Bernstein *et al.* take two high-powered laser beams and collide them. Rather than passing through each other unscathed, the beams couple and exchange energy, up to 7%, with one beam amplifying the other at its own expense. Being able to tune the output of the collision in terms of the energy and frequency distribution of the modified light pulses should provide a powerful and flexible method for remote sensing applications. — ISO

Phys. Rev. Lett. **102**, 123902 (2009).

CELL BIOLOGY

A Store Manager

Cells stockpile nutrients and metabolites in storage compartments that can be raided when environmental conditions change. Lipid droplets are dynamic cellular caches of neutral lipids, such as triacylglycerol, which can be used as high-energy reserves, signaling molecules, and membrane building blocks. On the other hand, lipid droplets have been implicated in devastating metabolic diseases, such as diabetes and atherosclerosis, and are found in almost all cells from yeast to mammals. Nevertheless, relatively little is known about how they are formed.

Eastman *et al.* have established that the protein SPG20 (also known as spartin) regulates lipid droplet formation. Using cultured human cells, they found that SPG20 localized to lipid droplets and interacted with the lipid droplet–associated protein TIP47. SPG20 localization was regulated by WWP1, a member of the HECT-ubiquitin ligase family that modulates diverse cellular functions by tagging proteins with ubiquitin. Further, mutations in SPG20 have been linked to the rare neurological disease Troyer syndrome, which is characterized by muscle spasticity and limb paralysis; a disease-associated SPG20 mutant did not localize to lipid droplets. — HP*

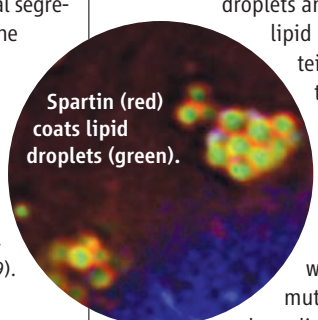

Spartin (red) coats lipid droplets (green).

J. Cell Biol. **184**, 881 (2009).

*Helen Pickersgill is a locum editor in *Science*'s editorial department.

CREDITS (TOP TO BOTTOM): WHITEY HAGADORN; EASTMAN *ET AL.*, *J. CELL BIOL.* **184**, 881 (2009)

Published by AAAS

www.sciencemag.org

Science

1200 New York Avenue, NW
Washington, DC 20005
Editorial: 202-326-6550, FAX 202-289-7562
News: 202-326-6581, FAX 202-371-9227
Bateman House, 82-88 Hills Road
Cambridge, UK CB2 1LQ
+44 (0) 1223 326500, FAX +44 (0) 1223 326501

Subscription Services For change of address, missing issues, new orders and renewals, and payment questions: 866-434-AAAS (2227) or 202-326-6417, FAX 202-842-1065. Mailing addresses: AAAS, P.O. Box 96178, Washington, DC 20090-6178 or AAAS Member Services, 1200 New York Avenue, NW, Washington, DC 20005

Institutional Site Licenses please call 202-326-6755 for any questions or information

Reprints: Author Inquiries 800-635-7181
Commercial Inquiries 803-359-4578

Permissions 202-326-7074, FAX 202-682-0816

Member Benefits AAAS/Barnes&Noble.com bookstore www.aaas.org/bn; AAAS Online Store www.apisource.com/aaas/ code MKB6; AAAS Travels: Betchart Expeditions 800-252-4910; Apple Store www.apple/eppstore/aaas; Bank of America MasterCard 1-800-833-6262 priority code FAA3YU; Cold Spring Harbor Laboratory Press Publications www.cshlpress.com/affiliates/aaas.htm; GEICO Auto Insurance www.geico.com/landingpage/go51.htm?logo=17624; Hertz 800-654-2200 CDP#343457; Office Depot https://bsd.officedepot.com/portalLogin.do; Seabury & Smith Life Insurance 800-424-9883; Subaru VIP Program 202-326-6417; VIP Moving Services www.vipmayflower.com/domestic/index.html; Other Benefits: AAAS Member Services 202-326-6417 or www.aaasmember.org.

science_editors@aaas.org	(for general editorial queries)
science_letters@aaas.org	(for queries about letters)
science_reviews@aaas.org	(for returning manuscript reviews)
science_bookrevs@aaas.org	(for book review queries)

Published by the American Association for the Advancement of Science (AAAS), *Science* serves its readers as a forum for the presentation and discussion of important issues related to the advancement of science, including the presentation of minority or conflicting points of view, rather than by publishing only material on which a consensus has been reached. Accordingly, all articles published in *Science*—including editorials, news and comment, and book reviews—are signed and reflect the individual views of the authors and not official points of view adopted by AAAS or the institutions with which the authors are affiliated.

AAAS was founded in 1848 and incorporated in 1874. Its mission is to advance science, engineering, and innovation throughout the world for the benefit of all people. The goals of the association are to: enhance communication among scientists, engineers, and the public; promote and defend the integrity of science and its use; strengthen support for the science and technology enterprise; provide a voice for science on societal issues; promote the responsible use of science in public policy; strengthen and diversify the science and technology workforce; foster education in science and technology for everyone; increase public engagement with science and technology; and advance international cooperation in science.

Information for Authors
See pages 807 and 808 of the 6 February 2009 issue or access www.sciencemag.org/about/authors

EDITED BY CONSTANCE HOLDEN

Darwin's Egg

The University of Cambridge's zoology museum has come across a long-forgotten egg that Charles Darwin collected during his famous voyage on the *Beagle*. The 4.7-centimeter-long egg, from a partridgelike bird, is cracked: "The great man put it into too small a box, and hence its unhappy state," according to records found with it.

"It's the only egg that we know for sure was collected by Darwin," even though he collected eggs and nests from at least 16 types of birds on his travels, says museum director Michael Akam.

A volunteer rediscovered the egg while cataloging the museum's egg collection, which had lain uninventoried for a century. It was in a collection belonging to Alfred Newton, a zoologist and friend of Darwin's, who noted in his journal: "One egg, received through [Darwin's son] Frank Darwin, having been sent to me by his father who said he got it at Maldonado [now in Uruguay] and that it belonged to the Common Tinamou [now the spotted nothura] of those parts."

"This is an extremely interesting and significant ornithological find," says Douglas Russell, bird curator at the Natural History Museum in London. It should encourage other researchers "looking for famous missing specimens."

UCSD Backs Off On Bone Bid

Officials at the University of California, San Diego, have withdrawn a request to the federal government to rebury 10,000-year-old skeletal remains unearthed on UCSD property.

The bones were found in 1976 near the chancellor's house in San Diego, and they're even "older and better preserved" than Kennewick Man, says UCSD anthropologist Margaret Schoeninger. In 2006, the local American Indian group, the Kumeyaay nation, requested the bones for reburial. Two university committees ruled against the request, saying there is no evidence of cultural affiliation with living groups, as the federal Native American Graves Protection and Repatriation Act (NAGPRA) requires. Nonetheless, UCSD officials decided to hand over the bones.

The chancellor's house double burial.

Now they've withdrawn that request—not because of loud protests that came from anthropologists but because the Kumeyaay don't like the wording, according to a UCSD statement. Kumeyaay leaders objected last week to UCSD's calling the remains culturally unidentifiable—an acknowledgment that could hurt their cause in this and future cases before the NAGPRA review committee, which meets in Seattle, Washington, in May.

Schoeninger, co-director of the UCSD Working Group that reviewed the original request, reported at the annual meeting of the American Association of Physical Anthropologists in Chicago, Illinois, last week that her lab's analysis of the bones indicated a marine diet, suggesting the bones were from coastal inhabitants rather than from the desert-dwelling Kumeyaay. Besides, she says, other evidence suggests the Kumeyaay moved into the region just 2000 years ago.

Caveat Vendor

Defective spermatozoa can be covered by product liability law, a Pennsylvania federal district judge has ruled. A 13-year-old girl with fragile X syndrome has gotten the go-ahead to sue the New York sperm bank that supplied her mother with the wherewithal to conceive her, *The Legal Intelligencer* reported this month. New York state has a "blood shield statute" prohibiting liability suits on blood products, but it doesn't cover sperm, the judge ruled.

RETURN OF THE NATIVE

Tony Chan, formerly dean of physical sciences at the University of California, Los Angeles (UCLA), and currently in charge of mathematical and physical sciences at the U.S. National Science Foundation, is joining Asia's reverse brain drain: After almost 40 years in California, he's returning to his hometown to take on the presidency of the Hong Kong University of Science and Technology (HKUST). "He is really an ideal president for HKUST," says Ping Sheng, a physicist at the school.

Founded in 1991, HKUST aspires to become the Massachusetts Institute of Technology of Asia. So far, it's relatively small, with 5868 undergraduates, 3259 grad students, and 461 faculty members. "Its culture and tradition are still being developed," says Chan, and it has yet to attract the top high school graduates.

A mathematician and computer scientist, Chan, 57, has his work cut out for him. The faculty will have to grow as all Hong Kong universities move from a 3-year to a 4-year undergraduate curriculum in 2012. He also has to bring HKUST's new Institute for Advanced Study, which aims to be a "premier intellectual center in Asia," up to speed. As yet, it has no resident scholars, and construction of a home for it won't start until later this year. "The most immediate task is to recruit a visionary director," says Chan.

Chan, whose 5-year contract starts in September, says his return to Hong Kong may be permanent, but he'll retain professor emeritus status at UCLA.

CREDITS (TOP TO BOTTOM): UNIVERSITY OF CAMBRIDGE ZOOLOGY MUSEUM; JAN AUSTIN; HKUST

Published by AAAS

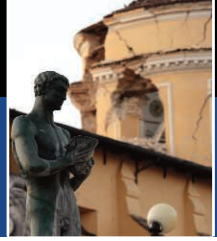

Aftershocks from quake prediction
322

Q&A with Obama's science adviser
324

U.S. SCIENCE POLICY

NIH Stimulus Plan Triggers Flood Of Applications—and Anxiety

The past month has been a blur for neuroscientist Chiara Cirelli. She's been so busy preparing grant applications to the National Institutes of Health (NIH) that she has stopped reviewing papers by colleagues. She's barely set foot in her lab at the University of Wisconsin, Madison, not to mention her garden.

Cirelli's group already has two basic R01 research grants and a center grant for its sleep research. But the chance to use a piece of NIH's $10.4 billion share of the recent stimulus package to hire students and postdocs, buy equipment, and expand their studies of adult animals to young mice is proving irresistible. "I just can't not do it," says Cirelli.

Nor can thousands of her peers. As a result, biomedical scientists across the country have been cranking out grant applications for the $8.2 billion in NIH funds for extramural research in the American Recovery and Reinvestment Act (ARRA) of 2009. "It's like the day after Thanksgiving, when everybody's lined up at Wal-Mart for the new Tickle Me Elmo doll," says Brian Dedecker, a cell biologist at the University of Colorado, Boulder, who has decided not to enter the fray. NIH's shelves are stocked with infrastructure grants, extensions of existing awards, and enticing new competitions, in particular Challenge Grants of up to $1 million apiece. Research deans say the proposals flooding their offices reflect the pent-up need across a 5-year period in which NIH's budget lost 13% of its purchasing power.

The excitement, however, is tinged with anxiety. The ARRA grants require scientists to report quarterly on how they're spending the money and how many jobs are created and saved. With up to 10,000 applications for perhaps 200 Challenge Grants, the competition is also expected to cause a spike in applications for NIH's regular R01 grants in the next few years as investigators who come up empty recycle their proposals. That surge will be combined with scientists reapplying in 2011 to continue work funded with ARRA money.

If NIH's budget—now $30.3 billion—doesn't keep pace, the pain could be even more acute than what scientists experienced after a 5-year doubling of NIH's budget ended in 2003. "What really worries me is that we could fall off a cliff again," says Karen Antman, dean of the Boston University School of Medicine. At the same time, she says, "I've never seen the faculty so happy" for a chance to compete for additional funding.

As dictated by the Recovery Act, $7.4 billion is split among NIH's 27 institutes and centers, many of which plan to spend the lion's share on 2-year awards for proposals that just missed the cut last year. Another $1.3 billion is going to construction and instrumentation. The NIH director's office has divvied up about two-thirds of its allotted $800 million among four competitions: $200 million for the Challenge Grants, another $200 million for Grand Opportunities (GO) Grants of at least $1 million, $100 million for new faculty hiring at core academic facilities (*Science*, 3 April, p. 27), and $21 million for summer research experiences for students and teachers. Five institutes have joined to offer $60 million for autism research, and more announcements are expected. The agency hasn't yet determined the final split between funding existing proposals and new competitions.

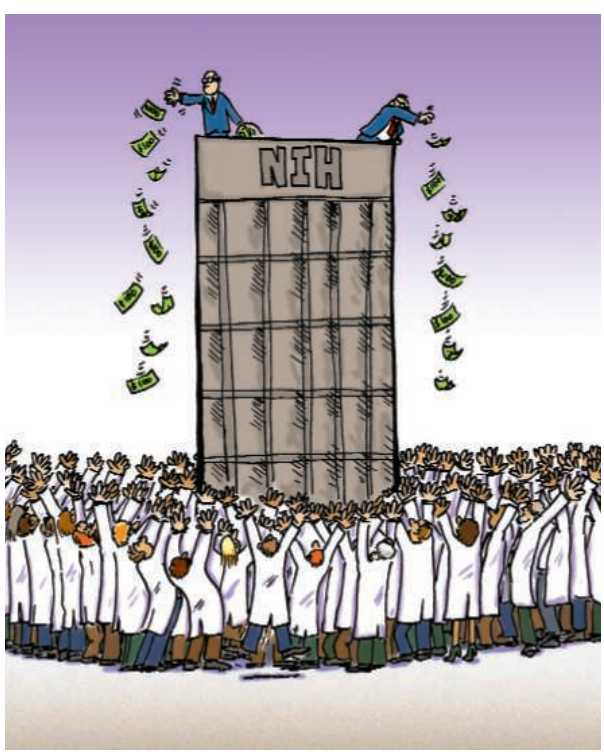

CREDIT: JOE SUTLIFF/WWW.CDAD.COM/JOE

The recovery money has thrown a lifeline to investigators who missed the funding cutoff last year and were surviving on other funds. Heidi Hamm, chair of pharmacology at Vanderbilt University in Nashville, Tennessee, says four of 24 people in her department have been told that they will likely receive 2-year grants. "That's huge," she says. Many others, including Cirelli, are requesting supplements to existing grants or proposing an extension of the work, known as a competing supplement.

The most alluring prize, however, seems to be the Challenge Grants, which can cover research on any of 15 broad categories, from bioethics to stem cells. The 12-page maximum for proposals is only half the current length of an R01 application, and applicants don't need to show preliminary data. Susan Bryant, vice chancellor for research at the University of California, Irvine, says her campus will be submitting "over 200" such applications. Johns Hopkins University molecular pathologist Anirban Maitra is working on three Challenge Grants, two for early detection of pancreatic cancer and one for nanotechnology. "My philosophy is, let's try to maximize our chances," says Maitra.

University of Minnesota cancer biologist Peter Bitterman is submitting a Challenge proposal and a GO proposal, both involving drug discovery. He says it's worth the effort even though the odds are long. "It's obvious. Once you've prepared a grant [application] and it's ready to go, it can be submitted as an investigator-initiated R01."

Processing these proposals is expected to strain the federal online

Published by AAAS

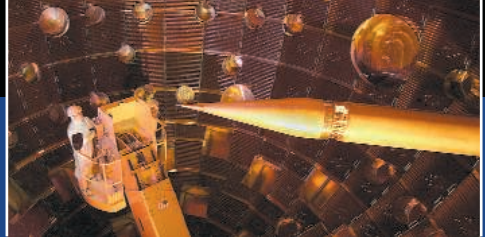

Laser fusion's critical point
326

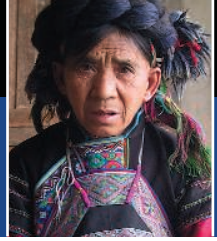

China's linguistic heritage
332

NSF IS KEEPING IT SIMPLE

The National Science Foundation (NSF) is using its $2 billion windfall from the American Recovery and Reinvestment Act to fund more proposals already in the pipeline, reducing what officials say is a $2-billion-a-year backlog of good ideas. That's quite a contrast from the National Institutes of Health (NIH), which has rolled out an array of mechanisms, including new competitions and several types of supplemental grants targeting various audiences, to allocate its $8.2 billion in research funds from the $787 billion stimulus package (see main text).

Two weeks ago, an advisory panel for NSF's math and physical sciences directorate spent a large chunk of its 2-day meeting discussing how various federal agencies are spending the stimulus money. They were particularly concerned about NSF's policy not to top off existing grants with supplement awards, citing new competitions at NIH to support teachers and students, to broaden participation, and to welcome back researchers whose scientific careers have been interrupted.

NSF Director Arden Bement defended his approach during a lunch with the committee, explaining that Congress has told NSF to boost success rates—approximately one in four grant proposals is funded—within the parameters of the overall goal to create or preserve jobs. "Our philosophy is KIS—keep it simple," he said. "That's the only way to get [the money] out the door in a timely fashion." Bement also said the "robust" tracking requirements of the legislation preclude supplements to existing projects. "We can't mix the money," he said.

In synch. Bement says he's following the wishes of Congress.

Despite those stipulations, he said, NSF isn't ignoring the needs of early-career scientists. NSF can still use its regular budget to support requests for supplements from current grantees, he said, citing $7 million in supplemental grants that NSF's math division has allocated from its just-passed 2009 budget to create an additional 30 or more postdoctoral positions at the seven NSF-funded mathematics research institutes. "All this angst over supplements is not well-founded," he scowled.

Sally Rockey, acting head of NIH's extramural research program, says that NIH has managed to go where NSF feared to tread by making each supplement a separate grant. However, she emphasizes that "institutions will have to track [the spending] carefully."

The lack of alternatives bothered Héctor Abruña, a chemist at Cornell University and a member of the advisory panel. "Where's his vision?" asked Abruña. "NSF seems more concerned with process, reducing paperwork, and making things easier for program managers than with the challenges facing the scientific community."

Panelist and Yale University chemist William Jorgensen also spoke in favor of supplements, noting that they would boost undersized NSF grants as well as help fledgling scientists. But Jorgensen, a longtime NSF grantee who's not currently receiving NSF funding, says he's not unhappy that the foundation is concentrating on boosting success rates. Giving the money to established scientists, he says, "sends the right message to PIs [principal investigators] and is very clean."

–JEFFREY MERVIS

site, Grants.gov, through which all NIH applications must pass. Antman says she's asked her grants' staff to work on weekends and at night when the volume of traffic is lower: "You push the button 20 times and it doesn't go through," she says. Some universities have moved up NIH deadlines by a week or more to ease the strain on harried staff.

Once the proposals are submitted—each competition has its own deadline, and the rules for supplements vary by institute—reviewing the Challenge Grants, GO grants, and other competing proposals is "going to be a major amount of work," says Sally Rockey, acting director of NIH's office of extramural research. For the Challenge Grants, NIH expects to test out a new "editorial board" model where proposals will be e-mailed to subject experts. The board will then meet in person to assign global scores.

The scope of the proposals is expected to be very broad. Drawing from their strategic plans, institutes have described nearly 900 topics as worthy of consideration, with 150 highlighted as priority areas. Although NIH is under no obligation to fund work in any single area, the competition is nonetheless expected to be fierce. One saving grace: Institutes have the option of tapping their recovery money to award additional Challenge Grants.

Some researchers are passing on the current competitions. Instead, they've elected to wait a few months to submit a regular R01 proposal for 4 years of funding, betting that they'll have a better shot because of a dip in applications. Early-career investigators have a second reason to eschew Challenge Grants. NIH now relaxes the pay line for young scientists who haven't yet received an R01, and officials have decided that the Challenge Grant is large enough to strip new investigators who win them of their protected status.

"I'd give up my advantage in applying for an R01. That's a big deal," says Dedecker, who came to Colorado in 2006 and hasn't hit NIH pay dirt yet. He adds, only half in jest, "Besides, I would rather have my regular grant rejected in a thoughtful fashion."

The big question is whether NIH's budget will grow at anywhere close to the rate needed to handle the blizzard of new ideas and expanded scientific work force. Last month, Acting NIH Director Raynard Kington warned a congressional spending panel that success rates could drop "several points" if NIH does not receive a "substantial" budget increase. The National Institute of Allergy and Infectious Diseases, for example, is already warning on its Web site that it "will be very difficult for people to secure funding" from NIH's regular budget once the stimulus money runs out.

To help smooth things out, NIH has announced that researchers can ask for a 1-year unfunded extension of their grant. But that may not be enough to avoid a second crash landing.

–JOCELYN KAISER

With reporting by Eliot Marshall and Jeffrey Mervis.

CREDIT: NIST

REPRODUCTIVE BIOLOGY

Study Suggests a Renewable Source Of Eggs and Stirs More Controversy

A new study has turned up the heat on an already blazing—and sometimes nasty—debate over one of the dogmas of reproductive biology: that female mammals start life with a limited number of eggs and cannot produce new ones after birth.

The work, done in mice by stem cell biologist Ji Wu and colleagues at Shanghai Jiao Tong University in China, suggests that adult ovaries harbor primitive germline cells that can give rise to new eggs, or oocytes, and those in turn, when fertilized, can produce healthy offspring. If confirmed, the implications for reproductive biology and the possible treatment of infertility are enormous.

"It's a beautiful paper," says Evelyn Telfer, a reproductive biologist at the University of Edinburgh in the United Kingdom. It is "very tight," she says, and shows "quite clearly that there are cells in the ovary that have the capacity to form germ cells" that are progenitors of eggs.

Developmental geneticist Robin Lovell-Badge of the National Institute for Medical Research in London takes the opposite view. "To me, this is a very incomplete piece of work that will only add to the confusion," he says.

For at least 50 years, the theory that female mammals do not produce new eggs after birth has been thought to explain why fertility declines with age; in women, menopause is believed to commence when the store of eggs is exhausted. Reproductive biologist Jonathan Tilly and colleagues at Harvard Medical School in Boston kickstarted the current debate with a 2004 paper that claimed that oocytes in mouse ovaries die too quickly for a limited supply to last the animals' reproductive life span. They also identified cells expressing a gene unique to the germ cells that give rise to sperm and eggs. When they grafted pieces of normal ovaries into mice with ovaries expressing green fluorescent protein (GFP), they later observed green fluorescing oocytes in the grafted tissue, presumably generated by the host's germ cells (*Science*, 12 March 2004, p. 1593).

Some subsequent studies supported Tilly's findings, while others contradicted them. In a review published in the January 2009 issue of *Biology of Reproduction*, Tilly cited 16 previous commentaries that were split on whether the preponderance of evidence supported the orthodox or heretical view. "The viciousness of the debate has scared a lot of people away from this area," Tilly says.

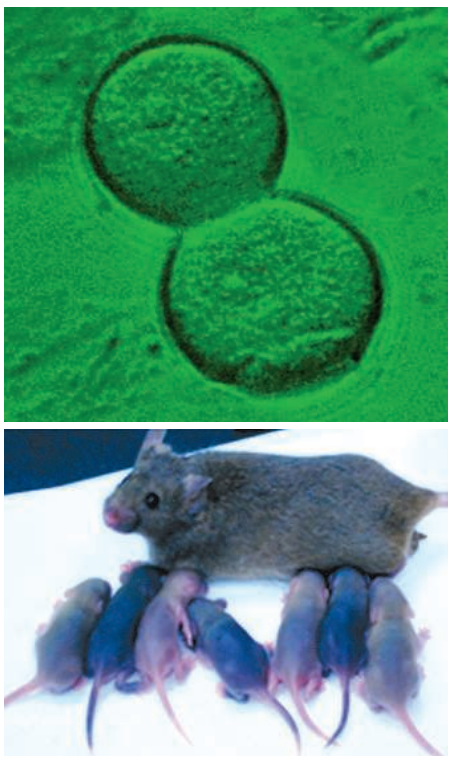

Ultimate test. When transplanted into sterile mice, female germline stem cells, shown dividing (*top*), can give rise to eggs that when fertilized produce healthy offspring.

In particular, no one had succeeded in culturing the putative female germline stem cells (FGSC) until Wu's team tried an overlooked technique called immunomagnetic isolation. In this approach, tiny magnetic beads coated with an antibody latch onto a protein expressed only by germline stem cells. A magnetic screen collects cells with attached beads. The group then cultured FGSCs collected from the ovaries of newborn and adult mice through numerous cycles of division, even freezing and thawing them without any apparent ill effects. Next, they infected the cells with a harmless virus carrying the GFP gene and transplanted them into the ovaries of sterilized mice. After mating with normal males, the females gave birth to healthy, fertile offspring, some of which carried GFP throughout their bodies. The group's paper was published on 12 April by *Nature Cell Biology*.

Telfer, who co-authored two critical reviews of Tilly's work, says the paper "vindicates" Tilly's 2004 conclusion that germline stem cells exist in mouse ovaries. But not everyone is convinced. "Large claims require searing critical scrutiny, and I will reserve final judgment until it is replicated elsewhere," says Roger Gosden, a reproductive biologist at Weill Cornell Medical College in New York City. "Replication has been a historic problem for many stem cell studies."

Lovell-Badge says there are alternative explanations for many of the group's findings, and additional experiments would have bolstered the claims had they been done. He also questions how immunomagnetic isolation could work on a protein found within cells and not on the surface.

In an e-mail exchange with *Science*, Wu pointed to reports by others indicating that a part of the protein extends beyond the cell membrane. Jeffrey Kerr, a developmental biologist at Monash University, Clayton, in Australia, agrees that the Wu team captured germline stem cells. The "molecular signatures are commensurate with known characteristics of other stem cells including germ cells," he says. "Based on the data reported, these cells qualify as FGSCs."

Telfer adds that "by producing live young, these cells have passed the ultimate test to prove their germline credentials." Tilly predicts confirmation won't be long in coming, as Wu and her colleagues "spell out a simple protocol [for isolating FGSCs] that any lab can now try," he says.

Both sides agree that if the findings are confirmed and if FGSCs are found in human ovaries, they might offer new options to treat human infertility caused by cancer therapies, disease, or aging. "Identification and isolation of such [cells] in the human ovary may revolutionize the field of fertility preservation," says Kutluk Oktay, a reproductive endocrinologist at New York Medical College in Valhalla. "I have not been excited about a scientific piece like this for a long time." David Albertini, a reproductive scientist at the University of Kansas Medical Center in Kansas City, adds a caution: "Let's be careful about how relevant this is for humans." Telfer suspects that the debate will soon shift to the physiological role these cells normally play. She suspects that FGSCs are usually quiescent and become active only if the ovary is damaged. Wu, on the other hand, thinks that "under normal conditions, [FGSCs] can renew themselves and differentiate into oocytes." "This paper opens up so many questions, we could spend an hour talking about possibilities," says Tilly.

–DENNIS NORMILE

CREDITS: K. ZOU *ET AL.*, *NATURE CELL BIOLOGY* (ADVANCE ONLINE PUBLICATION, 12 APRIL 2009)

GEOCHEMISTRY

Great Oxidation Event Dethroned?

The wait was worth it for the pond scum. For more than a billion years, one-celled denizens of early Earth had held their own under an atmosphere devoid of oxygen. Finally, 2.4 billion years ago, photosynthesis had built up free oxygen so that life could begin to move toward complex, active organisms and eventually to us. At least, that's the story a clever isotopic analysis seemed to tell, muffling a decades-long debate over when oxygen first gained the upper hand.

But new laboratory results reported in this issue challenge that mainstream scenario by showing how supposed signs of an early lack of oxygen could have come from unrelated geochemical reactions. Still, the Great Oxidation Event will likely reign a while longer. "Now we can go back to arguing the preponderance of evidence," says geochemist Ariel Anbar of Arizona State University, Tempe. "I think it still would be on the side of there not being a lot of oxygen" before 2.4 billion years ago.

By 2000, mineralogical and isotopic evidence had convinced most researchers that not even a whiff of oxygen was in the air before the event. But some, such as geochemist Hiroshi Ohmoto of Pennsylvania State University (PSU), University Park, still argued that oxygen was abundant much earlier.

Then in 2000, geochemist James Farquhar of the University of Maryland, College Park, came up with a nifty technique involving sulfur isotopes. The proportion of one isotope to another of the same element can change during a chemical reaction. Normally, the change depends on the masses of the isotopes. But Farquhar found isotopic shifts among three sulfur isotopes before 2.4 billion years ago that hadn't depended on isotope mass. As far as anyone knew, such "mass-independent fractionation" (MIF) could have happened only under solar ultraviolet radiation in an oxygen-free atmosphere—and MIF sulfur disappeared 2.4 billion years ago. That result "shut down the discussion" about oxygen's arrival, says Anbar.

Undaunted, Ohmoto and Yumiko Watanabe of PSU set out to confirm theoretical hints that MIF sulfur can also be produced in the presence of hot, solid proteins. On page 370, they and Farquhar—who performed the critical isotopic analyses—report that, under conditions crudely mimicking ancient hot springs, two amino acids can indeed produce very small degrees of MIF. "The results defy all expectations," says early-life specialist Bruce Runnegar of the University of California, Los Angeles.

In a carefully worded conclusion, the paper suggests that the newly discovered reactions reopen the question of early oxygenation. "This is at least a possibility that we should be thinking about," Ohmoto says. Personally, he adds, "I feel the findings we made fit nicely to what I've been saying for years." Farquhar, on the other hand, thinks the lab results may be relevant to the geologic record but considers it "much more likely" that the MIF signal marks the first appearance of atmospheric oxygen, he writes in an e-mail.

Other specialists, including Runnegar, agree with Farquhar. The effect in the lab is small—10% of the amount of MIF found in the geologic record—observers note, and there's no convincing reason why the hot-spring reactions would have shut off at 2.4 billion years. "I think it is still more likely to be of atmospheric origin," says geochemist Shuhei Ono of the Massachusetts Institute of Technology in Cambridge, "so the current idea of an [early oxygen-free] atmosphere still holds."

–RICHARD A. KERR

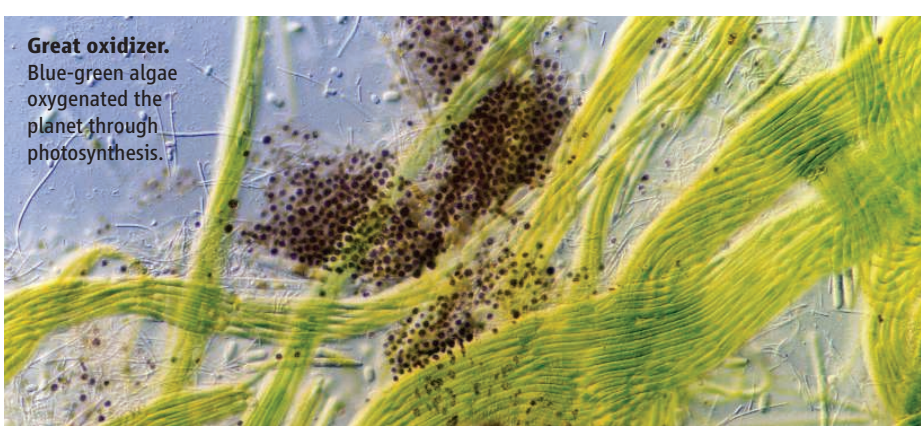

Great oxidizer. Blue-green algae oxygenated the planet through photosynthesis.

CREDITS (TOP TO BOTTOM): COURTESY JEROME PASQUERO/MCGILL UNIVERSITY; (PHOTO) LEE PRUFERT-BEBOUT, NASA MICROBES IMAGE GALLERY, MICROBES.ARC.NASA.GOV/GALLERY/LIGHTMS.HTML

ScienceNOW.org

From *Science*'s Online Daily News Site

Blasting for Ice on Mars. The Phoenix lander has given scientists a close look at the ice in one spot high in the martian arctic, but researchers have also been surveying fresh craters across the planet for signs of frozen water. Now two teams reported at the recent Lunar and Planetary Science Conference in The Woodlands, Texas, that they have detected ice that is relatively pure—far purer than expected on a dusty, dirty planet. The finds lend support to a scenario of an ancient "iceball Mars" in which ice encased much of the planet. http://tinyurl.com/avj6g7

What You See Is What You Feel. Stare at a waterfall long enough, and nearby stationary objects such as rocks and trees will seem to drift up. The optical illusion is called motion aftereffect, and it may trick more than just your eyes, according to a new study published in *Current Biology*. When subjects watched a stationary stripe on a computer screen after a machine stroked their fingertips, the motion of the stroking created the illusion that the stripe was moving. The discovery demonstrates for the first time a two-way crosstalk between touch and vision, challenging long-held notions of how the brain organizes the senses. http://tinyurl.com/c4b92j

Want to Stop Malaria? Target the Geezers. Kill 'em fast, kill 'em young. That's been the unofficial motto in insect control for the past 50 years. But a new paper in *PloS Biology* suggests that, at least in the case of malaria, the strategy may be misguided. By choosing insecticides that act more slowly, or that specifically target older mosquitoes, researchers may be able to prevent the evolution of pesticide resistance, a problem that has long bedeviled malaria-control efforts. http://tinyurl.com/c5tzct

Read the full postings, comments, and more on **sciencenow.sciencemag.org**.

Published by AAAS

Shocker. The quake smashed old buildings like L'Aquila's Duomo.

EARTHQUAKE PREDICTION

After the Quake, in Search of the Science—or Even a Good Prediction

Did technician Gioacchino Giuliani successfully predict last week's quake that crumbled buildings in the Italian city of L'Aquila, killing more than 270? He thinks so, and he's been all over the Italian media since then, claiming credit and demanding an apology from Italian authorities who silenced him a week before the quake and from Italian scientists who said there was no merit in his methods.

Neither side is backing down. The scant documentation of Giuliani's methods of prediction that has begun to surface offers no real evidence of the technique's efficacy, scientists say. Giuliani's recent predictions were wrong or reported after the quake struck, they note, and earlier efforts to correlate releases of radon gas—the marker on which Giuliani bases his predictions—with the seismic record are unconvincing.

"I think Giuliani is speaking in good faith," says Warner Marzocchi, a chief scientist at the National Institute of Geophysics and Volcanology in Rome, "but all the things he's presented, may I say, are at a very low level from a scientific point of view. That does not mean radon is not a potential precursor, [but] I didn't see any evidence the method could work."

As central Italy suffered a disquieting "earthquake swarm"—a surge in seismic activity—beginning this past January, Giuliani began attracting national attention by aggressively promoting his seismic predictions through the media. On 24 March, in an interview posted on the Italian-language blog *Donne Democratiche* (www.donnedemocratiche.com/?p=2219), he explained how he and two colleagues got into quake prediction and what their work meant for the quake-prone region around the city of L'Aquila, northeast of Rome. In 2000, while working on a particle physics experiment in a subterranean laboratory of the National Institute of Nuclear Physics near L'Aquila—where Giuliani still works—they incidentally detected a rise in radon at the same time an earthquake struck Turkey more than 1200 kilometers away.

Radon-earthquake connections had spurred scientists in the 1970s and '80s to try to predict quakes, but decades of work came to nothing. Levels of radon seeping from the ground rose and fell a lot, it seemed. Sometimes quakes followed; often they didn't. Undeterred, Giuliani and his colleagues designed and built five radon monitors that now dot the region around L'Aquila.

Asked what light he could shine on the intensifying seismic activity of the L'Aquila region, Giuliani gave *Donne Democratiche* a prediction: The swarm of low-level quakes was a "normal phenomenon" for the region, was not a precursor to a larger event, and would diminish by the end of March. On 30 March, the largest event in the series up to that time—a magnitude 4.0—struck L'Aquila.

About a week before the 6 April magnitude-6.3 quake, Giuliani made his second prediction. He has not responded to repeated inquiries from *Science*, but according to media reports, Giuliani told the mayor of the town of Sulmona, 55 kilometers to the southeast of L'Aquila, to expect a damaging earthquake within 6 to 24 hours. As widely reported in the media, vans mounted with loudspeakers blared warnings to residents to flee. Sulmona never got its quake, but by then Italian authorities had told Giuliani that he was panicking an already jittery populace and they would not allow him to publicize any predictions.

That meant Giuliani's third claimed prediction—a forecast of the L'Aquila quake, which Giuliani told reporters he had shared with colleagues—went unverified. After the fact, Giuliani told the media he had found alarming rises in radon levels in the hours before the big one, even as two of the strongest quakes in the intensifying swarm struck. As levels of both radon and seismic activity rose, his predictions mounted as well, until he was foretelling an imminent quake of greater than magnitude 4.0, he told reporters and talk show hosts. A quake did indeed strike within hours, but it was 1000 times more powerful than that minimum prediction. Such an open-ended prediction of magnitude—from minimally damaging to catastrophic—is of little use to those responsible for public safety, scientists say.

Marzocchi, who works on the forecasting of earthquakes and volcanoes, has examined two Italian-language documents containing examples of Giuliani's radon records used to make predictions: a patent application (www.wipo.int/pctdb/en/wo.jsp?WO=2004061448) and a chronological account of the method's development (www.chiocciolandia.it/index2.php?option=com_docman&task=doc_view&gid=2&Itemid=38). He is not impressed. "It's very hard to find anything good in this work," says Marzocchi. The problem is too many peaks in radon records that are too short, he says (see figure). Earthquakes ("ev" 1 and 2 dots) are associated with supposedly precursory radon peaks with no obvious rhyme or reason, he says. For example, there's no correlation between the size of the peaks and the magnitudes of the subsequent quakes. "These figures are unacceptable from a scientific point of view," he concludes.

–RICHARD A. KERR

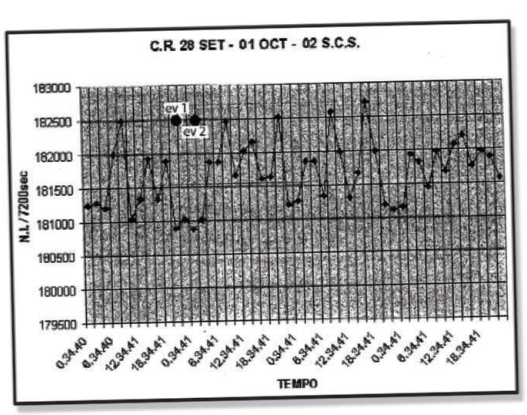

Correlated? In a prediction scheme, a quake ("ev") follows a notable radon peak.

CREDITS (TOP TO BOTTOM): ALESSANDRO GAROFALO/REUTERS/LANDOV; WORLD INTELLECTUAL PROPERTY ORGANIZATION (WIPO)

CLIMATE CHANGE

New Push Focuses on Quick Ways To Curb Global Warming

NASA climate modeler Drew Shindell knew his research would raise eyebrows. But he was overwhelmed by the response to a paper published last week in *Nature Geosciences* that modeled the causes of Arctic warming over the past century. " 'Did you really say aerosols are responsible for half or more of the warming in the Arctic?' " he describes a typical e-mail.

He did. Carbon dioxide may get all the attention, Shindell says, but black carbon—a component of soot—is also an important factor in global warming. He and other scientists say that reducing emissions of black carbon and other short-lived pollutants that contribute to global warming could buy the world crucial time while governments begin the slow overhaul of global energy systems that will be required to reduce emissions of CO_2, which comprise 77% of all greenhouse gas emissions. "Short-lived carbon forcers like methane, black carbon, and tropospheric ozone contribute significantly to the warming of the Arctic," Secretary of State Hillary Clinton said in a speech last week. "Because they are short-lived, they also give us an opportunity to make rapid progress if we work to limit them."

Dirtier air has slowed global warming over the past century by blocking solar radiation. But the four short-lived pollutants that scientists are targeting actually warm the atmosphere. Methane and hydrofluorocarbons (HFCs) are greenhouse gases like CO_2, trapping radiation after it is reflected from the ground. Black carbon and tropospheric ozone, an element of smog, are not greenhouse gases, but they warm the air by directly absorbing solar radiation. Compared with CO_2, which can persist in the atmosphere for up to 3000 years, black carbon remains for only 2 weeks and methane for no more than 15 years.

Environmental activists such as Durwood Zaelke of the nonprofit Institute for Governance and Sustainable Development want Clinton to ask the eight Arctic nations, whose foreign ministers will meet in Norway on 29 April, to create a partnership to support technology and joint demonstration projects that limit diesel emissions globally and particulates from cookstoves and chimneys in the developing world. The U.S. Environmental Protection Agency is also considering including particulate emissions in an upcoming ruling on using the Clean Air Act to fight climate change, says the agency's Paul Gunning. "It's important," says University of California, San Diego, atmospheric scientist V. Ramanathan. "The joint benefits for human health and climate would be considerable."

For methane, Rafe Pomerance of the nonprofit Clean Air-Cool Planet would like the Obama Administration to broaden its well-respected Methane to Markets Partnership, which features demonstration programs to limit emissions from farms, landfills, and energy installations.

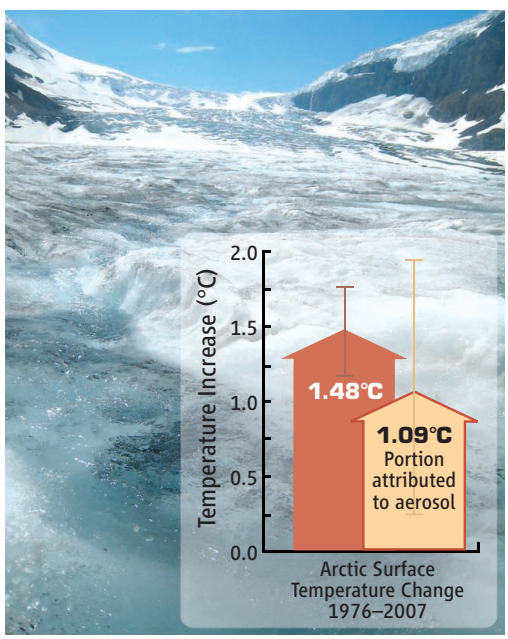

Black mark. A new analysis pins a significant portion of recent Arctic warming on soot (foreground).

Representative Henry Waxman (D–CA), chair of the House Energy and Commerce Committee, has asked the Administration to propose adding HFC language to the Montréal Protocol, which controls ozone-destroying chemicals. (HFCs don't destroy ozone, but they are 1400 times more potent than CO_2 as a warming agent, making up 2% of world greenhouse gas emissions and rising fast.) The Administration says it is considering doing so, although it must act by next month to be considered by the next official meeting of treaty participants in November. Last month, Waxman proposed the first-ever federal regulation of HFCs as part of a massive climate bill he introduced in draft form.

–ELI KINTISCH

CREDITS: (DATA SOURCE) NASA; (PHOTO) MARK FLANNER/NCAR

ScienceInsider

From the *Science* Policy Blog

When the U.S. government funds **energy research** at U.S. national laboratories or universities, who owns the resulting inventions? During a recent tour of the national laboratories, Energy Secretary Steven Chu said he hoped federally funded scientists would "share all intellectual property as much as possible." But Representative James Sensenbrenner (R–WI) of the House Science and Technology Committee has demanded clarification on the Department of Energy's policies in the area. Experts say that solving the climate crisis will require nations to share their technologies more widely.

A researcher who pricked herself last month with a needle containing the **Ebola-Zaire virus** has returned to the Bernard Nocht Institute in Hamburg, Germany. The researcher was inoculated within 48 hours after the accident with a Canadian experimental vaccine. Based on a livestock pathogen called vesicular stomatitis virus, it had never been tested in humans before. The patient is now healthy, but scientists don't know whether the vaccine actually prevented an infection. Scientists are looking for telltale antibodies in the researcher's blood for clues as to whether the vaccine made a difference.

Irish scientists were wondering whether their **golden age of research** has ended after the government announced spending cuts that will hit 3000 publicly funded Irish scientists to the tune of roughly €6000 each. This comes on the heels of budget cuts that cut pay by an additional €2000. More cuts to government-funded science in Ireland are expected in the next 2 years.

Elsewhere ... An online story suggested that the U.S. Centers for Disease Control and Prevention could have done more in 2007 to publicize data on **lead poisoning**. Woes continued at **Grants.gov** as stimulus-hungry scientists swamp the site. A new approach to **particle physics** could make giant accelerators, now the staple of modern experimental physics, obsolete.

For the full postings and more, go to **blogs.sciencemag.org/scienceinsider**.

Published by AAAS

NEWSMAKER INTERVIEW

John Holdren Brings More Than Energy To His Role as Science Adviser

President Barack Obama's three domestic priorities—energy, health care, and education—provide John Holdren with a road map for serving as the president's science adviser. They also point to three different ways in which the 65-year-old physicist, on leave from Harvard University's John F. Kennedy School of Government, may carry out his second job, that of director of the 50-person Office of Science and Technology Policy (OSTP) within the White House.

On energy, Holdren told *Science* last week in one of his first interviews since his Senate confirmation 19 March, he hopes to wield considerable influence. "Energy is one of my big things. I'm going to pay a lot of attention to energy," says Holdren, who has extensive experience in energy, climate, and nuclear-proliferation issues. At the same time, Holdren signaled that the President's Council of Advisors on Science and Technology (PCAST), co-chaired by medicine Nobelist and former National Institutes of Health director Harold Varmus and Eric Lander of the Massachusetts Institute of Technology, is likely to be the nexus for any health care debates within OSTP. He acknowledged that he expects the president to rely heavily on Education Secretary Arne Duncan, a fellow Chicagoan and basketball buddy, for guidance on improving U.S. schools, with OSTP playing a complementary role in reforming science, technology, engineering, and mathematics education.

Three weeks into his job, Holdren says OSTP and government scientists are "energized" by his boss's bold promise to "restore science to its rightful place." In a conversation with *Science*'s Jeffrey Mervis, Holdren spoke frankly on issues ranging from nuclear proliferation to the teaching of evolution. The following is an edited transcript; a complete version is available online at *Science*'s policy blog, *Science*Insider (blogs.sciencemag.org/scienceinsider/2009/04/in-full-intervi.html).

–JEFFREY MERVIS

Q: Are you concerned that reporting requirements for the American Recovery and Reinvestment Act (the $787 billion stimulus package) will hamstring U.S. scientists? Or is that the price to pay for this massive influx of funding?

J.H.: There's clearly a tension there. When you do something as big as the recovery package, there's tremendous pressure to make sure that you don't just push the money out the door without any attention to assessment and evaluation. But the other side of the coin is that you don't want to burden people who are doing good work with a degree of reporting requirements that impair their productivity in any significant way. So it's a fundamental tension, and I'm not sure that we've got it exactly right. … If you overburden researchers with reporting requirements, then you've done a bad thing. And we'll try to avoid that.

Q: Do you expect OSTP to play a bigger role in national security?

J.H.: Steve Fetter is assistant director at large, so I can deploy him on energy, climate change, and nuclear weapons. Steve has a background very similar to my own, and Steve has a portfolio similar to mine, and when I can't be in two places at once, I have complete confidence that Steve will be bringing the same things to the table. We will ultimately have an associate director who will be dual-hatted in the [National Security Council]. But I also have a role in the NSC. Whenever science and technology are on the table, I'm there.

Q: Is building a renewable replacement weapon necessary to win Senate approval of the Comprehensive Test Ban Treaty (CTBT)?

J.H.: My personal view—I don't make the policy, but I provide advice—is that we do not need a new warhead. [A National Academies' report I led] concluded that the safety and effectiveness of the current nuclear stockpile could be maintained indefinitely without developing new warheads, by monitoring the situation and making modifications if necessary.

My personal view is that designing a nuclear warhead and deploying it would throw out a good part of the baby with the bath water. It negates a substantial advantage to ratifying the test ban treaty because it would send a message to the world that the United States still thinks that it can and should design and

CREDIT: PETE SOUZA/WHITE HOUSE PHOTO

Published by AAAS

On board. In his second day on the job, John Holdren (*left*) joined President Barack Obama and local students in a phone call to the space station.

deploy new warheads when circumstances require it. If that's the case, what have you accomplished with CTBT?

Q: Will additional shuttle missions be needed to complete the space station?
J.H.: The current plan is to get an additional shuttle mission to the space station within the 2010 framework. … If that can't be done and things slip, then consideration will be given to going beyond that date. And that would be the last shuttle mission. There will be a gap in our capacity to put people in space with U.S. vehicles, because we will not have a follow-on to the shuttle ready before 2015.

Q: Will it be only 5 years?
J.H.: I wouldn't want to speculate. It's going to be at least that long. I don't see any way we can do it before 2015, and if things go as they often do, it might be a little later than 2015. And what we'll have to do in that interim period is rely on our international partners, which means the Russians. It might also be the Chinese, depending on how our relationship develops.

Q: Do you have confidence in China's ability to launch our astronauts?
J.H.: I think it's possible in principle to develop the required degree of confidence in the Chinese. I put it out there only as speculation, but I don't think it should be ruled out.

Q: Will your review of scientific ethics include a review of conflict-of-interest policies at each agency?
J.H.: I think it has to look at that. I wouldn't prejudge what we're going to say. But the question is, "What are the appropriate boundaries?"

Q: What about full disclosure for all National Institutes of Health (NIH) grantees?
J.H.: I don't feel comfortable prejudging that. It's not a domain with which I'm closely familiar. I would be interested in the views of Harold Varmus and Eric Lander on that. They are co-chairs of PCAST, which has not yet been fully constituted. … And since I have, as co-chair of PCAST, the former director of NIH, and one of the smartest people I know, I'm not going to go on record on that issue without talking first to Harold.

Q: Will the portfolios of the associate directors be science, technology, energy/environment, and national security/international affairs?
J.H.: Yep. Although when you say energy, the title will be environment, and how energy will be handled remains to be seen. It depends in part on who we recruit for technology. Right now, the only associate director who has been nominated is Shere Abbott, for environment.

Q: So you haven't decided where energy will go?
J.H.: Well, energy is one of my big things. I'm going to pay a lot of attention to energy. Energy is one of Steve Fetter's big things. And we have Kevin Hurst, a senior policy analyst who's been working on energy. So right now we have a strong energy team, and we'll be bringing even more energy capability on board.

> *"Designing a nuclear warhead and deploying it … negates a substantial advantage to ratifying the [Comprehensive] Test Ban Treaty."*
>
> —JOHN HOLDREN

Q: Given the Administration's energy team—Steve Chu, Carol Browner, Lisa Jackson, among others—what special expertise and perspective do you bring?
J.H.: Number one, of the people you just named, the only other scientist is Steve Chu. And Steve Chu and I, in the interagency working group on energy and climate, represent the science and technology side. Steve and I are both knowledgeable about a wide variety of energy technologies, and we are very close partners. We both know a fair amount about climate science, and we have others working for us who know even more.

Carol Browner, the former EPA director, is a brilliant analyst of policy and regulation. And we have at the table Larry Summers, Christina Romer, and Peter Orszag, who cover the economic side. We also have Cabinet secretaries who have big stakes in the energy issue, and they bring to the table important constituencies.

Q: How will OSTP handle science education?
J.H.: It'll be within the associate director for science. Everybody has a stake in it, however. And we will have an associate director for science who is known for his or her commitment to strengthening science, technology, engineering, and math education. That's already clear.

Q: So you have somebody in mind?
J.H.: I do. And this is a big deal for the president. His commitment to education is clear, and it's shared by the education secretary, Arne Duncan. We're going to do a lot in that domain.

Q: Staying with education, do you think that the Texas state school board's recent decision to add a skeptical view of the study of evolution and the fossil record weaken the state's science standards and weaken national efforts to improve science education?
J.H.: Well, I have not reviewed that decision carefully. But my impression from reading about it is that it was not a step forward but rather a step backward. Of course, all science needs to be skeptical. It's hard to be against skepticism. But when you get into the domain of promoting particular views about the basis for skepticism of evolution, and those views are not really valid, then I think we have a problem. I think we need to be giving our kids a modern education in biology, and the underpinning of modern biology is evolution. And countervailing views that are not really science, if they are taught at all, should be taught in some other part of the curriculum.

Q: Is there anything you can do?
J.H.: I'm not aware of any leverage we have, at OSTP or within the federal government, over the science curriculum in Texas, other than exhortation. We can argue and we can beg and we can try to educate. But we have no authority to act.

Q: Were you troubled by the recent National Academies' report that one in six life scientists say they have self-censored some of their research because of security concerns, and is there anything you can do?
J.H.: That is a tough one. I think security concerns in the biological domain are real, and we cannot be cavalier about the propagation of findings that could be used by terrorists to harm us. But what the right approach to managing those risks is, is something we'll continue to struggle with.

There was self-censoring within the nuclear physics community in the late [19]30s and '40s, when it became clear to scientists that there was potential for weapons of vast destructive power. And I think that was a good thing.

Published by AAAS

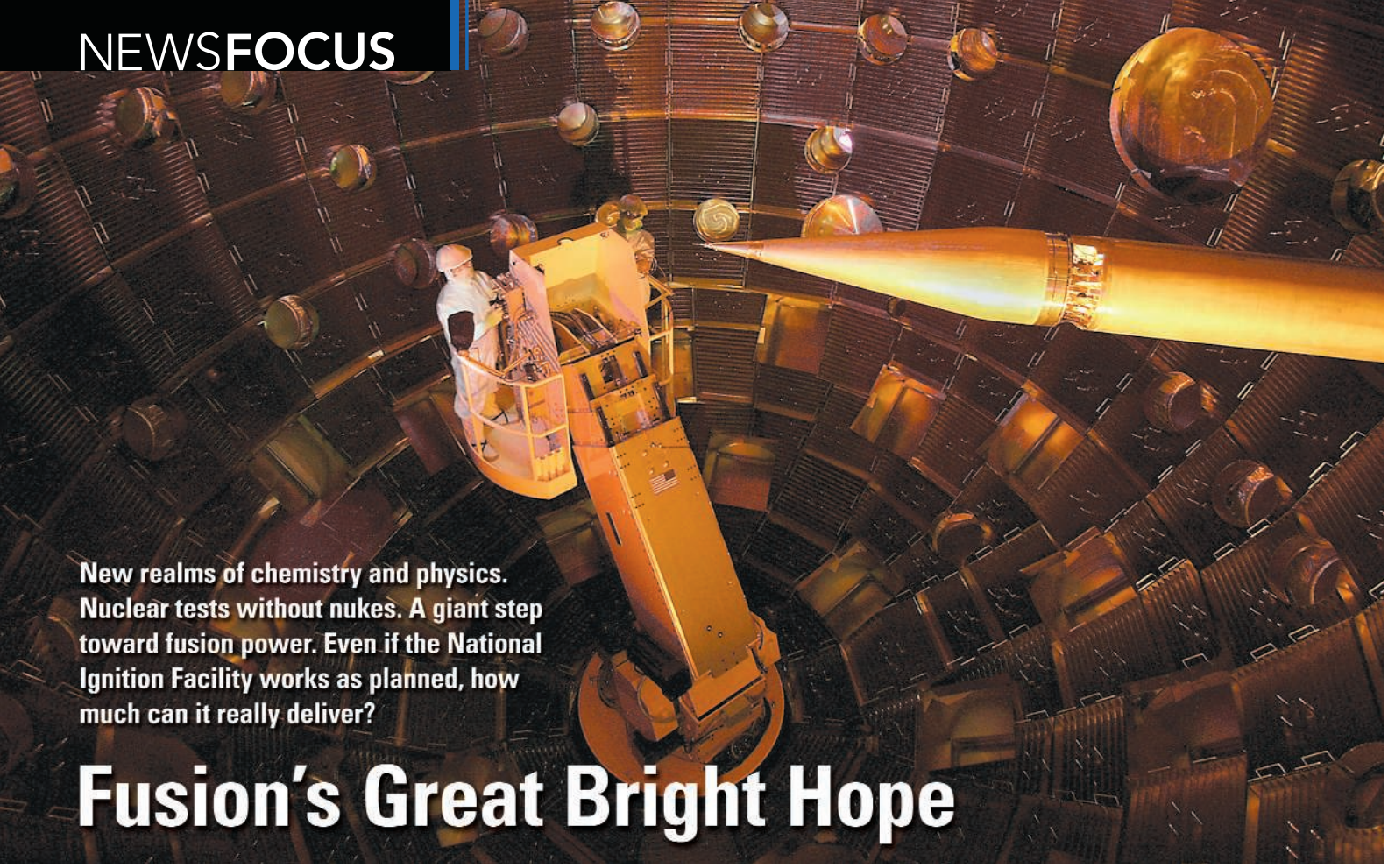

New realms of chemistry and physics. Nuclear tests without nukes. A giant step toward fusion power. Even if the National Ignition Facility works as planned, how much can it really deliver?

Fusion's Great Bright Hope

IN NOVEMBER 1957, GORDON GOULD, A grad student at Columbia University, jotted down in a notebook some ideas on how to make a laser, a term that he coined. Possible uses for such a device, he noted, included spectrometry, interferometry, radar, and nuclear fusion—all 3 years before a laser was actually demonstrated. Gould's innovations were disputed: He was not included in the 1981 Nobel Prize for the laser, and for 3 decades he fought in the patent courts to assert his inventions. He was eventually successful, and many of the applications he dreamed up, such as heating and evaporating materials, measuring distance, communications, and television, have come true—apart, that is, from nuclear fusion.

Next year, researchers at the Lawrence Livermore National Laboratory (LLNL) in California hope to tick that box off Gould's list. Despite his foresight, Gould could not have imagined the lengths to which scientists and engineers would have to go to bring his prediction to reality. LLNL's National Ignition Facility (NIF), which was officially completed last month, is a laser on a truly epic scale. The building housing it is 10 stories high and covers an area the size of three football fields; for a very brief instant, its beams deliver a power of 500 terawatts, more than the power-generating capacity of the entire United States.

If all goes according to plan, some time in 2010 the power of those beams will be directed at a small beryllium sphere filled with hydrogen isotopes. The resulting implosion will crush the hydrogen to a temperature and pressure higher than in the core of the sun. If NIF's scientists get everything right, the hydrogen isotopes will do what they do in the sun: fuse together into helium nuclei and release a huge store of energy. NIF's principal aim is to reach "ignition": a self-sustaining fusion burn that gives off more energy than was put in to make it happen—something that so far has occurred only in nuclear explosions and stars.

"People have been waiting for this moment for a long time," says NIF Principal Associate Director Edward Moses. The achievement could have profound implications for our future energy supply. If the fusion gain—the ratio of energy out over energy in—is high enough and a laser could be developed to spark such ignitions at a steady rate, laser fusion could provide almost limitless energy with little radioactive waste. "This will ignite a change in the political debate," says Mike Dunne, head of the Central Laser Facility of the Rutherford Appleton Laboratory near Oxford, U.K.

Energy production is not NIF's raison d'être, however. Its funding comes not from energy or science budgets but from the coffers of the National Nuclear Security Administration (NNSA), the agency tasked with the maintenance and security of nuclear weapons and naval reactors. NIF's overarching role is to provide hard data that can confirm computer simulations of nuclear explosions. In the absence of nuclear testing, NIF is the best way weapons

Online
sciencemag.org
Podcast interview with author Daniel Clery.

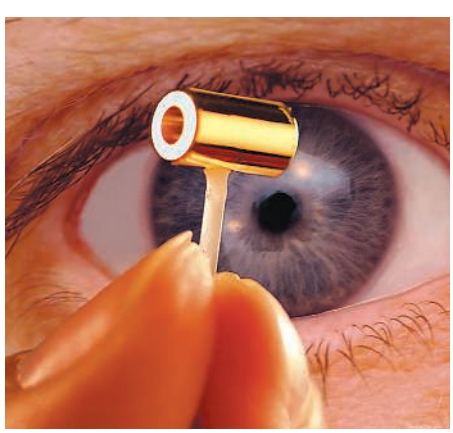

Pin point. All 192 beams must shine into the ends of this gold cylinder, which encloses the target.

CREDITS: LAWRENCE LIVERMORE NATIONAL LABORATORY

Published by AAAS

Focal point. Engineers prepare the target assembly at the center of NIF's cavernous target chamber.

designers can know what happens when one of their bombs goes off. But basic science should be a big beneficiary: Researchers plan to use NIF to simulate the interiors of supernovas, stars, and giant planets, as well as to shed light on how materials behave under such previously unattainable conditions. "Really, it's a very, very exciting period for all of plasma physics," says Jacques Ebrardt of France's Atomic Energy Commission and one of the leaders of a rival fusion project, Laser Megajoule.

After a dozen years of construction, researchers are keen to see these dreams realized soon. NIF staff members think they won't have long to wait. "We're feeling pretty confident," says Moses. But some other researchers say such temperatures and pressures are uncharted territory, and controlling them may not be as straightforward as NIF's proponents think. "It's just very, very complicated. Shots even close to this power have never been done before," says Steven Cowley, director of the Culham Science Centre, the U.K. fusion research lab near Oxford. Some think NIF is bound to fail: that the leap in laser technology is too great or that we don't yet understand enough about how plasmas and other materials will behave under these conditions.

Practical questions have also dogged NIF. Technical and managerial problems early on stretched out construction by 7 years and drove up costs; at $3.5 billion, the price tag is several times the original estimate. Some say that money should have paid for several smaller, less risky facilities.

NIF is perhaps one of the most scrutinized scientific projects in recent history, the subject of countless reviews, panels, and investigations. But the time for predicting its future has passed. That future will soon be decided by a brilliant flash of light and whether it does what researchers hope it will do. Either it will usher in a new era of fusion research, or some hard questions will have to be answered. If NIF works, "we're going to have a gold rush of people being interested. It'll grab the attention of the world," says Robert McCrory, director of the Laboratory for Laser Energetics at the University of Rochester in New York state.

"Every scale of problem"

The route to fusion that has won the most attention and funding is magnetic confinement fusion, which uses huge electromagnets to confine a hot but low-density plasma inside

A LONG, WINDING ROAD TO IGNITION

The National Ignition Facility (NIF) beam starts life in one of two ytterbium-doped optical fiber lasers known as the master oscillators. These produce an infrared flash (1053 nanometers in wavelength) that has an energy in nanojoules. This flash is split into 48 beams and passed through 48 preamplifier modules, slabs of neodymium glass pumped with bright light just before the beams arrive. Four passes through the preamplifiers boost the total energy 10 billion times to about 6 joules. Each of the 48 beams is then split further into four beamlets.

The 192 beamlets pass through the power amplifier into the main beamline, which includes the 48 main amplifiers, each made of 11 1-meter-long slabs of neodymium-doped phosphate glass. Just before the beam is first generated, the amplifiers are pumped full of light by 7680 xenon flash lamps, storing 400 megajoules (MJ) of electrical energy. As the beams pass through, the amplifiers dump that energy into the beam. An optical switch called a Pockels cell traps the light between two mirrors so that the beams pass back and forth through the amplifiers four times before they are switched back up through the power amplifier and on toward the switchyards. The beams now have a total energy of 6 MJ.

The 10-story-high switchyards use mirrors to route the beams into the 10-meter-wide target chamber from all directions around the sphere. Just before entering the chamber, the beams pass through the final optics assemblies, which condition the beams and step down their wavelengths. Frequency converters made from thin sheets cut from single crystals of potassium dihydrogen phosphate convert the infrared beams first to green (527 nanometers) and then to ultraviolet (351 nanometers), which is much more effective at heating the target. Losses bring the total energy down to 1.8 MJ. But because the flash is only 20 nanoseconds long, its power is 500 terawatts, more than the generating capacity of the entire United States. All told, the beam travels 305 meters from master oscillator to target, a journey that takes 25 nanoseconds.

The target is a tiny, hollow sphere made of beryllium about the size of a peppercorn. Inside is 150 micrograms of deuterium and tritium, two isotopes of hydrogen, chilled to 18 kelvin so that they form a uniform layer of ice on the inside of the sphere. The target capsule sits at the center of a tiny gold cylinder about the size of a pencil eraser, called a hohlraum. The beams shine into the ends of the hohlraum, heating its inside surface to such an extreme temperature that it emits a pulse of x-rays. The x-rays cause the beryllium capsule to explode, and the outward blast drives the deuterium-tritium ice inward toward the center of the capsule.

If the implosion is completely spherically symmetric, it will compress the fuel to a density 100 times that of lead. But the fuel still needs a spark to ignite fusion. A shock wave from the original beryllium explosion arrives in the center and heats the core of the fuel to 100 million kelvin. As nuclei fuse in the core, they release enough heat to trigger more fusion in the surrounding fuel in a chain reaction. If all goes according to plan, the reactions will generate enough heat to make the fusion burn self-sustaining and will generate more energy than the laser pumped into the hohlraum, a result known as "ignition"—one of the ultimate goals of NIF.

–D.C.

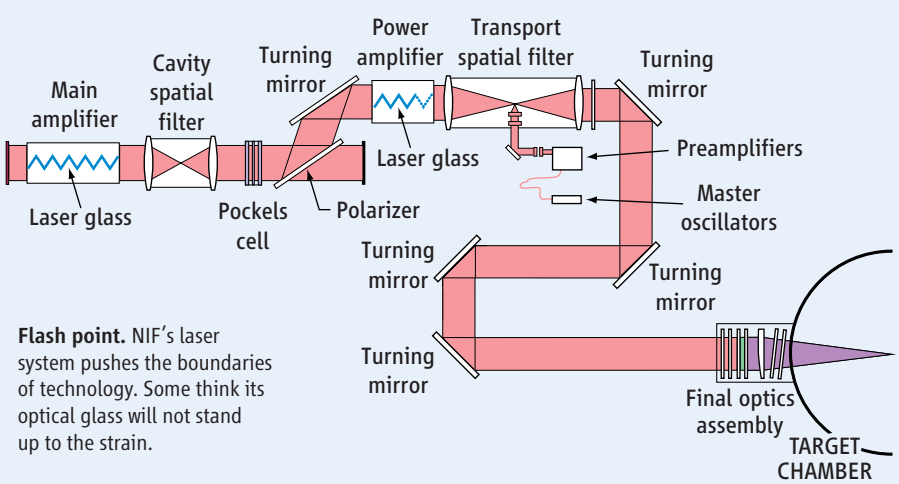

Flash point. NIF's laser system pushes the boundaries of technology. Some think its optical glass will not stand up to the strain.

Published by AAAS

a vessel known as a tokamak. The premier magnetic fusion device, which aims to show large energy gain for extended periods, is ITER, currently being constructed by a worldwide collaboration in southern France. Meanwhile, a smaller community has attempted to achieve fusion by imploding small capsules of fuel using light or particle beams—a technique known as inertial confinement fusion (ICF) because inward inertia of the implosion holds the fuel in place.

The first experiments with ICF were carried out in the 1960s using ruby lasers soon after they were invented. But a key paper by LLNL physicist John Nuckolls in 1972 predicted that ignition would need laser pulses of 1 kilojoule and that high gain would require 1 megajoule (MJ). There followed a series of attempts at fusion: During the 1970s, LLNL built increasingly powerful lasers—Janus, Cyclops, Argus, and finally Shiva, a 20-beam, 10-kilojoule laser with amplifiers made from neodymium-doped silica glass. With every attempt, however, researchers encountered new difficulties with power-draining interactions between the beam and the plasma and achieving a smoothly symmetric implosion of the fuel capsule.

In 1980, researchers at Rochester developed crystals that could triple the frequency of high-intensity laser light, converting it from infrared to ultraviolet, which interacts with plasma less and causes a better implosion. Rochester soon put the crystals into practice with its 24-beam Omega laser, and LLNL followed suit with Nova in 1984. Funding for fusion stagnated during the 1980s, but Nova and Omega advanced the science enough that by the late 1980s and early 1990s, several labs were developing designs for a next-generation machine.

> ***"There needs to be more than one miracle for everything to work in time."***
>
> **—DAVID HAMMER, CORNELL UNIVERSITY**

In 1992, the United States stopped testing nuclear weapons, and new methods were needed to ensure that existing weapons would still work when needed and that new weapons could be developed without testing. In discussions between the national weapons laboratories, officials decided that an ICF device was needed to validate computer simulations of nuclear explosions. In 1994, a design for NIF emerged that would produce a 1.8-MJ ultraviolet beam at a cost of just over $1 billion with completion penciled in for 2002.

Problems emerged with the design soon after construction began in 1997. Capacitors failed in the pulse power modules that supply current to the flash lamps that pump the laser amplifiers, and there were persistent problems with dust on optical surfaces: Powerful beams would heat up the dust specks and damage the surfaces. NIF staff members hid delays and cost overruns from government officials, and in September 1999, NIF Associate Director E. Michael Campbell stepped down after anonymous tips revealed he had not finished a claimed doctorate from Princeton University.

Those revelations caused the Department of Energy (DOE) to carry out a thorough reevaluation of the project, and Congress ordered an independent review by the Government Accountability Office. GAO's damning report prompted DOE to rebaseline the project with a new cost estimate of about $4 billion and completion slated for 2008.

Moses took over the troubled project in 1999 and found "every scale of problem," he says. He worked to develop a "partnership" with vendors and a cultural shift among the staff so that they would speak up if there were a problem. He tackled the dust issue by building a huge clean room where optical elements are enclosed in sealed units that could easily be slotted into and out of the beamline. He also began commissioning the beamlines one at a time, beginning in 2001, rather than all of them in parallel, so that any bugs in the first completed beamlines could be corrected in later ones. "That had a huge impact," says Mark Newton, leader of NIF's engineering division.

Under the new management, NIF has pretty much kept to the revised schedule and budget, culminating in last month's official completion and, according to Moses, a test shot with an energy of 1.1 MJ. Researchers will now test all parts of the system before taking a shot at ignition. They will make sure

WHAT'S NEXT FOR ICF?

If the National Ignition Facility (NIF) reaches its goal of ignition—a self-sustaining fusion burn that produces more energy than was put in to create it—researchers will celebrate a triumph of plasma science. But they will still be far from showing that inertial confinement fusion (ICF) is a viable energy source for the future.

One key stumbling block for an ICF energy reactor is laser technology. NIF managers hope to perform about two shots a day because of the time needed to let optical elements cool down, check for damage, replace any damaged parts, and install a new fuel capsule. At that rate, with each shot producing fusion burns of 20 megajoules—its initial target—NIF will barely generate enough power to keep a single light bulb glowing. According to Steven Cowley, director of the Culham Science Centre, Britain's fusion research lab near Oxford, "laser fusion has all the problems of magnetic fusion, but ICF also has to find a laser that can fire many times per second and is 20% to 30% efficient, plus how to make fuel pellets at low cost."

The National Nuclear Security Administration, which funds NIF, has also been backing the High Average Power Laser (HAPL) program, bringing together researchers at national labs, universities, and industry to develop the technology needed for such a power reactor. Its goals include a laser that can fire as many as 10 shots a second, optics that can withstand that much power for long periods, a target chamber that can absorb the neutrons produced by fusion and convert their energy into heat, and a target factory that can churn out fuel capsules at the required rate. That's a tall order: At 10 shots per second, more than 850,000 fuel capsules would be needed every day.

The favored laser design is a krypton fluoride gas laser pumped with electron beams that is being developed at the Naval Research Laboratory (NRL) in Washington, D.C. NRL's Electra laser has recently

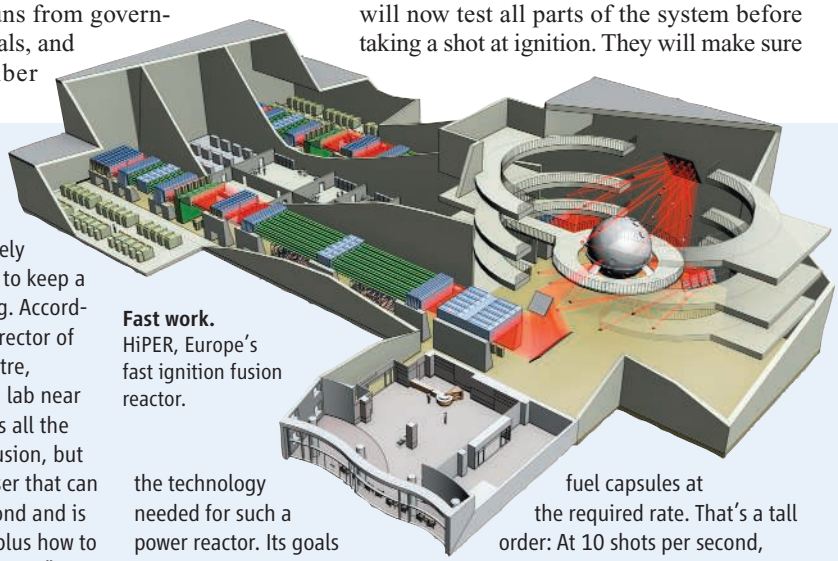

Fast work. HiPER, Europe's fast ignition fusion reactor.

CREDIT: © 2009 HIPER PROJECT

Published by AAAS

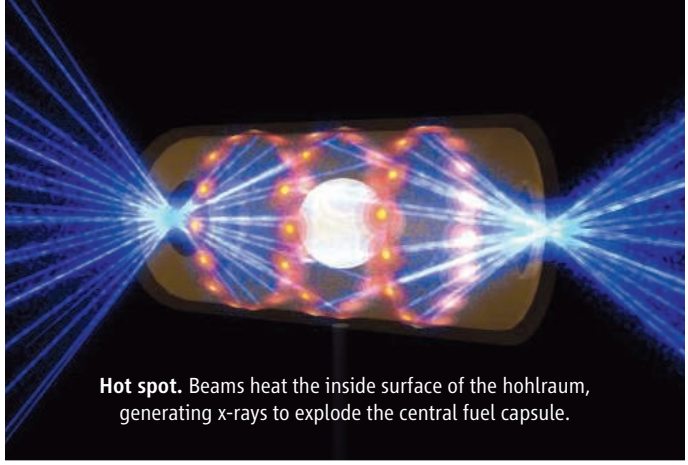

Hot spot. Beams heat the inside surface of the hohlraum, generating x-rays to explode the central fuel capsule.

that all 192 beamlets can be focused, smoothed, and targeted accurately; that they can direct them into the ends of the hohlraum, the gold cylinder that houses the fuel capsule; and that they can get a capsule to implode symmetrically. "By the end of the campaigns, we'll have a pretty good idea of what to expect," says Gilbert Collins, leader of NIF's shock physics group. Moses is similarly confident: "Ignition is a grand challenge. Our aim is to do it in 2010," he says.

Other researchers have heaped praise on LLNL's achievements. "The laser is really quite tremendous and truly awe-inspiring," says particle physicist Roy Schwitters of the University of Texas, Austin, who chairs the JASON Defense Advisory Group, an organization of scientists that assesses defense-related projects, such as NIF, for government clients. Cowley is similarly effusive: "NIF is a triumph of laser construction." But few agree with Moses that NIF will be able to move rapidly to ignition by next year. "The schedule looks almost unattainable," says Cowley. And according to nuclear engineer David Hammer of Cornell University, "There needs to be more than one miracle for everything to work in time for the first ignition experiment."

Wrestling instabilities

Most researchers cite two areas where nature may throw NIF a curve ball: laser-plasma interactions (LPI), which affect the beams as they enter the hohlraum; and hydrodynamic instabilities (HDI), which can cause the fuel capsule not to implode symmetrically. Both effects plagued earlier ICF experiments, and NIF researchers have spent years simulating and testing ways to control them. But NIF's huge energies may still spring surprises. "Until they put a beam into the hohlraum, we won't know what nature will do," says Hammer.

LPI happens when the beams enter the hohlraum and hit its inside wall, kicking up enough gold atoms to create a plasma inside the cylinder. The interaction of the beams with this plasma can reduce the power deposited into the beryllium capsule and can preheat the fuel, making it harder to compress. The plasma can even reflect some of the beam out through the hole again, reducing efficiency. "We have a woeful ability to predict" LPI, says Dunne. Mordy Rosen of LLNL's Weapons and Complex Integration Directorate agrees. "We're going to a place we've never been before. It's going to be a new game," he says. Nevertheless, he adds, "I think we've got what it takes to respond to those issues that come up."

Steven Bodner, retired head of laser fusion at the Naval Research Laboratory in Washington, D.C., says NIF has even bigger problems: He believes the quality of its beams is not up to specification. The design describes a maximum beam spot size that will fit into the hohlraum without touching the entrance hole or the fuel capsule, as well as a bandwidth the beams must be detuned to in order to combat LPI. Bodner says that in results released so far, beams have achieved both of these criteria, but not at the same time while operating at full power. "If they can't focus the beam into the hohlraum, they can't get ignition," he says. Bodner thinks NIF's chance of reaching ignition "is worse than a snowball's chance in hell." NIF counters by citing the conclusion in February this year of the National Ignition Campaign Review Committee, which stated that "each and every one of the laser performance completion criteria has been met or exceeded."

Compressing the fuel capsule is also fraught with difficulties, collectively known as HDI. If you imagine trying to squeeze a balloon with your two hands, you'll see what the exploding capsule is trying to do: compress the contents uniformly without bits of it bulging out again. Many things can cause HDI: The bath of x-rays coming from the heated hohlraum may not be uniform or there

demonstrated continuous operation for 10 hours firing 2.5 shots per second at ultraviolet wavelengths. Researchers still have to ensure that a working laser can keep that up for years and boost its power to the levels needed for ICF.

The Lawrence Livermore National Laboratory in California, home of NIF, is working on a high-repetition-rate version of the neodymium-doped glass lasers used on NIF. Livermore's Mercury laser dispenses with the inefficient and slow flash lamps used to pump NIF's laser amplifiers and replaces them with solid-state laser diodes. Mercury has shown a repetition rate of 10 hertz firing at infrared wavelengths.

The HAPL project is currently stalled, however, because it received no funding in the 2009 omnibus funding bill. "Hopefully, through some combination of actions by the new Administration and Congress, the challenge of funding HAPL and other such inertial fusion energy research in the U.S. will be resolved soon," says Steven Obenschain, head of NRL's laser plasma branch.

"Laser fusion has all the problems of magnetic fusion," and more.

—STEVEN COWLEY, CULHAM SCIENCE CENTRE

In Europe, researchers are plotting a slightly different route to laser fusion energy. In traditional ICF, a single laser pulse plays two roles: compressing the fuel and sparking fusion at its center. An alternative, known as fast ignition fusion, uses one laser to compress the fuel and a second pulse, with extremely high power (10^{15} watts) but short duration, to set off the fusion burn. The advantage is a significant reduction in the energy requirement of the lasers. "If it works, it could lower the energy necessary to get high gain, making the economics more tantalizing," says NIF Principal Associate Director Edward Moses.

The idea of fast ignition was conceived 15 years ago, and early experiments with the Gekko laser at Osaka University in Japan suggested it might work. Researchers at the University of Rochester in New York state are hoping to put it to some sterner tests with their newly upgraded Omega EP laser. But a design study funded by the European Union is planning something bigger: a dedicated fast-ignition facility with high repetition rates, dubbed HiPER. "We're putting together all the building blocks so that politicians can make a decision," says HiPER Director Mike Dunne of the Rutherford Appleton Laboratory's Central Laser Facility near Oxford, U.K. He's hoping construction could start in 2015. Some caution, however, that fast ignition should learn to walk before it tries running. Says nuclear engineer David Hammer of Cornell University, "Fast ignition is one of those attractive ideas that haven't been tested yet." **–D.C.**

CREDIT: LAWRENCE LIVERMORE NATIONAL LABORATORY

Published by AAAS

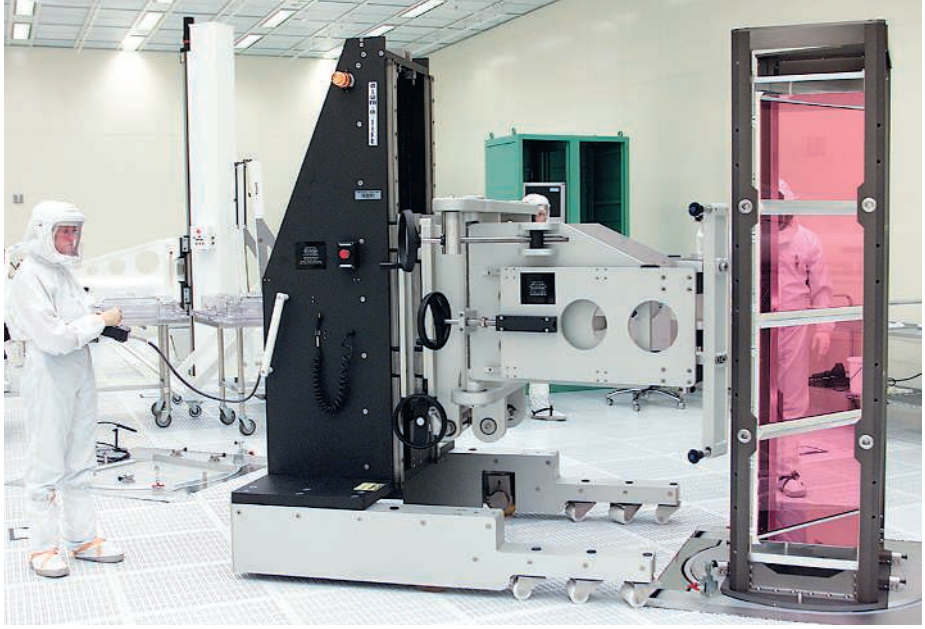

Clean machines. In conditions worthy of a semiconductor plant, technicians prepare a laser glass slab (*right*) for insertion into the beamline.

may be some flaw in the capsule or fuel layer. Even under ideal conditions, instabilities are inevitable, researchers say. The key to beating them is speed: "We need to do it fast enough so instabilities don't get big. It's extremely hot and high pressure. It wants to blow itself apart," Rosen says.

Breaking glass

Apart from LPI and HDI, other issues could prove a headache for NIF's managers. According to some outside LLNL, the risk of damage to the laser optics has not gone away. The energy contained in each laser pulse is not huge, but because it is pumped through in only a few nanoseconds, the power is enormous. Hammer says NIF can cope with a certain amount of damage to glass, "but if 192 beams destroy several optical elements, a lot of optics is involved." The "triplers," which convert the final beam into ultraviolet, are particularly tricky, he says, and because they are very close to the target chamber, they could do substantial damage if they explode. Moses says scientists have done a huge amount of research on damage mechanisms and removing defects from surfaces. "We've shown we can get surfaces to work at full performance. … That was our biggest challenge."

Some experts also worry that NIF's choice of beryllium for the capsule material, which requires more energy to explode than alternatives such as plastic, leaves little margin for error in reaching ignition. In 2005, a JASON panel investigated NIF's chances of achieving ignition. Noting plans to start out at energies of about 1 MJ, it concluded "that success in the early attempts at ignition in 2010, while possible, is unlikely." The panel was invited back to view progress in January of this year, but its report has yet to be released by NNSA. Hammer, who co-chaired the panel, says that in his own opinion there's still not enough power available. He thinks that a couple of years after the first attempts at ignition, they will have a 50:50 chance of success. "They will throw everything at it to get there," says Cowley. "By 2010, they might, but if they operate it for a long time they'll learn how to do it."

Illuminating the stars

Some researchers are less concerned about the trials of reaching ignition than what they can do once it's achieved. These are the plasma physicists, planetary scientists, and astrophysicists who want to use NIF to do basic research. Twenty percent of time at NIF is earmarked for basic research, and several groups are gearing up to take advantage of it. Planetary scientist Raymond Jeanloz of the University of California, Berkeley, is preparing experiments for NIF that will replicate pressures at the cores of giant planets. "NIF will give us 100 times the energy we can currently deposit into samples," he says. "We will begin to turn the page on a new kind of chemistry that wasn't accessible before." Cowley, who has worked in astrophysics as well as plasma physics, says ignition at NIF will produce "an unbelievable neutron flux if you get really close"—conditions akin to extreme astrophysical events such as supernovas. This will open up new opportunities in the burgeoning field of experimental astrophysics. "There are wonderful things you can do with NIF," Cowley says.

> ***"We're going to a place we've never been before. It's going to be a new game."***
>
> **—MORDY ROSEN, LAWRENCE LIVERMORE NATIONAL LABORATORY**

Also hoping to do wonderful things, although with less visible results, are the weapons scientists involved in stockpile stewardship. Ever since the idea of NIF was first mooted, it has faced controversy over how useful it really will be to weapons research, including sniping from other national laboratories that benefited less from NNSA's largess. "I've never viewed it as relevant to weapon design. The parameters are very different, it's orders of magnitude wrong," says Bodner. A 2007 report on stockpile stewardship from the Federation of American Scientists concluded that the nation's nuclear weapons were being kept safe and reliable through careful monitoring and the judicious replacement of parts. "The NIF could be ended without reducing the confidence in the existing nuclear stockpile," it said.

NIF's relevance to weapons "has been reviewed for 20 years by blue-ribbon panels, everyone under the sun," says Moses. "The community has spoken, the NNSA continues to fund us, that's pretty much put to bed." What's more, France is spending billions constructing Laser Megajoule, a similar machine that will carry out its first experiments by the end of 2012, also aiming for ignition and weapons verification. "The architecture is basically the same," says Ebrardt, and some components, such as the amplifier glass, were developed jointly by the two teams.

Nevertheless, just as NIF reaches the stage at which it can prove itself, the tide of politics is flowing away from its original mission. President Barack Obama has spoken much more about nuclear disarmament than about maintaining a credible deterrent, and his appointments and funding decisions show a keen interest in developing new sources of energy. It's perhaps no coincidence that most news coverage of NIF's completion last month focused on its significance for energy, not weapons. LLNL researchers have also been busy developing designs and technology for fusion-energy projects that would come after NIF (see sidebar, p. 328). "[NIF] is not a power-production machine," Collins acknowledges, but it "will unveil the science needed to get there."

For NIF researchers, waiting to see if a dozen or more years of work will pay off, there is now some respite from the constant probing and questioning of NIF's abilities and rationale. "Some of our most serious critics are waiting and seeing. The rhetoric has really dropped down," says Collins. Rosen, for one, is ready. "It's up to us now," he says. "Mother Nature is waiting."

–DANIEL CLERY

With reporting by Robert F. Service.

CREDIT: LAWRENCE LIVERMORE NATIONAL LABORATORY

Published by AAAS

CONSERVATION BIOLOGY

Will Captive Breeding Save Africa's King of Beasts?

One nonprofit claims its lion reintroduction program will ensure a stable population of the iconic predator; many experts are dubious

VICTORIA FALLS, ZIMBABWE—Two young male lions trail a middle-aged South African couple through parched savanna. The waist-high cats may appear to be stalking human prey, but suddenly, off script, they bound into the bush. Handlers with a company called African Encounter chase after the captive-bred lions and with threatening waves of sticks cow them back onto the trail. The predators are coaxed to pose for pictures with the two tourists, who have paid $200 for the chance to take a wilderness stroll with the tame beasts.

"Walking with lions" may be little more than a petting zoo with claws. But the nonprofit African Lion and Environment Research Trust (ALERT) claims its captive-breeding and reintroduction program, supported by tourism revenue from the African Encounter operation, is "ensuring the future of the African lion." ALERT, which also runs a breeding facility in Gweru, Zimbabwe, opened a lion-walk center in Zambia last December and plans to release a pride with seven female members into a 4000-hectare site there later this year. "No one has done what we've done," says David Youldon, ALERT's chief operating officer.

Some experts are unimpressed. They argue that ALERT's program diverts donations and volunteer attention from efforts to stem what they say is the greatest threat facing lions: dwindling habitat. "There's no sound science behind what they're doing," charges Paula White, a lion ecologist at the University of California, Los Angeles, Center for Tropical Research. "In most cases, lion reintroductions are poorly thought out, do little to benefit conservation, and use valuable resources that could be used to benefit existing populations desperately in need of protection," adds Andrew Loveridge, a research fellow at the University of Oxford in the U.K. who studies lions in Zimbabwe. He doubts ALERT's program is an exception. Youldon disagrees and says critics are missing the point. "We're realists," he says. "We think there has to be a commercial aspect."

ALERT's center, started in 2005, follows a standard reintroduction protocol. Before release, captive-bred animals live in incrementally larger enclosures and are weaned off human contact. ALERT claims that "walking with lions" helps juveniles, taken from mothers when they are 3 weeks old, bond in a pride. "If it was pure science, you wouldn't do it," acknowledges Pieter Kat, a wildlife geneticist at Investigação Veterinária Independente in Lisbon and a scientific adviser to ALERT. "There is a tourism aspect involved, but they have to make ends meet."

Showtime. ALERT lion cubs play fight for tourists.

CREDIT: DAVID JENKINS

ALERT's initial reintroduction foray met with mixed results. In August 2007, the center released seven lions into a 200-hectare enclosure near Gweru. Within 2 months, males had killed two females—uncharacteristically lethal aggression thought to be linked to a captive upbringing. ALERT removed the males and reconstituted an all-female pride that thrived for a year before the center was shuttered for renovations. The pride led a sheltered existence in the enclosure, says Roseline Mandisodza, a Zimbabwean ecologist who studied it for her master's degree. The release site was too small and had too few competing predators such as hyenas, cheetahs, or leopards to simulate hunting conditions in the wild, she says. "There is very little or no chance of [their] survival in the wild."

To be fair, carnivore reintroduction is a high-risk endeavor. In 2001, Urs and Christine Breitenmoser, co-chairs of the World Conservation Union Wild Cat Specialist Group, reported that only 30% of felid releases are successful, and almost all of these were translocations, in which wild animals were moved from one habitat to another. Captive breeding and release is a more drastic approach but may be the only hope for critically endangered species such as the Iberian lynx, estimated at fewer than 200 individuals, and the Amur leopard, of which only 30 remain in the wild. Lions are a different story. With some 23,000 lions in Africa, the most pressing need is habitat preservation, not adding to an ample population, argues Luke Hunter, executive director of New York City–based cat conservation nonprofit Panthera. "Reintroduction of captive-bred animals as a means to establish wild carnivores is probably the last resort," he says.

Unless, that is, the lion population were to crash—a possibility that ALERT says supports its program. Feline immunodeficiency virus (FIV), once thought to be a relatively harmless cousin of HIV, infects more than 90% of wild lions. In a recent survey of 68 lions in Botswana, Melody Roelke, Stephen O'Brien, and colleagues at the U.S. National Cancer Institute found that 70% exhibited at least one AIDS-like symptom. ALERT's captive-bred animals offer an opportunity to study FIV in a controlled environment, says Kat. "We can now track the progress of this virus among individuals, a difficult thing to do in the wild," he says. Later this year, Kat and colleagues at the University of Glasgow in the U.K. will begin taking blood samples from infected lions and examine them for immunodeficiency.

But to Hunter and others, the FIV threat appears minimal and hardly justifies captive breeding—or walking with lions. "Even if ALERT was going to succeed, so what?" Hunter asks. "It's not an answer at any scale that's going to matter."

–JERRY GUO

Jerry Guo is a writer in New Haven, Connecticut.

Published by AAAS

LINGUISTICS

How Many Languages? Linguists Discover New Tongues in China

Researchers working in remote China have uncovered dozens of languages that had been hidden by mountainous terrain and administrative practice

After a long day in the field, deep in the mountains of southwestern China near the border with Vietnam, retired environmental health professor Gary Shook was surprised to meet another American, Jamin Pelkey, staying in the same government guesthouse. The two exchanged pleasantries.

"I'm collecting tiger beetles," explained Shook, who had found four new species in the region. "What about you?"

"I'm collecting new species of languages," replied Pelkey, then a graduate student at La Trobe University in Australia doing fieldwork for his dissertation. In 2006, Pelkey and his wife were gathering linguistic data in 41 villages in a 100,000-square-kilometer area of Yunnan Province. Over the course of a year, they drove 15,000 kilometers across rugged terrain in a Jeep. At the end, Pelkey had identified 24 languages associated with the Phula ethnic group, 18 of which had never been defined scientifically before. Until Pelkey's work, these languages had been invisible because their speakers were lumped together under a single ethnic label, the Yi, which is officially considered to have one language.

At a time when hundreds of languages are disappearing because children don't learn them and adults don't speak them, it may seem surprising that many existing languages have never even been named (though they are not "new," especially not to the people who speak them). Yet there are potentially hundreds of undiscovered languages in China, Burma, the Amazon, and elsewhere, linguists say. Pelkey's 24 are listed for the first time this month, in the latest edition of *Ethnologue: Languages of the World*, an authoritative, worldwide gazetteer of languages maintained and published by SIL International, a nonprofit based in Dallas, Texas. This newest edition of *Ethnologue* lists 6909 living languages from 156 countries, including 83 "new" languages from 19 countries.

Pelkey's new entries are the most from any single country. China is "one of the last places on earth where there are large numbers of unreported and undescribed languages," says linguist David Bradley of La Trobe, who also works in Yunnan. The reasons have to do with geography, history, and politics. Bradley speculates that Yunnan alone may have over 150 languages, and Western and Chinese linguists are now surveying the region more thoroughly. "In the last few years, there's been very much a heightened interest [by Chinese] in their diversity and a desire to study and work on language maintenance," says linguist Arienne Dwyer of the University of Kansas, Lawrence. Yet this interest in linguistic diversity sometimes conflicts with the notion of a multiethnic but unified Chinese state. "The reason that language is particularly sensitive is that, in southwestern China, language was the principal way of categorizing people," says Thomas Mullaney, a historian at Stanford University in Palo Alto, California.

Language lumping

How can there be so many undiscovered languages in one region? One reason is the remoteness of villages. "Yunnan has so many mountains, and transportation was so limited before the Communists started building roads, and ethnic groups have been proliferating for so many centuries there," Pelkey says. "The astonishing thing would be to walk into the situation and find only a few dozen languages."

Yunnan is most frequently identified by the colorfully embroidered clothes and quilted hats of the non-Han ethnic groups who have called the mountains and lowlands home for thousands of years. Because their languages were rarely written down, linguistic change went unchecked. Local and imperial governments had little interest in languages, leaving them uncounted.

Centuries of isolation widened the gap between varieties descended from the same parent tongue. Today, the 500 speakers of Alo Phola can't understand speakers of a sister language spoken less than 8 kilometers away, says Pelkey. One of Pelkey's main criteria for judging language separateness is "mutual intelligibility," or how well speakers of different varieties are able to understand each other. Among speakers of the 24 Phula languages, mutual intelligibility is so low that if they ever got together, they would have to communicate in a regional variety of Mandarin, Pelkey says.

Many Chinese languages are being described only now in part because a tradition of lumping ethnic groups together has masked

CREDITS: JAMIN PELKEY

Published by AAAS

Mutual unintelligibility. Many distinct Phula languages have evolved among the Yi people, who live in mountainous southwestern China.

the extent of the diversity. Chinese social scientists of the 1930s and '40s streamlined the number of ethnic minority groups, which were based mainly on language. "The logic was, 'It does no one any good to have an ethnic group of 100 people,'" says Mullaney. In the 1950s, about 50 surveyors spent 6 months in Yunnan and divided a population of 2 million into 20 official groups, even though 212 ethnic group names had been discovered. In 1991, China permanently froze the number of recognized ethnic nationalities, known as *minzu*, at 56: the majority Han plus 55 minority groups, 25 in Yunnan. Until the 1980s, it was forbidden to suggest that China had more than 55 languages, Bradley wrote in 2005 in the *International Journal of the Sociology of Language*. "Any additional linguistic entities had to be classified as '*fangyan*.'" Although the word fangyan is often translated as "dialect," it refers more specifically to "a language spoken in a specific area," or a "topolect," in contrast to *yuyan*, or an autonomous language.

This legacy has led to some disagreement between Chinese and Western linguists over what counts as a language. "We are very strict, while foreign researchers are very loose," says linguist Sun Hongkai of the Chinese Academy of Social Sciences in Beijing. Sun began doing fieldwork in 1953 in Sichuan Province and Yunnan and has helped identify 19 languages. He promotes a method different from that of Western linguists, saying that the boundary between a language and a dialect should be determined by comparing grammatical patterns, vocabulary, and sound rules. If they are similar, the varieties are dialects of the same language. Other Chinese scholars add that varieties that come from the same parent language and have the same writing system must be *fangyan*, not *yuyan*, and reject mutual intelligibility as unscientific. Using such criteria, the roughly 230 European languages would be *fangyan* of a handful of languages. Chinese linguists "are still constrained by political realities as well as the traditional macrocategories imposed by the Han Chinese majority on their minorities," says Bradley.

For example, in a 2008 report to UNESCO of endangered languages in China, Sun listed a single language for the Yi *minzu*. Although some of the Phula languages Pelkey described are endangered, they cannot be identified as such because the Yi officially have only one language. So it may be harder to target those languages with revitalization resources.

Into the field

All the same, since the 1980s, Chinese linguistic diversity has become an open secret, and Chinese researchers have become freer to identify new languages as *yuyan*, says Bradley. In 1992, Sun helped establish an academy project on new languages, for example. Overall, Chinese linguists have identified a total of 134 languages, and the 80 identified in the last 25 years are called *yuyan*, not *fangyan*.

The Chinese have also opened their doors to foreign researchers such as Pelkey, who studied under Bradley. In 2005, Pelkey joined SIL International, the world's biggest player in describing minority languages. SIL has a Christian goal: It describes and analyzes languages to aid in Bible translation and literacy projects. In the past, a Christian organization might have had difficulties in China, but such survey work has been encouraged recently because it helps to provide education in mother tongues and coordinate language revitalization, Pelkey says. Pelkey did his research using his affiliation with SIL, which has been registered as a nongovernmental organization in Yunnan since 2004.

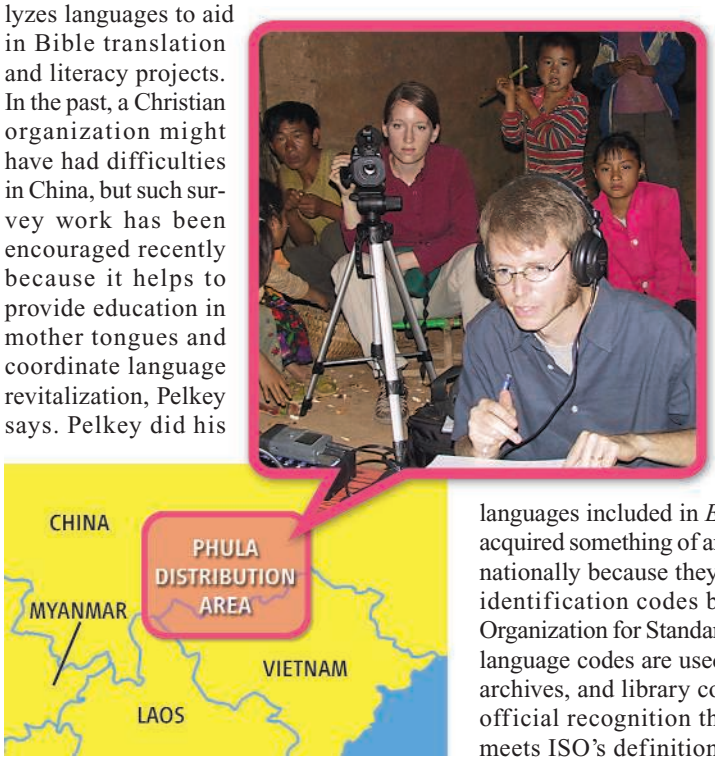

Listen and learn. Jamin Pelkey (with earphones) traveled through remote villages in southwestern China to identify the languages spoken there.

Pelkey stayed 3 to 5 days at a time in Yunnan villages, interviewing 10 or so local people. Using a list of 1200 words, he would say a word in southwestern Mandarin Chinese and show a picture of the object, then record people saying the word in their language. On breaks, he recorded people telling stories and played recordings of people from other villages in order to determine mutual intelligibility.

Originally, Pelkey had hypothesized that the languages associated with the Phula eponym were related to each other. They are all tonal languages, have a default subject-object-verb word order and very simple word structure. However, he found that although they have the same ancient ancestry, they're not siblings or even distant cousins. Using a distance matrix, a tool from evolutionary biology that is new to historical linguists, Pelkey determined that Azha (spoken by 53,000 people) and Pholo (spoken by 30,000) don't share the recent ancestry of the other 22 Phula languages. Thus these two would not be *fangyan* even by Chinese criteria. The speakers of all these languages have been subsumed under the Yi *minzu*.

For some communities, linguistic description and discovery is welcomed, but others are uncomfortable with losing traditional affiliations, linguists say. In Sichuan, Bradley says, speakers of 20 to 25 languages in the Tibetan *minzu* strongly reject any claim that they're anything but Tibetan and so don't want distinct languages to be identified as such.

The 24 new Phula languages included in *Ethnologue* have now acquired something of an official status internationally because they have been assigned identification codes by the International Organization for Standardization (ISO). Such language codes are used in software, digital archives, and library collections and are an official recognition that a speech variety meets ISO's definition of a "language." It remains to be seen how the Chinese government will react to this recognition. Says Mullaney, "When people start to talk about there being new languages out there, it really starts to pull the thread out of this idea that there are a set number of *minzu*."

Pelkey hopes a discussion will ensue. "You start out with assumed categories, then you find a lot of diversity inside them, and then you use a scientific approach to modify your understanding," he says. "The two don't have to be in dissonance, and they don't have to be in consonance, either." Otherwise, defining a language invites so much controversy, discovering species of beetles looks like a walk in the park.

–MICHAEL ERARD

Michael Erard is a freelance writer in Portland, Maine. With reporting by Chen Xi in Beijing.

To foster creativity 337

Traces of weight-bearing steps 341

LETTERS

edited by Jennifer Sills

Scientists: Listen Up!

C. REDDY'S EDITORIAL "SCIENTIST CITIZENS" (13 MARCH, p. 1405) underscores the need for scientists to better explain their work to policy-makers and the general public. If we as scientist citizens want to be understood, we should begin by listening.

AAAS recognized this over 30 years ago when it established its Science and Technology Policy Fellowship program, which gives Ph.D. science graduates the opportunity to collaborate with policy-makers and play an active role in decision-making. Shorter-term immersions can also help. The Consortium for Science, Policy, and Outcomes and the American Meteorological Society both offer 2-week policy experiences in Washington, DC, for early-career scientists. Participants converse with, challenge, and share ideas with policy-makers, including congressional staffers, agency officials, lobbyists, regulators, journalists, academics, and museum curators. In this give-and-take atmosphere, participants discover that many policy-makers understand science far better than most scientists understand policy. This enriched appreciation for the work done by policy-makers helps scientists understand their role and better equips them to contribute constructively.

Science museums also provide excellent practical experience in communication. For instance, the Museum of Science in Boston and Harvard's School of Engineering and Applied Sciences have developed an immersive program that gives graduate students an opportunity to explain the nature of their work (and its impact on society) to museum visitors. These discussions both introduce the public to the questions modern science is tackling and expose scientists to the public's hopes and concerns about the direction of science.

If scientists are going to be citizens, they need practice in not just communicating their ideas, but having a two-way dialogue with policy-makers and the public.

JAMESON M. WETMORE,[1]* IRA BENNETT,[2] WILLIAM H. HOOKE,[3] TIM MILLER[4]

[1]School of Human Evolution and Social Change, Arizona State University, Tempe, AZ 85287, USA. [2]Consortium for Science, Policy, and Outcomes, Arizona State University, Tempe, AZ 85287, USA. [3]Policy Program, American Meteorological Society, Washington, DC 20005, USA. [4]Divine Wind Design, Somerville, MA 02144, USA.

*To whom correspondence should be addressed. E-mail: jameson.wetmore@asu.edu

Type 2 Polio Still in Our Midst

WHEN THREATS TO THE GLOBAL POLIO Eradication Initiative (GPEI) are discussed ("Polio: Looking for a little luck," L. Roberts, News Focus, 6 February, p. 702), type 2 vaccine-derived poliovirus ($VDPV_2$) outbreaks are generally dismissed as rare and easily contained (*1*). However, we should not be in such a hurry to eliminate type 2 polio vaccination. $VDPV_2$-associated poliomyelitis outbreaks have occurred since its eradication in 1995 (*1*). For example, a current Nigerian outbreak (*2*) occurred after resumption of vaccination with trivalent oral poliovirus vaccine (OPV) in the absence of >50% coverage. In addition, two separate clusters of highly diverged, highly neurovirulent $VDPV_2$ have been silently maintained or circulated in limited populations in Israel. They have been detected over long time intervals: more than 3 years in one case and more than 10 years in the other (*3*). Molecular analysis suggests that persistently infected individuals and/or their contacts are the sources of these $VDPV_2$ occurrences, which were isolated intermittently during routine sewage surveillance but did not lead to any reported cases. In 2008, Sabin 2-derived $VDPV_2$s had evolved by about 10 to 15%, compared with less than 3% for Nigerian outbreak $VDPV_2$s.

There is a clear and urgent need to develop new vaccines to replace OPV. High-coverage, global vaccination against all three types of polio must continue as long as such $VDPV_2$s are excreted into the environment.

LESTER M. SHULMAN,* YOSSI MANOR, DANIT SOFER, ELLA MENDELSON

Central Virology Laboratory, Ministry of Health, Sheba Medical Center, Tel Hashomer 52621, Israel.

*To whom correspondence should be addressed. E-mail: lvlester@sheba.health.gov.il

References

1. O. M. Kew, R. W. Sutter, E. M. de Gourville, W. R. Dowdle, M. A. Pallansch, *Annu. Rev. Microbiol.* **59**, 587 (2005).
2. Centers for Disease Control and Prevention (CDC), *Morb. Mortal. Wkly. Rep.* **56**, 996 (2007).
3. L. M. Shulman *et al.*, *PLoS ONE* **1**, e69 (2006).

Synthesizing Knowledge in the Classroom

IN HIS PERSPECTIVE "FAREWELL, LECTURE?" (2 January, p. 50), E. Mazur advocated a shift from the lecture paradigm to interactive models that engage students by fostering discussion and problem-solving. We believe that such innovative, practical concepts can be applied well beyond undergraduate levels and basic science fields. We observed a similar phenomenon in our graduate students, who

Letters to the Editor

Letters (~300 words) discuss material published in *Science* in the previous 3 months or issues of general interest. They can be submitted through the Web (www.submit2science.org) or by regular mail (1200 New York Ave., NW, Washington, DC 20005, USA). Letters are not acknowledged upon receipt, nor are authors generally consulted before publication. Whether published in full or in part, letters are subject to editing for clarity and space.

Published by AAAS

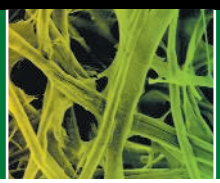

Sizing up quantum states

342

Oxygen sensitivity

343

transformed from learners of fragmented rote-type knowledge to active participants in our radiation oncology program after we replaced the traditional lecture-based teaching with an intense interactive curriculum and "hands-on" labs.

M. Hadjiargyrou ("For teachers, all the classroom's a stage," Letters, 20 February, p. 1009) proposed that the lecturer should be an actor to captivate students' attention. Perhaps a teacher should be even more: a conductor deployed in the center of the two-way road of information exchange to synthesize knowledge and guide critical thinking. This model can be applied in any field and anywhere.

NINA A. MAYR,[1]* SIMON S. LO,[1] JIAN Z. WANG,[1] WILLIAM T. C. YUH[2]

[1]Department of Radiation Medicine, College of Medicine, The Ohio State University, Columbus, OH 43210, USA. [2]Department of Radiology, College of Medicine, The Ohio State University, Columbus, OH 43210, USA.

*To whom correspondence should be addressed. E-mail: Nina.Mayr@osumc.edu

When Scientific Data Become Legal Evidence

IN THE 9 JANUARY ISSUE, THE NEWS OF THE Week story "Brain scans of pain raise questions for the law" (G. Miller, p. 195) and the Books review "Grappling with the gulf" (D. Greenbaum and M. Gerstein, p. 210) highlight an important misunderstanding between lawyers and scientists concerning what constitutes "proof." Scientists hesitate to accept evidence for a hypothesis unless they can demonstrate a statistical probability of over 95% that the observations are not due to chance. In civil cases, such as contract or tort cases by insured patients against their insurers, the decision is made on the basis of a "preponderance of the evidence"—essentially a 51% probability (*1*). I fear that by using the scientific criterion of proof rather than the legal one, expert witnesses arbitrarily bias the case against one of the parties.

HARVEY S. FREY

Health Administration Responsibility Project, Inc., Santa Monica, CA 90402–2908, USA. E-mail: hsfrey@harp.org

Note

1. Criminal cases use a different standard of proof: "beyond a reasonable doubt." In these cases, perhaps even the standard 5% confidence level would not be strict enough.

Response

THE STATISTICAL SIGNIFICANCE OF THE UNDERlying science should not be conflated with the plaintiff's ultimate burden of proof in a trial. Frey's argument that less rigorous standards for science should be applied in a legal case fails: Invalid or unreliable science—as evaluated by the rigorous standards of scientific

practice—cannot be of any useful assistance to jurors in making a determination, regardless of the burden of proof required (*1*).

It is also worth noting that under the rules of evidence (*2*), the bar that is set for the ultimate burden of proof is conceptually quite different from that which is set for the admissibility of expert scientific evidence. In American courts, the judge first evaluates the validity of scientific evidence that is sought to be introduced into evidence, either directly or, in some states, by looking for "general acceptance" by the scientific community. In either case, science that is unreliable (e.g., low statistical significance or poor methodology) or irrelevant to the purpose will not be admitted. Only if it is admitted will the judge or jury decide how much weight to accord to that evidence, in light of the relevant burden of proof for the trial (*3*).

Trials are not tidy. They cannot be executed in labs, where the pursuit of truth is generally unconstrained by social values such as deterrence, justice, or liberty. Rather than conflating legal outcomes with *P* values, perhaps trials are more like a tennis match. Scientific experts can help us determine whether the server hit the ball. The state then decides how far from the center to place the net. But it is the job of the jury or the judge, and only theirs, to decide whether or not the ball was inside the line.

TENEILLE BROWN,[1,2] EMILY R. MURPHY,[2] MARK GERSTEIN,[3] DOV GREENBAUM[4]*

[1]Stanford Center for Biomedical Ethics, Center for Integration of Research on Genetics and Ethics, Palo Alto, CA 94304, USA. [2]Stanford Law School, Stanford, CA 94305, USA. [3]Department of Biomedical Informatics, Department of Molecular Biophysics and Biochemistry, and Department of Computer Science, Yale University, New Haven, CT 06511, USA. [4]McDermott, Will, and Emery, LLP, Menlo Park, CA 94025, USA.

*To whom correspondence should be addressed. E-mail: dov.greenbaum@aya.yale.edu

References

1. *Rosen v. Ciba-Geigy Corp.*, 78 F.3d 316, 318 (7th Cir. Ill. 1996) (Posner, J.).
2. USCS Fed. Rules Evid. R 702 (2009).
3. *Daubert v. Merrell Dow Pharms.*, 509 U.S. 579 (U.S. 1993).

CORRECTIONS AND CLARIFICATIONS

News of the Week: "Tracking CO_2's comings and goings from space" by D. Normile (16 January, p. 325). Peter Rayner's name was misspelled.

Random Samples: "The priestess's tale" (9 January, p. 189). Lady Meresamun is 2800, not 4800, years old.

TECHNICAL COMMENT ABSTRACTS

COMMENT ON "Atmospheric Hydroxyl Radical Production from Electronically Excited NO_2 and H_2O"

Scott Carr, Dwayne E. Heard, Mark A. Blitz

Li *et al*. (Reports, 21 March 2008, p. 1657) suggested that the reaction between electronically excited nitrogen dioxide and water vapor is an important atmospheric source of the hydroxyl radical. However, under conditions that better approximate the solar flux, we find no evidence for OH production from this reaction.

Full text at www.sciencemag.org/cgi/content/full/324/5925/336b

RESPONSE TO COMMENT ON "Atmospheric Hydroxyl Radical Production from Electronically Excited NO_2 and H_2O"

Shuping Li, Jamie Matthews, Amitabha Sinha

Carr *et al*. failed to detect hydroxyl radical formation from the reaction of excited state nitrogen dioxide with water, contrary to our findings. We present several reasons, based on energetic and spectroscopic considerations, that the OH radicals we observed from this reaction are not likely to be due to multiphoton excitation as they suggest.

Full text at www.sciencemag.org/cgi/content/full/324/5925/336c

Comment on "Atmospheric Hydroxyl Radical Production from Electronically Excited NO_2 and H_2O"

Scott Carr,[1] Dwayne E. Heard,[1] Mark A. Blitz[1,2]*

Li *et al*. (Reports, 21 March 2008, p. 1657) suggested that the reaction between electronically excited nitrogen dioxide and water vapor is an important atmospheric source of the hydroxyl radical. However, under conditions that better approximate the solar flux, we find no evidence for OH production from this reaction.

The most important radical for driving the chemistry of the atmosphere is the hydroxyl radical, OH, because of its ability to react with almost all the gases emitted into the atmosphere (*1*). OH is predominately formed when $O(^1D)$, produced from ozone photolysis ($\lambda \leq 340$ nm), reacts with water vapor in the atmosphere, and subsequently OH is removed by reaction with, among other compounds, CO, NO_2, and hydrocarbons. The rapid rate of formation and removal of OH results in a steady-state daytime concentration that is sensitively controlled by the concentration of OH sources and sinks. There have been a number of newly identified sources and sinks for OH, for example, the regeneration of OH after the oxidation of isoprene (*2*). Li *et al*. (*3*) recently identified a new atmospheric source of OH, in which nitrogen dioxide excited by visible light (denoted NO_2*) was found to react with water vapor to generate OH:

$$NO_2 + h\nu\ (\lambda > 420\ nm) \rightarrow NO_2^* \quad (1)$$

$$NO_2^* + H_2O \rightarrow OH + HONO \quad (2)$$

$$NO_2^* + H_2O \rightarrow NO_2 + H_2O \quad (3)$$

Li *et al*. report that only about one collision in a thousand between NO_2* and water vapor gives OH (Eq. 2), with the rest deactivating NO_2* (Eq. 3). However, the solar flux in the visible region of the spectrum is so large that despite being inefficient (OH yield ~ 0.001), this reaction still represents a major source of OH—up to 50% of that produced from $O(^1D)/H_2O$ (*3*) at high solar zenith angles under polluted conditions.

Verifying the existence of reaction 2 is very demanding because of the low yield of OH. In addition, other molecules present in the experiment may deactivate NO_2* (*3*–*5*):

$$NO_2^* + M \rightarrow NO_2 + M \quad (\text{where M is } NO_2, He, O_2) \quad (4)$$

Such a low yield of OH places very stringent demands on its detection, and high initial NO_2* concentrations are required to facilitate the experiment, achieved by Li *et al*. using a combination of a large excitation laser pulse energy and a lens to focus the laser light and generate a large fluence.

We also measured the OH yield from reaction 2 but have failed to observe OH, finding an OH yield of <0.00006. In our experiments, we used a sensitive off-resonance laser induced fluorescence (LIF) scheme to detect OH (*6*), using a laser fluence for the visible excitation radiation at least an order of magnitude lower than that used by Li *et al*. The observed OH LIF signal gives only a relative measure of concentration and must be calibrated using a known concentration of OH, which we generated by frequency doubling the laser light (either at 563.5 or 567.5 nm) to the ultraviolet, where acetone is photolysed (*7*):

$$(CH_3)_2CO + h\nu\ (\lambda \sim 280\ nm) \rightarrow CH_3CO + CH_3 \quad (5)$$

In the presence of oxygen, OH is formed with a known yield (*8*) by

$$CH_3CO + O_2 \rightarrow OH + products \quad (6)$$

We reduced the laser fluence so that the OH concentration as predicted by Li *et al*. from reaction 3 should be similar to that generated by our calibration reaction 6. Figure 1 shows the two experimental OH time profiles for the OH calibration reaction and the reaction of NO_2* with water vapor, together with a calculated profile for OH from reaction 2 using the reported yield from Li *et al*. Our results provide no evidence for the occurrence of reaction 2. Using the standard deviation of the noise of our experiment, we estimate an upper limit for the OH yield from reaction 2 to be a factor of 17 lower than that reported by Li *et al*. (*3*), at the 2σ level. This result is in agreement with Crowley *et al*. (*9*).

The reason for this difference is not clear but both Crowley *et al*. (*9*) and our current study used unfocused laser light, whereas Li *et al*. used a lens to focus the laser light. Multiphoton processes were ruled out by Li *et al*. because the dependence of the OH signal on laser fluence was observed to be linear, but the plots shown in Li *et al*. to support this conclusion show negative intercepts, whereas a genuine single-photon process should only produce zero OH signal at zero pulse energy.

Another intriguing result from the work of Li *et al*. is the observation of vibrationally excited hydroxyl radical, OH(v), even at red wavelengths, where its formation is not thermodynamically possible [566 nm is the limit (*10*)]. It was suggested that OH(v) results from reaction between NO_2* with vibrationally excited water vapor (H_2O*), with the latter being formed by rapid collisional energy transfer

$$NO_2^* + H_2O \rightarrow NO_2 + H_2O^* \quad (7)$$

followed by the reaction between H_2O* and NO_2*.

$$NO_2^* + H_2O^* \rightarrow OH(v) + HONO \quad (8)$$

As noted by Li *et al*., this mechanism requires two NO_2* molecules to form OH(v), so the LIF signal from OH(v) should exhibit a squared dependence on the laser fluence used to excite NO_2*. It was suggested that this mechanism was minor because of the linear dependence of the OH signal on the NO_2 excitation laser energy. However, if the OH signal versus the NO_2 excitation laser energy of Li *et al*. were indeed squared, it could explain both the observed negative intercepts of their linear fits and the absence of any OH signal in our lower fluence experiments. Unfortunately, the maximum laser fluence used in our experiments was below the threshold required by Li *et al*. to generate OH signal, so we were unable to test this hypothesis.

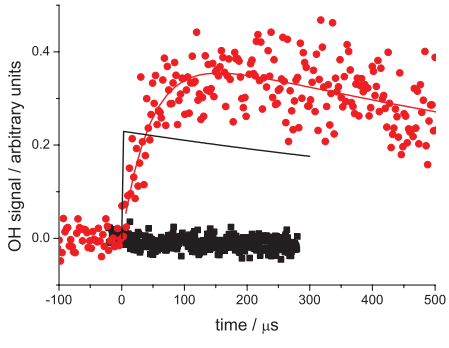

Fig. 1. OH time profiles for the reference reaction 6 (red circles) and the reaction NO_2* + H_2O vapor, 2 (black squares), together with that predicted from Li *et al*. (*3*) for reaction 2 (black line). Reaction 6 data were obtained from laser excitation of NO_2* at 567.5 nm, 3.3 mJ/pulse; reaction 2 data were obtained after laser photolysis of acetone at 283.75 nm, 0.11 mJ/pulse.

[1]School of Chemistry, University of Leeds, Leeds LS2 9JT, UK. [2]National Centre for Atmospheric Science, School of Chemistry, University of Leeds, Leeds LS2 9JT, UK.

*To whom correspondence should be addressed. E-mail: m.blitz@leeds.ac.uk

In conclusion, we studied the reaction between excited state nitrogen dioxide, NO_2*, and water vapor and, contrary to the study by Li *et al*. (*3*), failed to observe the formation of the hydroxyl radical. We assign an upper limit for reaction 2 and suggest that this reaction has little impact on atmospheric chemistry.

References and Notes

1. D. E. Heard, M. J. Pilling, *Chem. Rev.* **103**, 5163 (2003).
2. J. Lelieveld *et al*., *Nature* **452**, 737 (2008).
3. S. Li, J. Matthews, A. Sinha, *Science* **319**, 1657 (2008).
4. G. H. Myers, D. M. Silver, F. Kaufman, *J. Chem. Phys.* **44**, 718 (1966).
5. V. Sivakumaran, K. P. Subramanian, V. Kumar, *J. Quant. Spectrosc. Radiat. Transf.* **69**, 525 (2001).
6. Materials and methods are available as supporting material on *Science* Online.
7. M. A. Blitz, D. E. Heard, M. J. Pilling, *J. Phys. Chem. A* **110**, 6742 (2006).
8. M. A. Blitz, D. E. Heard, M. J. Pilling, *Chem. Phys. Lett.* **365**, 374 (2002).
9. J. N. Crowley, S. A. Carl, *J. Phys. Chem. A* **101**, 4178 (1997).
10. www.iupac-kinetic.ch.cam.ac.uk/

11. We acknowledge the support of Engineering and Physical Sciences Research Council for a studentship for S.C. and for a grant (GR/T28560/01) under which this work was carried out and the Composition Directorate of the National Centre for Atmospheric Science (NCAS). We also thank P. Seakins and M. Pilling for useful discussion.

Supporting Online Material

www.sciencemag.org/cgi/content/full/324/5925/336b/DC1
Materials and Methods
Table S1
Figs. S1 to S3
References

1 October 2008; accepted 20 March 2009
10.1126/science.1166669

Response to Comment on "Atmospheric Hydroxyl Radical Production from Electronically Excited NO_2 and H_2O"

Shuping Li, Jamie Matthews, Amitabha Sinha*

Carr *et al*. failed to detect hydroxyl radical formation from the reaction of excited state nitrogen dioxide with water, contrary to our findings. We present several reasons, based on energetic and spectroscopic considerations, why the OH radicals we observed from this reaction are not likely to be due to multiphoton excitation as they suggest.

The reaction of electronically excited nitrogen dioxide with water, NO_2*+ H_2O, can be an important source of atmospheric OH radicals if its reaction rate is sufficiently fast (*1*–*3*). Carr *et al*. (*2*) report a rate for this reaction that differs from the rates we reported (*3*) by more than an order of magnitude. In their study, Carr *et al*. report being unable to detect any OH from the reaction in the vicinity of 560 nm, whereas we reported detecting OH products over the region from ~560 to 635 nm by electronically exciting NO_2 in the presence of water vapor (*3*). The reasons for the differences in the results of the two studies are not obvious, although it is well known that the reaction under consideration is a difficult one to study because of rapid quenching of the electronically excited NO_2 by water and the low product yields (*1*–*3*). The main difference in the approaches between the two studies apparently involves the laser power density used to excite the NO_2 reagent and the calibration reaction used to quantify OH yields.

In our experiment, we used a lens to introduce the excitation laser into the reaction cell and electronically excite NO_2 (*3*). This was necessitated by the low electronic absorption cross section of NO_2 over the red end of the spectral range covered in our study. By contrast, Carr *et al*. did not use a lens, and thus their measurements used an unfocused laser beam (*2*). With regard to the OH calibration reaction, we used OH from the vibrational overtone–induced unimolecular dissociation of CH_3OOH ($5\nu_{OH}$) to calibrate OH yields, whereas Carr *et al*. used the photodissociation of acetone followed by the reaction of the resulting acetyl radical with O_2 for their calibrations. Carr *et al*. suggest that the difference in their results and those of our study are likely due to multiphoton effects contributing to the OH signal in our study arising from the greater laser power density created by the presence of the lens. Carr *et al*. cite the presence of an intercept appearing in the linear power dependence plot in (*3*) as indicative of multiphoton effects. However, the authors do not provide any particular mechanism to suggest how the OH radicals we observed are produced by the multiphoton excitation process, nor do they provide any data on the effect of increasing laser power density in their measurements on the OH yield. In (*3*), we suggested that the intercepts in our power dependence plots likely arose from our detection electronics. Indeed, we looked at the power dependence for OH formation from the unimolecular dissociation of CH_3OOH ($5\nu_{OH}$) and HNO_3 ($5\nu_{OH}$), which are both linear processes, using the same experimental setup as that used for the NO_2*+H_2O study and found small intercepts in the power dependence plots for these unimolecular processes as well (intercepts of ~1 to 2.5 mJ, corresponding to 6 to 8% of the peak power range). Hence, the presence of an intercept in an otherwise linear power dependence plot does not in itself signify the occurrence of multiphoton effects.

Based on the OH spectrum recorded and the action spectrum presented in (*3*), we have little doubt that we observed OH from the excitation of NO_2 in the presence of water. Could the OH we detected arise from multiphoton effects? As reported in (*3*), we considered the possibility of several multiphoton mechanisms and found no compelling evidence for their occurrence. First, multiphoton dissociation of NO_2 can result in the production of electronically excited oxygen atoms such as $O(^1D)$. However, it is well known that a common characteristic of $O(^1D)$ atoms is that they react rapidly with H_2 to produce OH radicals (*4*). When we introduced H_2 into the experimental cell in place of H_2O, we did not observe any OH being produced (*3*). This lack of OH formation, which would be expected if $O(^1D)$ were present, nullifies the production of these electronically excited atoms through multiphoton excitation of NO_2. A second multiphoton process that was also considered involved the possibility of producing translationally hot ground state $O(^3P)$ atoms from the multiphoton dissociation of NO_2. These oxygen atoms could in principle then react with water to produce OH radicals. This scenario was ruled out on the basis that the reaction of $O(^3P)$+H_2O is endothermic by roughly 17 Kcal/mole (*4*). Measurements of Brouard and Vallance (*5*) show that $O(^3P)$ atoms generated from the photodissociation of NO_2 at 308 nm have an average translational energy of 0.3 eV (~6.9 kcal/mole) with a full-width at half-max of 0.2 eV. As we also observed OH production for NO_2 excitation wavelengths between 610 and 630 nm, which corresponds to a two-photon excitation energy equivalent to exciting between 305 and 315 nm, the results of Brouard and Vallance then suggest that the average translational energy of the oxygen atoms potentially generated by two-photon dissociation of NO_2 at these wavelengths will not be sufficiently energetic to initiate the $O(^3P)$+H_2O reaction. Hence, this multiphoton mechanism for OH production was also ruled out. Third, the possibility of populating long-lived bound excited quartet electronic excited states of NO_2 through multiphoton excitation, which then reacts with H_2O, has also been considered. According to the calculations of Bera *et al*. (*6*), NO_2 has several excited quartet states in the vicinity of 3.61 to 4.37 eV. Accessing these bound excited electronic states of NO_2 from the ground state requires the involvement of spin-forbidden transitions. These bound excited states could potentially be accessed through sequential two-photon excitation by the intermediate A $^2B_2$ electronic state of NO_2 initially populated through excitation in the visible range. However, spectral features of bound-to-bound transitions such as these should be reflected in their characteristic structured excitation spectrum. The action spectrum generated from the NO_2*+ H_2O reaction in (*3*), however, match that expected from the traditional $X\,^2A_1 \rightarrow A\,^2B_2$ excitation of NO_2 in the visible range. Also, in addition to being spin-forbidden with respect to their photochemical formation, the subsequent bimolecular reaction of these quartet NO_2 states with H_2O to form OH + HONO is expected to be spin-forbidden as well. Finally, we also considered the possibility that the primary source of OH signal in our experiments were due to the collision of electronically excited nitrogen dioxide, NO_2*, with vibrationally excited water through the following reaction sequence.

$$NO_2^* + H_2O \rightarrow NO_2 + H_2O(v) \quad (1)$$

$$NO_2^* + H_2O(v) \rightarrow OH + HONO \quad (2)$$

The pseudo-first order rate constant for OH production through this mechanism would be expected to go as the square of the NO_2 concentration. Our experiments using different starting NO_2 concentrations did not show this squared dependence for the pseudo-first order rates; hence, this mechanism was ruled out as the main source of the observed OH signal, although it could contribute to small background levels as noted in (*3*). Thus, based on the above reasoning, it is difficult to justify the suggestion that the OH signal observed

Department of Chemistry and Biochemistry, University of California–San Diego, 9500 Gilman Drive, La Jolla, CA 92093–0314, USA.

*To whom correspondence should be addressed. E-mail: asinha@ucsd.edu

in our study and the rate we measured arise from multiphoton effects.

References

1. J. N. Crowley, S. A. Carl, *J. Phys. Chem. A* **101**, 4178 (1997).
2. S. Carr, D. E. Heard, M. A. Blitz, *Science* **324**, 336 (2009); www.sciencemag.org/cgi/content/full/324/5925/336b.
3. S. Li, J. Matthews, A. Sinha, *Science* **319**, 1657 (2008).
4. S. P. Sander *et al., Chemical Kinetics and Photochemical Data for Use in Stratospheric Modeling, Evaluation No. 15, JPL Publication* 06-2 (NASA Jet Propulsion Laboratory, Pasadena, CA, 2006).
5. M. Brouard, C. Vallance, *Phys. Chem. Chem. Phys.* **3**, 3602 (2001).
6. P. P. Bera, Y. Yamaguchi, H. F. Schafer, *J. Chem. Phys.* **127**, 174303 (2007).

29 October 2008; accepted 20 March 2009
10.1126/science.1166877

INTERNET AND SOCIETY

Sharing, Trading, Creating Culture

Yochai Benkler

At least one of you, your kids, your friends, or your students is probably a criminal, given the persistently high rates of Internet users who illegally share music online. Lawrence Lessig's *Remix: Making Art and Commerce Thrive in the Hybrid Economy* is an eminently readable argument that "the copyright wars" (the expansion of copyright law and its enforcement that led to this widespread criminalization) are harmful to a large body of both amateur and new commercial creativity. He finds them a form of regulation unnecessary except to support "Hollywood films, some kinds of blockbuster movies, maybe Justin Timberlake–like music, and maybe a few types of books." Lessig, the leading public intellectual in the field of copyright and lead founder of Creative Commons, knows what he speaks of, and he writes beautifully. The result is an engaging read about how the Internet affects our cultural production system and the policy implications of these effects. A substantial portion will particularly attract readers interested in cooperation, reciprocity, and prosocial motivations.

Remix
Making Art and Commerce Thrive in the Hybrid Economy
by Lawrence Lessig
Penguin Press, New York, 2008. 351 pp. $25.95, C$28.50. ISBN 9781594201721.

The argument has two main elements. First, Lessig emphasizes the centrality of remix—borrowing and re-creation from existing materials—to all creativity. Quotation is central to culturally anchored creativity. We cite and quote in academic articles. *West Side Story* builds on *Romeo and Juliet*. There is nothing new in this. What is new is that we can now quote liberally from film and recorded music as well as text. But our current approach to copyright developed at a time when quotation from recorded music and audiovisual works was only available to commercial entities, and thus it was designed to regulate such entities. So, Lessig tells us, while it is legal to excerpt a paragraph from Hemingway's *For Whom the Bell Tolls*, taking a snippet from Sam Wood's film version and posting a mashup on YouTube presents a thornier issue. Under these new technical conditions, rights regimes developed as an internal political negotiation between the only players who could realistically breach them (commercial entities in a commercial economy) are governing the day-to-day cultural practices of millions of amateurs who are the foundation of Internet culture.

YouTube success. Obama Girl's "I Gotta Crush on Obama" (2007) reflects the spirit of online creativity mix and match, with cultural and political overtones.

The second part of Lessig's argument is that creativity on the Net will take the form of both noncommercial sharing and hybrids of commercial economic activity with voluntary, non–cash-based forms of online work. This part seeks to answer the concerns of those who ask: Well, if we moderate copyright protection for creative industries, how will we sustain a cultural production system? Lessig contends that some of the most creative Internet startups are constructing complex cooperative relationships with the volunteer practices they facilitate and harness. These relationships are becoming a new form of sustainable commercial creativity, emerging alongside similarly sustainable volunteer production. Together, the two approaches constitute a production system no less sustainable than the 20th-century version they are replacing. But it is a system that is hurt, much more than it is helped, by the excesses of late-20th-century copyright law. Lessig caps his account with a series of proposed legal reforms that would improve the ease with which amateur creativity can thrive and create a system in which entrepreneurship in the hybrid economy can flourish.

Two aspects of *Remix* are likely to be of primary interest to scientists. The first is that the concerns he raises about excessive property rights getting in the way of creative uses of existing materials apply as well to data and the technical and legal constraints on sharing them, to research tools and patents constraining their application, to materials and material transfer agreements that can impede their employment across institutions and labs, and to open access publishing. Understanding how copyright law in particular can undermine creation, not only support it, offers a valuable background from which to understand these more science-centric problems. Second, Lessig weaves his tapestry from many stories about human cooperation, a subject of increasing interest to social and evolutionary scientists alike. The author starts with the better-known paradigm cases of Wikipedia and the GNU/Linux operating system, but he quickly moves on to some 20 less well-known examples that encompass both pure volunteer and mixed commercial-volunteer efforts—from Dogster to Last.fm. Two or three of these touch on efforts to harness decentralized contributors to scientific projects, as in NASA's 2000–2001 experiment with recruiting amateurs to help map Mars and in distributed computing projects like Einstein@ Home. Lessig describes instances of simple mutualism (such as Skype or the links used in Google's search algorithm) and direct and indirect reciprocity (in motivations reported by contributors to free and open-source software projects). Other examples demonstrate drivers of human cooperation such as inequity aversion and motivation crowding-out—the increasingly well-supported idea that financial rewards can crowd out intrinsic motivations (*1*), e.g., the classic argument that introducing

The reviewer is at the Harvard Law School, Berkman Center for Internet and Society, Harvard University, Cambridge, MA 02138, USA. E-mail: yochai_benkler@harvard.edu

Published by AAAS

a blood market displaces voluntary blood donations. His descriptions of how successful hybrids, like craigslist, attend to the delicate interface between commercial and social motivations are particularly illuminating. The emphasis on the need of new companies in the hybrid economy to "get it"—to understand that you cannot express pleasure in love-making by leaving a fat check at the end of the evening—provides some fascinating insights into cooperation.

Reference
1. S. Bowles, *Science* **320**, 1605 (2008).

10.1126/science.1172790

INTERNET AND SOCIETY

Growing Up Connected

Jennifer Preece

Digital natives are everywhere—in Europe, America, Japan, China, Korea, Brazil, South Africa, …. These tech-savvy youngsters come from different cultures, but they use technology in surprisingly similar ways. They include the teenage girls on the metro texting each other while giggling and listening to music and the boy entranced by a collaborative game who refuses to come to dinner with his parents. Born during the Internet and mobile phone era, digital natives live in online communities and physical spaces with equal ease, often simultaneously. They meet in Facebook and MySpace and text the friend walking next to them and strangers many kilometers and time zones away. Switching between media and devices, doing two or three things at once—listening to music, tackling homework, and chatting to friends—comes naturally to them. They have grown up with technology and they are comfortable with it.

Digital natives like to experiment with media and to share stories, pictures, and videos online. They comment on one another's blogs and explore different ways of representing themselves online. Everything online can be interacted with, commented on, changed, or added to, including their identities. Identity appears to be malleable just like information.

The reviewer is at the College of Information Studies, University of Maryland, College Park, MD 20742, USA. E-mail: preece@umd.edu

CREDIT: JOE SUTLIFF/WWW.CDAD.COM/JOE

Born Digital
Understanding the First Generation of Digital Natives

by John Palfrey and Urs Gasser

Basic Books, New York, 2008. 383 pp. $25.95, C$27.95. ISBN 9780465005154.

We who are not digital natives may watch with puzzled expressions as we try to make sense of their online world. Even the technology pioneers wonder what kind of society they are creating, how it will be different from today's society, and whether these changes are for better or worse?

John Palfrey and Urs Gasser (law professors at, respectively, Harvard University and the University of St. Gallen, Switzerland) are trying to help us "separate what we need to worry about from what's not so scary, what we ought to resist from what we ought to embrace." Their goal is to "present the good and the bad in context and to suggest things that all of us—parents, teachers, leaders of companies, and lawmakers—can do to manage this extraordinary transition to a globally connected society."

Through the course of 12 carefully documented chapters, Palfrey and Urs address many thorny issues. They ask how digital natives view identity and question why young people willingly divulge so much personal information online, without questioning the consequences. The authors point out that digital natives appear to be redefining privacy. Palfrey and Urs discuss safety online, exploring such concerns as online predation, exposure to indecent material, and aggressive behavior. They question the digital natives' ability to evaluate information quality and consider the problems of dealing with information overload.

Palfrey and Gasser remind us that although print, radio, and television each transformed society in its day, the "interactivity" of the Internet makes it different. The ability to engage with, change, personalize, and distribute content—sending it out, at the click of a button, to hundreds, thousands, and millions of people in seconds—goes beyond the power of other media. The Internet enhances collaboration, creativity, and innovation in new ways. For example, activists can organize political demonstrations so quickly that standard police tactics are impotent. Students can find and share information for a homework assignment in minutes and can work together on collaborative projects.

Born Digital offers a compelling account for parents, teachers, policy-makers, lawyers, and technical developers who want to know more about digital natives' online activities and how these are changing society. I particularly welcome the broad coverage of topics, presented in a coherent and balanced way, illustrated with a rich set of examples. The chapters vary somewhat in depth, but each draws on current research by the authors and others. Palfrey and Gasser present a balanced view, highlighting problems and calling for solutions. They recommend that parents and teachers educate themselves more about technologies and how digital natives use them. Parents who stand back and do not involve themselves in their offspring's online activities are, they suggest, missing an opportunity to protect, engage with, and help their children. *Born Digital* is timely and informative; although a little repetitive in the early chapters, it challenges the reader to think deeply about how our society is changing.

The book would have gained additional influence if it had offered deeper discussions of solutions, including challenges to technology designers and entrepreneurs. For example, the authors provide evidence suggesting that "shoot 'em up" games may predispose children to violent acts. They could also have mentioned successful games that encourage learning, collaboration, and friendship. Challenging clever developers to work with young users to create games that encourage creativity, responsibility, empathy, and altruism might bring about new genres of games. Because peace, the environment, and sustainability also interest the young, wouldn't such topics be candidates for novel applications? Although Palfrey and Gasser encourage parents and teachers to guide children, their fine book would be even stronger if they had emphasized the roles of technology developers and of digital natives themselves. These issues invite further research by the authors and others. Just like a good film, *Born Digital* sets the scene for a sequel.

10.1126/science.1171818

SCIENCE AND GOVERNMENT

Governance and Environmental Change in the Arctic Ocean

Strategies are being sought that will promote international cooperation and reduce the risks of discord in the Arctic Ocean.

Paul Arthur Berkman[1,2]* and Oran R. Young[2]

The Arctic Ocean is crossing an environmental threshold expected to transform it from a perpetually ice-covered region to a seasonally ice-free sea within the next few decades (*1*, *2*). This environmental change has awakened global interests in Arctic energy, fishing, shipping, and tourism. The Arctic could slide into a new era featuring jurisdictional conflicts, increasingly severe clashes over the extraction of natural resources, and the emergence of a new "great game" among the global powers. However, the environment provides a physical and a conceptual framework to link government interests in the Arctic Ocean, as well as a template for addressing transboundary security risks cooperatively.

The Arctic coastal states are collectively and individually reinforcing their sovereign rights and jurisdiction from their coastlines seaward, as stated in the May 2008 Ilulissat Declaration (*3*), the January 2009 Arctic Region Policy directive of the United States (*4*), and the March 2009 Arctic State Policy of the Russian Federation (*5*). Non-Arctic nations are seeking an enhanced role in the Arctic Council and asserting Arctic policy strategies of their own, as exemplified by the October 2008 Resolution of the European Parliament (*6*) and the November 2008 Communication from the European Commission (*7*). Military interests in the Arctic Ocean are mounting as reflected by the Canadian decision to purchase ice-breaking patrol vessels, the rebuilding of Russia's northern fleet, and the emerging interest in the Arctic on the part of the North Atlantic Treaty Organization.

At the same time, these developments present the international community with a historic opportunity to integrate science and diplomacy. As with the governance of other international spaces, such as Antarctica, science has a dual role: to interpret the dynamics of the Earth system (e.g., phenomena of stratospheric ozone depletion and climate change) and to carry out the monitoring, reporting, and verification needed to maintain trust in international cooperation. Success of science diplomacy in the Arctic will depend on knowledge-sharing and the steady generation of scientific findings ranging from climate feedbacks to human adaptations under conditions of rapid biophysical and socioeconomic change.

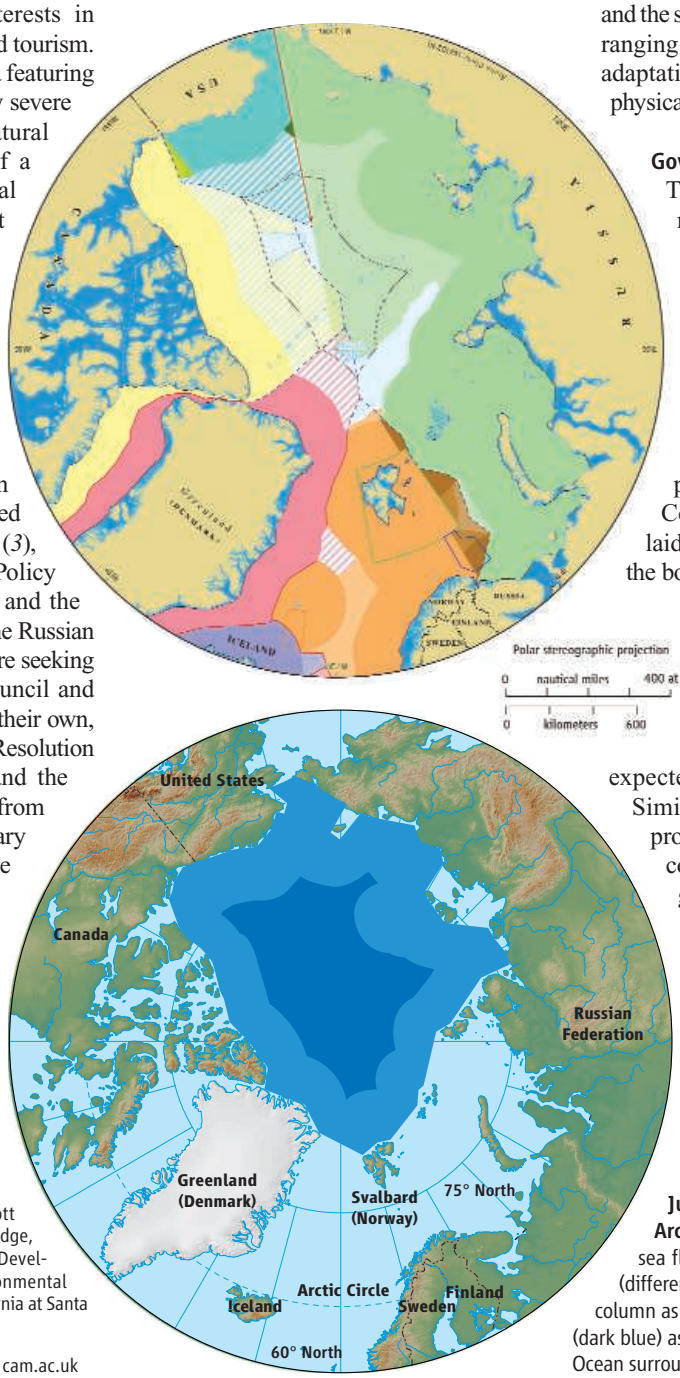

Jurisdictional representations of the Arctic Ocean with boundaries based on (**top**) sea floor as a source of conflict among nations (different colors) (*17*) and (**bottom**) overlying water column as a source of cooperation, with the high seas (dark blue) as an international space in the central Arctic Ocean surrounded by EEZs (light blue) (*18*).

CREDITS: (TOP) INTERNATIONAL BOUNDARIES RESEARCH UNIT, UNIVERSITY OF DURHAM; (BOTTOM) ADAPTED FROM CANADIAN POLAR COMMISSION

Governance Challenges

The Arctic Ocean is already subject to a number of governance systems (*8*). The 1982 United Nations Convention on the Law of the Sea (LOSC) applies to the entire Arctic Basin and is in force for all Arctic rim states except the United States, which accepts the relevant provisions of LOSC as customary international law. This governance system is playing a major role in the Arctic today. Coastal states are following the rules laid out in LOSC Article 76 to establish the boundaries of their jurisdiction over the seabed beyond the limits of the Exclusive Economic Zone (EEZ) (*9*). Russia and Norway have made submissions to the Commission on the Limits of the Continental Shelf; others are expected to follow suit (see figure, top). Similarly, the coastal states are using the provisions of LOSC Article 234 on ice-covered areas as a basis for regulatory guidelines applicable to Arctic shipping. Canada is extending the reach of its Arctic Waters Pollution Prevention Act. A number of related legal regimes, such as the 1973–78 Convention for the Prevention of Pollution from Ships and the 1995 United Nations Fish Stocks Agreement, are fully applicable to the Arctic.

[1]Arctic Ocean Geopolitics Programme, Scott Polar Research Institute, University of Cambridge, CB2 1ER, UK. [2]Governance for Sustainable Development Program, Bren School of Environmental Science and Management, University of California at Santa Barbara, Santa Barbara, CA 93106, USA.

*Author for correspondence. E-mail: pb426@ cam.ac.uk

Published by AAAS

At the other end of the spectrum lies the intergovernmental forum of the Arctic Council (*10*, *11*). Although the council has no regulatory authority, it has achieved considerable success in generating policy-relevant knowledge about the Arctic and bringing Arctic issues to the attention of global forums, such as the negotiating committee that produced the 2001 Stockholm Convention on Persistent Organic Pollutants. The council's primary products have been scientific assessments, including the 1997 State of the Arctic Environment Report, 2004 Arctic Climate Impact Assessment, 2004 Arctic Human Development Report, and 2008 Arctic Oil and Gas Assessment. An Arctic Marine Shipping Assessment is scheduled for release during 2009, and science is likely to continue to play a key role in the conduct of similar assessments.

Intermediate regulatory arrangements are emerging. The International Maritime Organization adopted a set of voluntary "Guidelines for Ships Operating in Ice-Covered Arctic Waters" in 2002 (*12*). The scope of some regional fisheries management organizations (RFMOs) created pursuant to LOSC Article 118 (e.g., the Northeast Atlantic Fisheries Commission) is broad enough to cover parts of the Arctic Basin (*13*). The 1992 Convention for the Protection of the Marine Environment of the North-East Atlantic, which focuses on pollution, is applicable to a significant segment of the Arctic Ocean.

Further developments of this sort are needed, including a mandatory polar code covering all forms of shipping, an Arctic-wide agreement designed to control marine pollution, a system of RFMOs specifically applicable to large marine ecosystems located wholly or partially in the Arctic, and a regulatory regime for tourism along the lines of the International Association of Antarctic Tour Operators. Such arrangements should be in place before severe ecological damage occurs and conflicts of interest become intractable.

Yet these sectoral regimes cannot avoid the dangers of institutional fragmentation. They also cannot provide integrated governance for the Arctic Ocean treated as a large, complex, and highly dynamic socio-ecological system (*14*). Some relevant precedents for integration exist. The 1980 Convention on the Conservation of Antarctic Marine Living Resources, for example, is based squarely on the goal of ecosystem-based management (EBM). But there is a clear need for enhanced scientific understanding of both biophysical and socio-economic systems in the Arctic as a basis for applying EBM. An important step is to strengthen the International Arctic Science Committee to further facilitate cooperation in all aspects of Arctic research (*15*). We also need to carry forward the shared momentum of the 2007–09 International Polar Year to stimulate ongoing interdisciplinary research and analysis relevant to the practice of EBM in the Arctic.

One useful approach in developing effective governance for a rapidly changing Arctic may be to treat the central Arctic as an international space and to draw a clear distinction between the overlying water column and the sea floor. Ecologically and legally distinct from the sea floor, the overlying water column and sea surface of the central Arctic can remain an undisputed international area (see figure, page 339, bottom) in which the interests of Arctic and non-Arctic states alike play a role in the development of effective governance. This region involves the high seas, a sea zone universally accepted as beyond national jurisdictions. Focus on the high seas opens the door to treating the central Arctic as an international space subject to cooperative decision-making regarding a variety of issues (e.g., fishing and shipping) through regulatory arrangements articulated under the auspices of LOSC and customary international law.

Environmental Security

As the European Commission Communication points out, environmental changes are altering geostrategic dynamics of the Arctic, and these changes could have consequences for international stability (*7*). The resultant risk of political, economic, or cultural instability has become a matter of global security. However, an inclusive dialogue about security risks and responses relating to the Arctic Ocean has yet to emerge. The injunction in the 1996 Ottawa Declaration that the Arctic Council should not deal with matters related to military security (*11*) is a serious constraint on efforts to address security and to come to grips with transboundary challenges. This has not precluded ad hoc measures directed toward specific concerns, like mitigating the impacts of radioactive waste associated with decommissioned nuclear submarines (*16*). But it has truncated efforts to design a coherent and inclusive approach to Arctic Ocean governance that prevents international discord.

The success of the Antarctic Treaty, founded on scientific cooperation and denuclearization, offers inspiration, although differences between the polar regions rule out a similar treaty in the Arctic. Moreover, in the Arctic, the combination of national and common interests will expand the policy choices for governments to enhance their own security.

Harmonization of international law with national approaches is a difficult task, especially without detracting from the authority of the Arctic rim states over their coastal and continental shelf regions. Nonetheless, national implementation strategies lack the consistency needed to resolve transboundary issues in a dynamic natural system. Holistic integration of EBM and other maritime management strategies pertaining to the Arctic Ocean requires coordination that acknowledges the special role and responsibilities of the Arctic States and indigenous peoples organizations. Before sectoral activities accelerate with the diminished sea ice, the window of opportunity is open for all legitimate stakeholders to forever establish their common interests in the central Arctic Ocean as an international space dedicated to peaceful uses.

References and Notes

1. M. M. Holland, C. M. Bitz, B. Tremblay, *Geophys. Res. Lett.* **33**, L23503 (2006).
2. Arctic Climate Impact Assessment, *Impacts of a Warming Arctic: Arctic Climate Impact Assessment* (Cambridge Univ. Press, Cambridge, 2004).
3. The Ilulissat Declaration from the Arctic Ocean Conference (Ilulissat, Greenland, 28 May 2008).
4. United States National Security Presidential Directive 66: Arctic Region Policy (Washington, DC, 9 January 2009).
5. *Basics of the State Policy of the Russian Federation in the Arctic for the Period until 2020 and for a Further Perspective* (Moscow; adopted 18 September 2008, promulgated 30 March 2009, published in *Rossiyskaya Gazeta* in Russian).
6. European Parliament Resolution on Arctic Governance [European Union (EU), Brussels, 9 October 2008].
7. European Commission Communication on the European Union and the Arctic Region (EU, Brussels, 20 November 2008).
8. T. Koivurova, E. J. Molenaar, *International Governance and Regulation of the Marine Arctic: Overview and Gap Analysis* (World Wildlife Fund International Arctic Programme, Oslo, 2009).
9. A. Proelss, T. Müller, *Heidelberg J. Int. Law* **68**, 651 (2008).
10. The Arctic Council involves the eight Arctic nations as members, six indigenous peoples organizations as permanent participants, and additional nations as observers.
11. Declaration on the Establishment of the Arctic Council (Ottawa, 19 September 1996).
12. Ø. Jensen, *The IMO Guidelines for Ships Operating in Arctic Ice-Covered Waters* (Fridtjof Nansen Institute, Lysaker, Norway, 2007).
13. E. J. Molenaar, R. Corell, *Arctic Fisheries: Background Paper for the Arctic TRANSFORM project of the European Commission* (Ecologic, Berlin, 9 February 2009).
14. L. Crowder *et al.*, *Science* **313**, 617 (2006).
15. International Arctic Science Committee, *IASC in Transition: Facing New Challenges in Arctic Science, Open Forum Discussion*, Arctic Science Summit Week, Bergen, Norway, 25 March 2009 (program brochure, IASC, Potsdam, Germany, 2009); www.imr.no/assw2009/__data/page/9019/IASC_In_Transition_-_Brochure.pdf
16. Declaration on Arctic Military Environmental Cooperation between the United States, Russian Federation, and Norway (Bergen, Norway, 26 September 1996).
17. International Boundaries Research Unit, University of Durham; www.dur.ac.uk/ibru/resources/arctic/.
18. R. Macnab, O. Loken, A. Anand, *Meridian* **2007,** 1 (Fall/Winter 2007); www.polarcom.gc.ca/rt.php?mode=ViewPost&postingID=88692.

19. We thank the Judge Business School for core support of the interdisciplinary Arctic Ocean Geopolitics Programme at the University of Cambridge.

10.1126/science.1173200

PALEONTOLOGY

Emerging onto a Tangled Bank

Fossils reveal how early tetrapods moved from water to land at an individual—rather than a phylogenetic—scale.

Matt Friedman

Open any paleontology text or children's book on prehistoric animals, and you will find something between fish and tetrapod, forelimbs or fins planted on the land, tail receding into the water, eyes cast hopefully forward. These images encapsulate an episode of vertebrate history spanning the latter half (390 to 360 million years ago) of the Devonian, the waning days of the "Age of Fishes." Research on the fish-tetrapod transition overwhelmingly targets changes across the evolutionary tree, but the phylogenetic shift from water to land must have been mirrored by transitions within individual life spans as species began to explore shores and banks. On page 364 of this issue, Callier *et al.* (*1*) report the earliest evidence for just such a life-history transformation.

Artist's impression of *Ichthyostega*.

The authors examined the humeri of two iconic tetrapods from East Greenland: *Ichthyostega* (see the first figure) and *Acanthostega*. Found in both the forelimbs of tetrapods and the lobed fins of their "fish" relatives, the humerus is the single bone that links the appendage to the body. It is a complicated, festooned with bumps and ridges marking muscle origins and insertions. Because humeri are integral to the pectoral appendages, they record the biomechanical signature of the shift from fins to weight-bearing limbs.

Callier *et al.* examined nine humeri of *Ichthyostega* from six individual animals, and four humeri from three *Acanthostega* specimens. By arranging these bones based on size and other probable proxies of maturity, they identified divergent developmental trajectories in *Acanthostega* and *Ichthyostega*. All the usual problems in reconstructing growth series from fossils are here—plus the added wrinkle that the *Ichthyostega* specimens under study derive from multiple locations and species—but the authors argue that the shifts they observe represent a developmental signal rather than an artifact.

In *Ichthyostega*, *Acanthostega*, and other tetrapods, the ventral (lower) surface of the humerus bears the pectoral process, a raised area marking the insertion of pectoral muscle. This feature occupies the conventional tetrapod position near the leading edge of the humerus in all *Acanthostega* and the most mature *Ichthyostega*, but in smaller *Ichthyostega*, the process lies close to the center of the bone (see the second figure).

On the basis of their new interpretations of humeri in close "fish" relatives of tetrapods, Callier *et al.* argue that the change within *Ichthyostega* development mirrors evolutionary patterns across phylogeny. Callier *et al.* reject earlier identifications (*2*) of a pectoral process in osteolepiforms (lobe-finned fishes closely related to tetrapods) and provide fresh perspectives on an isolated Devonian humerus (ANSP 21350) from an animal that probably lies just outside of the tetrapod group. The authors argue that this specimen bears a pectoral process in the same position—the center of the bone—as do the smallest *Ichthyostega*. In *Tiktaalik* (which is more closely related to ANSP 21350 plus tetrapods than are osteolepiforms), Callier *et al.* identify a potential precursor to the pectoral process, and this, too, is centrally placed. The implication is clear: The geometry of the pectoral process in younger *Ichthyostega* resembles that of the most immediate "fish" relatives of tetrapods, whereas the derived marginal position characteristic of tetrapods is limited to older *Ichthyostega*.

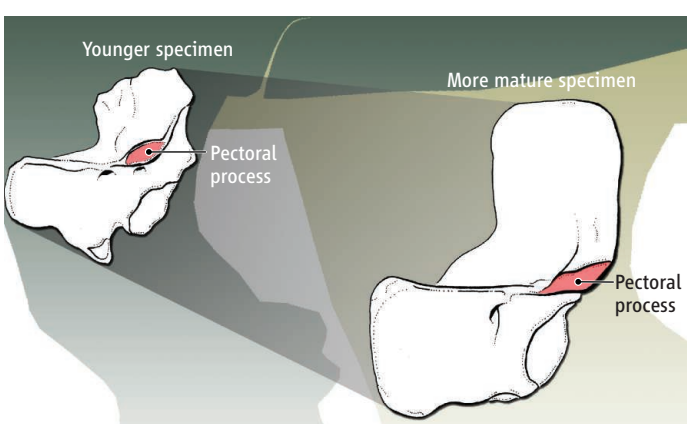

Remodeling of the humerus in *Ichthyostega*. In small *Ichthyostega* (**left**), the pectoral process (pink) lies near the center of the lower surface of the humerus, whereas, it rests near the anterior margin of the bone in larger specimens (**right**). Callier *et al.* (*1*) argue that this pattern reflects increasingly terrestrial habits during the life spans of *Ichthyostega* individuals.

Developmental migration of the pectoral process indicates shifts in muscle insertions and corresponding changes in function. The geometry seen in large *Ichthyostega* appears to have facilitated humeral retraction and pronation—movements associated with terrestrial locomotion. The resculpturing of the humerus in *Ichthyostega* during growth is complemented by transformations of shoulder girdle structure (*1*). Here, too, Callier *et al.* infer that the signal points to more time spent on land by older individuals than by younger ones, and conclude that they have captured the oldest fossil evidence for a devel-

Committee on Evolutionary Biology, University of Chicago, 1025 East 57th Street, Chicago, IL 60637, USA, and Department of Geology, Field Museum, 1400 South Lake Shore Drive, Chicago, IL, 60605 USA. E-mail: mattf@uchicago.edu.

opmental transition between aquatic and terrestrial environments.

These functional inferences are the latest addition to the diverse range of locomotor styles reconstructed for early tetrapods and their kin: terrestrial wriggling in *Panderichthys* (*3*), push-ups in *Tiktaalik* (*4*), inchworm crawling in *Ichthyostega* (*5*), and paddling in *Acanthostega* (*6*). Quantitative study is needed to evaluate these qualitative scenarios; comparative research that draws on living animals in addition to fossils provides a template for future work (*7, 8*).

Making sense of new results will require a phylogeny, and here too Callier *et al.* make contributions. They highlight features that are common to all *Ichthyostega* humeri but seem primitive relative to those in *Acanthostega* and other tetrapods. This observation hints at an inversion of the current consensus that *Ichthyostega* is more closely related to living tetrapods than is *Acanthostega* (*9*). Despite these new insights on humerus anatomy, the authors' most complete analyses invariably recover the conventional branching order: *Ichthyostega* above *Acanthostega*. These two switch positions only when certain fossils are excluded from consideration, and support for this unorthodox arrangement is always equivocal.

After 150 years of paleontological research dedicated to filling the gap between fishes and tetrapods (*10*), it is time to move past the simple formula of "the next missing link" and confront broader questions about tetrapod origins. The field has come far from its pre-Darwinian roots and ancestor-descendant daisy-chains, and now yields a profusely branching tree (*9*) and correspondingly nuanced scenarios of terrestrialization, including that proposed by Callier *et al*: in a very real sense, a tangled bank.

References

1. V. Callier, J. A. Clack, P. E. Ahlberg, *Science* **324**, 364 (2009).
2. S. M. Andrews, T. S. Westoll, *Trans. R. Soc. Edinb.* **68**, 207 (1970).
3. E. Vorobyeva, A. Kuznetsov, *Fossil Fishes as Living Animals* (Academy of Sciences of Estonia, Tallinn, 1992).
4. N. H. Shubin, E. B. Daeschler, F. A. Jenkins Jr., *Nature* **440**, 764 (2006).
5. P. E. Ahlberg, J. A. Clack, H. Blom, *Nature* **437,** 137 (2005).
6. M. I. Coates, J. A. Clack, *Nature* **347**, 66 (1990).
7. M. J. Markey, C. R. Marshall, *Proc. Natl. Acad. Sci. U.S.A.* **104,** 7134 (2007).
8. A. Canoville, M. Laurin, *Acta Zool.* **90**, 110 (2009).
9. M. Ruta, M. I. Coates, D. L. J. Quicke, *Biol. Rev.* **78**, 251 (2003).
10. R. Owen, *Rep. Br. Assoc. for the Adv. Sci.* **29**, 153 (1859).

10.1126/science.1172783

PHYSICS

Less Is More

Martin B. Plenio

Even though the complexity of a quantum system grows exponentially with size, we may ignore details in determining key properties

Quantum mechanical systems may exhibit correlations between their parts that are stronger than those permitted by classical physics. These correlations have challenged our understanding of the concepts of locality and reality in quantum mechanics (*1*). It was the crucial insight that entanglement actually represents a resource that has led to the rapid development of modern quantum information science, in which entanglement is used to realize novel information processing tasks. Unfortunately, the current experimental realizations are still imperfect and noisy. For the development of practical quantum technologies, it is therefore necessary to be able to verify quantitatively the presence of entanglement, as well as the quality of that entanglement and of the quantum information processors. Recent advances toward this goal have been made.

The traditional approach to this problem is to completely characterize the quantum state of the system by means of tomography—a method that provides a statistical map of the entire system's input and output. Gathering this information requires a large number of measurements on identically prepared copies of the system. If this data is taken in the right way, the quantum state of this system may be estimated. This is called state tomography (*2*, *3*). Similarly, the operations of a particular physical device (or process) on an arbitrary state can be measured by process tomography (*4*, *5*), as can the action of a measuring device, by detector tomography (*6*, *7*). Once the quantum state has been determined, all the properties of the system, including its entanglement, can be computed (*8*).

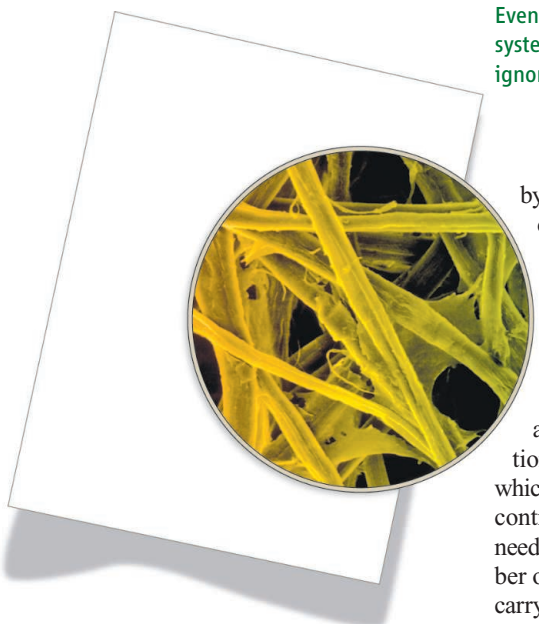

Discarding details. When investigating a physical system we are often concerned with some general features of the system (size, color, etc., of a sheet of paper) rather than the fine detail of its structure (fibers in the paper). A similar approach is useful when studying the properties of quantum systems. Rather than studying all the details of the system, we are often content with knowing single quantities, such as entanglement, that are easier to obtain than reconstructing the complete state of the system.

This approach, however, requires a data set that grows exponentially with the number of subsystems. The reason is that, say, N two-level systems can exist in a superposition of all the possible combinations of their excited and ground states, of which there are 2^N. The relative weight of each contribution, called probability amplitude, needs to be specified. Even for a modest number of subsystems, it is out of the question to carry out such a reconstruction in a reasonable time. The expectation is not to be able to go much beyond that of the complete characterization of an entangled state of eight ions as was obtained recently in an ion trap (*9*).

We face a dilemma here. On the one hand, it is the exponential growth of the state space that gives quantum systems their computational power—having the ability to explore an exponentially large number of computational paths at the same time. On the other hand, this large state space makes it hard to extract all the information about the quantum process that the system can carry out, or even to determine its quantum state. This situation clearly calls for more economic approaches. Perhaps a clever measurement could reveal the entanglement content of a state directly,

Department of Physics and Institute for Mathematical Sciences, Imperial College London, London SW7 2PG, UK. E-mail: m.plenio@imperial.ac.uk

without taking the detour of measuring the entire quantum state first. Unfortunately, this is not possible without making additional assumptions about properties of the quantum state that require full state tomography to be ascertained.

So, how can all the parameters that contribute to the state's entanglement be determined? Perhaps many of these parameters can be neglected with only a small error. But how do we know that the approximation is good—and what do we mean by "good"? Rather than obtaining an approximation, we need to determine rigorous lower bounds from a very small number of available data points (much fewer than those required for full state tomography). More precisely, given some measured data, the problem is to identify the quantum state with the least amount of entanglement that is consistent with the data. This is a somewhat daunting optimization problem but one that can be addressed using techniques from optimization theory (*10*). Such an approach allows for both numerical and analytical results to be obtained and applied to the (limited) experimental data at hand (*11*–*14*).

In this "less-is-more" approach, a considerable amount of information that is not needed to provide good bounds on the entanglement content of the state can be discarded. Concentrating on the crucial properties of the system in exchange for a substantial reduction of experimental and computational effort has proven fruitful in a variety of areas now and has been adopted, for example, in the study of the impact of environments on the dynamics of systems (*15*). Here, we are not perhaps interested in exploring every nook and cranny of the environment action, but just need to know specific aspects of its effect that provide enough knowledge to design techniques to combat the noise caused by the environment.

This idea of ignoring the details does seem to pay off in a variety of important instances in the characterization of quantum mechanical properties of states and operations or the dynamics of quantum systems. In the long run, following such an approach will be essential. As the size of quantum processors increases, it will not be possible to tell what it does perfectly, because it will not be possible to completely characterize the system. We could then well end up in a situation where we hold a perfectly fine device in our lab but cannot actually prove that it works. The ability to test key functionalities of quantum devices efficiently will thus be essential for further progress in the field.

References and Notes

1. M. Bell, K. Gottfried, M. Veltmann, *J. S. Bell on the Foundations of Quantum Mechanics* (World Scientific Publishing, Singapore, 2001).
2. K. Vogel, H. Risken, *Phys. Rev. A* **40**, 2847 (1989).
3. D. T. Smithey, M. Beck, M. Raymer, A. Faridani, *Phys. Rev. Lett.* **70**, 1244 (1993).
4. I. L. Chuang, M. A. Nielsen, *J. Mod. Opt.* **44**, 2455 (1997).
5. J. B. Altepeter *et al.*, *Phys. Rev. Lett.* **90**, 193601 (2003).
6. G. M. D'Ariano, L. Maccone, P. Lo Presti, *Phys. Rev. Lett.* **93**, 250407 (2004).
7. J. S. Lundeen *et al.*, *Nat. Phys.* **5**, 27 (2009).
8. M. B. Plenio, S. Virmani, *Quant. Inf. Comp.* **7**, 1 (2007).
9. H. Haeffner *et al.*, *Nature* **438**, 643 (2005).
10. S. Boyd, L. Vandenberghe, *Convex Optimization* (Cambridge Univ. Press, Cambridge, 2004).
11. K. M. R. Audenaert, M. B. Plenio, *New J. Phys.* **8**, 266 (2006).
12. O. Guehne, M. Reimpell, R. F. Werner, *Phys. Rev. Lett.* **98**, 110502 (2007).
13. J. Eisert, F. G. S. L. Brandao, K. M. R. Audenaert, *New J. Phys.* **9**, 46 (2007).
14. O. Guehne, G. Toth; http://arxiv.org/abs/0811.2803.
15. J. Emerson *et al.*, *Science* **317**, 1893 (2007).

16. I acknowledge support from the European Commission through the Integrated Project Qubit Applications (QAP), from the U.K. Engineering and Physical Sciences Research Council, and from The Royal Society.

10.1126/science.1170616

CELL BIOLOGY

Ceramides—Friend or Foe in Hypoxia?

Molecular details of how nematode cells respond to a low-oxygen environment suggest a possible mechanism by which mammalian cells survive hypoxic conditions.

C. Michael Crowder

Without oxygen, the cells of aerobic animals will eventually die. However, the amount and duration of hypoxia (an abnormally low-oxygen environment) required for cell death vary widely in the animal kingdom. Even cells within the same animal can differ greatly in their sensitivity to hypoxia. The ability of an animal to adapt to and survive hypoxia determines fundamental traits such as habitat range and hibernation potential. In humans, cellular injury due to hypoxia causes the most common forms of stroke and heart attack. Cancer cells are often resistant to hypoxic death, and this promotes their tendency to survive after metastasis (*1*). Thus, the cellular mechanisms that control hypoxic sensitivity are of considerable interest. Most of the known determinants of hypoxic sensitivity have been defined through hypothesis-driven experiments in mammalian cells. By contrast, exploratory genetic strategies that have been so successful at elucidating other complex biological pathways have been relatively underutilized. On page 381 of this issue, Menuz *et al.* (*2*) report a serendipitous result from a screen in the worm *Caenorhabditis elegans* for genes controlling anoxic (severely hypoxic) sensitivity.

C. elegans

Oxygen Deprivation

Ceramide synthase	Ceramides produced	Cell response to anoxia	Cell/organism outcome
HYL-1	C_{24-26}	Sensitivity increases	Death
HYL-2	C_{20-22}	Sensitivity decreases	Survival

Carbon chain conundrum. In the worm, ceramides with different lengths of fatty acid chains (ranging from 20 to 26 carbons) are produced in response to low oxygen, with different effects on survival. This raises the question of which human ceramide synthases are critical to surviving hypoxic and ischemic injury, such as stroke or heart attack.

By testing mutations in candidate genes that might regulate worm sensitivity to anoxia, Menuz *et al*. discovered a previously unknown set of vicinal mutations in the *hyl-2* gene, which encodes a homolog of the yeast longevity assurance gene, *LAG1*. *LAG1* and *LAC1* encode yeast dihydroceramide synthases (*3*, *4*). The amount of *LAG1* transcription varies with the replicative age of yeast

Departments of Anesthesiology and Developmental Biology, Washington University School of Medicine, St. Louis, MO 63110, USA. E-mail: crowderm@morpheus.wustl.edu

CREDIT: C. BICKEL/*SCIENCE*

cells, and deletion of *LAG1* increases the life span of haploid yeast cells, suggesting a role for this synthase in cellular aging (*5*). Expression of wild-type *hyl-2* in yeast cells lacking both *LAG1* and *LAC1* genes restored yeast viability, indicating that *hyl-2* encodes an authentic ceramide synthase.

Ceramide synthases acylate sphingoid bases with different lengths of fatty acid chains, ranging from 14 to 26 carbon atoms, to produce a family of ceramides (*6*). Ceramides serve as intermediates for sphingolipids, a major component of cell membranes. Beyond their structural role, ceramides have been implicated as signaling molecules in diverse biological processes in mammalian cells including inflammation, cellular differentiation, and cellular stress responses (*7*–*10*). In response to various stresses such as hypoxia and restricted blood supply (ischemia), total cellular ceramide concentration increases, which in turn can activate molecules that induce cell death (apoptosis) (*7*, *11*).

But *C. elegans* has two other ceramide synthase gene homologs, *hyl-1* and *lagr-1*. Both *hyl-1* and *lagr-1* are required for radiation-induced apoptosis, and germline injection of the 16-carbon ceramide can restore germline apoptosis in a *hyl-1* or *lagr-1* deletion mutant (*12*). Thus, ceramide (at least the 16-carbon ceramide) appears to promote radiation-induced germline apoptosis in *C. elegans*. Unlike worms lacking *hyl-2*, *hyl-1* deletion mutants were more resistant to anoxia than wild-type cells, as might be expected for loss of a proapoptotic gene. Like HYL-2, HYL-1 expression in yeast can rescue the lethal phenotype of a *lag1 lac1* double-deletion mutant (*13*). Thus, *hyl-1* also encodes an authentic ceramide synthase.

The contrasting anoxic sensitivity phenotypes of the *hyl-1* and *hyl-2* mutants indicates that the two ceramide synthases have distinct functions. By measuring the abundance of ceramide and sphingomyelin species in *hyl-1*(null), *hyl-2*(null), and wild-type worms by mass spectrometry, Menuz *et al*. determined that *hyl-1* mutant worms contained more 20- to 22-carbon ceramides and sphingomyelin species than wild-type worms, whereas *hyl-2* mutant worms had decreased amounts of these ceramide and sphingomyelin species compared to wild-type worms. Measurement of ceramide synthase activity in isolated microsomes of mutant and wild-type animals confirmed that HYL-1 and HYL-2 have distinct fatty acyl specificities, with *hyl-1* mutant microsomes synthesizing more 20- to 22-carbon ceramides and *hyl-2* mutant microsomes more 24- to 26-carbon ceramides. Together, these data suggest that 20- to 22-carbon ceramide and/or sphingomyelin molecules produced by HYL-2 are protective against anoxic injury. Alternatively, these ceramides and sphingomyelins may not be inherently protective against anoxic injury; rather, their synthesis by HYL-2 in a particular cellular or subcellular context or distribution may be protective.

Given the link between ceramides and apoptosis, Menuz *et al*. examined the relation between the well-defined apoptosis pathway in *C. elegans* and *hyl-2*. A double-mutant strain carrying a loss-of-function mutation of the apoptosis caspase gene *ced-3* and a *hyl-2* deletion mutation had anoxic sensitivity similar to that of the *hyl-2* deletion mutant strain, indicating that *hyl-2* does not require the canonical apoptosis pathway to control anoxic sensitivity. Menuz *et al*. also examined the relation between *hyl-2* and *daf-2*. *daf-2* encodes an insulin/insulin-like growth factor receptor homolog that negatively regulates worm life span, stress resistance, and hypoxia resistance (*14*, *15*). The authors found that a *daf-2* reduction-of-function mutant was anoxia resistant. The anoxia resistance of the *daf-2;hyl-2* double mutant was intermediate between that of the two single mutants, which suggests that the two pathways function in parallel to control anoxic sensitivity.

Most of what we know about the function of ceramides in hypoxic and ischemic injury is that they promote cell death in mammals. The findings by Menuz *et al*. indicate a broader role of ceramides beyond their established proapoptotic one in hypoxic cellular injury. Thus, inhibition of ceramide synthesis is unlikely to be a panacea for hypoxic injury. Rather, development of subtype-specific ceramide synthase inhibitors will likely be necessary. Are ceramide synthases a friend or foe in hypoxic injury? The answer is yes.

References and Notes

1. M. C. Brahimi-Horn, J. Chiche, J. Pouyssegur, *J. Mol. Med.* **85**, 1301 (2007).
2. V. Menuz *et al.*, *Science* **324**, 381 (2009).
3. S. Schorling, B. Vallee, W. P. Barz, H. Riezman, D. Oesterhelt, *Mol. Biol. Cell* **12**, 3417 (2001).
4. I. Guillas *et al.*, *EMBO J.* **20**, 2655 (2001).
5. P. D'Mello *et al.*, *J. Biol. Chem.* **269**, 15451 (1994).
6. Y. Pewzner-Jung, S. Ben-Dor, A. H. Futerman, *J. Biol. Chem.* **281**, 25001 (2006).
7. S. A. Novgorodov, T. I. Gudz, *J Cardiovasc. Pharmacol.* **53**, 198 (2009).
8. A. Jana, E. L. Hogan, K. Pahan, *J. Neurol. Sci.* **278**, 5 (2009).
9. C. E. Chalfant, S. Spiegel, *J. Cell Sci.* **118**, 4605 (2005).
10. A. H. Futerman, Y. A. Hannun, *EMBO Rep.* **5**, 777 (2004).
11. A. G. Basnakian *et al.*, *Am. J. Physiol. Renal Physiol.* **288**, F308 (2005).
12. X. Deng *et al.*, *Science* **322**, 110 (2008).
13. J. C. Jiang *et al.*, *Genome Res.* **8**, 1259 (1998).
14. A. Mukhopadhyay, S. W. Oh, H. A. Tissenbaum, *Exp. Gerontol.* **41**, 928 (2006).
15. B. A. Scott, M. S. Avidan, C. M. Crowder, *Science* **296**, 2388 (2002).

16. C.M.C. is supported by the National Institute of Neurological Disorders and Stroke, the National Institute of General Medical Sciences, the American Heart Association, and the McKnight Endowment Fund for Neuroscience.

10.1126/science.1173278

ENGINEERING

Can Technology Get Your Eyes Back on the Road?

John D. Lee

Technology can provide alerts as well as long-term feedback to help drivers pay attention to the road.

Paying attention to the right thing at the right time is important for many activities in daily life. For one—driving—it is critical. In the United States, more than 40,000 people die in motor vehicle crashes every year. More people die each month in crashes than the total killed in the terrorist attacks of 9/11 (*1*). Although alcohol impairment and speeding account for most of these fatalities, failures of attention also play an important role. The increasingly ubiquitous technology in our vehicles can either impair or improve how we distribute our attention, thus diminishing or enhancing safety. Driving provides a stark illustration of the importance of technology-mediated attention.

The degree to which technological distractions contribute to crashes is difficult to identify, because a glance away from the road leaves no physical evidence. To document driver behavior, small groups of volunteers have been filmed while they drive. In one such study, data collected with unobtrusive video cameras and instrumentation in 109 cars over 12 to 13 months found that failures of attention—including both drowsiness and distraction (performing nondriving tasks such as talking on a phone or adjusting

Department of Mechanical and Industrial Engineering, University of Iowa, Iowa City, IA 52242, USA. E-mail: jdlee@engineering.uiowa.edu

the radio)—contributed to 78% of the 69 crashes and 65% of the 761 near-crashes (*2*). Distraction associated with nondriving tasks contributed to 22% of crashes and near-crashes.

Increased complexity of the distracting task increased the likelihood of crashes and near-crashes; relative to undistracted driving, such incidents were about three times as likely for highly complex tasks (such as dialing a phone) and twice as likely for moderately complex tasks (such as inserting a CD). The frequency with which drivers engaged in distracting activities was strongly associated (correlation of 0.72) with drivers' involvement in attention-related crashes and near-crashes (*3*). Attention-related failures are thus not random occurrences. They are a consequence of enduring behavior patterns, in which frequent episodes of inattention make crashes more likely.

Driving, particularly while engaged in distracting activities, challenges the attentional capacity of people—it requires a constant shifting in the center of the driver's attention between competing demands and rapid reactions to "unexpected" events. Even when a driver's eyes are directed to the road, the cognitive demands of a nondriving task, such as a cell phone conversation, can disrupt scanning the environment around the vehicle (*4*) and can lead drivers to neglect important hazards (*5*). The more mentally demanding the task is, the greater the disruption (*6*). When the driver's eye movements are concentrated on the center of the road, critical hazards, such as the pedestrian on the right, can go unnoticed (see the figure, panel A).

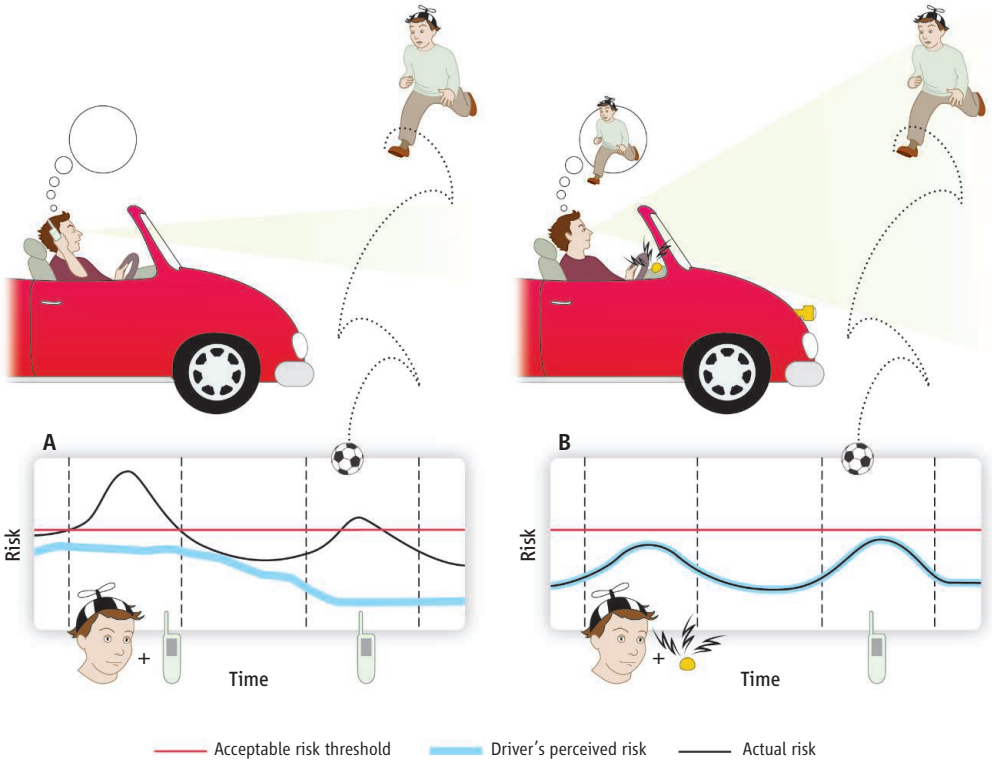

Attention and risk. (**A**) Technology such as cell phones can introduce distractions, as illustrated by a driver paying attention to a phone call and not the child pedestrian. The neglect of hazards and gaze concentration increases risk (shown in the graph as a solid black line) above an acceptable threshold (shown in red). Drivers usually underestimate risks (shown as the blue line). (**B**) Technology may mitigate distraction by helping drivers to distribute their attention and guiding them to engage distractions only when roadway demands are low. The driver, alerted to the hazard, now attends to driving. The cell phone interaction is now separated in time from the pedestrian encounter, and with repeated encounters, perceived risk is closer to the actual risk.

The failure to adequately attend to the roadway also contributes to a more insidious problem: Drivers who have been distracted might not be aware that they have had a near-miss of a crash—they cannot remember what they have not noticed. Drivers do not receive adequate feedback concerning how much distracting activities undermine their driving safety (even when they crash). Poor feedback contributes to a poor correspondence between actual and perceived performance decrements associated with distractions (*7*), which may lead drivers to adopt dangerous patterns of behavior.

Most drivers tend to overestimate their abilities (*8*). In a survey, 88% judged themselves to be safer than the average driver. Another survey found that this superiority bias persisted even with expert police drivers when they rated their ability relative to that of their peers (*9*). Drivers often fail to adjust their behavior even after surviving a crash involving a fatality (*10*). A similar bias afflicts those who engage in distracting activities; drivers who use a cell phone tend to perceive the probability of a distraction-related crash to be lower for themselves than for their peers (see the figure, bottom part of panel A) (*11*).

Technology need not only lead to distractions, however; it can also mediate driver attention to enhance driving safety. Drivers can be given an alert that directs their attention away from distractions and back to the roadway if they look away from the road for too long (*12*). Emerging technology can also record a history of distraction (such as drivers' eye movements and gadget usage) and the associated decline in driving performance. This information can then be shared with drivers to enhance their appreciation for the risks associated with driving while distracted.

Recent studies suggest that such postdrive feedback holds substantial promise for improving driver performance (*13*, *14*). Feedback given to people after they drove while engaging in distracting activities led these drivers to respond faster to vehicles braking ahead and to keep their eyes on the road (*15*). Another study tracked teenaged drivers who drove with a camera that captured abrupt braking and steering responses (*13*). The videos and a summary of these events were shared with the teens and their parents weekly. Results showed an 89% decline in the number of events triggered by risky drivers. Even after the feedback was removed, the rate of events remained low until the end of the study 6 weeks later. Enhanced feedback can thus lead to lasting changes in how drivers attend to the road. This positive influence of technology on driver attention might outweigh the negative effects of distracting technology (see the figure, panel B).

Whether such technology-mediated attention enhances or diminishes safety remains a critical question. Answering this question will require precisely controlled driving simulator studies to further understand the dynamics of technology-mediated attention, as well as naturalistic studies that collect information on how technology affects people's behavior on the road.

Published by AAAS

References and Notes

1. L. Evans, *Traffic Safety* (Science Serving Society, Bloomfield Hills, MI, 2004).
2. T. A. Dingus *et al.*, "The 100-Car Naturalistic Driving Study, Phase II—Results of the 100-Car Field Experiment," DOT HS 810 593 (Virginia Tech Transportation Institute, Blacksburg, VA, 2006).
3. S. G. Klauer, T. A. Dingus, V. L. Neale, J. D. Sudweeks, D. J. Ramsey, "The Impact of Driver Inattention on Near-Crash/Crash Risk: An Analysis Using the 100-Car Naturalistic Driving Study Data," DOT HS 810 594 (National Highway Traffic Safety Administration, Washington, DC, 2006).
4. M. A. Recarte, L. M. Nunes, *J. Exp. Psychol. Appl.* **9**, 119 (2003).
5. J. S. McCarley *et al.*, *Human Factors* **3**, 424 (2004).
6. T. W. Victor, J. L. Harbluk, J. A. Engstrom, *Transport. Res. F* **8**, 167 (2005).
7. W. J. Horrey, M. F. Lescha, A. Garabeta, *Accident Anal. Prevent.* **40**, 675 (2008).
8. O. Svenson, *Acta Psychol.* **47**, 143 (1981).
9. A. E. Waylen, M. S. Horswill, J. L. Alexander, F. P. McKenna, *Transport. Res. F* **7**, 323 (2004).
10. S. Rajalin, H. Summala, *Accident Anal. Prevent.* **29**, 277 (1997).
11. M. P. White *et al.*, *Risk Anal.* **24**, 323 (2004).
12. J. D. Lee, D. V. McGehee, T. L. Brown, M. L. Reyes, *Human Factors* **44**, 314 (2002)
13. D. V. McGehee, M. Raby, C. H. Carney, M. L. Reyes, J. D. Lee, *J. Safety Res.* **38**, 15 (2007).
14. T. Tomer, T. Lotan, *Transport. Res. Rec.* **1953**, 112 (2006).
15. B. Donmez, L. N. Boyle, J. D. Lee, *Accident Anal. Prevent.* **40**, 776 (2008).
16. The work presented is based in part on the SAVE-IT program [Safety Vehicle(s) Using Adaptive Interface Technology] sponsored by the National Highway Traffic Safety Administration, U.S. Department of Transportation.

10.1126/science.1168085

CELL BIOLOGY

Two Lipids That Give Direction

Precise and sequential intracellular signaling events involving two phospholipids direct an immune cell toward an attractant molecule gradient.

Jean-François Côté[1] and Kristiina Vuori[2]

Neutrophils are highly motile cells of the human immune system that specialize in clearing pathogens from infected tissue. Achievement of this task is no small feat: A neutrophil must relentlessly track its moving target (such as a bacterium) in a full-speed race, abruptly changing direction as needed before closing in on its prey. All this requires that neutrophils sense very small amounts of chemicals, known as chemoattractants, which are released by the escaping pathogens. Receptors on the surface of neutrophils recognize these attractants and initiate cascades of intracellular signaling events that ultimately polarize cell movement in the direction of the pathogen. On page 384, Nishikimi *et al.* (*1*) report that two phospholipids initiate this cellular polarization.

The morphological changes that allow a neutrophil to alter its direction of movement requires polarized remodeling of the actin cytoskeleton. At the center of these changes is Rac, a member of the Rho family of small guanine nucleotide (GTP)–binding proteins (GTPases), whose activation induces rapid actin polymerization. This event supports physical extension of the cell's plasma membrane (as a pseudopod) toward the pathogen (*2*). Previous studies have highlighted an important role for the atypical guanine exchange factor (GEF) DOCK2 in neutrophil polarization and migration (*3*). DOCK2 belongs to a family of Rho GTPase regulators that lack a canonical GEF signaling motif (Dbl-PH). Instead, these DOCK-related proteins use a DOCK homology region–2 (DHR-2) domain to mediate activation of target Rho GTPases (*4*–*6*). In addition, all DOCK proteins harbor a DHR-1 domain that binds to the phospholipid phosphatidylinositol 3,4,5-trisphosphate (PIP_3) (*7*). PIP_3 is generated at membranes by the phosphorylation of phosphatidylinositol 4,5-bisphosphate, a phospholipid component of membranes (*8*). Both the DHR-1 and -2 domains are required for properly localizing the activation of Rho GTPases by DOCK proteins (*9*). Kunisaki *et al.* showed that neutrophils lacking DOCK2 demonstrate impaired Rac activation, and consequently, fail both to polarize and display chemotaxis in response to chemoattractant (*3*).

How do neutrophils initiate polarization? PIP_3 is rapidly produced by phosphoinositide 3-kinases (PI 3-kinases) in response to activated chemoattractant receptors, and accu-

[1]Institut de Recherches Cliniques de Montréal, Université de Montréal, Montréal, Québec H2W 1R7, Canada. [2]Burnham Institute for Medical Research, La Jolla, CA 92037, USA. E-mail: jean-francois.cote@ircm.qc.ca, kvuori@burnham.org

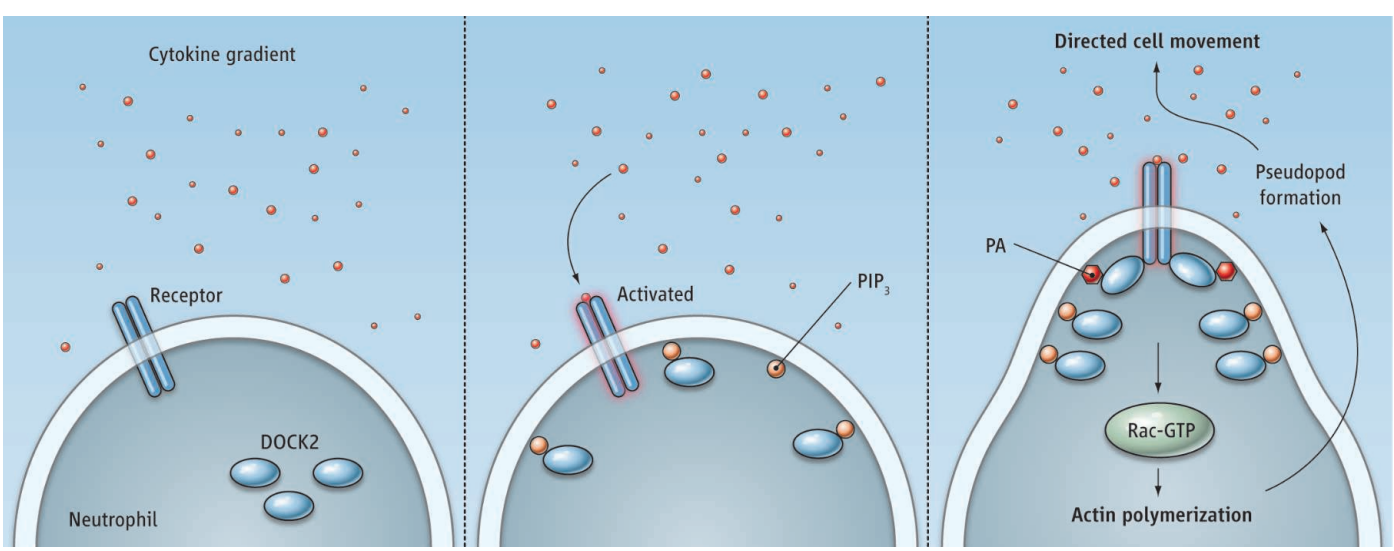

CREDIT: C. BICKEL/*SCIENCE*

Preparing to move. As a nonpolarized neutrophil senses a gradient of chemoattractant (such as a cytokine), signaling events lead to the localization of DOCK2 at the cell's leading edge in two stages, each dependent upon a different phospholipid—PIP_3 and phosphatidic acid (PA). This refinement of DOCK2 localization ensures rapid neutrophil movement toward the chemoattractant gradient.

mulates at the site of the plasma membrane that senses the highest concentration of the extracellular stimulant (*8*). By directly binding to the DHR-1 domain, PIP_3 recruits DOCK2 to this site of the plasma membrane to activate Rac (*3*). Although biochemical experiments with PI 3-kinase inhibitors suggest an important contribution of PIP_3 in cell polarization, in vivo experiments with neutrophils lacking PI3Kγ (the major isoform in neutrophils) have demonstrated that these cells can nevertheless establish a polarized "leading edge" (region of the cell that extends a pseudopod) toward the chemoattractant (*3*). Thus, the signaling events leading to neutrophil polarization in the absence of PI 3-kinase activity have remained elusive.

Nishikimi *et al.* report that global membrane recruitment of DOCK2, through DHR-1–PIP_3 interaction, is not sufficient for neutrophil polarization to occur. Instead, the authors demonstrate that an additional phospholipid, phosphatidic acid, narrows and enriches the localization of DOCK2 more precisely at the membrane site that will become the growing leading edge (see the figure). Phosphatidic acid is generated from the hydrolysis of the membrane component phosphatidylcholine by phospholipase D. By using an inhibitor of phospholipase D, the authors show that a signaling pool of phosphatidic acid is responsible for targeting DOCK2 at the leading edge.

What is the mechanism by which phosphatidic acid refines the localization of DOCK2? Nishikimi *et al.* identified a polybasic region at the carboxyl terminus of DOCK2 that interacts directly with this phospholipid. Mutations in these basic residues abrogated DOCK2–phosphatidic acid binding in vitro and also prevented DOCK2 interaction with the plasma membrane at the leading edge in neutrophils. This suggests that binding to phosphatidic acid is responsible for correctly targeting DOCK2. An elegant swapping experiment of the polybasic region of DOCK2 for a polybasic region of a different signaling protein demonstrated that it is indeed phosphatidic acid binding that localizes DOCK2 to the leading edge. Abrogating DOCK2–phosphatidic acid interaction affected both the polarized accumulation of DOCK2 and the ability of neutrophils to migrate rapidly. Thus, Nishikimi *et al.* uncover a two-step mechanism for initiating polarized neutrophil movement: a more global and less specific step that depends on PIP_3 to recruit DOCK2 to the leading edge of the plasma membrane, and a second step that depends on phosphatidic acid to precisely localize DOCK2 to the exact site in the leading edge that will extend the pseudopod. Nishikimi *et al.* also found that other DOCK proteins interact with phosphatidic acid, and thus may function in response to events that alter amounts of phosphatidic acid. Interestingly, these DOCK proteins are implicated in biological processes that require cellular polarization, including myoblast fusion, phagocytosis of apoptotic cells, and neuronal development.

It is not clear how phosphatidic acid accumulates to sufficient amounts at the site of the plasma membrane that senses the highest amount of the chemoattractant. In the case of PIP_3 production, studies have demonstrated the existence of a positive feedback loop, in which PIP_3 recruits a Rac GEF and the Rac-GTP produced in situ can further enhance PIP_3 production by activating PI 3-kinases. After establishing this feedback loop, the cell generates an intracellular lipid gradient, leading to efficient signaling (*10*). Perhaps a similar feedback loop exists for phosphatidic acid production. Further studies on the regulatory mechanisms governing phospholipase D signaling, such as putative activation by Rac-GTP, are required to fully explain the signaling events that control cell motility in neutrophils and in other systems.

References

1. A. Nishikimi *et al.*, *Science* **324**, 384 (2009); published online 26 March 2009 (10.1126/science.1170179).
2. L. Stephens, L. Milne, P. Hawkins, *Curr. Biol.* **18**, R485 (2008).
3. Y. Kunisaki *et al.*, *J. Cell Biol.* **174**, 647 (2006).
4. E. Brugnera *et al.*, *Nat. Cell Biol.* **4**, 574 (2002).
5. J. F. Cote, K. Vuori, *J. Cell Sci.* **115**, 4901 (2002).
6. N. Meller, M. Irani-Tehrani, W. B. Kiosses, M. A. del Pozo, M. A. Schwartz, *Nat. Cell Biol.* **4**, 639 (2002).
7. J. F. Cote, A. B. Motoyama, J. A. Bush, K. Vuori, *Nat. Cell Biol.* **7**, 797 (2005).
8. P. Rickert, O. D. Weiner, F. Wang, H. R. Bourne, G. Servant, *Trends Cell Biol.* **10**, 466 (2000).
9. N. Meller, S. Merlot, C. Guda, *J. Cell Sci.* **118**, 4937 (2005).
10. F. Wang *et al.*, *Nat. Cell Biol.* **4**, 513 (2002).

10.1126/science.1173646

OCEANS

Limits to Marine Life

Peter G. Brewer and Edward T. Peltzer

Ocean "dead zones" devoid of aerobic life are likely to grow as carbon dioxide concentrations rise.

Ocean chemistry is currently undergoing enormous change from the twinned impacts of higher carbon dioxide (CO_2) concentrations from fossil-fuel burning (*1*), inducing ocean acidification (*2*, *3*), and of rapidly declining mid-water oxygen (O_2) concentrations. The decline in O_2 results from lower sea-surface O_2 concentrations, reduced ventilation of the mid-water from ocean warming (*4*, *5*), and local eutrophication events, all of which lead to an expansion of oceanic dead zones. The reduced ventilation further elevates CO_2 concentrations at depth, because the decline in O_2 is accompanied by the equivalent respiratory CO_2 (*6*); as a result, ocean acidification penetrates more rapidly to lower depths than it would due to the fossil-fuel signal alone. Can the effects of these changes on marine life be quantified on the basis of existing data, and if so, how does one quantify them?

Initial concerns over ocean acidification focused on reduced calcification in coral reefs and other calcareous organisms (*7*, *8*), but other concerns soon arose. Elevated dissolved CO_2 concentrations may impose a physiological strain on marine animals, impairing performance and requiring energy that would otherwise be used for locomotion, predation, reproduction, or coping with other environmental stresses such as rising temperatures. However, there is as yet no formal way to estimate this impact or to relate observed oceanic chemical change to the physiological limits for marine organisms.

Ocean scientists today define the limits to aerobic life in the sea in terms of a minimum dissolved O_2 concentration (*5*), typically ~5 μM, below which it is inefficient for aerobic microbes to consume dissolved O_2; instead, the microbes turn to other electron acceptors such as IO_3, Mn(IV), and NO_3 (*9*). For higher animals, "dead zones" are defined as regions where normal respiration is greatly limited and the expenditure of effort is physiologically constrained, but there is no precise, universally accepted definition that would allow a common limit to be used when mapping changing conditions. In writing this limit in terms of dissolved O_2 [or oxygen partial pressure (pO_2)] alone, ocean scientists

Monterey Bay Aquarium Research Institute, Moss Landing, CA 95039, USA E-mail: brpe@mbari.org

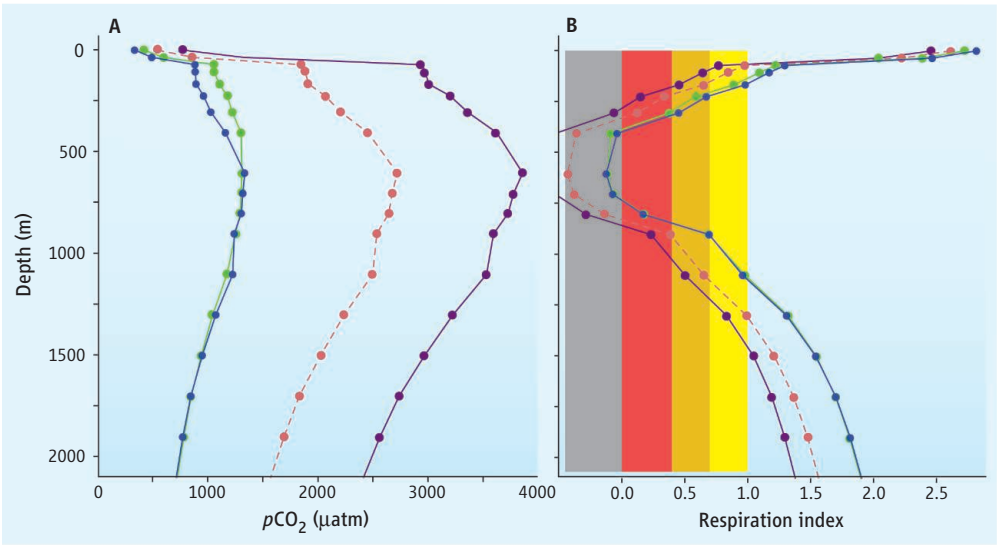

Expanding dead zones. An example of respiration stress at a station in the eastern tropical Pacific (WOCE P16C Sta 413: 13°01.75′N, 91°45.60′W). (**A**) The calculated pCO_2 rises with increasing atmospheric CO_2 concentration. The preindustrial profile was calculated from the modern data by removing the anthropogenic CO_2 at constant alkalinity. The projections (two times preindustrial and three times preindustrial) were calculated by determining the stepwise change in total CO_2 in the sea surface for each case and then propagating this change throughout the ocean. (**B**) Calculation of the respiration index with depth (RI) reveals the existence of a formal dead zone for aerobic life, where RI ≤ 0 (gray band). However, even at RI = 0.0 to 0.4 (red band), aerobic respiration is not observed. Bacteria appear to set the practical limit for all aerobic respiration at RI = 0.4 to 0.7 (orange band). Some marine animals can tolerate RI = 1 or slightly less, but others cannot (yellow band). With increasing atmospheric CO_2 concentrations, dead zones for aerobic life will grow in size. Rising ocean temperatures will further exacerbate the growth of the dead zones by decreasing oxygen saturation.

typically ignore the CO_2 side of the respiration equation, on the unspoken assumption that pCO_2 levels are low and are inversely proportional to the O_2 concentration via bacterial oxidation of marine organic matter. However, this may no longer be the case as atmospheric CO_2 concentrations rise and reset ocean chemical relations.

A simple way to approach this problem is to define the basic oxic respiration equation

$$C_{org} + O_2 \rightarrow CO_2 \quad (1)$$

and from this write out the free-energy relation

$$\Delta G = \Delta G^\circ - RT \bullet \ln\{[fCO_2]/[C_{org}][fO_2]\} \quad (2)$$

Here, ΔG° is the Gibbs free energy at standard conditions, R is the universal gas constant, T is temperature, and f is fugacity. From this equation, we can see that for all food sources there is a common term: the natural logarithm of the ratio of the gas fugacities. By substituting partial pressures for fugacities, $\log_{10}$ for the natural logarithm, and inverting the ratio to eliminate the minus sign, we obtain the expression $\log_{10}(pO_2/pCO_2)$, which provides a simple numerical constraint that is linearly related to available energy. We define this as the respiration index (RI), which may prove useful for estimating the physiological limits of deep-sea animals.

For a specific example, consider a station in the eastern tropical Pacific that is characteristic of the very large suboxic regions of the oceans. Here, the dissolved O_2 concentrations at depths between 300 and 600 m decline almost to zero, and large-scale reduction of nitrate to nitrite occurs. In this region, the calculated RI ranges from just below zero to 2 or more, depending on the ratio of pO_2 to pCO_2 (see the figure). Field data (*10*) suggest that denitrification begins to occur at RI ≈ 0.4 to 0.7, and this ratio likely sets the limit for aerobic respiration of higher animals. Actual limits will be species dependent and remain to be determined (see the figure for some hypothetical limits).

What is of concern is the impact of rising oceanic CO_2 concentrations on this ratio. Present-day pCO_2 at 500 m depth at this site is about 1000 µatm, but an increase of +280 parts per million by volume CO_2 to the atmosphere and surface ocean translates into a far greater change at depth. As surface sea water is transferred to depth, its buffer capacity is reduced by the acidic components of the normal Redfield cycle (*6*). A doubling of surface-water pCO_2 leads to a doubling or more of pCO_2 at depth (see the figure) due to the different geochemistry of the deeper water masses. From ocean equilibration with a doubled CO_2 atmosphere, the pCO_2 at the example station at 500 m depth will rise to 2500 µatm and possibly higher. Such levels have not been considered previously in many of the models designed to predict the status of the future ocean.

This simple example uses the fossil-fuel CO_2 signal alone, thereby greatly understating the case. The calculation assumes constant temperature, but oceanic warming is taking place and will drive the in situ pCO_2 higher. The calculation also assumes unchanging pO_2 levels, but deep-water O_2 concentrations are steadily declining. This affects the RI both through reducing pO_2 and through the associated increase in respiratory CO_2. Thus, we may anticipate a very large expansion of oceanic dead zones.

The expansion of dead zones also has other chemical side effects. The major redox cycles of the chemical elements are microbially driven, and thus an increase in production of N_2O—also a greenhouse gas—at depth seems likely, although any release of this to the atmosphere would be greatly limited by oceanic processes of mixing and consumption. Other redox species may serve as important tracers of the processes at work as these changes occur, with the $IO_3 \rightarrow I^-$ system being the most sensitive indicator.

For the vast areas of the ocean that are well-oxygenated, the rise in oceanic CO_2 concentrations will exert a negligible effect on the normal aerobic functioning of adult marine animals. However, based on our redefinition of dead zones, it is clear that even if oxygen levels do not decline, the oceanic dead zones will still expand as a result of rising CO_2 concentrations; with global warming reducing the oxygen levels as well, the combined effect will be severe.

References

1. C. L. Sabine *et al.*, *Science* **305**, 367 (2004).
2. J. C. Orr *et al.*, *Nature* **437**, 681 (2005).
3. S. C. Doney *et al.*, *Ann. Rev. Mar. Sci.* **1**, 169 (2009).
4. L. Stramma *et al.*, *Science* **320**, 656 (2008).
5. R. J. Diaz, R. Rosenberg, *Science* **321**, 926 (2008).
6. A. C. Redfield *et al.*, *The Sea* (Wiley-Interscience, New York, 1963), vol. 2.
7. J. A. Kleypas *et al.*, *Science* **284**, 118 (1999).
8. J. P. Gattuso *et al.*, *Glob. Planet. Chang.* **18**, 37 (1998).
9. E. L. Rue *et al.*, *Deep-Sea Res.* **44**, 113 (1997).
10. C. L. Sabine *et al.*, Global Ocean Data Analysis Project: Results and Data. ORNL/CDIAC-145, NDP-083. Carbon Dioxide Information Analysis Center, Oak Ridge National Laboratory, U.S. Department of Energy, Oak Ridge, TN. (2005).

10.1126/science.1170756

Strengthening Materials by Engineering Coherent Internal Boundaries at the Nanoscale

K. Lu,[1]* L. Lu,[1,2] S. Suresh[2]*

Strengthening materials traditionally involves the controlled creation of internal defects and boundaries so as to obstruct dislocation motion. Such strategies invariably compromise ductility, the ability of the material to deform, stretch, or change shape permanently without breaking. Here, we outline an approach to optimize strength and ductility by identifying three essential structural characteristics for boundaries: coherency with surrounding matrix, thermal and mechanical stability, and smallest feature size finer than 100 nanometers. We assess current understanding of strengthening and propose a methodology for engineering coherent, nanoscale internal boundaries, specifically those involving nanoscale twin boundaries. Additionally, we discuss perspectives on strengthening and preserving ductility, along with potential applications for improving failure tolerance, electrical conductivity, and resistance to electromigration.

Classical methods for strengthening materials rely on strategies that judiciously control the generation of, and interactions among, internal defects. Such defects include: atomic vacancies and interstitials (point defects); dislocations (line defects); grain, interphase boundaries, and stacking faults that introduce crystallographic disregistry between adjacent regions of the atomic lattice (planar defects); and strengthening precipitates and dispersed reinforcement particles (volume defects) of a different phase or material than the surrounding matrix. Disruptions in a lattice strained by internal defects impede dislocation motion by which plastic deformation occurs, and this result translates into an enhanced macroscopic strength. Fig. 1, A and B, shows examples of several commonly used strengthening methods for crystalline metals and alloys. These approaches invariably suffer from the undesirable consequence that an increase in strength facilitated by dislocation interactions with internal barriers also causes reduced ductility and increased brittleness.

Motivation for Nanoscale, Coherent Internal Boundaries

The internal boundaries introduced by conventional strengthening methods (such as hardening by dispersed particles or grain refinement) are incoherent in that they do not create close crystallographic registry between regions separated by the boundaries, as shown in Fig. 1B for a boundary separating two adjoining grains. With strengthening achieved by introducing particles of a harder phase or material in a softer matrix, the mechanisms by which dislocations engender plasticity are strongly influenced by the size, shape, spatial distribution, and properties of the particles, as well as the geometry and deformation characteristics of particle-matrix interfaces. For grain refinement, the high concentration of incoherent grain boundaries (GBs) provides barriers to transmission of dislocations from one grain to the next (Fig. 1B). Although these high-energy, incoherent boundaries are effective in obstructing dislocation motion, their ability to accommodate plastic deformation is also compromised by reducing ductility (*1*). This makes the material harder to deform further, as informed by the Hall-Petch relationship for microcrystalline alloys (*2*). Strengthening with grain refinement is observed for grain sizes as small as ~10 to 15 nm (*3*–*6*). Activation of lattice dislocations at nano grain sizes becomes more difficult, and thus, plastic deformation becomes more limited. Therefore, nanocrystalline materials exhibit substantially increased strength and hardness (*1*, *3*, *4*). These materials also show higher loading rate sensitivity during plastic deformation (*7*, *8*), better tolerance to fatigue crack initiation under cyclic stressing, and greater resistance to deformation during normal indentation or frictional sliding as compared with microcrystalline materials (*9*–*12*). These beneficial attributes come at the expense of substantially lowered ductility (*1*) and resistance to stable fracture under monotonic and cyclic loading.

In contrast to GBs, coherent internal boundaries with low excess energies are seldom introduced as major strengthening agents for structural materials. Some coherent boundaries (such as low-angle tilt or twist GBs with aligned edge or screw dislocations, respectively) are not effective at resisting penetration by moving dislocations. Hence, their strengthening ability is relatively weak. Coherent internal boundaries created as precursors to the formation of strengthening precipitates in alloys hardened by heat treatments also offer possible means to strength enhancement. For example, the Guinier-Preston zones in precipitation-

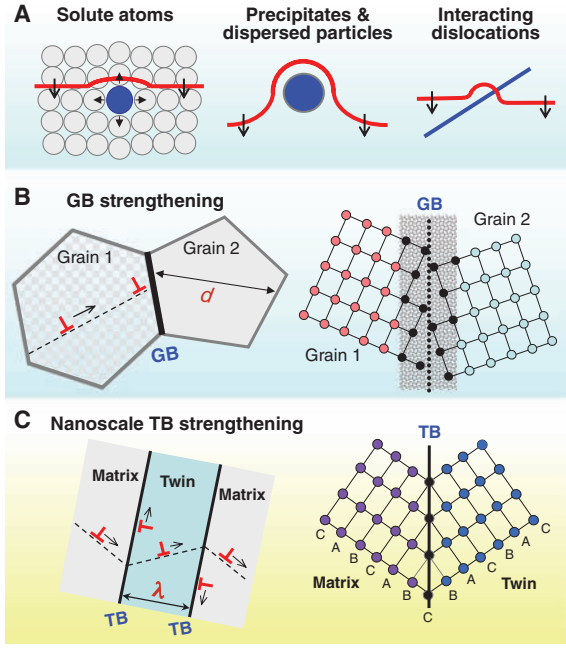

Fig. 1. Schematic illustration of examples of structural modifications for strengthening metals and alloys. Commonly used strengthening methods include (**A**) strengthening via solid solution, whereby solute atoms strain the matrix to impede the motion of a dislocation (red line) through the lattice; via precipitates or dispersed particles that interact with mobile dislocations, leading to overall strengthening of the material; or via elastic interactions between intersecting dislocations (blue and red lines), as well as geometry changes and subsequent obstructions to slip (as, for example, through the formation of sessile dislocation segments) associated with such encounters. GB strengthening (**B**) is another commonly used method in which dislocation (red ⊥ symbol) motion is blocked by GB (whose incoherent structure is schematically shown on the right) so that a dislocation pile-up is formed. A higher stress is needed to deform a polycrystalline metal with a smaller grain size *d* (more GBs). (**C**) Nanoscale TB strengthening is based on dislocation-TB interactions from which mobile and/or sessile dislocations could be generated, either in neighboring domains (twin or matrix) or at TBs. Gliding of dislocations along TBs is feasible because of its coherent structure [the right panel in (C) denotes a Σ3 TB]. Higher strength and higher ductility are achieved with a smaller twin thickness λ in the nanometer scale.

[1]Shenyang National Laboratory for Materials Science, Institute of Metal Research, Chinese Academy of Sciences, Shenyang 110016, China. [2]School of Engineering, Massachusetts Institute of Technology (MIT), 77 Massachusetts Avenue, Cambridge, MA 02139, USA.

*To whom correspondence should be addressed. E-mail: lu@imr.ac.cn (K.L.); ssuresh@mit.edu (S.S.)

hardenable Al-Cu alloys make up interfaces with the surrounding matrix that are easily penetrable by mobile dislocations (*13*). Another example involves the introduction of γ′ or γ precipitates in Ni-base superalloys and intermetallics intended for high-temperature applications (*2*). The thermal and mechanical stabilities of such zones are not sustained as precipitates grow in size and become increasingly incoherent with the surrounding matrix. In addition, the extent of strengthening achievable with such strategies is relatively limited, and even in cases of intermetallics where the extent of strengthening is acceptable, it is achieved at a major loss of ductility.

Internal boundaries can also be created within crystals by the introduction of twins. These planar defects form interfaces, one side of which contains arrangements of atoms that are mirror reflections of those on the other side separated by the twin composition plane, as schematically shown in Fig. 1C. Twin boundaries (TBs) within grains can be introduced either during processing (so called growth twins), plastic deformation (deformation twins), or recrystallization of deformed structures upon annealing (annealing twins). Compared with traditional high-angle GBs, TBs usually exhibit much higher thermal and mechanical stability. Strengthening of TBs is quantitatively identical to that of ordinary GBs (*14*), but strengthening from coherent TBs is relatively less pronounced than that from grain refinement when the TB spacing is of micrometer scale. Furthermore, the generation of a sufficiently high density of stable coherent (or semi-coherent) TBs for achieving even moderate strength enhancements is a technical challenge in the field of materials processing.

These considerations for designing material structures point to the need for strategies through which strengthening can be achieved for optimal mechanical performance in structural applications without compromising ductility and damage tolerance. Recent studies have shown that the controlled introduction of coherent, stable, and nanoscale internal boundaries offers the possibility for substantial strengthening while preserving acceptable levels of ductility, along with appealing electrical and thermal properties (*15*). Specifically, nanoscale twins that provide coherent internal interfaces within ultrafine-grained face-centered cubic (fcc) metals possess substantial strength. Unlike in conventional approaches, this marked increase in strength is not accompanied by a sharp reduction in ductility. Furthermore, when the twin thickness (the spacing between two adjoining twin boundaries) is taken as a characteristic structural dimension, analogous to the grain size, metals with coherent nanotwins exhibit comparable levels of yield strength, tensile strength, hardness, and strain rate sensitivity to deformation while still providing substantial ductility and work hardening when compared with the nanocrystalline metals of the same characteristic structural feature size (*15*–*18*).

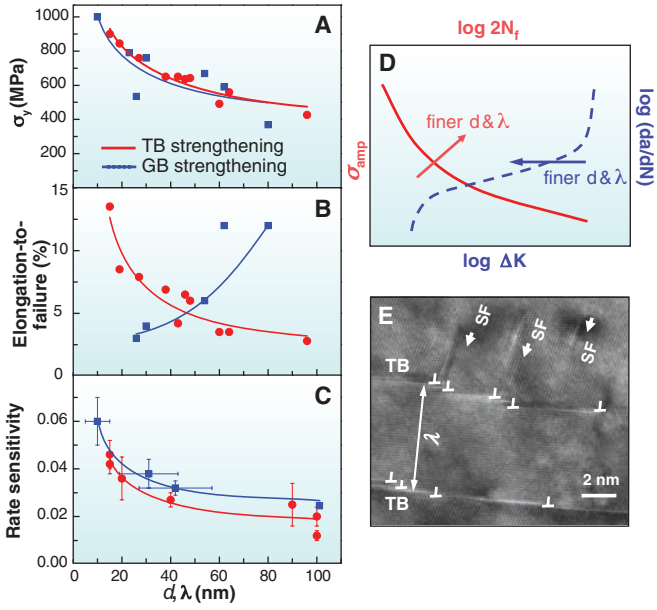

Fig. 2. Experimental results comparing the effectiveness of TBs in influencing mechanical properties with that of GBs for pure Cu. The characteristic structural dimensions used as a basis for comparison are λ and *d*. (**A**) Strength/hardness (σ_y), (**B**) elongation to failure, and (**C**) rate sensitivity of flow stress characterized by the parameter *m*. Error bars indicate ±SD from the mean of three samples. (**D**) Schematic illustration of the known effect of grain size *d* on stress-life fatigue response (left and top axes) characterized by the stress amplitude (σ_{amp}) and the number of stress reversals to failure ($2N_f$). Resistance to subcritical fatigue fracture characterized by the rate of fatigue crack growth (*da*/*dN*) versus the stress intensity factor range (Δ*K*) is plotted on a log-log scale on the bottom and right axes. Here, grain refinement generally leads to higher crack growth rates in the low- and mid-Δ*K* range. Similar behavior is anticipated for refinement of nanotwin thickness λ. (**E**) HRTEM image of the interaction of dislocations with nano TBs in pure Cu that had previously been deformed in tension. Arrows indicate the stacking faults (SF). Image reproduced with permission from (*19*).

Strategies for Strength Enhancements Without Severe Loss of Ductility

Figure 2A shows that for an ultrafine-grained Cu (grain size ~ 500 nm) with intragrain, nanoscale growth twins synthesized by pulsed electrodeposition, yield strength varies with twin thickness (λ) in the same manner as with grain size (*d*) for nanocrystalline Cu with incoherent GBs; both follow the empirical Hall-Petch relationship ($d^{-1/2}$ dependence) (*2*, *3*). Thus, nanoscale TBs impart as much strengthening as conventional high-angle GBs by blocking dislocation motion. Nanotwinned Cu also exhibits an elongation to failure of up to 14% at λ = 15 nm (*17*). A pronounced increment in tensile elongation to failure is observed with decreasing λ, in contrast to reduction in ductility at smaller *d* (Fig. 2B). The two characteristic structural dimensions λ and *d* influence the work-hardening response in very different ways. With a decrease in λ, a monotonic increase in work hardening occurs (*19*), in contrast to the near absence of work hardening in nano-grained fcc metals. This extraordinary work-hardening behavior demonstrates the unique strengthening effect of nanoscale TBs in contrast to that of GBs.

The effects of nanoscale TBs on strain rate sensitivity (*m*) in Cu have shown an increase in *m* with decreasing λ (Fig. 2C) (*16*). Here λ influences the rate sensitivity of deformation similarly to that by grain refinement in Cu and Cu alloys (*3*). Another measure of rate-controlling mechanism for plasticity is the activation volume (*v**); this quantity denotes the rate at which activation enthalpy decreases with yield stress at constant temperature. Experiments reveal a reduction in *v** from ~$1000b^3$ for microcrystalline fcc metals ($d \sim 1$ μm) without twins to ~$10b^3$ when either *d* or λ ~ 15 nm (here, *b* is the Burgers vector of Cu) (*16*).

Figure 2 implies that the presence of nanoscale TBs in ultrafine-grained Cu provides adequate barriers to dislocation motion for strengthening and creates more local sites for nucleating and accommodating dislocations, thereby elevating ductility and work hardening. These properties of nanotwinned materials originate from dislocation-TB interactions that differ fundamentally from the dislocation-GB interactions in nano-grained and coarse-grained metals.

In polycrystalline (nano-grained and coarse-grained) metals, GB strengthening results from impediment of GBs to dislocation motion. When a gliding dislocation encounters a GB, it is blocked, and a stress concentration is created at the dislocation-GB intersection. The localized stress concentration increases with an increasing number of incoming pile-up dislocations at a higher applied stress. When the stress concentration becomes large, new dislocations are nucleated on the other side of the GB in the neighboring grain, thereby eliminating the stress concentration at the GB. However, this process may not change the overall structure and energy state of the GB. Dislocation sliding is inhibited along GBs because of their disordered structures (as in Fig. 1B). Hence, the GBs have limited capacity to accommodate dislocations, resulting in a strength increase but a reduction in ductility.

Mechanistic models (*18*) ascribe increased strength and rate sensitivity in nanotwinned metals to the emission of partial or perfect dislocations into surrounding crystal from an existing boundary dislocation or site of stress concentration or crack in the sliding boundary. Continuum crystal plasticity models (*19*) of deformation in nanotwinned Cu invoke the possibility of softer

resistance to plastic flow and larger sensitivity to deformation rates within a small region (a few lattice parameters wide) of high dislocation density centered at the TB than that seen in elastic crystal lattice. These approaches also account for local plastic anisotropy with substantially easier shear deformation along the TBs than across them. With these assumptions, computational models correctly predict increased strength and rate sensitivity of nanotwinned Cu with finer twin thickness. If local failure is postulated to originate when a certain maximum slip deformation that can be accommodated by a TB is reached, these models reveal a qualitative trend of enhanced ductility with increasing twin density (*19*), consistent with experimental findings.

Atomistic simulations suggest that plastic response of nanotwinned metals is rate limited by slip transfer mechanisms as dislocations interact with TBs (*20*, *21*). As demonstrated systematically in (*20*), interactions between dislocations with a Σ3-TB (a special boundary with a coincident-site lattice separating two lattices with a particular misorientation so that one of every three sites is in coincidence) in different metals may result in glissile dislocations at the TB (i.e., twinning partials), sessile (immobile) dislocations or locks at the TB, and/or outgoing dislocations or stacking faults in the neighboring twin layer, depending on the nature of incoming dislocations. For instance, when an extended screw dislocation intersects a coherent TB in Cu under an applied stress, the dislocation can directly traverse across the TB with the incoming screw being absorbed into the TB and then desorbed through cross-slip (*20*) without any residual Burgers vector. Alternatively, direct transmission of the incoming extended screw dislocation can occur with the leading partial penetrating into the other side of the boundary. A sessile stair-rod dislocation temporarily develops on the TB until the trailing partial of the extended screw catches up.

These interactions could create sessile dislocations, stacking faults as well as steps along the TB, which can facilitate a loss of coherency (*20*). Figure 2E is a high-resolution transmission electron microscope (HRTEM) image of deformed nanotwinned Cu illustrating such a mechanistic process (*19*). The density of accumulated partial dislocations at TBs estimated from electron microscopy observations of deformed nanotwinned Cu is as high as 5×10^{16} m^{-2}, which is two orders of magnitude higher than that of lattice dislocations stored in coarse-grained Cu and much higher than that in the nanocrystalline Cu. Increasing TB density facilitates storage of these dislocations, thereby accommodating considerable strain hardening (*20*). Overall, high strength, rate-sensitivity of deformation, and improved ductility seen in nanotwinned fcc metals is attributed to the interaction between dislocation and a large number of initially coherent TBs, which gradually lose coherency as they harden during encounters with dislocations.

Apparently, coherent TBs may not only serve as sources and/or sinks of dislocations; they could also obstruct the transmission of dislocations from one side of the TB to the other. In addition, TBs may act as slip planes on which glissile dislocations can move and pile up; hence, the stress concentration at the dislocation-TB intersection may be effectively released by dislocation slip along TBs. This behavior allows accommodation of a considerable amount of plastic strain for a high density of TBs with a nanoscale TB spacing. Simultaneously, impediments to the easy flow of dislocations at the TBs and the continual loss of coherency contribute markedly to the enhancement in strength and ductility comparable to that of nanoscale grain refinement.

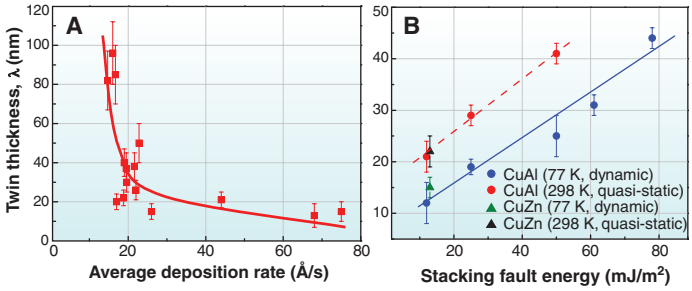

Fig. 3. Tailoring nanotwin thickness λ through control of pulsed electrodeposition processing parameters and material characteristics. Effects of (**A**) average deposition rate in Cu and (**B**) SFE in Cu alloys are shown. These alloys have been subjected to different plastic deformation processes by DPD at ~77 K (at a strain rate of 10^3 s^{-1}) and by quasi-static compression (at a strain rate of 10^{-3} s^{-1}) at room temperature (298 K) (*28*). Error bars indicate the standard measurement error from many TEM images on at least three individual samples.

Generation of Nanoscale Coherent Internal Boundaries

Coherent boundaries, including TBs and phase boundaries, can be generated through physical and chemical processes such as electrodeposition, sputter deposition, plastic deformation, recrystallization, and phase transformation. In electrodeposition of metals with appropriate stacking fault energies (SFEs), growth twins are frequently formed. As the propensity for twinning rises with deposition rate (Fig. 3A), pulsed electrodeposition is suitable for producing a high density of nanotwins (*15*). During the on period of pulsed deposition, a high transient deposition rate is induced by the high current density, resulting in a high density of twin nuclei and reduced twin thickness. During the off period, twin growth is interrupted.

Based on the imposed current density, nanotwins that are generated in ultrafine-grained pure Cu during pulsed electrodeposition—in which {111}/[112] type growth twins with mostly Σ3 coherent boundaries and some Σ9 boundaries—form parallel to the growth direction and extend through the grain. These edge-on twins formed in different crystals are oriented randomly around the foil normal (growth) direction. Twin thickness λ varies from a few nanometers to about 100 nm, depending on the deposition rate achieved by such processing parameters as current density, deposition temperature, and ratio of on time/off time (*17*). The formation of twins decreases total interfacial energy. Twins prefer to nucleate at GBs or triple junctions to reduce GB energies through orientation changes, and high twin density leads to lower average GB excess energy. Twin formation is kinetically driven, and the nucleation and growth rate of twins can be engineered by controlling deposition conditions and the nature of TBs and GB energy. Higher twin densities could be obtained in metals and alloys with low SFEs (e.g., Co and stainless steels) under the proper conditions.

By means of sputter deposition, nanoscale twins can be produced in various materials (*22*–*24*) at high deposition rates. When deposited on a substrate such as Si, GaAs, glass, or sapphire, thin films are grown with columnar grains in which coherent TBs evolve parallel to surface. As in electrodeposition, twin thickness decreases with increasing deposition rates; a minimum twin thickness of a few nanometers serves as the critical nucleus size that decreases substantially with an increase in deposition rate. Lower TB energies favor the formation of nanoscale twins. For materials with relatively higher TB energies such as Cu and Ni, sputtering at high deposition rates is needed to form high twin densities, whereas in alloys such as austenitic stainless steels with very low TB energies, high twin densities form at lower deposition rates of only a few nanometers per second. Large-scale production of nanotwinned copper foils (with diameter in centimeters) has been reported with the use of magnetron sputtering deposition (*25*).

Whereas these deposition processes produce thin foils with nanotwins, plastic deformation provides a practical approach to produce bulk metal and alloy specimens. Dislocation slip and deformation twinning are two competitive plastic deformation modes. Twinning is frequently observed in all body-centered cubic (bcc) metals and many fcc or hexagonal close-packed (hcp) metals when they are deformed at low temperatures and/or high strain rates, conditions that suppress dislocation motion. The size of deformation twins is controlled by their nucleation and growth kinetics, which depend on material characteristics [such as crystallographic structure, SFE, texture and grain size (*26*) and deformation conditions (strain, strain rate, and temperature)]. Twinning is easily achieved in bcc and hcp metals because of limited number of slip systems. In fcc metals with low SFEs [e.g., steels, Cu-Zn, and Cu-Al (*27*)], multiple twins are formed during deformation at conventional strain rates (<10° s^{-1}) and at ambient temperature. For those with higher SFEs such as

Cu and Ni, however, plastic deformation at high strain rates [i.e., dynamic plastic deformation (DPD)] and/or at lower temperatures is needed to induce twinning. Under the same deformation conditions, finer twins are formed in materials with lower SFEs, as shown in Fig. 3B. For the same material, twin density increases with increasing strain rates and/or lower temperatures (*28*).

Boundaries of deformation twins differ structurally from the coherent growth TBs or annealing TBs. High-density partial dislocations exist along deformation TBs, of which the excess energy is higher than that of fully coherent TBs. Upon further plastic straining, nanoscale deformation twins (usually in the form of bundles) may be transformed into nanosized grains via shear banding or fragmentation of twin/matrix lamellae. Then, the twin relationship across deformation TBs is destroyed by interaction with dislocations, forming high-angle GBs. Consequently, a composite structure is formed with nanoscale twin bundles embedded in nanosized grains (*29*).

Potential Applications and Challenges

A limited amount of published information appears to indicate that desirable electrical performance could also be achieved through the tailored creation of coherent nanoscale twins. Traditional strengthening approaches of metals and alloys generally promote a decrease in electrical and thermal conductivity, owing to an increase in scattering barriers. Thus, a tradeoff must be made between conductivity and mechanical strength. However, by introducing nanoscale coherent TBs in pure Cu, electrical conductivity is affected only slightly (comparable to that of coarse-grained high conductivity Cu), even though its mechanical strength increases by an order of magnitude (*15*). The combination of ultrahigh strength and high conductivity could possibly originate from the effective blockage of dislocation motion by numerous coherent nano-TBs with extremely low electrical resistivity, unlike other types of internal boundaries.

With reductions in feature size (well into the nanometer regime) of conducting metal lines in microelectronic circuits, high current densities result. The gradual migration of ions in a conductor from momentum transfer between diffusing metal atoms and conducting electrons leads to material transport. This causes depletion of material, which leads to voids and tensile stresses in the wake of electron transport, accumulation of material and formation of extruded regions (known as hillocks), and high compressive stresses at the opposite end. The ensuing failure process found in integrated circuits, which compromises their reliability, is commonly known as electromigration. Less-coordinated GBs within conducting metal lines are generally regarded as preferential electromigration paths. One recent study shows that by generating nanoscale twins within Cu grains, atomic transport at GBs driven by electrical current is reduced by an order of magnitude, possibly because of the presence of triple junctions of coherent TBs and GBs (*30*). Therefore, electromigration-induced failure of Cu lines in integrated circuits could be substantially suppressed when a high density of nanoscale TBs is introduced in Cu grains. Further experimental work is needed to elucidate the mechanisms underlying these effects.

Producing materials with nanoscale TBs in bulk form, which is essential to exploit their beneficial mechanical properties in structural applications, faces technical challenges. Electrodeposition is widely used to produce bulk metallic materials in industry. In principle, synthesizing bulk materials containing stable, coherent, nanoscale TBs by means of electrodeposition is feasible with proper deposition conditions. Optimization of deposition parameters and real-time closed-loop control of deposition kinetics are crucial for producing high deposition rates of twins during bulk processing. Copious coherent twins can be formed during recrystallization of deformed bulk metals upon annealing, driven by minimization of total excess energies of boundaries separating newly formed grains (*31*). The density of TBs depends on the number of new grain contacts made during recrystallization, as well as on their energy states. With proper plastic deformation followed by subsequent heat treatments, high density of coherent nanoscale TBs could be introduced in bulk metals (*32*).

Plastic deformation of metals at high strain rates and/or at cryogenic temperature provides practical approaches for producing materials in bulk form with nanoscale deformation twins (*29*). Bulk specimens comprising randomly oriented nanosized grains with embedded nanoscale twin bundles exhibit high strength and considerable ductility, owing to the strengthening from nanotwins and nanosized grains. Mechanical properties are determined by the concentration of nanotwin bundles, which varies greatly, depending on processing parameters and the material characteristics. Increased concentrations of nanotwin bundles can be achieved by optimizing initial crystallographic orientations (to favor twinning over slip) and/or suitable alloying to lower the SFE so that twinning is enhanced in each grain. The presence of high density of dislocations at TBs, characteristic of deformation twins, may lead to lower ductility compared with fully coherent TBs. Subsequent thermal and/or mechanical processes have been found to be effective in diminishing TB dislocations so that some plasticity is gained (*33*). Owing to the low energy state of TBs, the nanotwinned structures exhibit very high thermal stability and much better retention of strength upon annealing, as compared with nanocrystalline and ultrafine-grained metals (*34*). Annealing the nanotwin/nano-grain composite structure lead to recrystallization of the nano-grains, whereas the nanotwin bundles are retained. Such a composite structure with relative coarse grains (a few micron in size) embedded with nanotwin bundles would exhibit a good combination of high strength and ductility.

Another challenge is the applicability of these strategies to a broad variety of engineering materials. Whereas nanoscale twins form in many metallic materials, especially those with low SFE, some materials with high SFE (such as Al and Ni) may not easily form twins except under extreme conditions. Despite these challenges, the major gains in mechanical and physical characteristics and damage tolerance arising from the engineering of coherent internal boundaries in the nanoscale offer many potential opportunities in materials research and for engineering applications.

References and Notes

1. K. S. Kumar, H. V. Swygenhoven, S. Suresh, *Acta Mater.* **51**, 5743 (2003).
2. T. H. Courtney, *Mechanical Behavior of Materials* (McGraw-Hill, Boston, ed. 2, 2000).
3. J. Chen, L. Lu, K. Lu, *Scr. Mater.* **54**, 1913 (2006).
4. J. A. Knapp, D. M. Follstaedt, *J. Mater. Res.* **19**, 218 (2004).
5. C. A. Schuh, T. G. Nieh, H. Iwasaki, *Acta Mater.* **51**, 431 (2003).
6. H. Q. Li, F. Ebrihimi, *Acta Mater.* **54**, 2877 (2006).
7. R. Schwaiger, B. Moser, M. Dao, N. Chollacoop, S. Suresh, *Acta Mater.* **51**, 5159 (2003).
8. Q. Wei, S. Cheng, K.T. Ramesh, E. Ma, *Mater. Sci. Eng. A* **381**, 71 (2004).
9. T. Hanlon, Y.-N. Kwon, S. Suresh, *Scr. Mater.* **49**, 675 (2003).
10. A. B. Witney, P. G. Sanders, J. R. Weertman, *Scr. Mater. Mater.* **33**, 2025 (1995).
11. H. Mughrabi, H. W. Hoppel, *Mat. Res. Soc. Symp.* **634**, B2.1.1 (2001).
12. S. C. Bellemare, M. Dao, S. Suresh, *Mech. Mater.* **40**, 206 (2008).
13. J. Silcock, T. Heal, H. Hardy, *J. Inst. Met.* **82**, 239 (1953–1954).
14. W. J. Babyak, F. N. Rhines, *Trans. Met. Soc. AIME* **218**, 21 (1960).
15. L. Lu, Y. Shen, X. Chen, L. Qian, K. Lu, *Science* **304**, 422 (2004); published online 18 March 2004 (10.1126/science.1092905).
16. L. Lu *et al*., *Acta Mater.* **53**, 2169 (2005).
17. Y. F. Shen, L. Lu, Q. H. Lu, Z. H. Jin, K. Lu, *Scr. Mater.* **52**, 989 (2005).
18. R. J. Asaro, S. Suresh, *Acta Mater.* **53**, 3369 (2005).
19. M. Dao, L. Lu, Y. Shen, S. Suresh, *Acta Mater.* **54**, 5421 (2006).
20. T. Zhu, J. Li, A. Samanta, H. G. Kim, S. Suresh, *Proc. Natl. Acad. Sci. U.S.A.* **104**, 3031 (2007).
21. Z. H. Jin *et al*., *Acta Mater.* **56**, 1126 (2008).
22. X. Zhang *et al*., *Acta Mater.* **52**, 995 (2004).
23. X. Zhang *et al*., *Appl. Phys. Lett.* **88**, 173116 (2006).
24. S. K. Streiffer, E. M. Zielinski, B. M. Larison, J. C. Bravman, *Appl. Phys. Lett.* **58**, 2171 (1991).
25. A. M. Hodge, Y. M. Wang, T. W. Barbee, *Mater. Sci. Eng. A* **429**, 272 (2006).
26. X. L. Wu, Y. T. Zhu, *Phys. Rev. Lett.* **101**, 025503 (2008).
27. A. Rohatgi, K. S. Vecchio, G. T. Gray III, *Metall. Mater. Trans. A* **32**, 135 (2001).
28. Y. Zhang, N. R. Tao, K. Lu, *Scr. Mater.* **60**, 211 (2009).
29. Y. S. Li, N. R. Tao, K. Lu, *Acta Mater.* **56**, 230 (2008).
30. K.-C. Chen, W.-W. Wu, C.-N. Liao, L.-J. Chen, K. N. Tu, *Science* **321**, 1066 (2008).
31. J. E. Burke, D. Turnbull, *Prog. Mater. Sci.* **3**, 220 (1952).
32. M. Shimada, H. Kokawa, Z. J. Wang, Y. S. Sato, I. Karibe, *Acta Mater.* **50**, 2331 (2002).
33. Y. Zhang, N. R. Tao, K. Lu, *Acta Mater.* **56**, 2429 (2008).
34. X. H. Zhang, O. Anderoglu, R. G. Hoagland, A. Misra, *J. Met.* **60**, 75 (2008).

35. K.L. and L.L. are grateful for financial support of the National Natural Science Foundation (grants 50621091, 50431010, 50725103, and 50890171) and the Ministry of Science and Technology of China (grant 2005CB623604). L.L. and S.S. acknowledge support from the Office of Naval Research grant N00014-08-1-0510 and the Advanced Materials for Micro and Nano Systems Programme of the Singapore-MIT Alliance.

10.1126/science.1159610

Origin and Radiation of the Earliest Vascular Land Plants

Philippe Steemans,[1]* Alain Le Hérissé,[2] John Melvin,[3] Merrell A. Miller,[3] Florentin Paris,[4] Jacques Verniers,[5] Charles H. Wellman[6]*†

The earliest land plants (embryophytes) evolved from charophycean green algal ancestors and probably possessed bryophyte-like anatomy and physiology (*1*–*3*). Plant megafossils are rare, presumably because they lacked fossilizable tissues, although there is a large microfossil record of dispersed spores, termed cryptospores because they occur in unusual configurations such as dyads and tetrads (*3*–*6*). The oldest uncontroversial cryptospore record is Mid-Ordovician (Darriwilian) in age (Fig. 1A). Similar cryptospore assemblages have been reported throughout the globe, suggesting that the earliest terrestrial vegetation consisted of ecological generalists and was cosmopolitan. The cryptospore record shows little spatial or temporal variation over about 30 million years. Vascular plants are considered to have originated and adaptively radiated from the Early Silurian on the basis of major changes in spore assemblages (from cryptospore to hilate/trilete spore dominated) and the appearance of vascular plant megafossils.

We examined palynological preparations from 37 core samples from Ordovician-Silurian strata penetrated in the Qusaiba-1 corehole, northern Saudi Arabia (*7*). They yielded abundant, well-preserved, and thermally immature marine palynomorphs (chitinozoans and acritarchs) that were used to determine the age of the cores (*7*). Subsidiary land plant spores were present in all samples. The upper part of the Qasim Formation is a shallowing upward succession of offshore shelf sandy silt and mudstones topped by a sandstone. The oldest samples from this unit are no younger than Mid-Katian in age, and succeeding samples from the uppermost Qasim Formation are Late Katian in age (Fig. 1A) on the basis of chitinozoan and acritarch biostratigraphy. The Qasim Formation was unconformably overlain by glacial-marine sediments of the Sarah Formation. These sediments are characterized by Hirnantian acritarch species with reworked earlier Ordovician forms. The Qalibah Formation (Qusaiba Member) overlies the Sarah Formation and consists of marine shelf deposits of Early Silurian age.

The ancestral condition among embryophytes may have been meiotically produced spores dispersed in tetrad or dyad configurations (cryptospores). Dissociation of these units into individual hilate spores (from dyads) or trilete spores (from tetrads) is a more derived condition. Cryptospores were the most abundant plant spores recovered from the Late Ordovician sediments of the Qusaiba-1 corehole and are similar to forms in other coeval assemblages found worldwide. Surprisingly, all samples also contained plant spores naturally dissociated from polyads: one species of hilate spore and seven species of trilete spores (Fig. 1, B to I). Two trilete spore species were unornamented, whereas the other five had an ornament of verrucae and/or muri, indicating high species diversity. Neither hilate spores nor trilete spores have been reported from strata of this age (*3*–*6*). The oldest unornamented hilate spores are from the Llandovery, although rare specimens have been recorded in Hirnantian deposits from Turkey (northern Gondwana). Ornamented hilate spores and trilete spores have not been reported from strata older than Wenlock.

Trilete spores are generally considered to derive from the vascular plant lineage (*7*) because extant and fossil basal vascular plant groups (nonseed plants) nearly all produce dissociated single spores of trilete or the more derived monolete form. A small proportion of extant bryophytes produce trilete spores, but in these cases the trilete condition is likely nonfunctional or convergent (*3*, *7*). Also, the earliest reported vascular plant megafossils are more-or-less coincident with the appearance and diversification of hilate/trilete spores. Thus, hilate/trilete spores from the Late Ordovician may represent an earlier emergence and diversification of the vascular plant lineage in Gondwana. Hilate/trilete spores found elsewhere suggests that vascular plants may have subsequently migrated out of Gondwana and colonized other continents where they secondarily diversified.

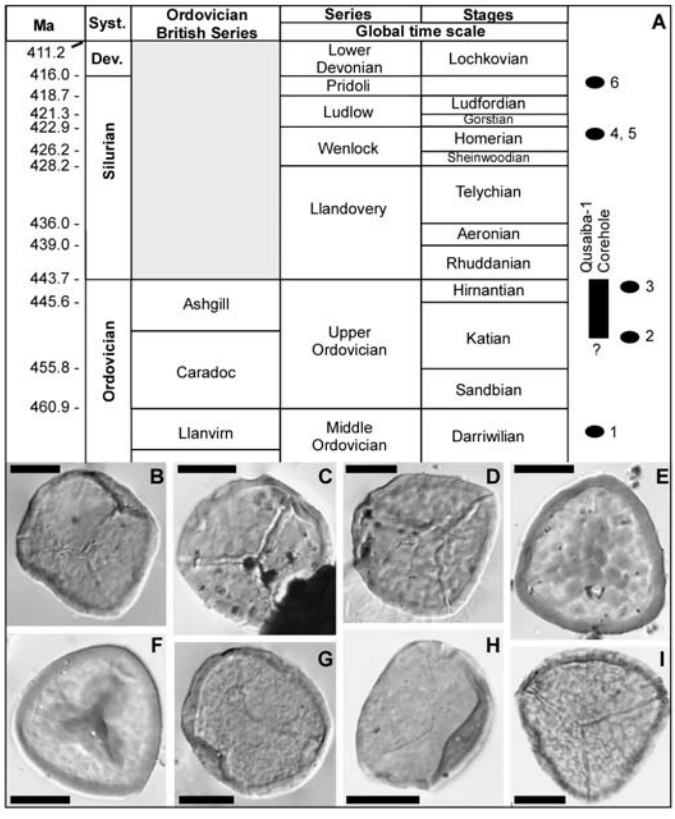

Fig. 1. (**A**) Ordovician to Lower Devonian time scale. Black bar represents the studied interval. Stratigraphic position of 1, the oldest cryptospores; 2, the oldest mesofossils of sporangia containing cryptospores; 3, the previous oldest laevigate trilete spores from Turkey; 4, the previous oldest ornamented trilete spores; 5, the oldest megafossils of the vascular plant lineage; and 6, the oldest vascular plant megafossils with preserved conducting tissues. (**B** to **I**) Fossil trilete spores from the Qusaiba-1 corehole. Descriptions of spores provided in (*7*). Scale bars indicate 10 μm.

References and Notes

1. D. Edwards, C. H. Wellman, in *Plants Invade the Land*, P. G. Gensel, D. Edwards, Eds. (Columbia Univ. Press, New York, 2001), chap. 2.
2. C. H. Wellman, P. L. Osterloff, U. Mohiuddin, *Nature* **425**, 282 (2003).
3. J. Gray, *Philos. Trans. R. Soc. London Ser. B* **309**, 167 (1985).
4. J. B. Richardson, in *Palynology: Principles and Applications*, J. Jansonius, D. C. McGregor, Eds. (AASP–The Palynological Society, Dallas, TX, 1996), vol. 2, chap. 18A.
5. P. Steemans, *Rev. Palaeobot. Palynol.* **113**, 189 (2000).
6. P. K. Strother, in *Phanerozoic Terrestrial Ecosystems*, R. A. Gastaldo, W. A. DiMichele, Eds. (Palaeontological Society Papers No. 6, Pittsburgh, PA, 2000), pp. 3–20.
7. Materials and methods, age dating, spore descriptions, and discussion of trilete spore affinities are available as supporting material on *Science* Online.

8. P.S. is a National Fund for Scientific Research Research Associate. Saudi Aramco provided material for study and publication. Work was undertaken as part of the Commission Internationale de Microflora du Paléozoïque/Saudi Aramco joint project "Understanding the Palaeozoic palynology of Saudi Arabia."

Supporting Online Material

www.sciencemag.org/cgi/content/full/324/5925/353/DC1
Materials and Methods
SOM Text
References

11 December 2008; accepted 17 February 2009
10.1126/science.1169659

[1]Palaeobotany, B-18, University of Liège, 4000 Liège, Belgium. [2]Université de Brest, UMR 6538 du CNRS, Institut Universitaire Européen de la Mer, 6 Avenue le Gorgeu, 29238 Brest-cedex 3, France. [3]Saudi Aramco, Dhahran, 31311, Saudi Arabia. [4]Université de Rennes 1, UMR 6118 du CNRS, 35042 Rennes-cedex, France. [5]Research Unit Palaeontology, Ghent University, Krijgslaan 281/S8, B-9000 Ghent, Belgium. [6]Department of Animal and Plant Sciences, University of Sheffield, Sheffield S10 2TN, UK.

*These authors contributed equally to this work.
†To whom correspondence should be addressed. E-mail: c.wellman@sheffield.ac.uk

Optical Deconstruction of Parkinsonian Neural Circuitry

Viviana Gradinaru,[1,2]* Murtaza Mogri,[1]* Kimberly R. Thompson,[1] Jaimie M. Henderson,[3] Karl Deisseroth[1,4]†

Deep brain stimulation (DBS) is a therapeutic option for intractable neurological and psychiatric disorders, including Parkinson's disease and major depression. Because of the heterogeneity of brain tissues where electrodes are placed, it has been challenging to elucidate the relevant target cell types or underlying mechanisms of DBS. We used optogenetics and solid-state optics to systematically drive or inhibit an array of distinct circuit elements in freely moving parkinsonian rodents and found that therapeutic effects within the subthalamic nucleus can be accounted for by direct selective stimulation of afferent axons projecting to this region. In addition to providing insight into DBS mechanisms, these results demonstrate an optical approach for dissection of disease circuitry and define the technological toolbox needed for systematic deconstruction of disease circuits by selectively controlling individual components.

Parkinson's disease (PD) is a debilitating neurodegenerative disorder resulting from the loss of dopaminergic (DA) neurons in the substantia nigra pars compacta (SNc), leading to abnormal neuronal activity in the basal ganglia (BG). DA depletion in the BG leads to altered activity of the subthalamic nucleus (STN) and globus pallidus pars interna (GPi), which has been linked to clinical deficits in movement initiation and execution (*1*–*3*). On the basis of these observations from animal models and the fact that lesions of the BG can be therapeutic in PD, high-frequency (>90 Hz) stimulation (HFS) of the STN (deep brain stimulation or DBS) has emerged as a highly effective treatment for medically refractory PD (*4*–*6*).

Exactly how DBS exerts its therapeutic effects is a matter of controversy (*7*–*10*) for three major reasons. First, because of the heterogeneity of brain tissue (*11*), it is unclear which circuit elements are responsible for the therapeutic effects. Second, HFS is intrinsically a complicated manipulation because target neurons can respond with increased, decreased, or mixed temporal patterns of activity; as a result, the magnitude and even the sign of target cell responses to DBS are unknown. Finally, it is difficult to assess the net outcome of DBS on overall activity in the target cells and region, because electrical stimulation creates artifacts that prevent direct observation of local circuit responses during HFS itself. Together, these challenges point to the need to understand, to improve, and to generalize (*12*–*15*) this important treatment modality.

[1]Department of Bioengineering, Stanford University, Stanford, CA 94305, USA. [2]Program in Neuroscience, Stanford University, Stanford, CA 94305, USA. [3]Department of Neurosurgery, Stanford University, Stanford, CA 94305, USA. [4]Department of Psychiatry and Behavioral Sciences, Stanford University, Stanford, CA 94305, USA.

*These authors contributed equally to this work.
†To whom correspondence should be addressed. E-mail: deissero@stanford.edu

We have developed and employed optogenetics technology based on single-component microbial light-activated regulators of transmembrane conductance and fiber optic– and laser diode–based in vivo light delivery (*16*–*24*). The channelrhodopsins, including VChR1 (*24*) and ChR2 (*19*), encode light-activated cation channels that can be expressed in neurons under cell type–specific promoters. In contrast, the halorhodopsins (e.g., NpHR) are light-activated Cl^- pumps, and NpHR-expressing neurons are hyperpolarized and inhibited from firing action potentials when exposed to 590-nm light in intact neural tissue (*20*, *21*). The ChR2–NpHR system is ideally suited to dissect PD circuitry because of three features that map well onto the challenges outlined above. First, optogenetics allows genetically targeted photosensitization of individual circuit components within the STN area and, therefore, testing of hypotheses regarding the causal role of individual cell types. Second, inhibition or excitation of target cells by direct hyperpolarization or depolarization can be achieved, which reduces complications such as soma-axon decoupling (*25*, *26*), in which cell bodies can be inhibited and axons stimulated by HFS. Third, optogenetics allows simultaneous optical control and electrophysiological recording of local neuronal activity in vivo with integrated fiber-electrode "optrodes" (*27*) and avoids electrical stimulus artifacts, which may mask crucial neural responses.

In all of this, optogenetics maintains the millisecond temporal precision of electrodes. Therefore, optogenetics, in principle, could be used to systematically probe specific circuit elements with defined frequencies of true excitation or inhibition in freely behaving parkinsonian rodents.

Optical inhibition of STN. To first address the most widely held hypothesis in the field, we asked if direct, reversible, bona fide inhibition of local-circuit excitatory STN neurons would be therapeutic in PD. The STN measures <1 mm^3 in rats (*28*), but targeting accuracy can be aided by extracellular recordings during opsin vector introduction, because STN is characterized by a particular firing pattern that is distinguishable from bordering regions (Fig. 1A and fig. S1C) (*29*).

The STN is a predominantly excitatory structure (*30*) embedded within an inhibitory network. This anatomical arrangement enables a targeting strategy for selective STN inhibition (Fig. 1B), in which enhanced NpHR (eNpHR) (*21*) is expressed under control of the calcium/calmodulin-dependent protein kinase IIα (CaMKIIα) promoter, which is selective for excitatory glutamatergic neurons and not inhibitory cells, fibers of passage, glia, or neighboring structures (*18*). In this way, true optical inhibition is targeted to the dominant local neuron type within STN.

Optical circuit interventions were tested in rats that had been made hemiparkinsonian by injection of 6-hydroxydopamine (6-OHDA) unilaterally into the right medial forebrain bundle (MFB). Loss of nigral dopaminergic cells after 6-OHDA administration was confirmed by decreased tyrosine hydroxylase levels unilaterally in the SNc (fig. S1A). These hemiparkinsonian rodents have specific deficits in contralateral (left) limb use and display (rightward) rotations ipsilateral to the lesion, which increase in frequency when the subjects are given amphetamine to facilitate functional evaluation and decrease in frequency on treatment with dopamine agonists (*31*) or after electrical DBS (Fig. 1D, right). This amphetamine-induced rotation test is widely used for identifying treatments in hemiparkinsonian rodents and can be complemented with other behavioral assays such as locomotion, climbing, and head position bias. To inhibit the excitatory STN neurons directly, we delivered lentiviruses carrying eNpHR under the CaMKIIα promoter to the right STN of the hemiparkinsonian rats. CaMKIIα::eNpHR labeled with enhanced yellow fluorescent protein (EYFP) expression was specific to excitatory neurons (as shown by CaMKIIα and glutamate expression; Fig. 1B, right; and fig. S2A), robust (95.73% ± 1.96% SEM infection rate assessed in $n = 220$ CaMKIIα-positive cells), and restricted to the STN (Fig. 1B, left and middle). To validate the resulting physiological effects of optical control, a hybrid optical stimulation–electrical recording device (optrode) was used in isoflurane-anesthetized animals to confirm that eNpHR was functional in vivo, potently inhibiting (>80%) spiking of recorded neurons in the STN (Fig. 1C; fig. S4, A and B; and fig S5A). This cell type–targeted inhibition was temporally precise and reversible, and it extended across all frequency bands of neuronal firing (Fig. 1C and fig. S7A).

For behavioral rotation assays in the hemiparkinsonian rats, the STN-targeted fiber optic was coupled to a 561-nm laser diode to drive eNpHR. Electrical DBS was highly effective in reducing pathological rotational behavior, but despite precise targeting and robust physiological efficacy of eNpHR inhibition, the hemiparkinsonian animals did not show even minimal changes in rotational

behavior with direct true optical inhibition of the local excitatory STN neurons (Fig. 1D). In addition, there was no effect on path length and head position bias in response to light during these experiments (*29*). Although muscimol and lidocaine administration to the region of the STN in monkeys and rodents can relieve parkinsonian symptoms (*32*), the data in Fig. 1 show that the more restricted intervention of selectively decreasing activity in excitatory local neurons of the STN appeared not to be sufficient by itself to affect motor symptoms.

Another possibility is that DBS could be driving secretion of glial modulators that would have the capability to modulate local STN circuitry; this would be consistent with recent findings (*33*) indicating that a glial-derived factor (adenosine) accumulates during DBS and plays a role in DBS-mediated attenuation of thalamic tremor. Indeed, the STN expresses receptors for glia-derived modulators (*34*), which can inhibit postsynaptic currents in the STN (*35*). ChR2 presents an interesting possibility for recruitment of glia; when opened by light, in addition to Na^+

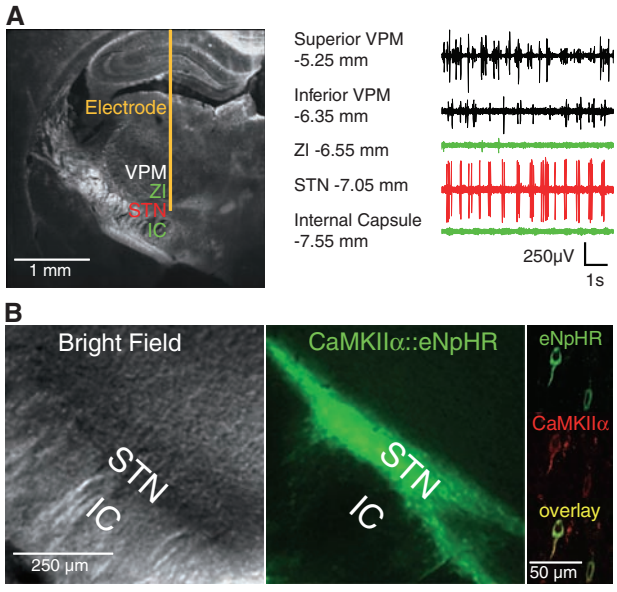

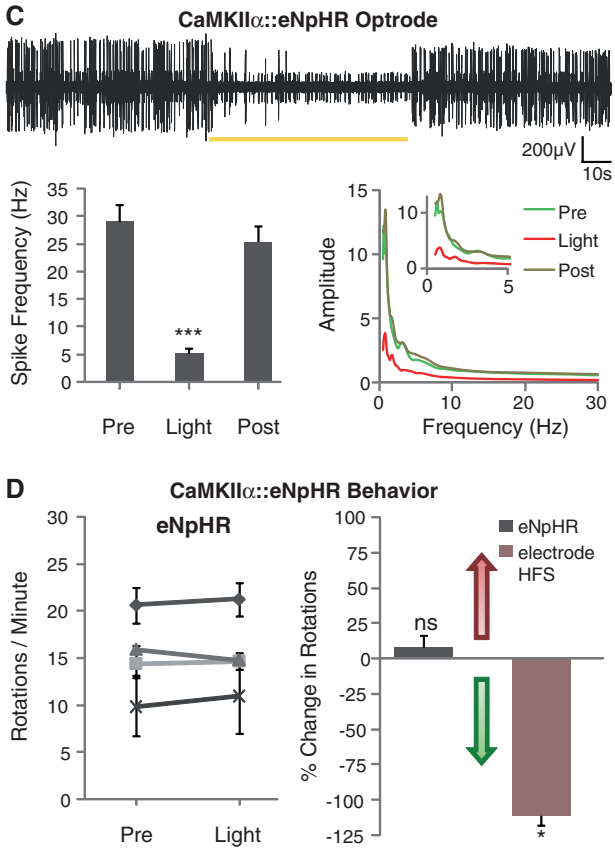

Fig. 1. Direct optical inhibition of local STN neurons. (**A**) Cannula placement, virus injection, and fiber depth were guided by recordings of the STN, which is surrounded by the silent zona incerta (ZI) and internal capsule (IC). (**B**) Confocal images of STN neurons expressing CaMKIIα::eNpHR-EYFP and labeled for excitatory neuron-specific CaMKIIα (right). (**C**) Continuous 561-nm illumination of the STN expressing CaMKIIα::eNpHR-EYFP in anesthetized 6-OHDA rats reduced STN activity; representative optrode trace and amplitude spectrum are shown. Mean spiking frequency was reduced from 29 ± 3 to 5 ± 1 Hz (means ± SEM, $P < 0.001$, Student's *t* test, n = eight traces from different STN coordinates in two animals). (**D**) Amphetamine-induced rotations were not affected by stimulation of the STN in these animals ($P > 0.05$, $n = 4$ rats, *t* test with $\mu = 0$). The red arrow indicates direction of pathologic effects; the green arrow indicates direction of therapeutic effects. The electrical control implanted with a stimulation electrode showed therapeutic effects with HFS (120 to 130 Hz, 60-μs pulse width, 130 to 200 μA, $P < 0.05$, *t* test with $\mu = 0$). Percentage change of −100% indicates that the rodent is fully corrected. Data in all figures are means ± SEM ns, $P > 0.05$; *$P < 0.05$; **$P < 0.01$; and ***$P < 0.001$.

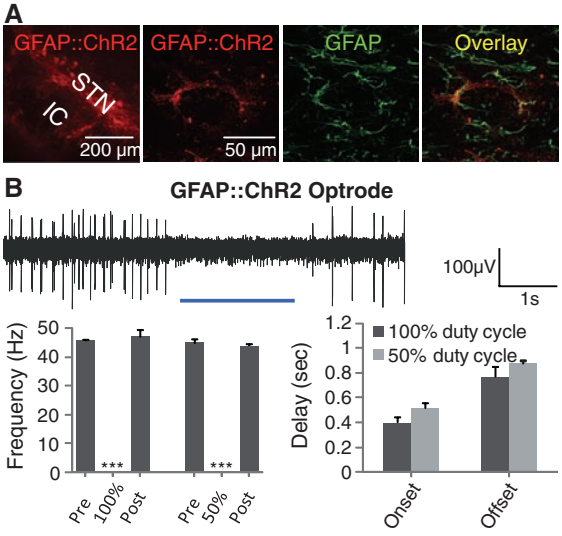

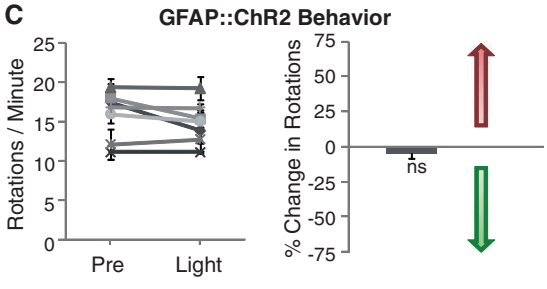

Fig. 2. Targeting astroglia within the STN. (**A**) Confocal images show STN astrocytes expressing GFAP::ChR2-mCherry, costained with GFAP (right). (**B**) A 473-nm illumination of the STN expressing GFAP::ChR2-mCherry in anesthetized 6-OHDA rats. Optrode recording revealed that continuous illumination inhibited STN activity with delay to onset of 404 ± 39 ms and delay to offset of 770 ± 82 ms (n = five traces from different STN coordinates in two animals), nevertheless, the 50% duty cycle also inhibited spiking, with delay to onset of 520 ± 40 ms and delay to offset of 880 ± 29 ms (n = three traces from different STN coordinates in two animals) with $P < 0.001$. (**C**) Amphetamine-induced rotations were not affected by 50% duty cycle illumination in these animals (right, $P > 0.05$, n = seven rats, *t* test with $\mu = 0$).

and K^+ ions, ChR2 can also pass trace Ca^{2+} currents (*36*, *37*) that trigger Ca^{2+} waves in and activate ChR2-expressing astroglia (*38*). We used a glial fibrillary acidic protein (GFAP) promoter to target ChR2 to local astroglia, validated with GFAP and S100β staining (Fig. 2A and fig. S2B, respectively). Optrode recordings revealed that blue light stimulation of STN following transduction with GFAP::ChR2 reversibly inhibited neuronal firing in the STN (Fig. 2B and fig. S3A), with variable delay on a time scale of seconds. However, recruiting astroglial cells by this mechanism was not sufficient to cause even trace responses in motor pathology in parkinsonian rodents (Fig. 2C and fig. S3B). Path length and head position bias were also not affected by light during these experiments (*29*). Although these data do not exclude the importance of local STN inhibition as a contributing factor in DBS response, as not all STN neurons may be affected in the same way by indirect glial modulation and, as in Fig. 1, breakthrough activity could occur, the direct activation of local glial cells appeared not to be sufficient to treat parkinsonian symptoms, pointing to consideration of other circuit mechanisms.

Optogenetic excitation of targeted STN cells. Network oscillations at particular frequencies could play important roles in both PD pathology and treatment. For example, PD is characterized by pathological levels of beta oscillations in the basal ganglia, and synchronizing STN at gamma frequencies may ameliorate PD symptoms, whereas beta frequencies may worsen symptoms (*39*, *40*). Because simple inhibition of excitatory cell bodies in the STN did not affect behavioral pathology and because HFS (90 to 130 Hz) is used for electrical DBS, we used ChR2 to drive high-frequency oscillations in this range within

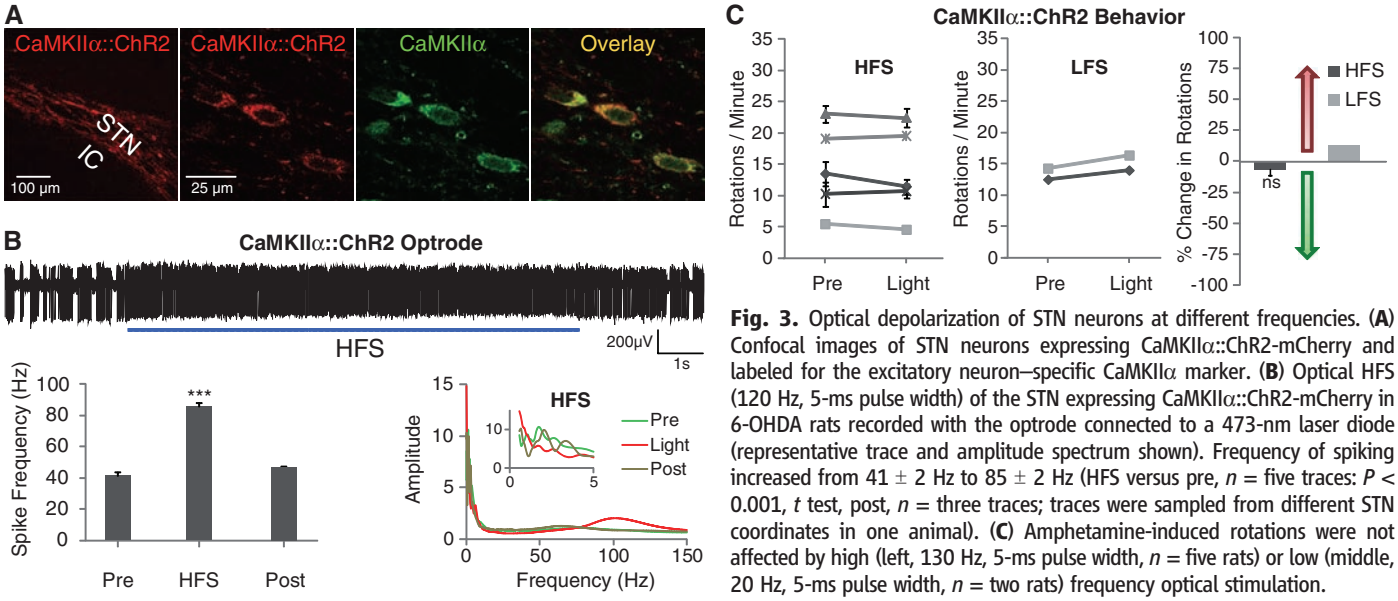

Fig. 3. Optical depolarization of STN neurons at different frequencies. (**A**) Confocal images of STN neurons expressing CaMKIIα::ChR2-mCherry and labeled for the excitatory neuron–specific CaMKIIα marker. (**B**) Optical HFS (120 Hz, 5-ms pulse width) of the STN expressing CaMKIIα::ChR2-mCherry in 6-OHDA rats recorded with the optrode connected to a 473-nm laser diode (representative trace and amplitude spectrum shown). Frequency of spiking increased from 41 ± 2 Hz to 85 ± 2 Hz (HFS versus pre, n = five traces: $P < 0.001$, t test, post, n = three traces; traces were sampled from different STN coordinates in one animal). (**C**) Amphetamine-induced rotations were not affected by high (left, 130 Hz, 5-ms pulse width, n = five rats) or low (middle, 20 Hz, 5-ms pulse width, n = two rats) frequency optical stimulation.

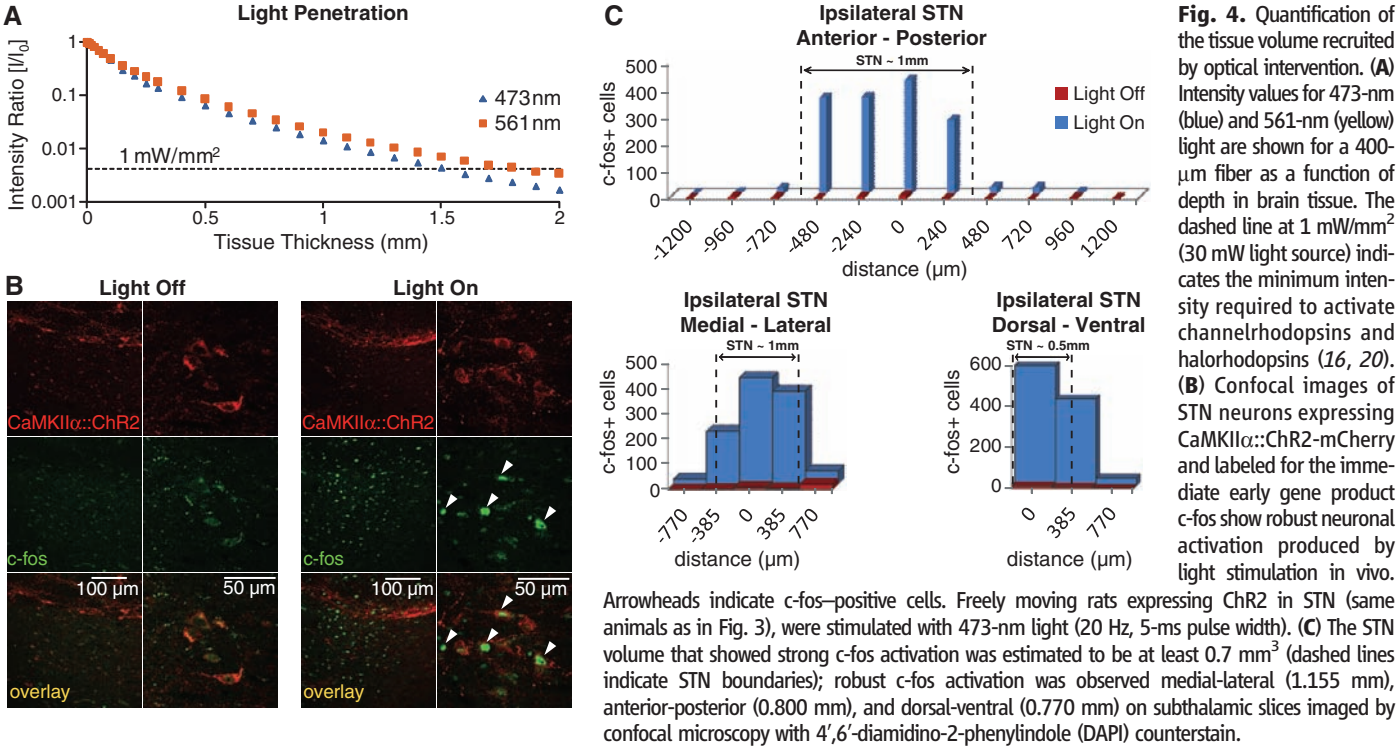

Fig. 4. Quantification of the tissue volume recruited by optical intervention. (**A**) Intensity values for 473-nm (blue) and 561-nm (yellow) light are shown for a 400-μm fiber as a function of depth in brain tissue. The dashed line at 1 mW/mm^2 (30 mW light source) indicates the minimum intensity required to activate channelrhodopsins and halorhodopsins (*16*, *20*). (**B**) Confocal images of STN neurons expressing CaMKIIα::ChR2-mCherry and labeled for the immediate early gene product c-fos show robust neuronal activation produced by light stimulation in vivo. Arrowheads indicate c-fos–positive cells. Freely moving rats expressing ChR2 in STN (same animals as in Fig. 3), were stimulated with 473-nm light (20 Hz, 5-ms pulse width). (**C**) The STN volume that showed strong c-fos activation was estimated to be at least 0.7 mm^3 (dashed lines indicate STN boundaries); robust c-fos activation was observed medial-lateral (1.155 mm), anterior-posterior (0.800 mm), and dorsal-ventral (0.770 mm) on subthalamic slices imaged by confocal microscopy with 4′,6′-diamidino-2-phenylindole (DAPI) counterstain.

the STN. We injected CaMKIIα::ChR2 into the STN (Fig. 3A) and used pulsed illumination with a 473-nm laser diode to activate excitatory neurons in the STN (Fig. 3B and fig. S5B), during behavioral testing in parkinsonian rodents (Fig. 3C and fig. S3C). Despite robust effects on the high-frequency power of neuronal spike rate in STN of anesthetized animals (fig. S7B), HFS delivered locally to the STN area failed to affect PD behavioral symptoms (path length and head position bias were unchanged by light) (*29*). Animals tested in parallel with beta frequency pulses also showed no behavioral response, indicating that (although not excluding a contributory role) directly generated oscillations within the STN excitatory neurons are not sufficient to account for therapeutic effects.

Measuring the volume of tissue recruited in STN. We have previously measured in cortical and hypothalamic tissue the propagation of blue light in the setting of laser diode–fiber optic illumination; we observed that substantial tissue volumes (comparable to that of the STN) could reliably be recruited at a light-power density sufficient to drive physiologically significant microbial opsin currents (*17*, *18*). It was important to repeat and extend these measurements to the PD setting. First, we confirmed that the propagation measurements of blue light (473 nm) in brain tissue represent a lower bound on the volume of tissue recruited, owing to reduced scattering of lower-energy photons delivered from the 561-nm laser diode; therefore, sufficient light power is present to activate opsins within 1.5 mm of the fiber for either wavelength of light (Fig. 4A). We next extended these findings with a functional assay for tissue recruitment under conditions mimicking our behavioral experiments (Fig. 4, B and C). After an in vivo optical stimulation paradigm targeted to the CaMKIIα**::**ChR2–expressing STN in freely moving rats, we performed immunohistochemistry for c-fos, a biochemical marker of neuronal activation. We observed robust c-fos activation in STN (Fig. 4B) over a widespread volume (Fig. 4C); indeed, as expected from our light-scattering measurements and tissue geometry, we found that at least 0.7 mm^3 of STN is recruited by light stimulation, which closely matched the actual volume of the STN (Fig. 4C). Therefore, light penetration was not limiting because the entire STN is recruited by the optical modulation paradigms of Figs. 1 to 3.

Optical control of afferent axons in STN. Therapeutic effects could arise from driving axonal projections that enter the STN, as DBS electrodes will potently modulate not just local cells and their efferents, but also afferent fibers. Optogenetics discriminates between these two possibilities, as the lentiviruses transduce somata without transducing afferent axons (*27*). To assess the possibility that PD motor behavioral responses are modulated by targeting afferent projections to the STN, we used Thy1::ChR2 transgenic mice (*22*, *23*) in which ChR2 is expressed in projection neurons, and we verified that in Thy1::ChR2 line 18, ChR2-YFP is excluded from cell bodies in the STN but is abundant in afferent fibers (Fig. 5A).

We conducted optrode recordings in anesthetized 6-OHDA mice (fig. S1B) (*41*, *42*) to assess local effects on STN physiology of driving afferent axons selectively and found frequency-dependent effects (Fig. 5B). First, we observed that HFS of afferent fibers to the STN potently reduced STN spiking across all frequency bands; this effect did not completely shut down local circuitry, as low-amplitude high-frequency oscillations persisted during stimulation (Fig. 5B; fig. S4, C and D; and fig. S5C). Next, we found that LFS of afferent fibers increased beta-frequency firing in the STN without affecting endogenous bursting (Fig. 5B, fig. S5D, and fig. S7E). We next assessed the impact of these specific interventions on PD behavior in 6-OHDA mice, and for the first time among the optogenetic interventions, we observed marked effects. Driving STN afferent fibers with HFS robustly and reversibly ameliorated PD symptoms, measured by rotational behavior and head position bias (Fig. 5C). The HFS effects were not subtle; indeed, in nearly

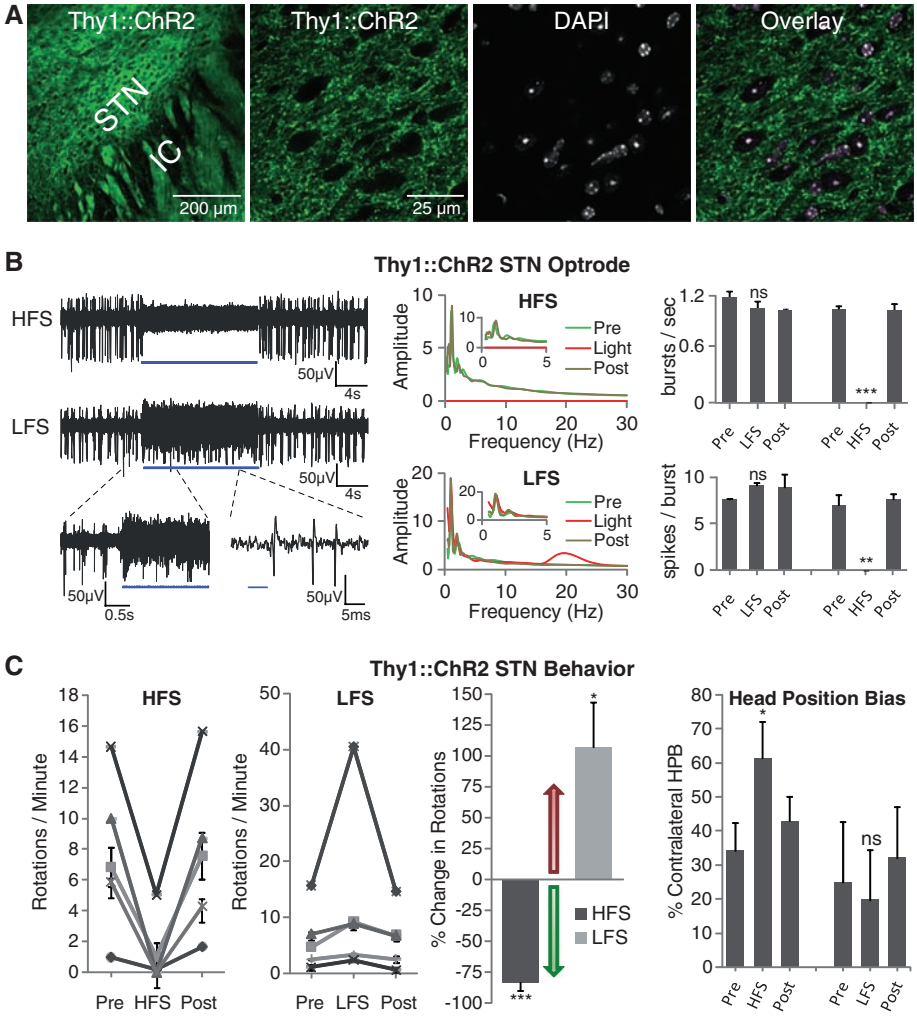

Fig. 5. Selective optical control of afferent fibers in the STN. (**A**) Confocal images of Thy1::ChR2-EYFP expression in the STN and DAPI staining for nuclei shows selective expression in fibers and not cell bodies (right). (**B**) Optical HFS (130 Hz, 5-ms pulse width) of the STN region in an anesthetized Thy1::ChR2-EYFP 6-OHDA mouse with 473-nm light inhibited STN large-amplitude spikes (sample trace, top left), while inducing smaller-amplitude high-frequency oscillations (figs. S4, C and D, and S5C). Optical LFS (20 Hz, 5-ms pulse width) produced reliable spiking at 20 Hz (bottom left). Whereas HFS prevented bursting (top right, $P < 0.001$, $n = 3$), LFS had no significant effect on burst frequency by two-sample t test ($P > 0.05$, n = three traces) nor on spikes per burst (bottom right, $P > 0.05$, n = three traces). (**C**) Optical HFS to STN in these animals (left, 100 to 130 Hz, 5-ms pulse width, n = five mice) produced robust therapeutic effects, reducing ipsilateral rotations and allowing animals to freely switch directions. In contrast, optical LFS (second left, 20 Hz, 5-ms pulse width, n = five mice) exacerbated pathologic effects, causing increased ipsilateral rotations. Both effects were reversible (post). Changes were significant by t test with $\mu = 0$ for both HFS ($P < 0.001$, n = five mice) and LFS ($P < 0.05$, n = five mice) compared with baseline (light off). (Right) Contralateral head position bias also showed robust correction with HFS by two-sample t test (HFS versus light off: $P < 0.05$; n = two mice), but not with LFS (LFS versus light off: $P > 0.05$, n = two mice).

every case these severely parkinsonian animals were restored to behavior indistinguishable from normal, and in every case, the therapeutic effect immediately and fully reversed, with return of ipsilateral rotations upon discontinuation of the light pulse paradigm. Notably, treated animals could freely switch directions of movement and head position from left to right and vice versa. In striking contrast with optical HFS, optical LFS (20 Hz) of the same afferent fibers worsened PD symptoms by driving increased ipsilateral rotational behavior (Fig. 5C), which demonstrated that the behavioral effects seen do not result simply from driving unilateral activity. Therefore, in contrast to direct STN cellular interventions, driving STN afferent fibers with HFS and LFS differentially modulated PD symptoms in a manner corresponding to frequencies of stimulation linked clinically to ameliorated or exacerbated PD symptoms.

Optical control of layer V motor cortex projection neurons. A diverse array of fibers from widespread brain areas converge on the STN, which may underlie the utility of the STN as a focal DBS target. Many of these afferents likely contribute together to the therapeutic effects, and it is unlikely that a single source of fibers completely accounts for the behavioral effects seen. However, we explored these afferents in greater detail to determine the general class of fibers that may be contributory.

Thy1::ChR2 animals display ChR2 expression chiefly in excitatory projection neurons (*22*, *23*). Indeed, the inhibitory markers glutamic acid decarboxylase isoform 67 (GAD67) and γ-aminobutyric acid (GABA) were not detectable in Thy1::ChR2 fibers within STN (Fig. 6A, left), which effectively ruled out contributions from the GABAergic pallidal projections (LGP–GPe). We also found no localization of major neuromodulatory markers (dopamine and acetylcholine) within the STN Thy1::ChR2 fibers (fig. S2C), which ruled out dopaminergic substantia nigra pars reticulata as a relevant fiber origin as well. We next explored possible sources of excitatory fibers and found no expression of ChR2-YFP in the cell bodies of the excitatory parafascicular or pedunculopontine nuclei, potential contributors of excitatory fibers to the STN. Within neocortex of these mice, however, ChR2-YFP is expressed strongly in excitatory neurons that project to STN (*22*, *23*). Because pathologically strong connectivity between STN and primary motor cortex M1 has been suggested to underlie PD circuit dysfunction (*43*, *44*), we therefore explored M1 as a possible contributor.

We verified in Thy1::ChR2 M1 the presence of strong and selective ChR2 expression largely restricted to layer V neurons and corresponding apical dendrites (*22*, *23*) but not in cells within other layers (Fig. 6A, right). To probe the functional connectivity between these layer V projection neurons and STN in the PD animals, we conducted a separated-optrode experiment in anesthetized animals in which the fiber-optic and recording electrodes were placed in two different brain regions in Thy1::ChR2 animals (Fig. 6B). By driving M1 layer V projection neurons and simultaneously recording in both M1 and STN, we found that precise M1 stimulation of this kind potently influenced neural activity in the STN (Fig. 6C and fig. S7, C and D) and that M1 layer V neurons could be antidromically recruited by optical stimulation in the STN (fig. S6). Whereas, as noted above, many local afferents in the STN region, including those from the ZI, are likely to underlie the complex therapeutic effects of DBS, functional influences between M1 layer V and STN could be significant contributors. Indeed, we found that selective M1 layer V HFS optical stimulation sufficed to ameliorate PD symptoms in a manner similar to that of STN stimulation in an array of measures ranging from rotational behavior (Fig. 6D) to head position bias and locomotion (Fig. 6, E and F). As with STN stimulation, pathological rotations and head position bias were reduced by optical HFS to M1; in con-

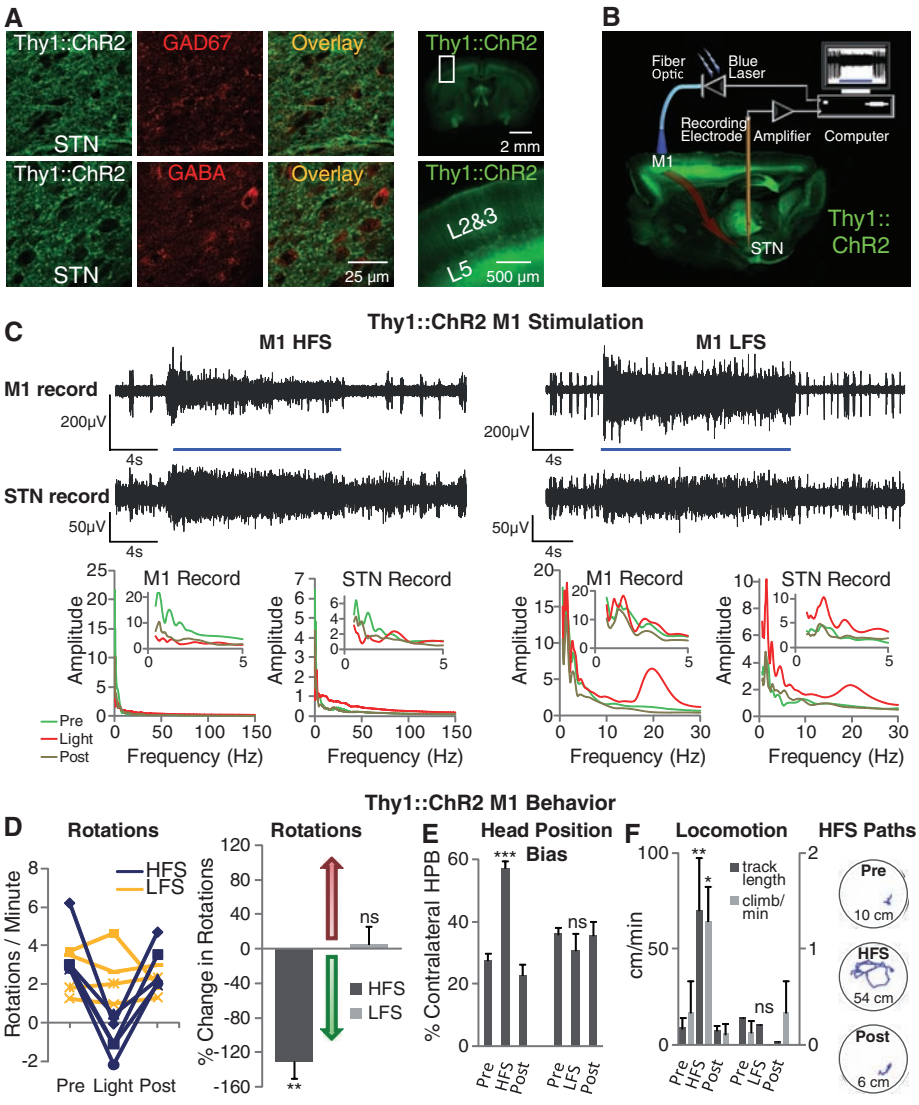

Fig. 6. Selective optical stimulation of layer V neurons in anterior primary motor cortex. (**A**) GAD67 and GABA staining showed no colocalization with Thy1::ChR2-EYFP in STN (left). Apical dendrites of layer V neurons can be seen rising to the pial surface (*22*, *23*) (right). (**B**) Schematic for optical stimulation of M1 with simultaneous recording in STN of Thy1::ChR2 mice. (**C**) Optical stimulation (473 nm) of M1 and simultaneous recording in STN of anesthetized Thy1::ChR2 mice. Optical HFS (130 Hz, 5-ms pulse width) of M1 modulated activity in both M1 and STN. Optical LFS (20 Hz, 5-ms pulse width) of M1 produced 20-Hz tonic firing in both M1 and STN. (**D**) Optical HFS (130 Hz, 5-ms pulse width) reduced amphetamine-induced ipsilateral rotations in 6-OHDA Thy1::ChR2 mice ($P < 0.01$, n = five mice) in contrast to optical LFS (20 Hz, 5-ms pulse width, $P > 0.05$, n = four mice); t test with $\mu = 0$. (**E**) Contralateral head position bias was corrected in HFS (HFS versus light off: $P < 0.001$, n = four mice), whereas LFS had little effect (LFS versus light off: $P > 0.05$, n = three mice); two-sample t test. (**F**) HFS but not LFS to M1 significantly increased path length (HFS, $P < 0.01$, n = two mice) and climbing ($P < 0.05$, n = three mice); two-sample t test. Sample paths before, during, and after HFS are shown (100 s each, path lengths noted in cm).

trast, without augmenting the pathology, optical 20 Hz (LFS) stimulation to M1 had no therapeutic effect (Fig. 6, D, E, and F), and even at the highest light intensities achievable without epileptogenesis, M1 LFS did not drive or modify rotational behavior, unlike M2 LFS cortical stimulation that can elicit contralateral rotations (*27*). Finally, increased functional mobility with M1 HFS but not LFS was confirmed with quantification of increased distance and speed of locomotion in PD Thy1::ChR2 mice; in the absence of amphetamine, M1 HFS allowed the otherwise bradykinetic animals to move freely without eliciting rotational behavior (Fig. 6F).

Discussion. A major promise of optogenetics has been the potential for dissection of disease circuitry and treatment mechanisms. Here, we demonstrate that this potential can be realized. Systematically targeting different elements of the disease circuit, we implicate direct frequency-dependent effects on afferents to the STN region as a major direct target of deep brain stimulation in PD.

Cortical-STN interactions have been previously considered in PD; indeed, motor cortex activity may be elevated in PD and reduced in PD treatment (*45*, *46*), and abnormal oscillatory activity may occur between the cortex and the basal ganglia in PD patients during movement (*32*, *47*, *48*). Cortical stimulation could restore balance to parkinsonian circuitry that is overly devoted to one kind of activity to the exclusion of others (*44*), either by disrupting the pathological activity pattern (e.g., low-frequency bursting), by promoting through-put of patterns encoding motor behaviors oppositional or compensatory to the lesion pathology, or both. Cortical stimulation in human beings has been a subject of interest and controversy (*49*), with some studies showing promising results for PD treatment (*50*–*55*) and others less supportive (*56*–*58*). Our data, in implicating deep layer V neurons as sufficient targets in primary motor cortex, may help address these issues by informing the design of cortical interventions with regard to subdural rather than superficial extradural stimulation. Even with subdural stimulation, optimal cortical stimulation in patients will certainly face particular challenges because of broad cortical representation, and identifying the cortical subregion most functionally connected to STN will be important. Clinical translation of these concepts will benefit from ongoing work in animal models to facilitate rapid mapping of stimulus space for identification of optimal duty cycles (percentage of time pulse is on during stimulation) and pulse patterns.

It is important to note that these findings do not exclude other important contributions to DBS targets or disease symptoms. Not only are other afferents to the STN potential upstream factors in STN-initiated therapeutic effects, but all STN-initiated effects will be implemented downstream through the interconnected basal ganglia, cortical, brainstem, and thalamic motor pathways, with many potential nodes for intervention. Both the disease and treatment are extraordinarily complex; the fact that DBS can improve many PD symptoms, including tremor, rigidity, and bradykinesia—but not others, such as speech impairment, depression, and dementia—points to the need for ongoing work to map and functionally interrogate disease circuitry beyond the brain regions investigated here. DBS can also encounter limitations as a therapy even for the symptoms that typically respond. These issues may be linked to cell type–specific responses and suggest that disease model investigations will be greatly facilitated by the optogenetic approach.

Axon tract modulation with high temporal precision could turn out to be a common theme in DBS (*12*–*15*, *26*), as these collections of fibers represent compact nodes for accessing activity converging from a broader area. Even without detailed knowledge of the relevant neural code, simple alterations in the propagation of activity through white matter tracts or disrupting circuit loops could represent final common pathways for disease and treatment (*59*). However, for PD as well as for other neurological and psychiatric diseases, maintaining high temporal precision of the circuit interrogation technology will be crucial, because as illustrated here, fundamentally different effects are seen when driving the same cell type at different temporal frequencies. Indeed, themes of synchrony and oscillations driven by particular cell and fiber types will likely be common to other brain stimulation–responsive diseases, such as depression and epilepsy, and will underscore the importance of understanding and generalizing DBS.

References and Notes

1. R. L. Albin, A. B. Young, J. B. Penney, *Trends Neurosci.* **12**, 366 (1989).
2. G. E. Alexander, M. D. Crutcher, *Trends Neurosci.* **13**, 266 (1990).
3. M. R. DeLong, *Trends Neurosci.* **13**, 281 (1990).
4. A. L. Benabid *et al*., *Stereotact. Funct. Neurosurg.* **62**, 76 (1994).
5. P. Limousin *et al*., *Lancet* **345**, 91 (1995).
6. A. R. Rezai *et al*., *Neurosurgery* **62** (suppl. 2), 809 (2008).
7. J. O. Dostrovsky, A. M. Lozano, *Mov. Disord.* **17**, (Suppl. 3), S63 (2002).
8. Y. Liu, N. Postupna, J. Falkenberg, M. E. Anderson, *Neurosci. Biobehav. Rev.* **32**, 343 (2008).
9. C. C. McIntyre, M. Savasta, L. Kerkerian-Le Goff, J. L. Vitek, *Clin. Neurophysiol.* **115**, 1239 (2004).
10. J. L. Vitek, *Mov. Disord.* **17**, (Suppl. 3), S69 (2002).
11. R. E. Gross, J. D. Rolston, *Clin. Neurophysiol.* **119**, 1947 (2008).
12. A. M. Lozano *et al*., *Biol. Psychiatry* **64**, 461 (2008).
13. H. S. Mayberg *et al*., *Neuron* **45**, 651 (2005).
14. H. E. McNeely, H. S. Mayberg, A. M. Lozano, S. H. Kennedy, *J. Nerv. Ment. Dis.* **196**, 405 (2008).
15. K. J. Ressler, H. S. Mayberg, *Nat. Neurosci.* **10**, 1116 (2007).
16. F. Zhang, A. M. Aravanis, A. Adamantidis, L. de Lecea, K. Deisseroth, *Nat. Rev. Neurosci.* **8**, 577 (2007).
17. A. R. Adamantidis, F. Zhang, A. M. Aravanis, K. Deisseroth, L. de Lecea, *Nature* **450**, 420 (2007).
18. A. M. Aravanis *et al*., *J. Neural Eng.* **4**, S143 (2007).
19. E. S. Boyden, F. Zhang, E. Bamberg, G. Nagel, K. Deisseroth, *Nat. Neurosci.* **8**, 1263 (2005).
20. F. Zhang *et al*., *Nature* **446**, 633 (2007).
21. V. Gradinaru, K. R. Thompson, K. Deisseroth, *Brain Cell Biol.* **36**, 129 (2008).
22. B. R. Arenkiel *et al*., *Neuron* **54**, 205 (2007).
23. H. Wang *et al*., *Proc. Natl. Acad. Sci. U.S.A.* **104**, 8143 (2007).
24. F. Zhang *et al*., *Nat. Neurosci.* **11**, 631 (2008).
25. C. C. McIntyre, W. M. Grill, *J. Neurophysiol.* **88**, 1592 (2002).
26. C. C. McIntyre, W. M. Grill, D. L. Sherman, N. V. Thakor, *J. Neurophysiol.* **91**, 1457 (2004).
27. V. Gradinaru *et al*., *J. Neurosci.* **27**, 14231 (2007).
28. C. Hamani, J. A. Saint-Cyr, J. Fraser, M. Kaplitt, A. M. Lozano, *Brain* **127**, 4 (2004).
29. Materials and methods are available as supporting material on *Science* Online.
30. Y. Smith, A. Parent, *Brain Res.* **453**, 353 (1988).
31. G. A. Metz, A. Tse, M. Ballermann, L. K. Smith, K. Fouad, *Eur. J. Neurosci.* **22**, 735 (2005).
32. R. Levy *et al*., *Brain* **124**, 2105 (2001).
33. L. Bekar *et al*., *Nat. Med.* **14**, 75 (2008).
34. S. A. Rivkees, S. L. Price, F. C. Zhou, *Brain Res.* **677**, 193 (1995).
35. K. Z. Shen, S. W. Johnson, *Neuroscience* **116**, 99 (2003).
36. Y. P. Zhang, T. G. Oertner, *Nat. Methods* **4**, 139 (2007).
37. G. Nagel *et al*., *Proc. Natl. Acad. Sci. U.S.A.* **100**, 13940 (2003).
38. L. P. Wang, K. Deisseroth, unpublished observations.
39. H. Bronte-Stewart *et al*., *Exp. Neurol.* **215**, 20 (2009).
40. B. Wingeier *et al*., *Exp. Neurol.* **197**, 244 (2006).
41. V. Tabar *et al*., *Nat. Med.* **14**, 379 (2008).
42. T. Matsuya *et al*., *J. Pharmacol. Sci.* **103**, 329 (2007).
43. S. Li *et al*., *J. Neurophysiol.* **98**, 3525 (2007).
44. B. Degos, J. M. Deniau, J. Le Cam, P. Mailly, N. Maurice, *Eur. J. Neurosci.* **27**, 2599 (2008).
45. M. C. Ridding, R. Inzelberg, J. C. Rothwell, *Ann. Neurol.* **37**, 181 (1995).
46. P. Payoux *et al*., *Arch. Neurol.* **61**, 1307 (2004).
47. P. Brown *et al*., *J. Neurosci.* **21**, 1033 (2001).
48. M. L. Kringelbach, N. Jenkinson, S. L. Owen, T. Z. Aziz, *Nat. Rev. Neurosci.* **8**, 623 (2007).
49. F. Fregni, D. K. Simon, A. Wu, A. Pascual-Leone, *J. Neurol. Neurosurg. Psychiatry* **76**, 1614 (2005).
50. S. Canavero, R. Paolotti, *Mov. Disord.* **15**, 169 (2000).
51. S. Canavero *et al*., *J. Neurosurg.* **97**, 1208 (2002).
52. C. A. Pagni, S. Zeme, F. Zenga, *J. Neurosurg. Sci.* **47**, 189 (2003).
53. J. P. Lefaucheur *et al*., *Clin. Neurophysiol.* **115**, 2530 (2004).
54. X. Drouot *et al*., *Neuron* **44**, 769 (2004).
55. E. M. Khedr, J. C. Rothwell, O. A. Shawky, M. A. Ahmed, A. Hamdy, *Mov. Disord.* **21**, 2201 (2006).
56. R. Cilia *et al*., *Mov. Disord.* **22**, 111 (2007).
57. A. P. Strafella *et al*., *Mov. Disord.* **22**, 2113 (2007).
58. J. E. Arle *et al*., *J. Neurosurg.* **109**, 133 (2008).
59. R. D. Airan *et al*., *Science* **317**, 819 (2007).

60. K.D. is supported by the Kinetics Foundation, the William M. Keck Foundation, the Snyder Foundation, the Albert Yu and Mary Bechmann Foundation, and the Wallace Coulter Foundation, as well as by California Institute for Regenerative Medicine, the McKnight Foundation, the Esther A. and Joseph Klingenstein Fund, NSF, National Institute of Mental Health, National Institute on Drug Abuse, and the NIH Pioneer Award. V.G. is supported by SGF and SIGF (Stanford Graduate Fellowships). M.M is supported by Bio-X and SGF Fellowships. K.R.T. is supported by NARSAD. J.M.H is supported by the Coulter Foundation, the John Blume Foundation and the Davis Phinney Foundation. We especially thank A. M. Aravanis for mentoring and advice on animal surgery and in vivo recordings, F. Zhang and H. C. Tsai for assistance with Cre-dependent opsin targeting, L. Meltzer for useful discussion, advice and help on immunohistochemistry, G. Feng and G. Augustine for collaboration on generation of the Thy-1 mice (available at the Jackson Laboratory), and V. Sohal for help with power spectra analysis. We also thank the entire Deisseroth lab for useful discussions. The materials and methods described herein are freely distributed and supported by the authors (www.stanford.edu/group/dlab).

Supporting Online Material

www.sciencemag.org/cgi/content/full/1167093/DC1
Materials and Methods
Figs. S1 to S7
Table S1
References

13 October 2008; accepted 20 February 2009
Published online 19 March 2009;
10.1126/science.1167093
Include this information when citing this paper.

Probing Interactions Between Ultracold Fermions

G. K. Campbell,[1] M. M. Boyd,[1] J. W. Thomsen,[1] M. J. Martin,[1] S. Blatt,[1] M. D. Swallows,[1] T. L. Nicholson,[1] T. Fortier,[2] C. W. Oates,[2] S. A. Diddams,[2] N. D. Lemke,[2] P. Naidon,[3]* P. Julienne,[3] Jun Ye,[1]† A. D. Ludlow[1]‡

At ultracold temperatures, the Pauli exclusion principle suppresses collisions between identical fermions. This has motivated the development of atomic clocks with fermionic isotopes. However, by probing an optical clock transition with thousands of lattice-confined, ultracold fermionic strontium atoms, we observed density-dependent collisional frequency shifts. These collision effects were measured systematically and are supported by a theoretical description attributing them to inhomogeneities in the probe excitation process that render the atoms distinguishable. This work also yields insights for zeroing the clock density shift.

Quantum statistics plays a critical role in shaping interactions between matter. This is apparent in the markedly different behavior of Bose-Einstein condensates (*1*, *2*) and degenerate Fermi gases of ultracold atoms (*3*). The quantum statistics of atoms can thus be a key factor in the choice of an atomic system for a given experiment. Such is the case for atoms at the heart of an atomic clock. Simultaneous interrogation of many atoms is favorable for achieving high measurement precision. However, when atoms interact with each other, their internal energy states can be perturbed, leading to frequency shifts of the clock transition (*4*, *5*). The use of identical fermions was prescribed to allow many atoms to strengthen the signal without such density-dependent collision shifts (*6*). Previous experiments seemed to confirm this fact for both single-component (*7*) and two-component fermion mixtures (*8*).

However, by probing an optical clock transition with thousands of fermionic Sr atoms confined in a one-dimensional optical lattice, we clearly observe density-related frequency shifts at a fractional precision of 1×10^{-16}. When the light-atom interaction introduces a small degree of inhomogeneous excitation, previously indistinguishable fermions become slightly distinguishable. This effect causes a time-dependent variation of the two-particle correlation function, giving rise to an apparent mean-field energy. The resulting collision effects have been measured systematically as a function of temperature, excitation probability, and interaction inhomogeneity. These observations are supported by a theoretical description of fermionic interactions that includes the effect of the measurement process.

The latest generation of optical atomic clocks such as those based on the $^1S_0$–$^3P_0$ transition in fermionic ^{87}Sr currently offers the highest measurement precision, useful for measuring possible atomic interactions (*9*, *10*). In an ultracold dilute gas with a mean-field energy, a narrow clock transition will experience a density-dependent frequency shift (*11*, *12*) given by $h\Delta\nu = (4\pi\hbar^2 G^{(2)}\rho a)/m$. Here, m is the atomic mass, ρ is the density of the atomic sample, a is the s-wave scattering length characterizing the atomic interaction, and $h = 2\pi\hbar$ is Planck's constant. $G^{(2)}$ is the two-atom correlation function at zero distance, which summarizes the quantum statistics of colliding bodies. For example, $G^{(2)} = 0$ for identical fermions and $G^{(2)} = 2$ for identical bosons in a thermal gas. The Fermi suppression arises from the Pauli exclusion principle, which prohibits even-partial-wave collisions between indistinguishable fermions. At ultracold temperatures, partial waves higher than s-wave are frozen out (*13*). For atoms excited in our two-level clock system, three possible s-wave interactions exist: those between two $^1S_0$ ground-state ($|g\rangle$) atoms, those between two $^3P_0$ excited-state ($|e\rangle$) atoms, and those between a $|g\rangle$ atom and a $|e\rangle$ atom. Including all possible in-

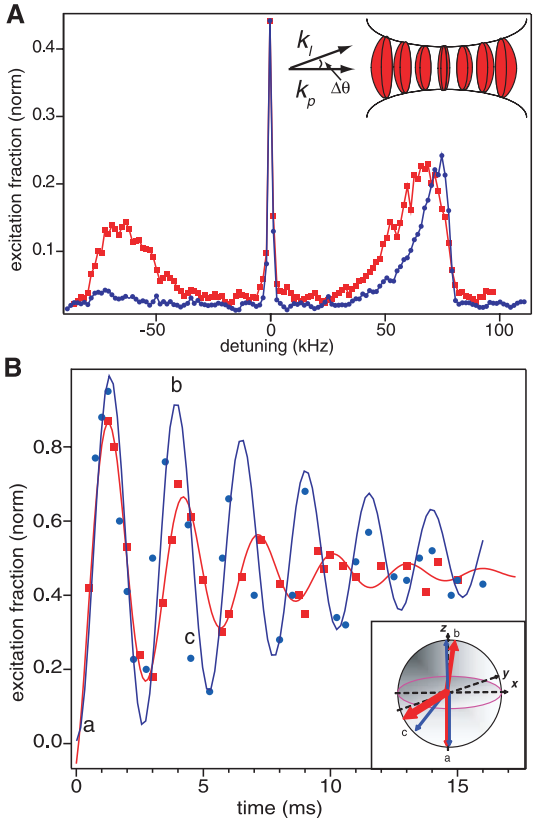

Fig. 1. (**A**) Sideband excitation spectra for $T = 1$ μK (blue circles) and 3 μK (red squares). The spectra are obtained in the resolved sideband limit and have three dominant features, the narrow carrier transition and broad red (blue) motional sidebands that are excited when an atom is transferred to a lower (higher) motional state during the transition. As the temperature of the sample is lowered, the atoms primarily occupy the ground state and the red sideband is suppressed. The temperature of the atomic ensemble can be extracted from a fit of the sidebands (*25*). The inset shows the lattice geometry and excitation scheme. The probe beam and lattice are coaligned and copolarized, minimizing the relative spread between $\vec{k}_l$ and $\vec{k}_p$. However, even with the best effort, a small angle $\Delta\theta$ between the probe and lattice beams may persist due to aberrations and misalignment. (**B**) Rabi oscillations for temperatures of 1 μK (blue circles) and 3 μK (red squares). For higher temperatures, more motional states are occupied. This leads to a larger spread in the Rabi frequencies and faster dephasing of the excitation between atoms. By fitting the decay of Rabi oscillations, we can determine the degree of excitation inhomogeneity. The inset illustrates the dephasing process with rotations on the Bloch sphere. At time a, before the excitation, the atoms are in a pure state. At time b, the atoms have undergone two oscillations. For the red curve, the temperature is hotter and there is a larger spread in Rabi frequencies. This is indicated by the increased width of the Bloch vector and dephasing of the observed oscillations. At time c, the effect is even more pronounced.

[1]JILA, National Institute of Standards and Technology and University of Colorado Department of Physics, University of Colorado, Boulder, CO 80309–0440, USA. [2]Time and Frequency Division, National Institute of Standards and Technology, Boulder, CO 80302, USA. [3]Atomic Physics Division and Joint Quantum Institute, National Institute of Standards and Technology, 100 Bureau Drive Stop 8423, Gaithersburg, MD 20899–8423, USA.

*Present address: ERATO (Exploratory Research for Advanced Technology) Macroscopic Quantum Project, Japan Science and Technology Agency, Tokyo, 113-0033, Japan.

†To whom correspondence should be addressed. E-mail: junye@jilau1.colorado.edu

‡Present address: Time and Frequency Division, National Institute of Standards and Technology, Boulder, CO 80302, USA.

teractions, the collisional frequency shift at ultracold temperatures is given by Eq. 1 (*8*, *12*, *11*):

$$\Delta\nu_{ge} = \frac{2\hbar}{m}(G^{(2)}_{ge}a_{ge}(\rho_g - \rho_e) + G^{(2)}_{ee}a_{ee}\rho_e - G^{(2)}_{gg}a_{gg}\rho_g) \quad (1)$$

where a_{ij} is the *s*-wave scattering length for collisions between atoms in state *i* and *j*, and ρ_i is the density of atoms in state *i*. Because indistinguishable fermions do not collide, $G^{(2)}_{gg} = G^{(2)}_{ee} = 0$. Fermions in different internal states are distinguishable, and for a completely incoherent mixture of the two states, $G^{(2)}_{ge} = 1$. However, if the two-state mixture is prepared by a uniform, coherent excitation of ground-state atoms, then the fermions evolve indistinguishably and $G^{(2)}_{ge} = 0$ (*8*). In this case, $\Delta\nu_{ge} = 0$.

Two possibilities exist for $\Delta\nu_{ge}$ to deviate from zero. First, the *p*-wave contribution may not be negligible. However, for ultracold atoms confined in a well-characterized optical trap, we show experimental evidence and theoretical calculations that conclude that *p*-wave collisions make no noticeable contribution to the observed clock frequency shift. Second, it is imperative to consider the entire interaction, including the measurement process, when exploring the question of whether fermions collide. Indeed, the measurement process, such as probing a clock transition, may strongly influence the value of $G^{(2)}$. We show here that an inhomogeneous interaction between light and atoms leads to the loss of indistinguishability of the fermions, thus making $0 < G^{(2)} < 1$.

Although a uniform, coherent excitation of identical fermions maintains $G^{(2)} = 0$, and no *s*-wave collisions occur, if a small nonuniformity in the excitation process arises, the atoms are no longer completely identical, and $G^{(2)} > 0$. The value of $G^{(2)}$ will depend on the degree of excitation inhomogeneity. This measurement-induced dynamic variation of quantum statistics leads directly to a change of the mean-field energy within the ultracold gas, resulting in a nonzero $\Delta\nu_{ge}$. It is interesting to contrast the present work with previous results observed with an ultracold gas of fermionic ^{6}Li, where the insensitivity of a radio-frequency (rf) transition to collisional shifts was demonstrated (*7*, *8*). It was shown that the fermionic insensitivity to collisional shifts was maintained even when a pure superposition state of the two-level system had decohered. This decoherence does allow interactions, but when a uniform rf probing field reintroduced coherence to the atoms in a homogeneous manner, the apparent value for $G^{(2)}$ again became zero, giving no collisional shifts within the measurement precision (*14*). From the current experiment, it is clear that any nonidentical evolutions during the interrogation process lead to the breakdown of Fermi suppression; this experiment is sensitive to very small inhomogeneities because of the high measurement precision.

An intuitive understanding emerges from considering two sample atoms in a pseudo spin-1/2 system with ground $|g\rangle$ and excited $|e\rangle$ states. Before applying the spectroscopy pulse, the atomic system is in a pure, polarized spin state with $|\psi_1\rangle = |\psi_2\rangle = |g\rangle$. The effect of the pulse is to perform a rotation on the Bloch sphere, as shown in the inset of Fig. 1B. For a coherent, homogeneous excitation, the wave function of the system becomes a coherent superposition $|\psi_1\rangle = |\psi_2\rangle = \alpha|g\rangle + \beta|e\rangle$. The wave functions of both atoms are identical, $G^{(2)}_{12} = 0$, and collisions cannot occur. An inhomogeneous spectroscopic excitation, such as that caused by varying Rabi frequencies for different atoms, results in slightly different rotations on the Bloch sphere for the two atoms (Fig. 1B, inset). Hence, we have $|\psi_1\rangle = \alpha|g\rangle + \beta|e\rangle$ and $|\psi_2\rangle = \gamma|g\rangle + \delta|e\rangle$. The fermions are distinguishable and $0 < G^{(2)}_{12} \leq 1$. The value of $G^{(2)}_{12}$ depends on the amount of inhomogeneity, and its time variation can be explicitly calculated from the antisymmetrized overlap of the two wave functions [details are provided in the supporting text (*15*)]:

$$G^{(2)}_{12}(\alpha(t),\beta(t),\gamma(t),\delta(t)) = 1 - |\alpha(t)\gamma^*(t) + \beta(t)\delta^*(t)|^2 \quad (2)$$

The resulting collision shift from Eq. 1 is then

$$\Delta\nu(t) = \frac{2\hbar a_{ge}}{m}G^{(2)}_{12}(\alpha,\beta,\gamma,\delta)(\rho_g - \rho_e) \quad (3)$$

Before proceeding with experimental results, we first summarize the system under study (*15*). In the ^{87}Sr optical clock, atoms are trapped in a one-dimensional (1D) optical standing-wave potential (1D optical lattice). Longitudinally the atoms are confined tightly, with an oscillation frequency $\nu_z \sim 80$ kHz. At temperature $T = 1$ μK, ~ 98% of the atoms occupy the ground state of the trap ($\bar{n}_z = 0.02$). The laser probing the clock transition propagates along the lattice axis, and spectroscopy is performed in the Lamb-Dicke regime. In the transverse plane the confinement is much weaker, with an oscillation frequency $\nu_x = \nu_y \sim 450$ Hz, and atoms occupy a large number of motional states ($\bar{n}_x = \bar{n}_y = 46$). Typically, ~$2 \times 10^3$ atoms are trapped in the optical lattice, resulting in 30 atoms per lattice site with a density of 2×10^{11} cm^{-3} (*15*). The optical lattice is nearly vertically oriented and is operated at the so-called magic wavelength of $\lambda_L \sim 813.429$ nm (*16*), where the ac Stark shifts of the $^1S_0$ and $^3P_0$ states are identical.

With a perfect alignment of the probe laser along the strong confinement axis, assuming cylindrical symmetry, a residual angular spread between the probe and lattice $\vec{k}$ remains due to the finite size of the lattice beam (*17*). However, an even larger effect occurs if the symmetry is broken due to either aberrations in the beam profile or angular misalignment ($\Delta\theta$) between the lattice and the probe beam. For our trap parameters, we estimate an effective $\Delta\theta \approx 10$ mrad (Fig. 1A, inset). The residual wave vector projected on the transverse plane leads to slightly different excitation Rabi frequencies $\Omega_{\vec{n}}$ for atoms in different (n_x, n_y) states (*15*, *18*, *19*). For a given *T*, the occupation of a transverse motional state $n_{x,y}$ is given by the normalized Maxwell-Boltzmann distribution. The inhomogeneity in the Rabi frequencies is thus affected by both *T* and $\Delta\theta$.

To calculate the density shift, we return to our two-atom model. Each atom has a slightly different $\Omega_{\vec{n}}$. For the entire atomic ensemble, we can define an average Rabi frequency $\overline{\Omega}$ and its

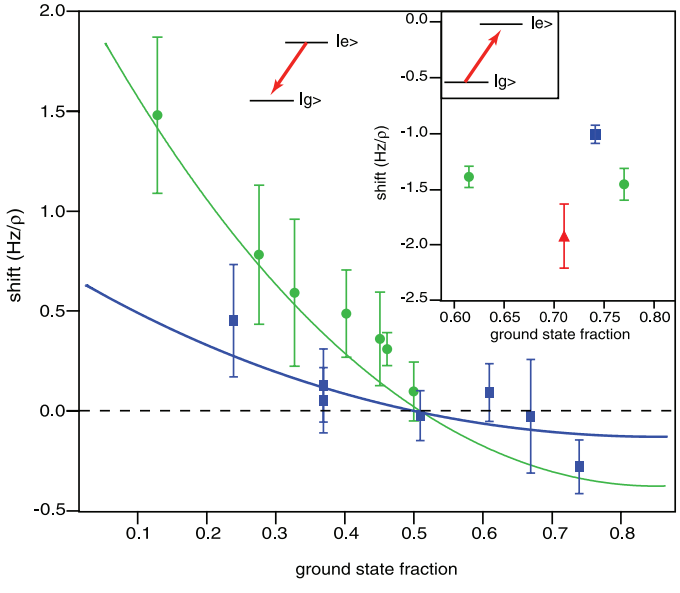

Fig. 2. Measured density-dependent frequency shift as a function of the final excitation fraction and temperature. Atoms are initially spin polarized and transferred to $^3P_0$ ($|e\rangle$) before the spectroscopy pulse is applied. The squares (circles) show the measured shift for $T = 1$ (*3*) μK. The lines show the calculated shifts when the two-atom model is used with only a single scaling factor. Near ~50% the shift goes through zero. In the inset, the measured shift is shown for atoms excited from the $^1S_0$ ($|g\rangle$) state for $T = 1$ μK (squares), 3 μK (circles), and 5 μK (triangles). However, the magnitude in this case could be influenced by imperfect spin polarizations. For both plots, as the temperature is decreased, the inhomogeneity also decreases, leading to a smaller collision shift. ρ is the atomic density of 10^{11}/cm^3. The density-dependent shift for each excitation fraction is determined with an interleaved scheme in which the density is varied every 100 s. Pairs of such data are then used to determine the frequency shift. Typical data sets include 20 to 30 pairs of density comparison, with the error bars indicating the standard error (SE).

root mean square spread $\Delta\Omega$. To approximate the average density shift, we set $\Omega_1 = \overline{\Omega} + \Delta\Omega$ and $\Omega_2 = \overline{\Omega} - \Delta\Omega$ for our two-atom model. Thus, the time-dependent quantities α, β, γ, and δ as defined in Eq. 2 are parameterized by $\overline{\Omega}$ and $\Delta\Omega$ (*15*). At a time t during the spectroscopy pulse, the atoms experience an ensemble-averaged shift:

$$\Delta\nu(t) = \frac{2\hbar a_{ge}}{m} G_{12}^{(2)}(\overline{\Omega} + \Delta\Omega, \overline{\Omega} - \Delta\Omega)(\rho_g - \rho_e) \quad (4)$$

This shift evolves during the spectroscopy pulse, and for the final density shift we time average $\Delta\nu(t)$ over the total pulse length t_F. This approximation is valid in the limit that the change in Ω due to atomic interactions is much less than $\Delta\Omega$. A more rigorous calculation with the optical Bloch equations that includes atomic interactions has also been made. Using our typical trap parameters, we find that the two-atom approximation is valid to within 5%. The time-dependent Rabi oscillation is only slightly affected by atomic interactions; however, the effect on the final clock shift is obvious.

For inhomogeneity-induced collision shifts, t_F is important. Atoms in close proximity to each other tend to have similar Rabi frequencies, whereas atoms located far apart are more likely to experience different excitations (and hence be distinguishable). If $t_F \nu_{x,y} \ll 1$, the atoms are effectively frozen in place and will experience no density shift. However, if $t_F \nu_{x,y} > 1$, atoms initially located far apart have time to interact. For the clock experiment requiring high spectral resolution, $t_F = 80$ ms and $1/\nu_{x,y} = 2.2$ ms, so collisions will occur.

To systematically study these effects, we implemented controlled variations of both T and $\Delta\theta$. To vary T, we perform cooling (heating) of the lattice-confined atoms in three dimensions: Doppler cooling (heating) along the transverse direction and sideband cooling (heating) along the longitudinal axis. Simultaneous with the sideband cooling (heating), the atoms are spin-polarized by optical pumping in a weak magnetic (B) bias field. Atoms are polarized into either the $m_F = +9/2$ or $m_F = -9/2$ Zeeman states. The $^1S_0$–$^3P_0$ clock transition, which is predicted to have a natural linewidth of ~1 mHz (*20*–*22*), is interrogated with a cavity-stabilized diode laser at 698 nm with a linewidth below 1 Hz (*23*). Spectroscopy is performed in the Lamb-Dicke regime and in the resolved sideband limit (*24*). To ensure that the polarized spin state is well resolved from other m_F levels, spectroscopy is performed under $B \sim 250$ mG, leading to a separation of 250 Hz between the $m_F = \pm 9/2$ states. A spectroscopy pulse length of $t_F = 80$ ms results in a Fourier-limited linewidth of ~10 Hz.

After the spectroscopy pulse is applied, atoms remaining in $|g\rangle$ are counted by measuring fluorescence on the strong $^1S_0$–$^1P_1$ transition. Atoms transferred to $|e\rangle$ are then pumped back to $|g\rangle$ via the intermediate $(5s6s)^3S_1$ states and are also counted. Combining these two measurements gives us a normalized excitation fraction $\rho_e/(\rho_e + \rho_g)$. The atomic temperature is determined by sideband spectroscopy (*25*, *15*) and time-of-flight analysis. In Fig. 1A, sample spectra are shown for two different values of T. Once T is measured, the degree of inhomogeneity is determined by fitting the decaying Rabi oscillations for the ensemble. In Fig. 1B, the Rabi oscillation at $T = 3$ μK (squares) clearly shows faster dephasing than that of $T = 1$ μK (circles), indicating a larger degree of inhomogeneity.

Density-dependent frequency shifts of the ^{87}Sr clock transition are measured with a remotely located calcium optical standard at the National Institute of Standards and Technology (NIST) (*9*) as a stable frequency reference, which is linked to JILA via a phase-coherent fiber network (*26*). This direct optical frequency measurement between two optical standards allows fractional measurement precision of a few times 10^{-16} after hundreds of seconds of averaging. To measure the clock center frequency, the spectroscopy pulse is first applied to atoms optically pumped to the $m_F = +9/2$ state. In the next cycle, atoms polarized to the $m_F = -9/2$ state are used. The center frequency is then determined by the average of both resonances. The density-dependent frequency shift is determined with an interleaved scheme, in which the density of the atomic ensemble is varied every 100 s. The density is varied by a factor of 2. Pairs of such data are then used to measure a frequency shift, and many pairs are averaged to decrease the statistical uncertainty. Typically, we lock the clock laser near the full-width at half-maximum of each resonance; however, the location of the lock points is varied to select the desired excitation fraction.

Spectroscopy is performed by means of two different experimental procedures. In the first, we probe the clock transition from $|g\rangle$ to $|e\rangle$ (Fig. 2, inset). The intensity of the probe is set to produce a π pulse on resonance. This direct scheme could suffer from imperfect polarization of the atomic sample, and spectator atoms could be left in other m_F levels. This scenario could potentially lead to density-dependent shifts due to collisions between different m_F states that are not suppressed by the Fermi statistics. The second scheme minimizes this effect by probing $|e\rangle$ to $|g\rangle$ (Fig. 2).

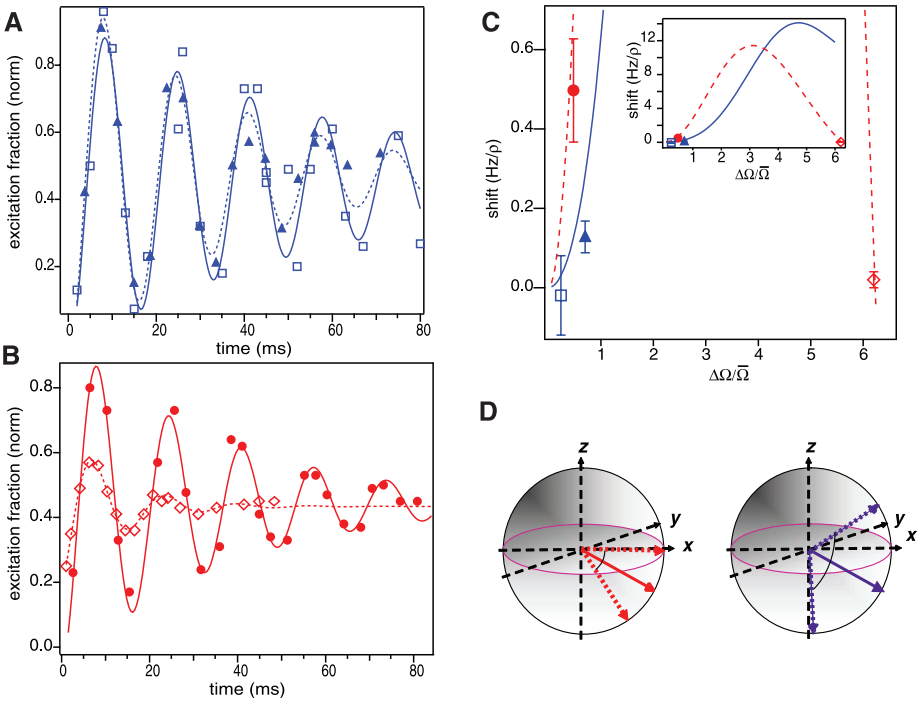

Fig. 3. Effect of probe misalignment on the density-dependent shift. (**A**) Rabi oscillations are shown for two different values of $\Delta\theta$ at $T = 1$ μK. The open squares show oscillations when the probe is aligned similar to that of Figs. 1 and 2. The solid triangles show a faster dephasing when the probe beam misalignment is increased further by 5 mrad. (**B**) Rabi oscillations for $T = 3$ μK. The circles show oscillations when the probe beam is aligned similar to that of Figs. 1 and 2, and the diamonds when the misaligment is increased further by 35 mrad. (**C**) The density shift measured for each misalignment shown in (A) and (B). From $\Delta\theta$ and T, the spread in Rabi frequency $\Delta\Omega$ is calculated. The lines show the expected shift as a function of $\Delta\Omega$ for $T = 1$ μK (solid line) and 3 μK (dashed line). The inset shows a zoomed-out plot. (**D**) For large misalignments, we observe a smaller density shift. This is described with the rotation on the Bloch sphere. As an example, two different values of $\Delta\Omega$ are shown. On each sphere, the average excitation fraction is shown with a solid line, and the spread is indicated by the dotted lines. For small misalignments, we have a small spread in Rabi frequencies. As the misalignment increases, the spread crosses the equatorial plane of the Bloch sphere. At 50%, the sign of the density shift changes, and therefore the portion of the spread centered around this plane averages to zero. The measured density shift is then reduced.

Here, we apply a strong pulse to first transfer the population from $|g\rangle$ to $|e\rangle$. The pulse power broadens the transition in order to decrease the sensitivity of population transfer to probe laser frequency, and transfers ~50% of the population to $|e\rangle$. This first pulse is resonant with atoms in one of the $m_F = \pm 9/2$ states, hence atoms left in other m_F states due to imperfect polarization are not transferred. Subsequently, all atoms remaining in $|g\rangle$ are removed from the lattice with a pulse of light resonant with the strong ${}^1S_0 - {}^1P_1$ transition, without affecting the temperature of the atoms in $|e\rangle$. This is confirmed with sideband spectroscopy (*15*). Finally, the clock transition of $|e\rangle$ to $|g\rangle$ is probed with the usual 80-ms π pulse. In both experimental procedures, we measure populations in $|e\rangle$ and $|g\rangle$ to determine the normalized excitation fraction.

Figure 2 summarizes the measured density-dependent frequency shift as a function of the normalized ground-state fraction for two different values of T, 1 μK (squares) and 3 μK (circles). The data indicate a clear trend that the density shift decreases under a more homogeneous excitation. The solid lines are the expected shifts calculated from the two-atom model. For clock operation, it is important to note that near 50% excitation fraction, for both values of T, the shift goes through zero.

As we change T, we vary both the excitation inhomogeneity and the p-wave contribution. To estimate the magnitude of p-wave collisions, we note that the van der Waals potential for all three interaction types (gg, ee, or eg) has been theoretically calculated (*27*, *21*, *28*), and the p-wave centrifugal barrier is expected to be greater than 25 μK. At $T \sim 1$ μK, $ka \ll 1$, where $k = 2\pi/\lambda_T$. $\lambda_T = h/\sqrt{2\pi m k_B T}$ is the thermal de Broglie wavelength, and k_B is the Boltzmann constant. Under these conditions, the ratio of p-wave to s-wave phase shift is $(bk)^2 b/a$, where b is the p-wave scattering length. For gg interactions, the s-wave scattering length has been measured (*29*) for ${}^{88}Sr$, and mass scaling gives $a_{gg} = 96.2(1)a_0$ for ${}^{87}Sr$, where a_0 is the Bohr radius. Combined with the van der Waals potential, the p-wave phase shift can be determined from the Schrödinger equation. For ${}^1S_0$, $b_{gg} = -76\ a_0$, and for $T = 1$ μK, $|(b_{gg}k)^2 b_{gg}/a_{gg}| \approx 0.01$. Thus, p-wave collisions for gg are suppressed by more than two orders of magnitude and are negligibly small. Although the s-wave scattering lengths a_{ee} and a_{ge} have not yet been measured and thus cannot directly constrain the values of b_{ee} and b_{eg}, calculations based on a theoretical potential predict that these p-wave collisions are similarly suppressed relative to s-wave collisions. An exception would be a p-wave shape resonance (*13*); however, this would occur only for a very small range of possible a_{ee} and a_{ge}, and the effect would be reduced by thermal averaging. We also note that in a trapping potential, k is modified due to the zero-point energy of the trap (k_{ZP}) and the effective thermal wave vector for collisions is given by $k_T = \sqrt{(k^2 + k_{ZP}^2)/2}$. For our trap, $k_{ZP} \sim 3.5$ μK, and p-wave collisions are still suppressed. The observed density shift scales as $G_{12}^{(2)} a_{ge}$, and for our typical temperatures we find values of $G_{12}^{(2)}$ between 0.03 and 0.15, whereas the p-wave scattering length is expected to be ~1% of a_{ge}. Hence, inhomogeneity-induced s-wave collisions dominate. In the unitarity limit where $k_T|a_{ge}| > 1$ (a_{ge} is the zero-temperature scattering length), the effective scattering length is $1/k_T$. For our lattice trap parameters and temperature range of 1 to 3 μK, this length is on the order of $-300\ a_0$, which is consistent in sign and magnitude with our observed frequency shifts, along with the values and uncertainties of $G_{12}^{(2)}$ and ρ.

To provide further evidence to exclude p-wave contributions, we vary the inhomogeneity by misalignment of the spectroscopy probe beam under a fixed T. This also helps rule out $\overline{n}_{x,y,z}$-dependent residual ac Stark shift of the trap. Typically the probe beam is coaligned with the lattice to minimize motional effects. However, by increasing the misalignment ($\Delta\theta$), we can also increase $\Delta\Omega$. Figure 3, A and B, show Rabi oscillations for two different probe beam misalignments at $T = 1$ μK (triangles and open squares) and 3 μK (circles and open diamonds), respectively. Figure 3C displays the measured density shift as a function of $(\Delta\Omega/\overline{\Omega})$ due to probe misalignment. For $T = 1$ μK, the shift becomes larger with increased $\Delta\Omega/\overline{\Omega}$. When $\Delta\Omega/\overline{\Omega}$ increases further, the 3 μK data indicate that the density shift becomes smaller. This behavior is reproduced by the theoretical curves shown in Fig. 3C and is illustrated in Fig. 3D. Consider two different $\Delta\Omega/\overline{\Omega}$, both with an average excitation fraction of 0.3. In the first case, for small misalignment, we find a spread in the excitation fraction of ±0.2; there is an inhomogeneity allowing collisions to occur, and we measure a small density shift. In the second case, with further misalignment the spread in the excitation fraction increases to ±0.4; there is now a larger spread in the Rabi frequencies, and collisions still occur. However, we now have atoms with an excitation fraction both above and below 50% where the shift crosses zero. Hence, the collisions of atoms with excitations between 0.3 and 0.7 will average to zero (this is consistent with the density shift going to zero at 50% excitation, regardless of the inhomogeneity), and the final collision shift is due only to atoms with excitation fractions between 0 and 0.3. The measured shift for the larger misalignment is therefore smaller.

Combining the measurements shown in Figs. 2 and 3 makes it clear that the observed density-dependent shifts arise from the change of the quantum statistics $G^{(2)}$ caused by the inhomogeneous measurement process. The inhomogeneous effect can be suppressed by decreasing the sample temperature and increasing the transverse confinement, or going to higher dimension traps. For clock operations, we have shown that near a 50% excitation fraction, the density shift goes to zero. Using these measurements, we can now reduce the uncertainty of the collision shifts for clock operation (*9*) to 5×10^{-17}. This time-dependent variation in quantum statistics will also apply to boson-based clocks, where the original $G^{(2)} = 2$ will decrease to a value between 1 and 2.

References and Notes

1. E. A. Cornell, C. E. Wieman, *Rev. Mod. Phys.* **74**, 875 (2002).
2. W. Ketterle, *Rev. Mod. Phys.* **74**, 1131 (2002).
3. B. DeMarco, D. S. Jin, *Science* **285**, 1703 (1999).
4. K. Gibble, S. Chu, *Phys. Rev. Lett.* **70**, 1771 (1993).
5. Y. Sortais *et al*., *Phys. Scr.* **T95**, 50 (2001).
6. K. Gibble, B. J. Verhaar, *Phys. Rev. A* **52**, 3370 (1995).
7. S. Gupta *et al*., *Science* **300**, 1723 (2003).
8. M. W. Zwierlein, Z. Hadzibabic, S. Gupta, W. Ketterle, *Phys. Rev. Lett.* **91**, 250404 (2003).
9. A. D. Ludlow *et al*., *Science* **319**, 1805 (2008).
10. G. K. Campbell *et al*., *Metrologia* **45**, 539 (2008).
11. P. J. Leo, P. S. Julienne, F. H. Mies, C. J. Williams, *Phys. Rev. Lett.* **86**, 3743 (2001).
12. D. M. Harber, H. J. Lewandowski, J. M. McGuirk, E. A. Cornell, *Phys. Rev. A* **66**, 053616 (2002).
13. B. DeMarco, J. L. Bohn, J. P. Burke, M. Holland, D. S. Jin, *Phys. Rev. Lett.* **82**, 4208 (1999).
14. In the experiments of (*8*), an rf transition was measured, where the effect due to inhomogeneous excitations and the motion of atoms was far below their measurement precision.
15. Materials and methods are detailed in the supporting material available on *Science* Online.
16. J. Ye, H. J. Kimble, H. Katori, *Science* **320**, 1734 (2008).
17. P. J. Martin, B. G. Oldaker, A. H. Miklich, D. E. Pritchard, *Phys. Rev. Lett.* **60**, 515 (1988).
18. D. J. Wineland, W. M. Itano, *Phys. Rev. A* **20**, 1521 (1979).
19. T. Akatsuka, M. Takamoto, H. Katori, *Nat. Phys.* **4**, 954 (2008).
20. M. M. Boyd *et al*., *Phys. Rev. A* **76**, 022510 (2007).
21. R. Santra, K. V. Christ, C. H. Greene, *Phys. Rev. A* **69**, 042510 (2004).
22. S. G. Porsev, A. Derevianko, *Phys. Rev. A* **69**, 042506 (2004).
23. A. D. Ludlow *et al*., *Opt. Lett.* **32**, 641 (2007).
24. D. Leibfried, R. Blatt, C. Monroe, D. Wineland, *Rev. Mod. Phys.* **75**, 281 (2003).
25. By analyzing the spectral components in sideband spectroscopy, the longitudinal temperature can be accurately determined. Extracting the transverse temperature is more complicated; however, using time-of-flight analysis, we have confirmed that the transverse and longitudinal temperatures are identical both before and after cooling (heating).
26. S. M. Foreman *et al*., *Phys. Rev. Lett.* **99**, 153601 (2007).
27. S. G. Porsev, A. Derevianko, *Phys. Rev. A* **65**, 020701 (2002).
28. We have calculated the phase shifts, and corresponding lengths, using a model S+P potential with variable short-range shapes to change the scattering length over its full range. The short-range shape parameter varies so as to change the threshold phase and scattering length, corresponding approximately to changing the number of bound states in the potential by one. This represents the possible ranges of variation of any Sr van der Waals potential.
29. Y. N. M. de Escobar *et al*., http://arxiv.org/abs/0808.3434v1 (2008).

30. We appreciate technical contributions of T. Zelevinsky and insightful discussions with K. Gibble, W. Ketterle, M. Zwierlein, E. Cornell, and S. Kokkelmans. We acknowledge funding support from NIST, NSF, Office of Naval Research, and Defense Advanced Projects Research Agency. G.K.C. and A.D.L. are supported by National Research Council postdoctoral fellowships. J.W.T. is a JILA visiting fellow, with a permanent address: The Niels Bohr Institute, Universitetsparken 5, 2100 Copenhagen, Denmark.

Supporting Online Material

www.sciencemag.org/cgi/content/full/324/5925/360/DC1
Materials and Methods
SOM Text
Fig. S1

12 December 2008; accepted 17 February 2009
10.1126/science.1169724

Contrasting Developmental Trajectories in the Earliest Known Tetrapod Forelimbs

Viviane Callier,[1]* Jennifer A. Clack,[1] Per E. Ahlberg[2]†

Ichthyostega and *Acanthostega* are the earliest tetrapods known from multiple near-complete skeletons, with *Acanthostega* generally considered the more primitive. New material indicates differing ontogenetic trajectories for their forelimbs: In *Ichthyostega*, the pattern of muscle attachment processes on small humeri (upper arm bones) resembles that in "fish" members of the tetrapod stem group such as *Tiktaalik*, whereas large humeri approach (but fail to attain) the tetrapod crown-group condition; in *Acanthostega*, both small and large humeri exhibit the crown-group pattern. We infer that *Ichthyostega* underwent greater locomotory terrestrialization during ontogeny. The newly recognized primitive characteristics also suggest that *Ichthyostega* could be phylogenetically more basal than *Acanthostega*.

The fish-tetrapod transition involved at least partial terrestrialization of the adult stage, but reproduction probably remained aquatic, which suggests that terrestrialization became a component of ontogeny. We present ontogenetic data from humeri of *Ichthyostega* and *Acanthostega*, the only Devonian tetrapods known from articulated limbs and multiple isolated limb bones.

Three presumed subadult humeri from a single locality belong to articulated postcrania showing *Ichthyostega* autapomorphies such as large flanged ribs and a semilunate ulna with a large olecranon process. They are ~40 to 45 mm in length (Fig. 1), and one shows incomplete ossification of the muscle attachment processes, a characteristic juvenile trait (fig. S1, "humerus b"). Six larger examples from different localities, up to 70 mm in length, represent four apparently adult individuals of the two species *I. stensioei* and *I. eigili* (*1*), including two previously figured (*2*). The large humeri are all quite similar, which suggests that species-specific differences are minor. For *Acanthostega gunnari* (*3*), four humeri from three individuals, between 32 and 48 mm long measured from the head to the distal end of the ectepicondyle, are available from the monospecific mass occurrence on

[1]University Museum of Zoology Cambridge, Downing Street, Cambridge CB2 3EJ, UK. [2]Subdepartment of Evolutionary Organismal Biology, Department of Physiology and Developmental Biology, Evolutionary Biology Centre, Uppsala University, Norbyvägen 18A, 752 36 Uppsala, Sweden.

*Present address: Department of Biology, Duke University, Durham, NC 27708, USA.

†To whom correspondence should be addressed. E-mail: per.ahlberg@ebc.uu.se

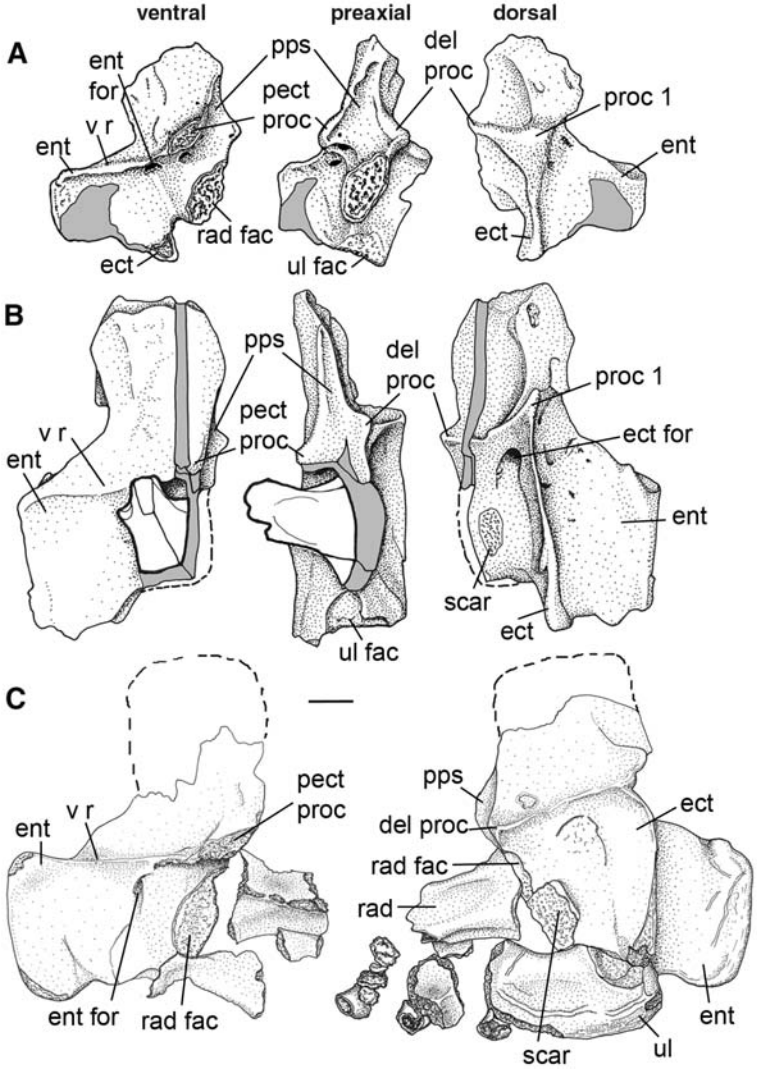

Fig. 1. Adult and subadult humeri of *Ichthyostega* drawn to the same scale. (**A**) Left to right: Specimen MGUH 29017a, left humerus in ventral, preaxial (anterior), and dorsal views, based on exposed region of specimen and CT scan model (the preaxial view shows more of the ventral surface than does the corresponding view in Fig. 4C). (**B**) Left to right: Specimen MGUH VP 6115, left humerus in ventral, preaxial, and dorsal views. Thick outline shows impacted radius, which obscures the entepicondylar foramen. (**C**) Specimen MGUH VP 6138, right humerus, reversed, in ventral (left) and dorsal (right) views, drawn from latex peels of part and counterpart. Radius, ulna, and metacarpals are also present. This humerus is very flattened, with the ectepicondyle compressed into a posterior orientation. Gray infill represents broken or missing bone (a saw cut in MGUH VP 6115). MGUH, Geological Museum, Copenhagen; VP, Vertebrate Palaeontology; del, deltoid; ect, ectepicondyle; ent, entepicondyle; fac, facet; for, foramen; pect, pectoral; pps, prepectoral space; proc, process; rad, radius/radial; ul, ulna/ulnar; v r, ventral ridge. Scale bar, 10 mm.

Stensiö Bjerg (East Greenland) (Fig. 2). In both the *Ichthyostega* and *Acanthostega* material, there is incongruence between size and ontogenetic state that presumably implies either individual or sexual variation in growth patterns. Given this and the small sample size, we are not able to reconstruct real ontogenetic series from our specimens, but we nonetheless feel confident that the consistent differences between small and large humeri of each genus provide ontogenetic information. To avoid confusing taphonomic distortion with genuine shape differences, we have focused our comparisons exclusively on the relative positions of landmarks, disregarding overall shape criteria such as length/breadth ratios that are highly susceptible to the effects of distortion (*4*).

The most important ontogenetic change in *Ichthyostega* concerns the pectoral process ["process 6" of (*2*)] and the associated oblique ventral ridge that is pierced by three foramina (the entepicondylar foramen and two slightly smaller and more proximally positioned openings) whose relative size is reduced in adults relative to subadults. The oblique ventral ridge in Tetrapodomorpha primitively traces a diagonal course across the ventral surface of the humerus and is pierced by several large foramina; this is the condition in all known "fish" tetrapodomorphs including *Eusthenopteron* (*5*), *Panderichthys* (*6*, *7*), and *Tiktaalik* (*8*) (Fig. 3). Previous authors have identified the proximal end of the oblique ridge as the pectoral process in most of these taxa (*5*, *6*), including the isolated humerus ANSP 21350 from the Late Devonian Catskill Formation of Pennsylvania (*9*). However, the subadult *Ichthyostega* specimens MGUH (Geological Museum, Copenhagen) 29018, 29017a, and 29017b show that the highly prominent pectoral process forms in the middle part of the ridge (Fig. 1).

The position of the pectoral process of *Ichthyostega* near the middle of the oblique ridge implies that the supposed pectoral processes of "osteolepiforms," *Panderichthys*, and ANSP 21350 have all been incorrectly identified (*5*, *6*, *9*) at the proximal end of the ridge. In *Panderichthys* (*6*, *7*) and *Tiktaalik* (*8*), the pectoral process is absent, although the height of the ridge is greatest around the middle. In the context of the new specimens, we are able to identify the pectoral process in ANSP 21350 as a weakly developed process in the highest middle part of the ridge (a slightly raised plateau where the ridge crest broadens) (Fig. 3).

In the small *Ichthyostega* humeri, the pectoral process lies some distance from the preaxial margin of the bone and from the radial facet. A triangular, anteroventrally facing area, which we designate the prepectoral space, is developed between the preaxial margin of the bone and the proximal limb of the ridge (Fig. 1 and Fig. 4). By contrast, in large *Ichthyostega* humeri such as MGUH VP 6115, the pectoral process is in a more anterodistal position closer to the preaxial edge and to the radial facet, and the prepectoral space is less than one-third of its former width. Both the distal and anterior components of the positional shift are specific to the pectoral process and oblique ridge, resulting in changed positions relative to the radial facet and deltoid process. The shift is thus not simply an effect of a growth gradient across the whole bone, but the result of local morphogenetic processes leading to the displacement of one specific landmark relative to neighboring landmarks. We are confident that it is not the result of taphonomic distortion.

An ontogenetic change that may be functionally related can be seen in the shoulder girdle. In adult girdles, a posterodorsal supraglenoid process (*2*) carries an anterolaterally facing extension of the glenoid surface that appears to form a locking contact for a posteriorly facing extension of the articular head of the humerus. This process is absent on the glenoid associated with the subadult humerus MGUH 29017a (Fig. 3).

In *Acanthostega*, the ontogenetic pattern of the humerus is different. In UMZC (University Museum of Zoology Cambridge) T.1295, the supinator process has not yet developed, the bony bridge over the ectepicondylar canal has not yet formed, and the posterior margin of the entepicondyle is unossified; it is therefore the least mature (though not the smallest) humerus. The other humeri are fully ossified. In all specimens, the pectoral process is adjacent to the preaxial margin of the humerus where it forms part of a deltopectoral crest (Figs. 2 and 4), reflecting the absence of the prepectoral space. As in more crownward tetrapods (*10*–*13*), the oblique ridge in *Acanthostega* has no proximal limb but ends at the pectoral process. The distal limb of the ridge is low and rounded, and it is pierced only by the entepicondylar foramen. In large specimens, the proximal part of the humeral shaft is proportionately longer and the deltopectoral crest is more distally positioned (Fig. 2). However, unlike in *Ichthyostega*, there is no movement of the different processes relative to each other; the distal displacement of the deltopectoral crest is matched by a similar displacement of the supinator process.

The most remarkable contrast between the ontogenetic transformations of *Ichthyostega* and *Acanthostega* is that the former appears to mirror the phyletic transformation of the humerus while the latter does not. The anterodistal ontogenetic shift of the pectoral process in *Ichthyostega* is directly comparable to the phyletic transformation of the oblique ventral ridge complex (Fig. 4). *Tiktaalik* and ANSP 21350, whose pectoral process (ANSP 21350) or highest part of the ridge (*Tiktaalik*) is located centrally on the ventral face of the humerus, both show a well-developed prepectoral space, wider than that in *Ichthyostega*; *Acanthostega* and post-Devonian stem and crown tetrapods (*10*–*13*), whose pectoral processes are

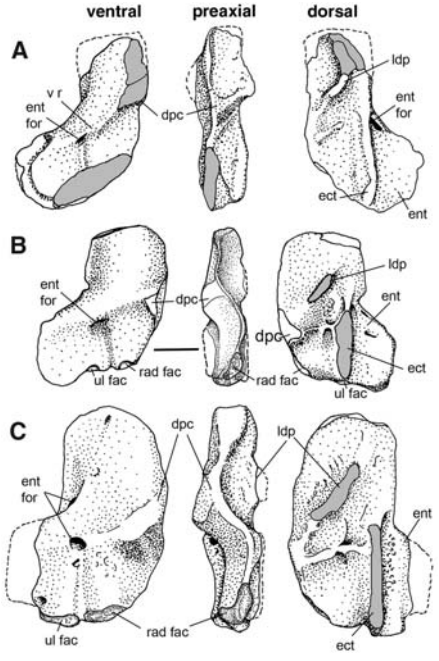

Fig. 2. Humeri of *Acanthostega* showing subadult and adult specimens, drawn to the same scale as Fig. 1. (**A**) Left to right: Specimen UMZC T.1295, left humerus in ventral, preaxial, and dorsal views. (**B**) Left to right: Specimen MGUH 29019, left humerus in ventral, preaxial, and dorsal views. Ventral and preaxial views incorporate information from the CT model and information from the right humerus of the same individual. (**C**) Left to right: Specimen MGUH 29020, right humerus; drawing is reversed for ease of comparison. An oblique, strap-shaped latissimus dorsi process is characteristic of *Acanthostega*. Gray infill shows eroded or missing bone. UMZC T., University Museum of Zoology Cambridge, Tetrapod; dpc, deltopectoral crest; ldp, latissimus dorsi process; others as in Fig. 1. Scale bar, 10 mm.

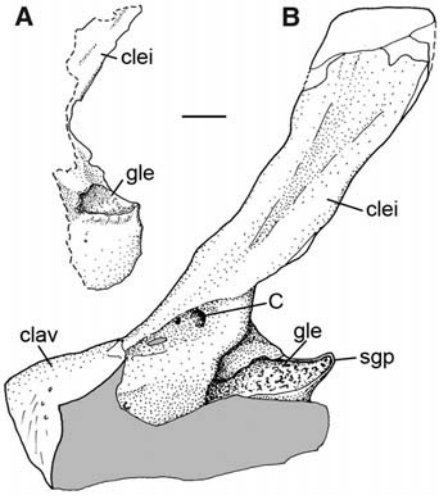

Fig. 3. Left-side pectoral girdles of *Ichthyostega*. (**A**) Specimen MGUH 29017a, subadult specimen, drawn from the CT scan model. Humerus in Fig. 1A lies adjacent to this element. (**B**) Specimen MGUH VP 6115, showing prominent supraglenoid process, absent in subadult. C, foramen C of (*3*); clav, clavicle; clei, cleithrum; gle, glenoid; sgp, supraglenoid process. Scale bar, 10 mm.

located at the preaxial margin of the humerus, are united by a synapomorphous absence of a prepectoral space. The subadult morphology of *Ichthyostega* thus reflects a more primitive condition than does the adult morphology.

The humeri of ANSP 21350 and *Acanthostega* both have a long undivided preaxial margin proximal to the junction with the oblique ridge (Fig. 4, B and E). This contrasts with *Ichthyostega*, where the oblique ridge meets the proximal end of the preaxial margin (Fig. 4, C and D). Comparisons with *Tiktaalik* (Fig. 4A), *Panderichthys*, and "osteolepiforms" suggest that *Ichthyostega* is primitive in this respect (*5*–*8*). The undivided proximal preaxial margin could thus be a synapomorphy of ANSP 21350, *Acanthostega*, and more derived tetrapods, but this conflicts with a suite of primitive characters suggesting that ANSP 21350 occupies a deep position in the phylogeny (*9*).

The emergence of a distinct pectoral process and the eventual loss of the oblique ridge probably correlated with the breakup of large muscle sheets into the discrete flexor muscles of the crown tetrapod limb. The anterodistal displacement of the process during ontogeny in *Ichthyostega* would have lengthened the pectoral muscle and marked a shift toward a stronger tendency to retract and pronate the humerus. Given the anteroventral position of the radial condyle, the long axis of the radius would be almost perpendicular to that of the humerus and would project anteroventrally. Humeral pronation would have rotated the forearm ventrally-posteriorly and thus both lifted the body off the ground and contributed to the stride. The development of the supraglenoid process in adults probably enabled the humerus to "lock" against the glenoid at maximal retraction and pronation. These changes, which may correlate with increased weight-bearing capacity, occurred at a relatively late stage in ontogeny, judging by the size of the subadults described here.

In *Acanthostega*, by contrast, the only functionally important ontogenetic changes in the limb musculature seem to be a slight lengthening of the pectoral and a late development of the supinator (presumably affecting forearm mobility), whereas the radial facet remains anterodistally oriented throughout. Two things can be concluded from this. First, the forelimb of *Ichthyostega* shows a degree of ontogenetic terrestrialization, whereas no such signal can be detected in *Acanthostega*. Second, the adult humeral morphology of *Ichthyostega* develops as a modification of a more "elpistostegid"-like subadult condition at a relatively late stage in ontogeny, whereas in *Acanthostega* the essentials of the adult morphology—including derived features shared with later tetrapods—are present throughout the recorded ontogenetic span.

Both subadult and adult humeri of *Acanthostega* resemble those of post-Devonian tetrapods more than do those of *Ichthyostega*. *Acanthostega* shares with *Tulerpeton* (*10*) and later tetrapods (*11*–*13*) the presence of a deltopectoral crest, absence of the proximal limb of the oblique ridge and prepectoral space, low-to-indistinguishable distal limb of the oblique ridge, and no major foramina other than the entepicondylar foramen piercing the ridge. In contrast, even the adult *Ichthyostega* lacks a deltopectoral crest, retains the prepectoral space and the proximal limb of the oblique ridge, has a sharp and distinct crest on both limbs of the ridge, and has one large and one smaller foramen piercing the ridge alongside the entepicondylar foramen. All these features are shared with ANSP 21350, *Tiktaalik*, *Panderichthys*, and *Eusthenopteron* (*5*–*9*).

This character distribution conflicts with the current consensus that *Acanthostega* is the less crownward of the two genera (*3*, *14*, *15*). A new phylogenetic analysis incorporating these characters [(*4*), modified from (*15*)] shows only ambiguous support for the consensus topology, with *Ichthyostega* recovered below *Acanthostega* in some of the runs. Perhaps more important, the analysis reveals a curious pattern of character incongruence among the less incomplete Devonian tetrapods. *Ventastega* and *Elginerpeton* (the latter not coded for humeral characters) respectively combine apparently derived *Acanthostega*- and *Ichthyostega*-like characters with primitive "fish" characters lacking in those genera. If *Ventastega* but not *Elginerpeton* is included in a run, *Acanthostega* always falls below *Ichthyostega* in the tree; if *Elginerpeton* but not *Ventastega* is included, *Acanthostega* falls above *Ichthyostega* in more than 60% of the trees from the run in which multistate characters are not ordered (*4*). This pattern may reflect "morphological experimentation" and small-scale parallel evolution among Devonian tetrapods.

Overall, the relative phylogenetic positions of *Acanthostega* and *Ichthyostega* are best regarded as uncertain; *Ichthyostega* may well be the more

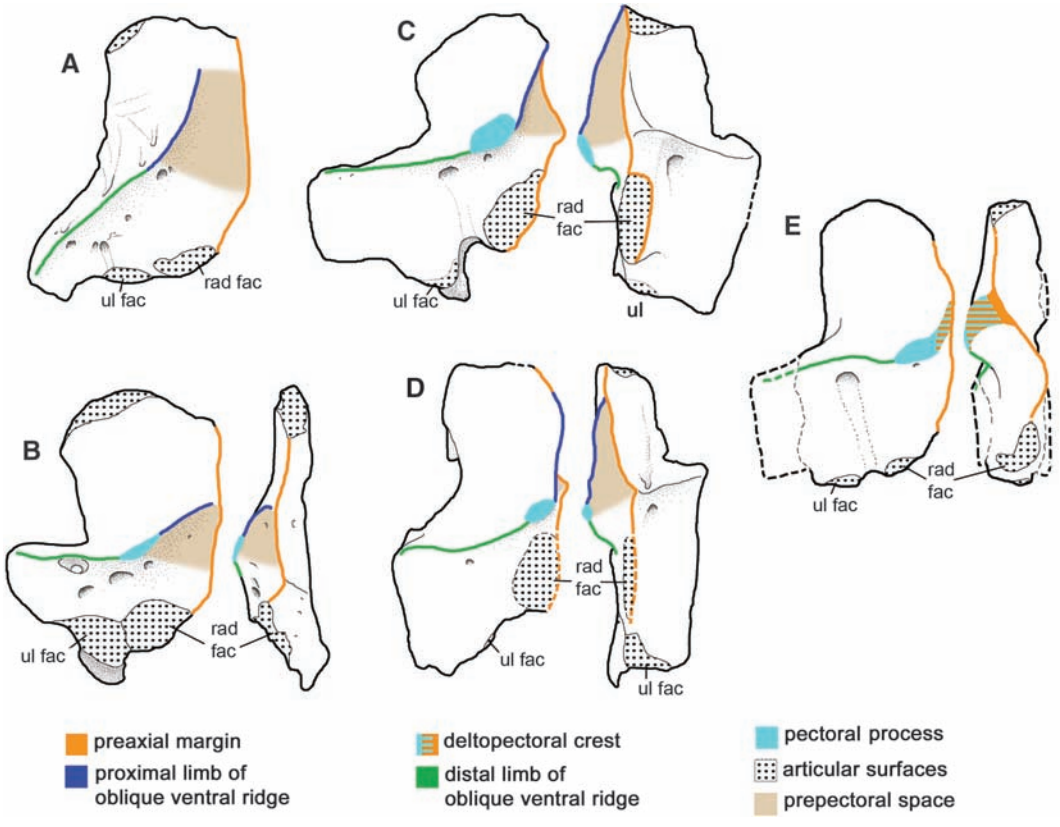

Fig. 4. Humeri of tetrapodomorphs in ventral (left) and preaxial (right) views to show oblique ventral ridge, pectoral process, and adjacent structures. (**A**) *Tiktaalik* from (*8*) (preaxial view not available). (**B**) ANSP 21350 from (*9*). (**C**) Subadult *Ichthyostega* (the preaxial view shows less of the ventral surface than does the corresponding drawing in Fig. 1A). (**D**) Adult *Ichthyostega*. (**E**) Adult *Acanthostega*. Abbreviations are as in Fig. 1. Note that the prepectoral space is a concave surface, whereas the deltopectoral crest is convex.

basal of the two. Such a placement of the more terrestrially adapted *Ichthyostega* (*16*), taken together with the features indicating weight-bearing ability (ventrally facing radial and ulnar facets) of the very primitive ANSP 21350 (*9*), would suggest a scenario of rapid early terrestrialization rather different from the currently predominant "aquatic Devonian tetrapods" model.

References and Notes

1. H. Blom, *Palaeontology* **48**, 111 (2005).
2. E. Jarvik, *Fossils Strata* **40**, 1 (1996).
3. M. I. Coates, *Trans. R. Soc. Edinburgh Earth Sci.* **87**, 363 (1996).
4. See supporting material on *Science* Online.
5. S. M. Andrews, T. S. Westoll, *Trans. R. Soc. Edinburgh* **68**, 207 (1970).
6. E. I. Vorobyeva, *Paleontol. J.* **34**, 632 (2000).
7. C. A. Boisvert, E. Mark-Kurik, P. E. Ahlberg, *Nature* **456**, 636 (2008).
8. N. H. Shubin, E. B. Daeschler, F. A. Jenkins, *Nature* **440**, 764 (2006).
9. N. H. Shubin, E. B. Daeschler, M. I. Coates, *Science* **304**, 90 (2004).
10. O. A. Lebedev, M. I. Coates, *Zool. J. Linn. Soc.* **114**, 307 (1995).
11. J. A. Clack, S. M. Finney, *J. Syst. Palaeontol.* **2**, 311 (2005).
12. S. J. Godfrey, *Philos. Trans. R. Soc. London Ser. B* **323**, 75 (1989).
13. R. Holmes, *Philos. Trans. R. Soc. London Ser. B* **306**, 431 (1984).
14. M. Ruta, M. I. Coates, D. L. J. Quicke, *Biol. Rev. Cambridge Philos. Soc.* **78**, 251 (2003).
15. P. E. Ahlberg, J. A. Clack, E. Luksevics, H. Blom, I. Zupins, *Nature* **453**, 1199 (2008).
16. P. E. Ahlberg, J. A. Clack, H. Blom, *Nature* **437**, 137 (2005).

17. We thank the Geological Museum, Copenhagen, for the loan of specimens; the staff of the University of Texas CT unit for scanning MGUH f.n. 301a; N. Shubin for access to the *Tiktaalik* material; and E. Rayfield for help with the Amira modeling software. Supported by a Churchill Fellowship from the Winston Churchill Foundation (V.C.) and by Vetenskapsrådet (the Swedish Research Council) (P.E.A.).

Supporting Online Material

www.sciencemag.org/cgi/content/full/324/5925/364/DC1
Materials and Methods
SOM Text
Figs. S1 to S4
Table S1
Movie S1
References

22 October 2008; accepted 5 March 2009
10.1126/science.1167542

A Ferroelectric Oxide Made Directly on Silicon

Maitri P. Warusawithana,[1] Cheng Cen,[2] Charles R. Sleasman,[2] Joseph C. Woicik,[3] Yulan Li,[4] Lena Fitting Kourkoutis,[5] Jeffrey A. Klug,[6] Hao Li,[7] Philip Ryan,[8] Li-Peng Wang,[9,10] Michael Bedzyk,[6,11] David A. Muller,[5] Long-Qing Chen,[4] Jeremy Levy,[2] Darrell G. Schlom[1]*

Metal oxide semiconductor field-effect transistors, formed using silicon dioxide and silicon, have undergone four decades of staggering technological advancement. With fundamental limits to this technology close at hand, alternatives to silicon dioxide are being pursued to enable new functionality and device architectures. We achieved ferroelectric functionality in intimate contact with silicon by growing coherently strained strontium titanate ($SrTiO_3$) films via oxide molecular beam epitaxy in direct contact with silicon, with no interfacial silicon dioxide. We observed ferroelectricity in these ultrathin $SrTiO_3$ layers by means of piezoresponse force microscopy. Stable ferroelectric nanodomains created in $SrTiO_3$ were observed at temperatures as high as 400 kelvin.

For decades, semiconductor device designers have envisioned numerous devices using ferroelectrics in combination with semiconductors. These concepts include nonvolatile memories (*1*, *2*), "smart" transistors that can be used as temperature or pressure sensors (*3*), and ferroelectric field-effect transistors whose logic states require no power to maintain (*4*, *5*). Missing, however, has been the ability to integrate ferroelectrics directly with mainstream semiconductors. Our work bridges this gap, demonstrating ferroelectric functionality in a $SrTiO_3$ thin film grown directly, without any intermediate layers and free of reaction, on the workhorse of semiconductor technology, silicon.

Recent work has explored ways to use epitaxial strain to induce or enhance ferroelectricity in thin films (*6*–*8*). Ferroelectric responses that are distinct from naturally occurring bulk ferroelectrics have also been obtained through the growth of nano-engineered superlattices containing different dielectric and ferroelectric phases (*9*–*11*). In all of the above-referenced studies, the substrate and film are isostructural. For commensurate $SrTiO_3$/(001) Si, the interface is structurally far more complex, connecting a diamond structure (silicon) with a perovskite ($SrTiO_3$) (Fig. 1). The high reactivity of silicon with many elements and their oxides (*12*) presents a formidable challenge to the integration of functional oxides with silicon, as does the tendency of a pristine silicon surface to rapidly form its own oxide.

Using molecular beam epitaxy (MBE), we have deposited epitaxial $SrTiO_3$ films on (001) Si substrates via a kinetically controlled growth process (*13*, *14*) (fig. S1), which synchrotron diffraction measurements reveal to be commensurately strained up to a thickness of ~24 Å. The growth method used differs substantially from those reported previously (*15*–*17*) for the epitaxial integration of $SrTiO_3$ with silicon (*13*) (figs. S1 and S2). Although bulk $SrTiO_3$ is not ferroelectric at any temperature, the large compressive strain (~1.7%) induced on commensurately strained $SrTiO_3$/Si is predicted to result in ferroelectricity (*13*, *18*) with a Curie temperature (T_C) near room temperature (fig. S3 and table S1) and an out-of-plane polarization (*6*, *8*, *19*). Films whose thickness exceeds the equilibrium critical thickness (*20*), however, are unstable to relaxation, which would lower the transition temperature and produce nanoscale heterogeneity.

We discuss data from five $SrTiO_3$ films identified by their nominal thickness in molecular layers (ML): 5 ML, 6 ML, 8 ML, 10 ML, and 20 ML. These $SrTiO_3$ films were grown on (001) Si substrates by MBE, in layers of one to a few molecular strata at a time, until the desired thickness was reached (*13*). The silicon substrates used in this study were doped with n-type phosphorus (1×10^{15} to 5×10^{15} phosphorus atoms/cm^3) having a resistivity of 1 to 4 ohm·cm. Each layer that was grown involved a controlled sequence of

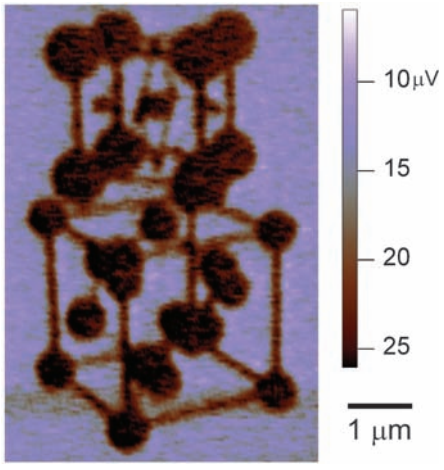

Fig. 1. Structure of the $SrTiO_3$/Si interface, written and imaged on a 6 ML $SrTiO_3$/Si sample by PFM. With the 45° in-plane rotational offset between the unit cells (*15*), the epitaxial orientation relationship is (001) $SrTiO_3$ // (001) Si and [110] $SrTiO_3$ // [100] Si.

[1]Department of Materials Science and Engineering, Cornell University, Ithaca, NY 14853, USA. [2]Department of Physics and Astronomy, University of Pittsburgh, Pittsburgh, PA 15260, USA. [3]National Institute of Standards and Technology, Gaithersburg, MD 20899, USA. [4]Department of Materials Science and Engineering, Pennsylvania State University, University Park, PA 16802, USA. [5]School of Applied and Engineering Physics, Cornell University, Ithaca, NY 14853, USA. [6]Department of Physics and Astronomy, Northwestern University, Evanston, IL 60208, USA. [7]Applied Research and Technology Center, Motorola Inc., Tempe, AZ 85284, USA. [8]Ames Laboratory, Ames, IA 50011, USA. [9]Intel Corporation, Santa Clara, CA 95052, USA. [10]TricornTech, San Jose, CA 95129, USA. [11]Department of Materials Science and Engineering, Northwestern University, Evanston, IL 60208, USA.

*To whom correspondence should be addressed. E-mail: schlom@cornell.edu

steps (*13*, *14*) that kinetically suppress the oxidation of the substrate and reduce the tendency of the film to form islands (*21*) (fig. S4).

X-ray diffraction reveals the structural quality and strain relaxation that occurs in the $SrTiO_3$ films as thickness is increased. Rocking curves in ω [where the angle of incidence (θ) between the x-ray beam and the sample is rocked while leaving the detector position (2θ) fixed] of the out-of-plane $SrTiO_3$ 002 reflection are shown in Fig. 2A. Each curve displays an intense and narrow central peak due to coherently strained $SrTiO_3$ on top of a broad background peak (*13*). The height of the sharp central peak in relation to the background on this log intensity scale gives an indication of the fraction of the $SrTiO_3$ film that is coherently strained. The coherently strained fraction of the $SrTiO_3$ films decreases as the film thickness is increased. The full width at half maximum (FWHM) of the 5 ML sample, 0.012°, is representative of the sharpness of the coherent peaks (fig. S5).

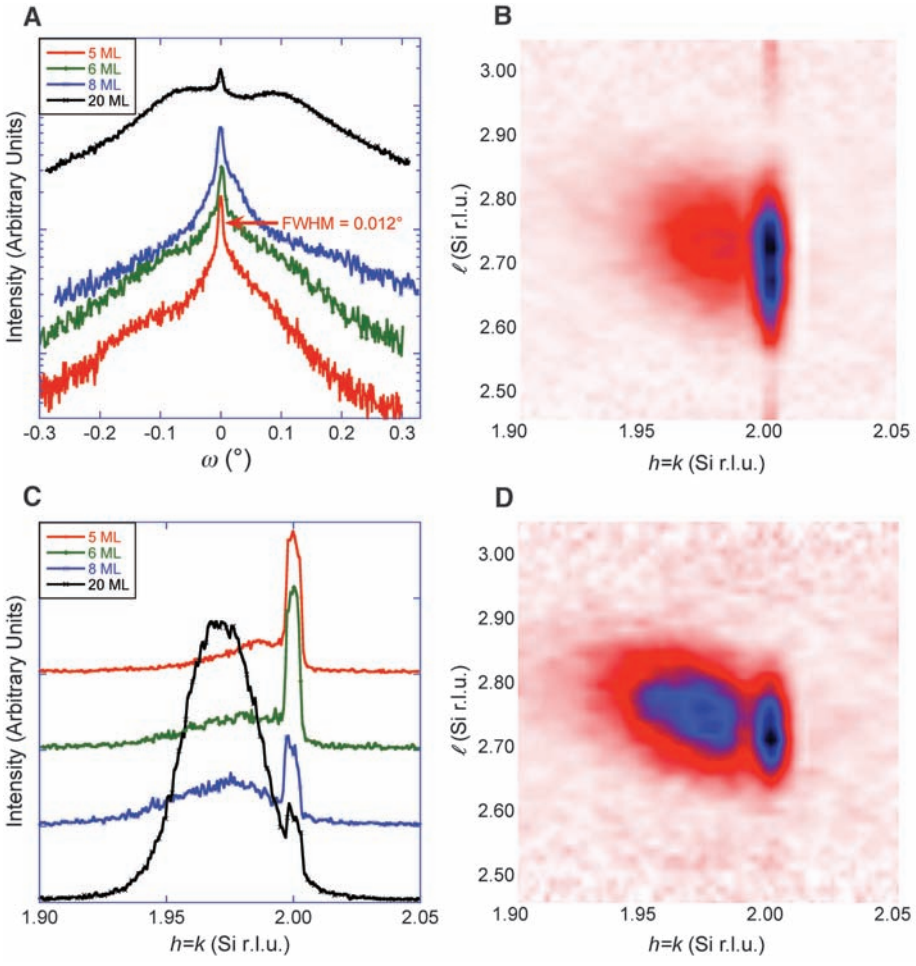

Fig. 2. The strain state of the $SrTiO_3$ films revealed by x-ray diffraction. (**A**) Rocking curves in ω of the out-of-plane $SrTiO_3$ 002 reflection. (**B**) Reciprocal space map of the 202 $SrTiO_3$ peak for the 6 ML sample. Note the beating along the ℓ direction. (**C**) Off-axis scans through the 202 $SrTiO_3$ peak. (**D**) Reciprocal space map of the 202 $SrTiO_3$ peak for the 8 ML sample. In (B) and (D), the intensity increases from white to red to blue to black.

We used x-ray diffraction to determine the in-plane strain of the $SrTiO_3$ films (*13*, *22*). Because the out-of-plane lattice constant of $SrTiO_3$ is distinct from that of silicon, the in-plane lattice constant of $SrTiO_3$ can be obtained by measuring an off-axis $SrTiO_3$ reflection where there is no overlap with a substrate peak. Figure 2C shows scans made through the $SrTiO_3$ 202 peak for the 5 ML, 6 ML, 8 ML, and 20 ML samples. The sharp peak observed at $h = k = 2.00$ Si reciprocal lattice units (r.l.u.) is due to the commensurate portion of the $SrTiO_3$ films with in-plane lattice constant = $a_{Si}/\sqrt{2} = 3.840$ Å. As the film thickness increases, the relative integrated intensity of the sharp peak decreases while that of a broad peak at $h = k < 2.00$ Si r.l.u. increases. The plot clearly shows the transition from mostly commensurate $SrTiO_3$ to mostly relaxed $SrTiO_3$ as the film thickness is increased. Reciprocal space maps of the $SrTiO_3$ 202 peak for the 6 ML and 8 ML samples are shown in Fig. 2, B and D, respectively. The 6 ML sample (Fig. 2B) has its diffracted intensity mostly centered at $h = k =$ 2.00 Si r.l.u., whereas for the 8 ML sample (Fig. 2D), more spectral weight is observed at lower values of $h = k$ (i.e., at larger in-plane lattice constants) because of relaxation of the $SrTiO_3$. The reciprocal space map for the 8 ML sample also shows how the spectral weight tails off to higher ℓ with smaller $h = k$ as strain relaxation sets in. From ℓ scans made across the coherent peak at $h = k = 2.00$ Si r.l.u., we find that the coherent peak occurs at $\ell \sim 2.71$ Si r.l.u.

To check for ferroelectricity in these strained $SrTiO_3$/(001) Si films, we used piezoresponse force microscopy (PFM), a technique that has been demonstrated on ferroelectric films as thin as 28 Å (*23*–*26*). With strain relaxation occurring for $SrTiO_3$/(001) Si film thickness as small as 8 ML (~32 Å), measurement of the piezoelectric

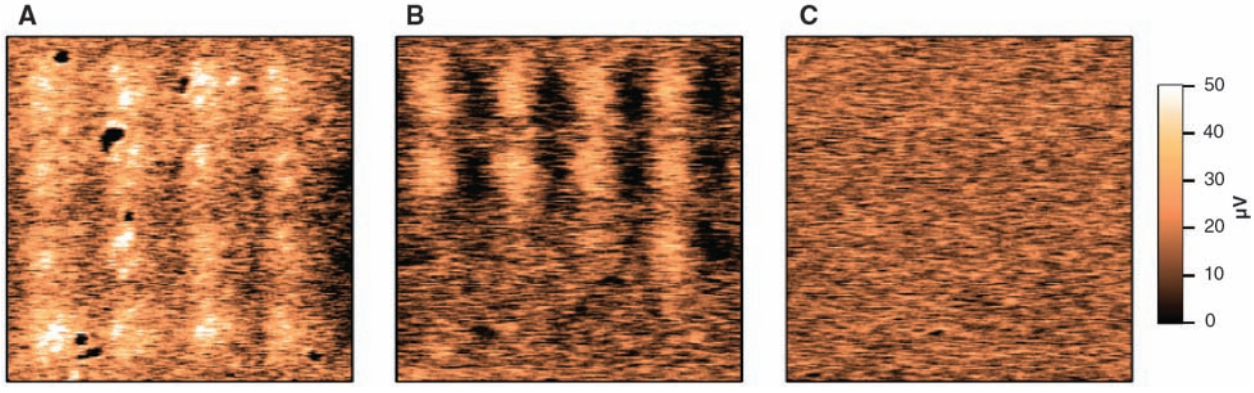

Fig. 3. PFM images (1 μm by 1 μm) of a 4 × 4 pattern of domains written on the 5 ML $SrTiO_3$/Si sample at different temperatures. (**A**) $T = 298$ K. (**B**) $T = 314$ K. (**C**) $T = 323$ K.

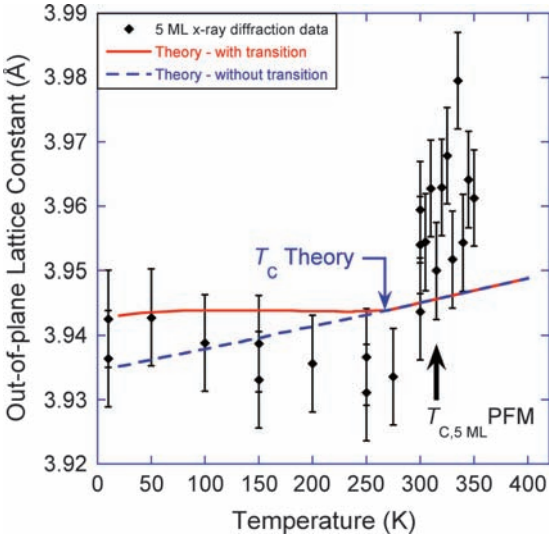

Fig. 4. Temperature dependence of the out-of-plane lattice constant of $SrTiO_3$ strained commensurately to the underlying silicon substrate. Theoretical prediction from thermodynamic analysis is shown, along with experimental data obtained from x-ray diffraction measurements of the 5 ML sample. The error bars reflect the maximum error expected considering systematic errors and variation in sample thickness. Some hysteresis between data taken on heating and cooling is evident. Also indicated is the transition temperature observed from PFM measurements for the 5 ML sample ($T_{C,5\ ML}$ PFM).

response of such thin layers is challenging. The large d_{33} coefficients predicted for strained $SrTiO_3$/(001) Si (fig. S6), however, make it a reasonable signal to probe. Local electric fields were applied across the $SrTiO_3$ layer by means of a biased, conducting atomic force probe, and the resulting piezoelectric response of the strained $SrTiO_3$ film was subsequently imaged using the same probe (*13*). At room temperature, we found that domains of both polarities could be patterned on the 5 ML, 6 ML, 8 ML, and 10 ML samples, but not on the 20 ML sample. Figure 1 shows a PFM image written on the 6 ML sample at room temperature. In all of the samples that exhibited ferroelectricity via piezoresponse, a preferred downward polarization was observed (fig. S7). This agrees with reported x-ray fine structure measurements (*27*) and indicates that strained $SrTiO_3$ films on (001) Si are prepoled in their as-grown state. The lack of observable ferroelectricity in the 20 ML sample is consistent with x-ray diffraction measurements showing that the 20 ML sample is mainly relaxed (Fig. 2C) and helps rule out other possible mechanisms, such as changes in surface chemistry, for the observed piezoelectric response in other samples. A retention study of the written domains was also carried out for the 6 ML sample at room temperature (*13*) (figs. S8 and S9). The domain pattern was observed to be stable over a 72-hour period, at which point the pattern was erased by rastering the atomic-force probe with a constant voltage over the patterned area.

PFM measurements performed as a function of temperature revealed a rather sharp phase transition, above which ferroelectric domains are unstable. Figure 3 shows a series of three PFM measurements made on the 5 ML sample at different temperatures. Each image was acquired ~30 min after writing a 4 × 4 array of square domains. Although some features that are associated with imperfections on the sample surface also showed up on these images, at T = 298 K each of the 16 domains could be observed (Fig. 3A). The temperature was increased, and at T = 314 K only 9 of the 16 domains could be seen (Fig. 3B). The existence of a single domain on the third row from the top rules out a variety of possible measurement artifacts, such as a "wandering" cantilever resonance frequency. At T = 323 K (Fig. 3C) or at higher temperatures, no stable domains could be observed. These PFM measurements provide a lower bound on the paraelectric-to-ferroelectric transition temperature (T_C): $T_{C,5\ ML} > 314$ K.

Measurements performed on the 6 ML sample, however, show that ferroelectric domains written on it are stable at even higher temperatures: $T_{C,6\ ML} > 410$ K (fig. S10). Such temperatures are much higher than that predicted by thermodynamic analysis (fig. S3). The theoretical calculation assumes an infinitely thick $SrTiO_3$ slab with complete polarization charge screening and with a uniform biaxial compressive strain equivalent to that obtained by growing commensurately strained $SrTiO_3$ on (001) Si. By leaving out surface effects such as structural and electronic discontinuities and the possibility of incomplete screening of the polarization charge, the thermodynamic analysis does not take into account the finite film thickness, which presumably would lead to a substantially reduced transition temperature, as has been shown for the related ferroelectrics $PbTiO_3$ (*28*) and $BaTiO_3$ (*29*). Thus, the observed experimental results indicate a substantially higher transition temperature than that predicted by theory. In the case of a metal in contact with a ferroelectric (*30*, *31*), polarization screening at the interface has been shown to enhance the ferroelectric T_C. Screening of the polarization charge as well as structural and electronic discontinuities at this heteroepitaxial $SrTiO_3$/Si interface, not considered in the present thermodynamic analysis, could play a role in understanding the quantitative differences between experiment and theory.

As an independent check of the ferroelectric phase transition, temperature-dependent x-ray diffraction measurements of the out-of-plane lattice constant were performed on the 5 ML sample (Fig. 4) to sense the structural transition (*7*, *8*, *32*) that should coincide with T_C. The average out-of-plane lattice constant was extracted from scans made of the $SrTiO_3$ 002 peak. With the in-plane lattice constant clamped to the silicon substrate and changing only by the thermal expansion of silicon, which is much smaller than that of $SrTiO_3$, the out-of-plane lattice constant should continuously expand with temperature in the absence of a structural transition. The measured out-of-plane lattice constant with temperature for the 5 ML sample shows a clear deviation from what is expected for thermal expansion with the in-plane lattice constant constrained to that of silicon. This deviation coincides in temperature with the transition temperature observed by PFM. The "kink" feature observed in the out-of-plane lattice constant with temperature (*7*, *8*, *32*) is qualitatively consistent with thermodynamic analysis of commensurate $SrTiO_3$/Si undergoing a ferroelectric transition (Fig. 4), although the agreement with T_C is likely to be coincidental.

A ferroelectric in direct contact with silicon invites hybrid ferroelectric-semiconductor devices (*1*–*5*). Although the low or almost nonexistent conduction band offset predicted (*33*) and measured (*34*) between $SrTiO_3$ and silicon could lead to practical difficulties in implementing such ferroelectric devices, it has been proposed that this problem can be overcome by carefully constructing the interface between $SrTiO_3$ and silicon (*35*, *36*).

References and Notes

1. M. Suzuki, *J. Ceram. Soc. Jpn. Int. Ed.* **103**, 1088 (1995).
2. P. Vettiger, G. Binnig, *Sci. Am.* **288**, 47 (January 2003).
3. Y.-R. Wu, J. Singh, *IEEE Trans. Electron. Dev.* **52**, 284 (2005).
4. J. A. Morton, U.S. Patent 2,791,761 (7 May 1957).
5. L. L. Chang, L. Esaki, *IBM Tech. Discl. Bull.* **14**, 1250 (1971).
6. J. H. Haeni *et al.*, *Nature* **430**, 758 (2004).
7. K. J. Choi *et al.*, *Science* **306**, 1005 (2004).
8. D. G. Schlom *et al.*, *Annu. Rev. Mater. Res.* **37**, 589 (2007).
9. M. P. Warusawithana, E. V. Colla, J. N. Eckstein, M. B. Weissman, *Phys. Rev. Lett.* **90**, 036802 (2003).
10. D. A. Tenne *et al.*, *Science* **313**, 1614 (2006).
11. E. Bousquet *et al.*, *Nature* **452**, 732 (2008).
12. K. J. Hubbard, D. G. Schlom, *J. Mater. Res.* **11**, 2757 (1996).
13. See supporting material on *Science* Online.
14. H. Li *et al.*, *J. Appl. Phys.* **93**, 4521 (2003).
15. H. Mori, H. Ishiwara, *Jpn. J. Appl. Phys.* **30**, L1415 (1991).
16. R. A. McKee, F. J. Walker, M. F. Chisholm, *Phys. Rev. Lett.* **81**, 3014 (1998).
17. Z. Yu *et al.*, *J. Vac. Sci. Technol. B* **18**, 2139 (2000).
18. A. Antons, J. B. Neaton, K. M. Rabe, D. Vanderbilt, *Phys. Rev. B* **71**, 024102 (2005).
19. N. A. Pertsev, A. K. Tagantsev, N. Setter, *Phys. Rev. B* **61**, R825 (2000).
20. J. W. Matthews, A. E. Blakeslee, *J. Cryst. Growth* **27**, 118 (1974).
21. L. F. Kourkoutis *et al.*, *Phys. Rev. Lett.* **100**, 036101 (2008).
22. J. C. Woicik *et al.*, *Phys. Rev. B* **73**, 024112 (2006).
23. C. H. Ahn *et al.*, *Science* **276**, 1100 (1997).
24. T. Tybell, C. H. Ahn, J. M. Triscone, *Appl. Phys. Lett.* **72**, 1454 (1998).
25. T. Tybell, C. H. Ahn, J. M. Triscone, *Appl. Phys. Lett.* **75**, 856 (1999).

26. C. Lichtensteiger *et al.*, *Appl. Phys. Lett.* **90**, 052907 (2007).
27. J. C. Woicik *et al.*, *Phys. Rev. B* **75**, 140103(R) (2007).
28. D. D. Fong *et al.*, *Science* **304**, 1650 (2004).
29. J. Junquera, P. Ghosez, *Nature* **422**, 506 (2003).
30. P. Ghosez, K. M. Rabe, *Appl. Phys. Lett.* **76**, 2767 (2000).
31. M. Stengel, D. Vanderbilt, N. A. Spaldin, http://arxiv.org/abs/0811.0632 (2008).
32. E. D. Specht, H.-M. Christen, D. P. Norton, L. A. Boatner, *Phys. Rev. Lett.* **80**, 4317 (1998).
33. J. Robertson, C. W. Chen, *Appl. Phys. Lett.* **74**, 1168 (1999).
34. S. A. Chambers, Y. Liang, Z. Yu, R. Droopad, J. Ramdani, *J. Vac. Sci. Technol. A* **19**, 934 (2001).
35. J. Junquera, M. Zimmer, P. Ordejón, P. Ghosez, *Phys. Rev. B* **67**, 155327 (2003).
36. C. J. Först, C. R. Ashman, K. Schwarz, P. E. Blöchl, *Nature* **427**, 53 (2004).

37. We thank C. H. Ahn, O. Auciello, V. Gopalan, D. A. Tenne, and F. J. Walker for stimulating discussions and interactions during the course of this work. Supported by Office of Naval Research grant N00014-04-1-0426 (M.P.W., L.F.K., D.A.M., and D.G.S.), NSF grants DMR-0507146 and DMR-0704022, Materials Research Science and Engineering Center program grants DMR-0520404, DMR-0520513, and DMR-0820404, and, for the work performed at Argonne National Laboratory, the U.S. Department of Energy, Basic Energy Sciences, Materials Sciences. Diffraction data were taken at sector 33BM of the Advanced Photon Source, which is supported by the U.S. Department of Energy, Basic Energy Sciences, Office of Science under contract W-31-109-ENG-38.

Supporting Online Material

www.sciencemag.org/cgi/content/full/324/5925/367/DC1
Materials and Methods
SOM Text
References
Figs. S1 to S10
Table S1

11 December 2008; accepted 26 February 2009
10.1126/science.1169678

Anomalous Fractionations of Sulfur Isotopes During Thermochemical Sulfate Reduction

Yumiko Watanabe,[1]* James Farquhar,[2] Hiroshi Ohmoto[1]

Anomalously fractionated sulfur isotopes in many sedimentary rocks older than 2.4 billion years have been widely believed to be the products of ultraviolet photolysis of volcanic sulfur dioxide in an anoxic atmosphere. Our laboratory experiments have revealed that reduced-sulfur species produced by reactions between powders of amino acids and sulfate at 150° to 200°C possess anomalously fractionated sulfur isotopes: $\Delta^{33}S$ = +0.1 to +2.1 per mil and $\Delta^{36}S$ = −1.1 to +1.1 per mil. These results suggest that reactions between organic matter in sediments and sulfate-rich hydrothermal solutions may have produced anomalous sulfur isotope signatures in some sedimentary rocks. If so, the sulfur isotope record of sedimentary rocks may be linked to the biological and thermal evolution of Earth in ways different than previously thought.

Large anomalous fractionations of sulfur isotopes (*1*–*5*) are present in many sedimentary rocks older than 2.4 billion years and are virtually absent in younger rocks (*6*–*10*). It has been argued that sulfur-bearing minerals [such as pyrite (FeS_2) and barite ($BaSO_4$)] in sedimentary rocks older than 2.4 billion years formed from native sulfur (S^0) and/or sulfate (SO_4^{2-}: S^{6+}) produced by ultraviolet (UV) photolysis of volcanic sulfur dioxide (SO_2) in an O_2-poor atmosphere (*6*, *8*, *10*), and thus that the record of anomalously fractionated S isotopes is evidence for the transition from an anoxic to oxic atmosphere about 2.4 billion years ago (*7*, *11*). These arguments have been based on the assumption that the only processes producing anomalously fractionated S isotopes for both $\Delta^{33}S$ and $\Delta^{36}S$ (*2*, *6*) are photochemical reactions involving gaseous S-bearing species [such as hydrogen sulfide (H_2S) and SO_2] (*6*, *12*). Laboratory experiments performed with UV photolysis of SO_2 under an O_2-free condition produced S^0 and SO_4^{2-} with large anomalous fractionations of S isotopes (*13*). A theoretical study also suggests a maximum partial pressure of oxygen (PO_2) of ~10^{-6} atm in order for the UV photolysis of SO_2 to produce S^0 and SO_4^{2-} (*14*). Here, we present experiments showing that reactions between powders of amino acids and SO_4^{2-} can also produce anomalous fractionations of S isotopes.

FeS_2, the most abundant sulfide mineral in sedimentary rocks, forms from a variety of reactions involving H_2S and Fe in sediments and solutions (*15*). Both bacterial sulfate reduction (BSR) and thermochemical sulfate reduction (TSR) using SO_4^{2-} and organic matter in waters and sediments are important in the production of H_2S

$$2(C - C^*) + SO_4^{2-} + 2H^+ \rightarrow 2CO_2 + 2C^* + H_2S \quad (1)$$

where C and C* refer, respectively, to reactive and nonreactive (residual) carbon atoms in organic compounds. This reaction typically results in positive correlations between the FeS_2 and C* contents of sedimentary rocks (*15*). The C/C* ratio and reaction rate vary depending on the type and maturation degree of organic compounds (for example, carbohydrates, hydrocarbons, amino acids, bitumen, and type I, II, and III kerogens). BSR is carried out by sulfate-reducing bacteria (SRB),

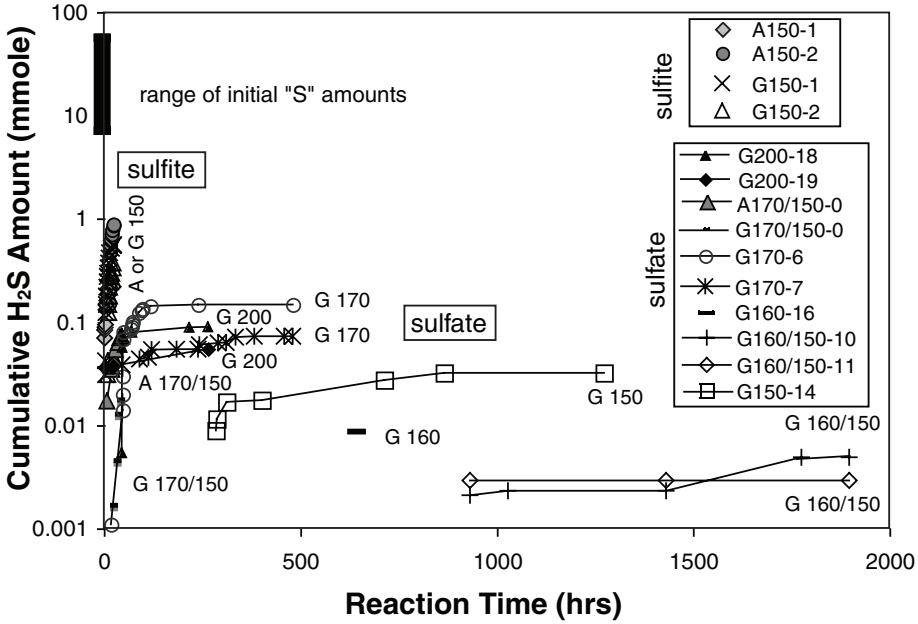

Fig. 1. Cumulative amounts of H_2S produced from SO_3^{2-} or SO_4^{2-} reductions by amino acids (alanine or glycine). Gray symbols represent the experiments using alanine (A) and solid, open, cross, or bar symbols represent those using glycine (G). The three-digit numbers (150, 160, 170, and 200) represent experiment temperatures, and the hyphenated numbers represent the run numbers.

[1]The NASA Astrobiology Institute and Department of Geosciences, Pennsylvania State University, University Park, PA 16802, USA. [2]Department of Geology and Earth System Science Interdisciplinary Center, University of Maryland, College Park, MD 20742, USA.

*To whom correspondence should be addressed. E-mail: yumiko@geosc.psu.edu

typically at temperatures (T) of ≲80°C, whereas TSR occurs at $T \gtrsim 100$°C (but possibly as low as ~80°C) without bacteria (*15*, *16*). Experiments have shown that neither BSR nor bacterial S disproportionation produce anomalously fractionated S isotopes (*4*, *17*). Most (but not all) Archean FeS_2 samples with large anomalous fractionations of S isotopes are hosted in black shales [organic carbon (C_{org}) = 1 to 15 weight percent (wt %)] with highly matured kerogen [H/C < 0.1], whereas those with no or small anomalous values are generally hosted in C_{org}-poor shales with relatively less matured kerogen (*9*, *18*). Positive correlations between FeS_2 and C_{org} contents are observed in these C_{org}-rich shales, which suggests that the FeS_2 formed by using the H_2S produced by organic SO_4^{2-} [and/or sulfite (SO_3^{2-}: S^{4+})] reduction during an early diagenetic stage (*19*). Also, shales with large anomalous fractionations of S isotopes typically exhibit various features of hydrothermal alteration at ~100° to 250°C (for example, enrichments of Zn and Cu, or O and Sr isotopic compositions of minerals) during the early diagenesis of sediments (*19*).

Previous TSR experiments used simple hydrocarbons or carbohydrates in the gas, liquid, or aqueous phase; the SO_4^{2-}source was always aqueous SO_4^{2-} (*20*). In contrast, we conducted our experiments using powders of amino acids and Na_2SO_3 or Na_2SO_4. We selected these starting materials because a recent theoretical investigation (*21*) showed that chemisorption involving a solid phase (such as kerogen) and aqueous or gaseous S-bearing species may result in the production of anomalously fractionated S isotopes. We chose amino acid powder to simulate immature (less altered) kerogen in Archean sediments because proteins (large polypeptides of amino acids) are the most abundant (55 to 75%) chemical class of the prokaryotes (such as cyanobacteria, SRB, and methanogens) that most likely dominated the Archean oceans (*22*–*24*). Although most of the proteins and amino acids must have decomposed through diagenetic and hydrothermal reactions, the presence of appreciable amounts of nitrogen even in highly matured kerogen (*25*–*27*) suggest that immature kerogen contained substantial amounts of the functional groups of amino acids. We investigated SO_3^{2-} reduction as well as SO_4^{2-}reduction because SO_3^{2-} may have been the principal oxidized S species in Archean oceans and because the $\delta^{34}S$ relations between FeS_2 and SO_4^{2-} minerals in Archean sedimentary rocks are similar to those obtained with laboratory experiments that use bacterial SO_3^{2-} reduction (*28*, *29*).

We conducted 32 series of experiments (including 103 sample analyses) at four different temperatures using five different amino acids (glycine, $C_2H_5NO_2$; alanine, $C_3H_7NO_2$; histidine, $C_6H_9N_3O_2$; arginine, $C_6H_{14}N_4O_2$; and tryptophan, $C_{11}H_{12}N_2O_2$) to investigate the influence of temperature, composition, and structure of amino acids on the rates of SO_4^{2-} or SO_3^{2-} reduction and the S isotope fractionations (table S1). A mixture of an amino acid and SO_4^{2-} or SO_3^{2-} was heated at a desired temperature with drops of H_2O to facilitate the transfers of SO_4^{2-} or SO_3^{2-} and aqueous amino acids between the solid compounds. Product H_2S was recovered as Ag_2S for determining the amounts and isotope ratios of reduced S (*30*). Each series of experiments lasted 1 to 75 days, and typically 1 to 15 mg of Ag_2S was recovered during each run (Fig. 1 and table S2). At the end of the experiments, no original well-crystallized amino acids remained in the residues. The residues consisted of water-soluble organic compounds, water- and 2N HCl–insoluble graphitized organic compounds, residual SO_4^{2-}, and reduced-S compounds other than H_2S, such as sulfide-bearing compounds (for example, Na_2S), S compounds with intermediate valences (for example, disulfide or S^0), and potential organic-S compounds. We treated the residues with a 6N-HCl solution, Cr-solution (*31*, *32*), and Kiba-solution (*33*, *34*) to successively release the various S-bearing compounds as H_2S. The amounts of H_2S released from the HCl treatment (Na_2S) were too small for weight and isotope analyses. The amounts of H_2S released with the Kiba solution, which represent the residual SO_4^{2-}, were typically more than 90% of the initial amounts of SO_4^{2-}.

Both alanine and glycine easily reduced SO_3^{2-} to H_2S at 150°C. Approximately 3 to 10% of an initial amount of SO_3^{2-} was reduced in 24 hours at average rates of ~1 to 4×10^{-3} moles of H_2S per mole of SO_3^{2-} per hour (Fig. 1). The produced H_2S possesses $\delta^{34}S$ values of –4.7 to +4.1 per mil (‰) (relative to the initial S from SO_3^{2-}) and very small $\Delta^{33}S$ values of –0.08 to +0.04‰, whereas the uncertainties [1 SD (σ)] of the $\delta^{33}S$, $\delta^{34}S$, and $\Delta^{33}S$ are within ±0.1, ±0.2, and ±0.02 ‰, respectively. The H_2S produced by alanine tended to have positive $\delta^{34}S$ and negative $\Delta^{33}S$ values, whereas that produced by glycine tended to have negative $\delta^{34}S$ and negative $\Delta^{33}S$ values (Fig. 2). These data imply that this type of SO_3^{2-} reduction does not account for the presence of the anomalously fractionated S isotopes in the Archean sedimentary rocks.

Previous researchers could not demonstrate SO_4^{2-} reduction using a variety of hydrocarbons or carbohydrates (for example, xylene, toluene, methane, and dextrose) at $T \lesssim 200$°C unless substantial amounts of H_2S and/or S^0 were added to the experimental systems; thus, H_2S and S^0 have been considered to be important catalysts of TSR at $T \lesssim 200$°C (*20*). In our experiments, SO_4^{2-} was reduced to H_2S at temperatures as low as 150°C and pH of ~6 to 7 (*30*) without the initial presence of H_2S or S^0. However, the SO_4^{2-} reduction rates from using glycine and alanine were three to four orders of magnitude slower than those from SO_3^{2-} reduction, and only about 1% (or less) of the initial SO_4^{2-} was reduced to H_2S in ~1000 hours at 150°C (Fig. 1 and table S1). The SO_4^{2-} reduction by using glycine and alanine always occurred along with a change in color of the mixture from white to black and the formation of water- and 2N HCl–insoluble graphitelike organic compounds. These results indicate that the reduction of SO_4^{2-} to H_2S was accompanied by the oxidation and polymerization of amino acids.

$\delta^{34}S$ values of H_2S produced with BSR are characteristically less than those of SO_4^{2-} by approximately 70 to 10‰: $\Delta^{34}S_{H_2S-SO_4} = \delta^{34}S_{H_2S} - \delta^{34}S_{SO_4} = -70$ to –10‰ (*15*). The $\Delta^{34}S_{H_2S-SO_4}$ for TSR by hydrocarbons at $T > 200$°C are typically around –25‰ (*15*). In contrast, the $\Delta^{34}S_{H_2S-SO_4}$ values in our experiments that used amino acids ranged from –20.8 to +5.0‰ (Fig. 3 and table S2). The difference in these $\Delta^{34}S_{H_2S-SO_4}$ values, especially the positive values, suggests different reaction pathways. These experimental observations may provide a way to distinguish between TSR and BSR in ancient and modern sedimentary environments.

$\Delta^{33}S$ values of the H_2S produced with TSR in our experiments ranged from +0.05 to +0.93‰ (+0.28 ‰ for the average) for the 44 samples, and their $\delta^{33}S/\delta^{34}S$ values ranged from 0.20 to 0.69 (table S2), as compared with the range of 0.51 ± 0.01 for the mass-dependently fractionated S isotopes (*3*, *21*). The $\delta^{34}S$ values of the residual SO_4^{2-} are within ±0.3‰ of the initial value, but

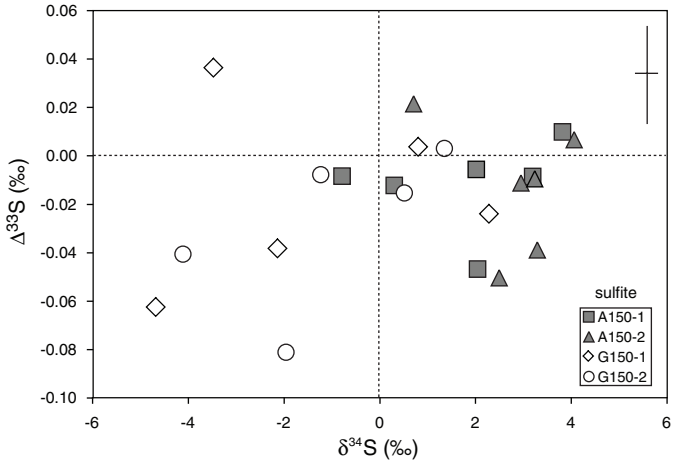

Fig. 2. $\delta^{34}S$ and $\Delta^{33}S$ values (relative to the initial SO_3^{2-}) of the H_2S produced from SO_3^{2-} reduction at 150°C. Gray symbols represent H_2S produced from experiments using alanine, and open symbols represent H_2S produced from those using glycine. Uncertainties (σ) in the $\delta^{33}S$, $\delta^{34}S$, and $\Delta^{33}S$ are within ±0.1, ±0.2, and ±0.02‰, respectively. Error bars represent the uncertainties (1 α) in the $\delta^{34}S$ and $\Delta^{33}S$ values.

the $\Delta^{33}S$ values are almost identical to that of initial SO_4^{2-} ($\Delta^{33}S = 0‰$) or only slightly shifted to negative values (–0.01 to –0.06‰) because less than a few percent of the original amount of SO_4^{2-} was reduced in our experiments.

H_2S that was extracted by the Cr solution from the residual materials of experiments performed at 170°C exhibited the largest isotope anomalies in products: $\Delta^{33}S_{t\text{-}i} = +2.06‰$, $\delta^{33}S/\delta^{34}S = 1.371$, $\Delta^{36}S_{t\text{-}i} = –1.1‰$, and $\delta^{36}S/\delta^{34}S = 1.45$ for glycine #7 series (table S2) and $\Delta^{33}S_{t\text{-}i} = +0.57‰$, $\delta^{33}S/\delta^{34}S = 0.849$, $\Delta^{36}S_{t\text{-}i} = 0.1‰$, and $\delta^{36}S/\delta^{34}S = 1.95$ for glycine #6 series (table S2). In most experiments, the Cr solution did not reduce SO_4^{2-} when reactive organic matter was absent (*31*). However, the Cr solution could reduce SO_4^{2-} to H_2S in the presence of amino acids, although slowly, when heated together at $T > 150°C$. Therefore, the H_2S released by a Cr solution of the residual materials most likely includes a contribution from the residual SO_4^{2-} as well as from the Cr-reduced S species with intermediate valence (such as disulfide or S^0). As a result, it is possible that the Cr-reduced S species in the residual materials had $\Delta^{33}S$ values of higher than +2.1‰ and $\Delta^{36}S$ values of lower than –1.1‰.

$\Delta^{36}S_{t\text{-}i}$ values for the 12 H_2S samples, which were analyzed at the University of Maryland, are both negative and positive, ranging from –0.2 to +1.1‰ with an average of approximately 0.1‰. However, compared with the analytical uncertainty of ±0.02‰ (1 σ value) for the $\Delta^{33}S$ values, the analytical uncertainty for the $\Delta^{36}S$ values was much larger (±0.2‰) because of the low abundance of ^{36}S (0.015%). Therefore, one may argue that seven of the nine H_2S samples and two of the three Cr-reduced S species samples did not possess anomalous S isotope signatures in ^{36}S. The presence of anomalously fractionated ^{33}S but not of ^{36}S may indicate that the isotope fractionations in our experimental systems were mostly governed by the magnetic isotope effects (MIEs), in which the production of S radicals affects the distributions of only the odd-numbered isotopes (*5*). However, the data on two samples, one with values of $\Delta^{36}S = +1.1‰$ and $\delta^{36}S/\delta^{34}S = 1.60$, and another with values of $\Delta^{36}S = –1.1‰$ and $\delta^{36}S/\delta^{34}S = 1.45$, cannot be explained by MIEs.

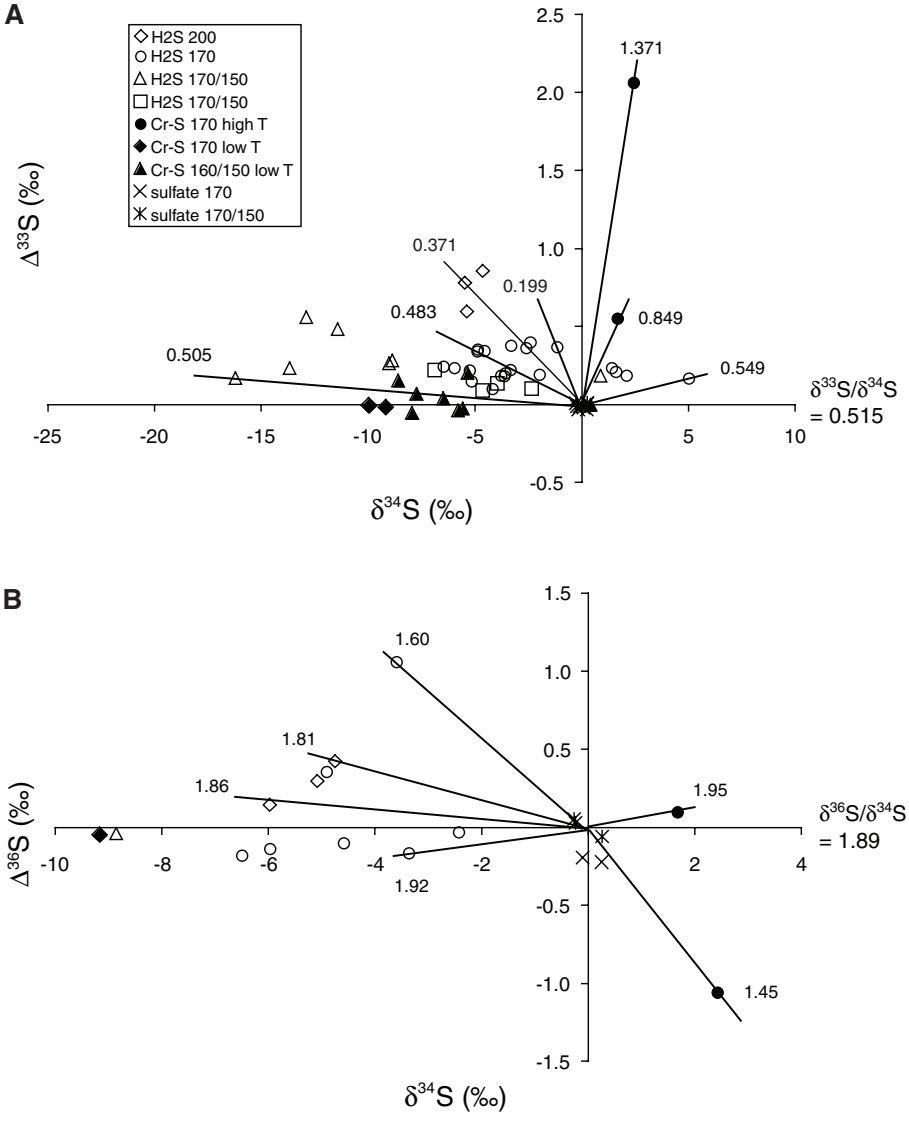

Fig. 3. (**A**) $\delta^{34}S$ versus $\Delta^{33}S$ values and (**B**) $\delta^{34}S$ versus $\Delta^{36}S$ values of the H_2S, Cr-reduced S species, and residual SO_4^{2-} from TSR experiments performed at 150° to 200°C. Open symbols represent H_2S(g) produced during the reactions, solid symbols represent Cr-reduced S species in residual solids, and crosses represent residual SO_4^{2-} extracted with Kiba solution. Numbers on each figure represent the values of $\delta^{33}S/\delta^{34}S$ (A) and $\delta^{36}/\delta^{34}S$ (B) of the experimental products. Uncertainties (1 α) in the $\delta^{33}S$, $\delta^{34}S$, and $\delta^{36}S$ values are within ±0.1, ±0.2, and ±0.4‰, respectively, but those of $\Delta^{33}S$ and $\Delta^{36}S$ values are within ±0.02 and ±0.2‰, respectively.

Lasaga *et al.* (*21*) predicted that anomalous fractionation of S isotopes may accompany heterogeneous reactions (for example, adsorption of S-bearing compounds on a solid surface) when the chemisorption energy is small (20 to 40 kJ/mole), which may cause discontinuities in the number of bound energy levels for different S isotopes. The magnitudes and signs of $\delta^{33}S$, $\delta^{34}S$, $\delta^{36}S$, $\Delta^{33}S$, and $\Delta^{36}S$ values for the adsorbed S species may vary greatly, depending on the surface bonding energy, the number of energy levels for the adsorbed S species, and other molecular characteristics. These predictions agree with our experimental data in that the $\delta^{34}S$ values of the H_2S and other reduced compounds produced from TSR varied from positive to negative and the $\Delta^{33}S$–$\Delta^{36}S$ relations of the run products varied from combinations of $+\Delta^{33}S$ and $+\Delta^{36}S$ to $+\Delta^{33}S$ and $-\Delta^{36}S$ (Fig. 3), possibly reflecting the variations in surface characteristics of the solid reactants at different parts of the reaction vessels during the experiments. This interpretation is supported by the large heterogeneity in physical and chemical characteristics of the solid run products (fig. S2). Production of the H_2S with $+\Delta^{36}S$ values and that with $-\Delta^{36}S$ values at different parts of the same reaction vessel would have resulted in the commonly observed values of $\Delta^{33}S_{H_2S} \approx 0‰$. The magnitude of anomalous isotope fractionation also increased with increasing temperature: $\Delta^{33}S_{H_2S} = +0.05$ to $+0.57‰$ at $T = 150$ to 170°C and +0.33 to +0.93‰ at $T = 200°C$.

The relationships between $\Delta^{33}S$ (all positive values) and $\Delta^{36}S$ (both positive and negative) of H_2S and Cr-reduced S species from the experiments closely match the predicted isotope effects during adsorption of SO_2 on a graphite surface (*34*). The $\Delta^{33}S$ and $\Delta^{36}S$ values obtained in our TSR experiments were associated with SO_4^{2-} reduction in open systems with respect to H_2S and that the isotopic compositions of the residual SO_4^{2-} changed little because of the small amounts of H_2S production. In nature, depending on the open or closed system characteristics for SO_4^{2-} and H_2S, the $\Delta^{33}S$ and $\Delta^{36}S$ values of H_2S (and SO_4^{2-}) may be further amplified from those obtained by single-step TSR experiments (*35*).

The $\Delta^{33}S$–$\Delta^{36}S$ relationships of sulfides (mostly FeS_2) in sedimentary rocks older than 2.4 billion years are highly variable, much like

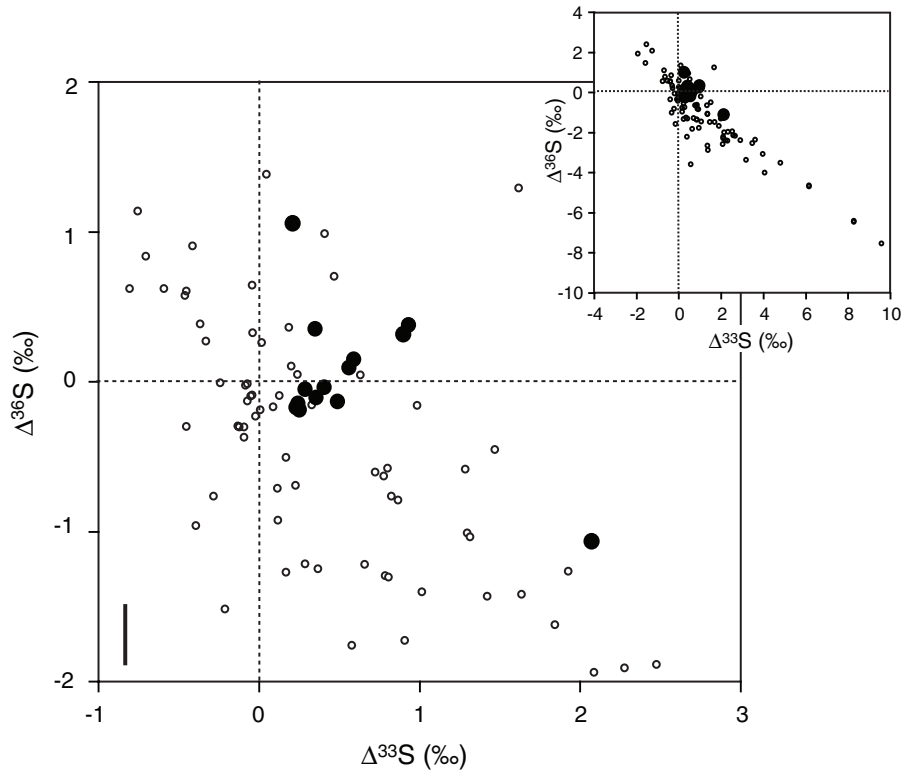

Fig. 4. Comparisons of the S isotope compositions of H_2S and Cr-reduced S species from the TSR experiments with those of sulfides in sedimentary rocks older than 2.4 billion years. Solid circles represent sedimentary sulfides, and solid circles represent the TSR experimental products. Isotope data of the sedimentary sulfide samples from (*6*, *9*, *36*) are shown. An error bar represents the 1 α value of $\Delta^{33}S$ and $\Delta^{36}S$.

those observed in our experimental products (Fig. 4). The most common relations in natural samples are combinations of positive $\Delta^{33}S$ and negative $\Delta^{36}S$ values (*6*), but the combinations of positive $\Delta^{33}S$ and negative (or positive) $\Delta^{36}S$ values are equally observed in our experimental products (Fig. 4). The results of our experiments provide another process that yields anomalously fractionated S, raising the possibility that TSR was responsible for anomalous S isotope signatures in some sedimentary rocks. If this was the case, the frequent occurrences of anomalous S isotope signatures in sedimentary rocks older than 2.4 billion years may suggest that the conditions that are favorable for TSR but not BSR (such as the combination of the abundance of reactive organic matter, SO_4^{2-}-rich seawater, and extensive submarine hydrothermal activity during the early diagenesis of marine sediments) were more common on early Earth. If so, the important questions for future research are why such favorable conditions for TSR diminished after about 2.4 billion years ago.

References and Notes

1. The abundance ratios of the stable isotopes of S (^{32}S, ^{33}S, ^{34}S, and ^{36}S) in a material (*i*) are typically reported as *d* values relative to the Vienna-Canyon Diablo troilite (V-CDT), such as $\delta^{33}S_i$ (‰) = $[(^{33}S/^{32}S)_i/(^{33}S/^{32}S)_{V\text{-}CDT} - 1] \times 1000$. $\delta^{33}S_i$, $\delta^{34}S_i$, and $\delta^{36}S_i$ values of most Earth materials, especially those younger than ~2.4 billion years, are typically related by $\delta^{33}S_i \approx 0.51 \times \delta^{34}S_i$ and $\delta^{36}S_i \approx 1.9 \times \delta^{34}S_i$, which are termed mass-dependent fractionation (MDF). Deviations from the MDF lines (or reference arrays) are commonly expressed with $\Delta^{33}S_i$ and $\Delta^{36}S_i$. In this study, we define $\Delta^{33}S_i = \delta^{33}S_i - 0.515 \times \delta^{34}S_i$ and $\Delta^{36}S_i = \delta^{36}S_i - 1.89 \times \delta^{34}S_i$. When $\Delta^{33}S_i$ and/or $\Delta^{36}S_i$ values deviate from the MDF lines by at least ±0.2‰ and ±0.4‰, respectively, and $\delta^{33}S_i/\delta^{34}S_i$ and/or $\delta^{36}S_i/\delta^{34}S_i$ values fall outside of 0.51 ± 0.01 and 1.9 ± 0.1, respectively, the material is deemed to contain either mass-independently fractionated (MIF), non–mass dependently fractionated, or anomalously fractionated S isotopes. We used anomalously fractionated S isotopes in this report, rather than MIF-S, because MDF relationships vary substantially depending on the types of reactions (for example, equilibrium, kinetic, chemisorption, or radical) and species involved.
2. J. R. Hulston, H. G. Thode, *J. Geophys. Res.* **70**, 3475 (1965).
3. T. Otake, A. C. Lasaga, H. Ohmoto, *Chem. Geol.* **249**, 357 (2008).
4. J. Farquhar, B. Wing, *Earth Planet. Sci. Lett.* **213**, 1 (2003).
5. A. L. Buchachenko, *Pure Appl. Chem.* **72**, 2243 (2000).
6. J. Farquhar, H. Bao, M. Thiemens, *Science* **289**, 756 (2000).
7. D. Papineau, S. J. Mojzsis, A. K. Schmitt, *Earth Planet. Sci. Lett.* **255**, 188 (2007).
8. S. Ono *et al.*, *Earth Planet. Sci. Lett.* **213**, 15 (2003).
9. A. J. Kaufman *et al.*, *Science* **317**, 1900 (2007).
10. S. J. Mojzsis, C. D. Coath, J. P. Greenwood, K. D. McKeegan, T. M. Harrison, *Geochim. Cosmochim. Acta* **67**, 1635 (2003).
11. A. Bekker *et al.*, *Nature* **427**, 117 (2004).
12. J. F. Kasting, *Science* **293**, 819 (2001).
13. J. Farquhar, J. Savarino, S. Airieau, M. H. Thiemens, *J. Geophys. Res.* **106**, 32829 (2001).
14. A. A. Pavlov, J. F. Kasting, *Astrobiology* **2**, 27 (2002).
15. H. Ohmoto, M. B. Goldhaber, in *Geochemistry of Hydrothermal Ore Deposits*, H. L. Barnes, Ed. (Wiley, New York, 1997), pp. 517–611.
16. H. G. Machel, *Sediment. Geol.* **140**, 143 (2001).
17. D. T. Johnston *et al.*, *Am. J. Sci.* **305**, 645 (2005).
18. H. Ohmoto, Y. Watanabe, H. Ikemi, S. R. Poulson, B. E. Taylor, *Nature* **442**, 908 (2006).
19. H. Ohmoto *et al.*, in *Evolution of Early Earth's Atmosphere, Hydrosphere, and Biosphere: Constraints from Ore Deposits*, S. E. Kesler, H. Ohmoto, Eds. (Geological Society of America, Boulder, CO, 2006), vol. 198, pp. 291–331.
20. M. B. Goldhaber, W. L. Orr, in *Geochemical Transformations of Sedimentary Sulfur*, A. Vairavamurthy, M. A. A. Schoonen, Eds. (American Chemical Society, Washington, DC, 1995), pp. 412–425.
21. A. C. Lasaga, T. Otake, Y. Watanabe, H. Ohmoto, *Earth Planet. Sci. Lett.* **268**, 225 (2008).
22. M. T. Madigan, J. M. Martinko, J. Parker, in *BROCK Biology of Microorganisms*. (Prentice-Hall, Upper Saddle River, NJ, 2000), pp. 29–47.
23. S. M. S. Libes, *An Introduction to Marine Biogeochemistry* (Wiley, New York, 1992).
24. A. Knoll, *Geobiology* **1**, 3 (2003).
25. J. M. J. Hunt, *Petroleum Geochemistry and Geology* (Freeman, New York, ed. 2, 1996).
26. Y. Watanabe, H. Naraoka, D. J. Wronkiewicz, K. C. Condie, H. Ohmoto, *Geochim. Cosmochim. Acta* **61**, 3441 (1997).
27. H. Strauss, T. B. Moore, in *The Proterozoic Biosphere*, J. W. Schopf, C. Klein, Eds. (Cambridge University Press, New York, 1992), pp. 709–798.
28. G. W. Skyring, T. H. Donnelly, *Precambrian Res.* **17**, 41 (1982).
29. A. L. Kemp, H. G. Thode, *Geochim. Cosmochim. Acta* **32**, 71 (1968).
30. Materials and methods are available as supporting material on *Science* Online.
31. D. E. Canfield, R. Raiswell, J. T. Westrich, C. M. Reaves, R. A. Berner, *Chem. Geol.* **54**, 149 (1986).
32. We prepared the Cr-solution by the reducing the acidified chromic (III) chloride solution to chromous (II). This solution does not reduce organic S or S from SO_4^{2-} to H_2S but does reduce S from FeS_2, elemental S, and acid-volatile monosulfide S (such as FeS and ZnS) to H_2S. We used this solution after removing acid-volatile monosulfide S with a 6-N HCl solution.
33. A. Sasaki, Y. Arikawa, R. E. Folinsbee, *Bull. Geol. Surv. Japan* **30**, 241 (1979).
34. We prepared the Kiba-solution [Stannous (II)–strong phosphoric acid] by adding tin (II)–chloride dehydrate to dehydrated ortho-phosphoric acid. In contrast to the Cr-solution, the Kiba solution reduces S from SO_4^{2-} and organic S, as well as S from FeS_2, to H_2S.
35. Suppose the initial $\Delta^{33}S$ and $\Delta^{36}S$ values of H_2S were +2.1 and −1.1‰, respectively, with respect to the initial SO_4^{2-}. $\Delta^{33}S$ and $\Delta^{36}S$ of H_2S generated with TSR after a 90% SO_4^{2-} reduction would be −2.6‰ and +1.4‰, respectively, and those of residual SO_4^{2-} would be −4.6‰ and +2.4‰, respectively. In systems in which the product H_2S is removed from its parental SO_4^{2-} and then reoxidized to SO_4^{2-} by some oxidants (such as ferric iron oxides), $\Delta^{33}S$ and $\Delta^{36}S$ of the second generation of H_2S may be +4.2‰ and −2.2‰, respectively.
36. J. Farquhar *et al.*, *Nature* **449**, 706 (2007).

37. We are grateful to H. Naraoka for the suggestion to use amino acids in SO_4^{2-} reduction and for discussions. We thank D. Walizer, H. Hamasaki, A. Klarke, B. Wing, A. L. Masterson, and S.-T. Kim for technical assistance; A. C. Lasaga, T. Otake, S. R. Poulson, and I. Johnson for discussions and review of an earlier manuscript; and three anonymous reviewers for useful comments. This study was supported by grants to H.O. from the NASA Astrobiology Institute (CA#NNA04CC06A), NASA Exobiology Program (CA#NNG04GK00G), and NSF (EAR-0229556).

Supporting Online Material

www.sciencemag.org/cgi/content/full/324/5925/370/DC1
Materials and Methods
SOM Text
Figs. S1 and S2
Tables S1 and S2

3 December 2008; accepted 9 March 2009
10.1126/science.1169289

Origin of Nucleosynthetic Isotope Heterogeneity in the Solar Protoplanetary Disk

Anne Trinquier,[1] Tim Elliott,[2] David Ulfbeck,[1] Christopher Coath,[2] Alexander N. Krot,[1,3] Martin Bizzarro[1]*

Stable-isotope variations exist among inner solar system solids, planets, and asteroids, but their importance is not understood. We report correlated, mass-independent variations of titanium-46 and titanium-50 in bulk analyses of these materials. Because titanium-46 and titanium-50 have different nucleosynthetic origins, this correlation suggests that the presolar dust inherited from the protosolar molecular cloud was well mixed when the oldest solar system solids formed, but requires a subsequent process imparting isotopic variability at the planetary scale. We infer that thermal processing of molecular cloud material, probably associated with volatile-element depletions in the inner solar system, resulted in selective destruction of thermally unstable, isotopically anomalous presolar components, producing residual isotopic heterogeneity. This implies that terrestrial planets accreted from thermally processed solids with nonsolar isotopic compositions.

The presence of isotope anomalies (*1*) of nucleosynthetic origin in meteorites is commonly interpreted as reflecting large-scale isotope heterogeneity resulting from inefficient mixing of stellar-derived dust and gas following collapse of the protosolar molecular cloud core (*2*–*4*). Late-forming planetary bodies like Earth and Mars record the lowest levels of isotope heterogeneity compared to that of the solar system's oldest dated solids, calcium-aluminum–rich inclusions (CAIs), possibly reflecting progressive isotope homogenization of the protoplanetary disk or, alternatively, sampling of disk material at a much broader scale. However, this is apparently at odds with the observation that ^{26}Al—a short-lived nuclide injected into the nascent solar system from a nearby star (*5*)—was evenly distributed in the accretion regions of the terrestrial planets and chondrite meteorites (*6*) at levels comparable to that observed in CAIs (*7*–*10*).

Establishing how and when presolar components were homogenized within the solar protoplanetary disk is uncertain, but central to test models of solar system formation. Titanium is a refractory iron-group element comprising five isotopes (^{46}Ti, ^{47}Ti, ^{48}Ti, ^{49}Ti and ^{50}Ti) synthesized by distinct processes during hydrostatic and explosive nucleosynthesis in stars (*11*). Therefore, we used titanium isotopes to understand the origin and degree of isotope heterogeneity in the inner solar system and track the isotopic evolution of solids that formed the terrestrial planets. Previous studies have identified nonterrestrial, and hence anomalous, titanium isotope compositions in bulk carbonaceous chondrites and in chondritic components such as CAIs and isolated hibonites ($CaAl_{12}O_{19}$), as well as in presolar grains (*2*, *12*–*17*). Whereas titanium isotope anomalies in solar system materials are typically expressed as variations in the neutron-rich ^{50}Ti nuclide, presolar grains display a wider spectrum of anomalous compositions affecting most titanium isotopes.

We obtained high-precision titanium isotope measurements of early solar system materials, by multicollection inductively coupled plasma mass spectrometry in two laboratories [Bristol and Copenhagen (*18*)] (Fig. 1). Apart from enstatite chondrites, enstatite achondrites, and lunar meteorites, all solar system objects show significant correlated variations in ε^{46}Ti and ε^{50}Ti compared to terrestrial values, defining a single line with slope 5.48 ± 0.27 and intercept −0.04 ± 0.20. Whole-rock carbonaceous chondrites record variable excesses in ε^{46}Ti and ε^{50}Ti, whereas ordinary chondrites are characterized by uniform deficits in these isotopes with respect to Earth. With the exception of the NWA 2976 basalt, which has a titanium isotope composition similar to that of carbonaceous chondrites, all samples originating from differentiated asteroids (eucrites, diogenites, angrites, mesosiderites, pallasites, and ureilites) and Mars exhibit deficits in ε^{46}Ti and ε^{50}Ti. One chondrule extracted from the Dar al Gani 313 ordinary chondrite has a titanium isotope composition similar to the average defined by whole-rock ordinary chondrites. In contrast, chondrules from the Allende carbonaceous chondrite show variable correlated titanium isotope compositions, with both excesses and deficits in ε^{46}Ti and ε^{50}Ti. Four coarse-grained igneous CAIs, compact Type A and Type B, and one amoeboid olivine aggregate (AOA) from the Allende and Efremovka CV carbonaceous chondrites display relatively uniform excesses in ε^{46}Ti and ε^{50}Ti of 1.7 ± 0.3 and 9.4 ± 0.9 ε units, respectively.

The chemical dissolution procedures that we used are not expected to dissolve refractory phases such as SiC or hibonite grains present in fine-grained matrices of chondritic meteorites. This raises the possibility that the titanium isotope heterogeneity among chondrites reflects incomplete dissolution of these potentially isotopically anomalous phases or of other unidentified presolar grains. However, mass balance

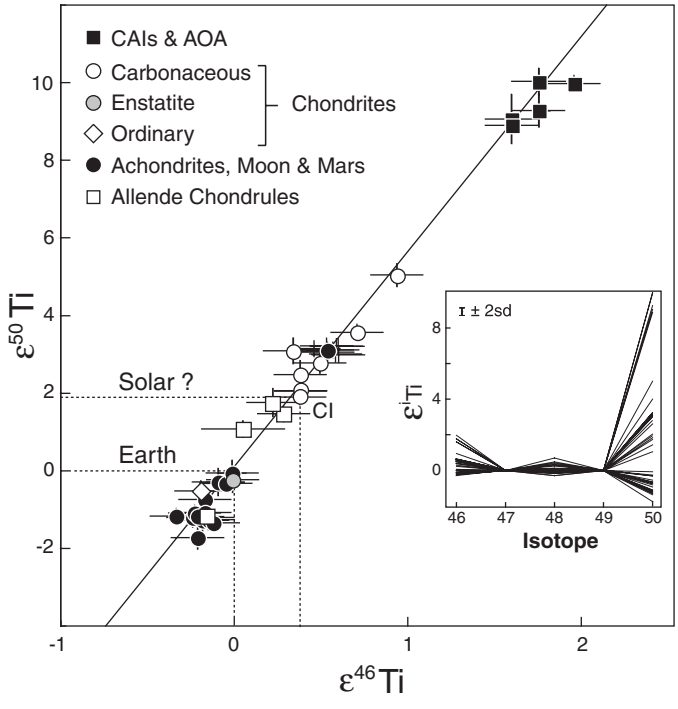

Fig. 1. ε^{46}Ti-ε^{50}Ti variation diagram for inner solar system planetary materials. Data are reported in the ε notation (deviations in parts per 10,000 from the terrestrial ^{50}Ti/^{47}Ti and ^{46}Ti/^{47}Ti ratios) and internally normalized to ^{49}Ti/^{47}Ti = 0.749766 (*12*). This normalization approach assumes that the ^{49}Ti/^{47}Ti ratios of samples we analyzed are terrestrial. Error bars represent the external reproducibility or the internal precision, whichever is larger. (**Inset**) ε^{46}Ti, ε^{48}Ti, and ε^{50}Ti variations for the same samples, with the external reproducibility indicated.

[1]Center for Stars and Planets, Natural History Museum of Denmark, University of Copenhagen, Copenhagen DK-1350, Denmark. [2]Bristol Isotope Group, Department of Earth Sciences, University of Bristol, Bristol BS8 1RJ, UK. [3]Hawai'i Institute of Geophysics and Planetology, University of Hawai'i at Manoa, HI 96822, USA.

*To whom correspondence should be addressed. E-mail: bizzarro@snm.ku.dk

calculations indicate that incomplete dissolution of SiC or hibonite grains will only lead to a shift in the bulk ^{50}Ti composition of <0.3 ε unit (SOM Text 1), which is inconsistent with the range of ε^{50}Ti values observed among chondrites (Fig. 1). Apart from CAIs and AOA, all meteorites display the terrestrial ^{48}Ti/^{47}Ti ratio when the ^{49}Ti/^{47}Ti ratio is used to correct for instrumental mass fractionation (Fig. 1, inset) and, hence, using a different pair of isotopes (^{48}Ti/^{47}Ti or ^{49}Ti/^{48}Ti) to correct for instrumental mass fractionation yields identically correlated anomalies in ^{46}Ti and ^{50}Ti. Therefore, the most straightforward interpretation of these data is that Ti isotope anomalies are restricted to ^{46}Ti and ^{50}Ti, whereas the ^{47}Ti, ^{48}Ti and ^{49}Ti abundances of most samples that we analyzed are terrestrial within the resolution of our analyses (SOM Text 2).

The ^{50}Ti anomalies that we found for inner solar system materials are comparable to ^{54}Cr compositions for the same meteorites and components (Fig. 2). We attribute the lack of correlation between the ^{54}Cr and ^{50}Ti anomalies in carbonaceous chondrites to the presence of variable amounts of CAIs in these meteorites. CAIs are elementally enriched in titanium and depleted in chromium compared to solar system abundances (*19*) such that addition of small quantities [<10 weight percent (wt%)] of this material to a CAI-free chondrite matrix will almost exclusively modify its bulk titanium isotope composition (Fig. 2). In contrast, the well-correlated abundances of ^{54}Cr and ^{50}Ti in samples from terrestrial planets and most differentiated asteroids, as well as from ordinary and enstatite chondrites, imply that their accretion regions were essentially free of CAIs. Therefore, the ^{46}Ti-^{50}Ti covariation recorded by inner solar system planets and asteroids cannot uniquely reflect admixing of variable amounts of CAIs in their precursor material.

To understand the scale of this heterogeneity, we have subjected the CI chondrite Orgueil to a stepwise-leaching procedure aimed at providing a crude chemical separation of the various mineralogical components (*3*, *20*). Composed of matrix material with the highest abundances of presolar grains, CI chondrites are generally considered to represent the least chemically fractionated and least thermally processed meteorites (*21*). Analysis of the different leach fractions show that none has a terrestrial titanium isotope composition (Fig. 3) and that the bulk of the titanium (>99.5%) resides in acid-soluble nonrefractory silicate minerals. Most fractions plot off the ^{46}Ti-^{50}Ti correlation line defined by the inner solar system solids (Fig. 3), implying the existence of multiple titanium nucleosynthetic components in Orgueil silicates. The largest excess of ^{50}Ti was identified in fractions where significant excesses ^{54}Cr have been previously reported (*3*, *20*), thereby suggesting a common carrier for ^{50}Ti and ^{54}Cr. In contrast, the positively anomalous ^{46}Ti apparently resides in a distinct mineralogical component and, hence, in a different carrier. Given that the magnitude of the titanium isotope heterogeneity we report for chondrites cannot be explained by addition or removal of typical presolar grain assemblages retrieved from the matrices of carbonaceous chondrites, it must represent the existence of additional—as yet unidentified—presolar carriers of anomalous titanium inherited from the protosolar molecular cloud. We infer that the titanium isotope heterogeneity defined by the various fractions of Orgueil reflects admixing of multiple generations of presolar silicates, possibly of distinct stellar origins, given that the nucleosynthesis of ^{46}Ti and that of ^{50}Ti are believed to be decoupled (*11*). Silicates are the most abundant presolar phases in carbonaceous chondrites, but are typically difficult to identify with conventional techniques given their minute size and fragile nature. However, we note that addition or removal of ~500 parts per million (ppm) of presolar silicates with chondritic titanium concentrations and ^{50}Ti enrichments similar to that present in other presolar components (e.g., SiC) to a terrestrial composition is sufficient to produce the ^{50}Ti variability observed in planetary materials.

It is unlikely that the ^{46}Ti-^{50}Ti correlation line defined by solar system objects results from simple heterogeneous distribution of presolar silicates within the inner protoplanetary disk, given that the anomalous ^{46}Ti and ^{50}Ti reside in different carriers. Instead, it suggests that the presolar dust inherited from the protosolar molecular cloud was initially homogeneously distributed within the inner protoplanetary disk, but requires the existence of a secondary process imparting selective loss of presolar silicates before the formation of solar system solids and accretion of planetary bodies. The magnitude of the ^{54}Cr excesses in carbonaceous chondrites—and by extension that of the ^{46}Ti and ^{50}Ti excesses—correlates with a degree of depletion in moderately volatile elements of the host meteorite matrices (Fig. 4). The chemical fractionations of moderately volatile elements in carbonaceous chondrite matrices and the survival of their presolar grain assemblages are believed to reflect the degree of thermal processing experienced by the matrix before parent body accretion (*21*–*23*). Therefore, we propose that the thermal event(s) responsible for moderately volatile element fractionation in the inner solar system also resulted in the preferential loss by sublimation of thermally unstable presolar silicates containing ^{46}Ti and ^{50}Ti excesses. However, the ^{46}Ti-^{50}Ti correlation observed in Fig. 1 requires that the ^{46}Ti and ^{50}Ti carriers were removed in approximately the same proportion and, hence, have similar thermal properties, which is not unexpected if they are both nonrefractory silicates. Thus, nucleosynthetic anomalies in meteorites may reflect the degree of thermal pro-

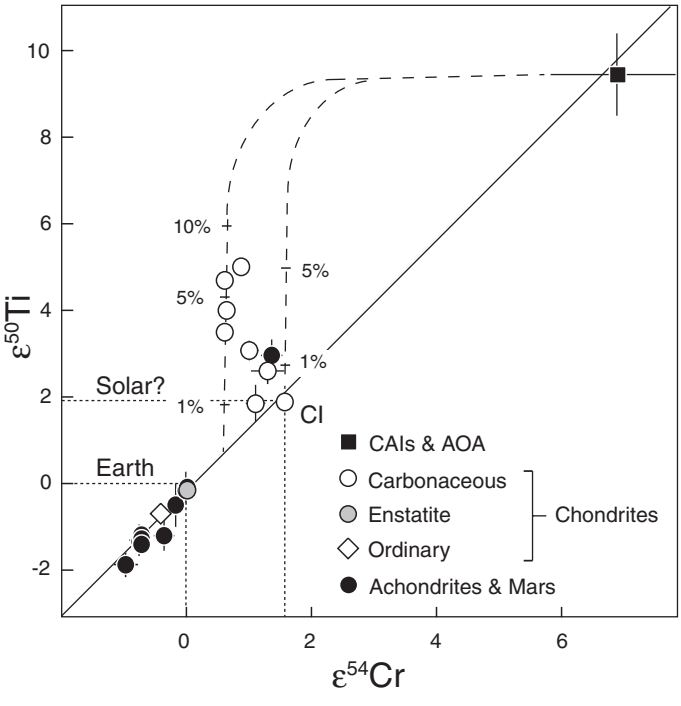

Fig. 2. ε^{54}Cr-ε^{50}Ti variation diagram of inner solar system planets, asteroids, and chondrite components. CAIs, the CI chondrite Orgueil, martian meteorites, and ordinary and enstatite chondrites, as well as most differentiated meteorites, define a correlation line with slope and intercept of 1.4 ± 0.1 and −0.2 ± 0.1, respectively (mean square weighted deviation = 1.3). Bulk CO, CV, CR, and CK carbonaceous chondrites plot above this line, and we attribute this feature to the presence of CAIs in these objects. The dashed lines are mixing curves between CAIs and CAI-free compositions defined by the correlation line, with percent mixing indicated. For the CAI reservoir, we used chromium and titanium concentrations of 200 and 5400 ppm, respectively, and ε^{54}Cr and ε^{50}Ti compositions from (*24*) and as defined here, respectively. We adopted Orgueil as a proxy for the CAI-free chondritic reservoir, using titanium and chromium concentrations from (*19*) and ε^{54}Cr and ε^{50}Ti compositions from (*3*) and as defined here. These models show that a decoupling in ε^{54}Cr and ε^{50}Ti can be explained by addition of small quantities of CAI material (<10 wt %). Error bars represent the external reproducibility or the internal precision, whichever is larger.

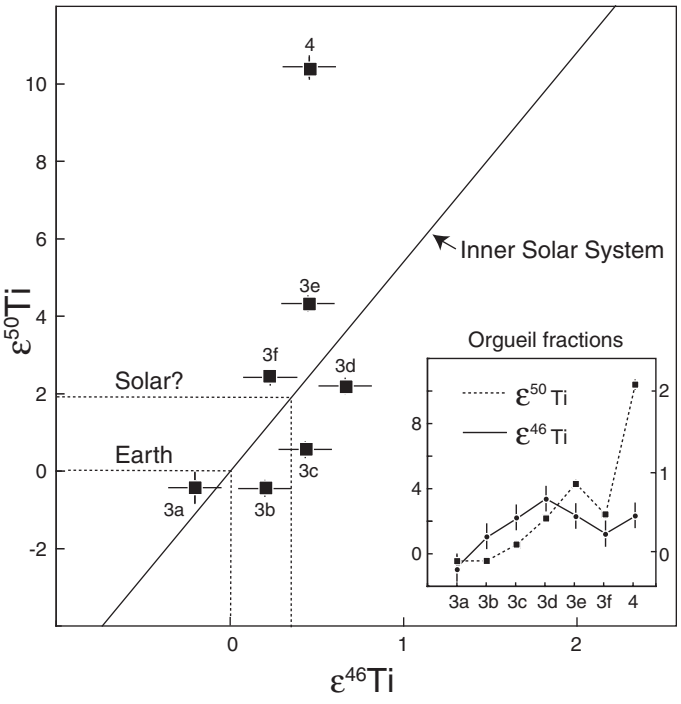

Fig. 3. ε^{46}Ti-ε^{50}Ti variation diagram for fractions of the Orgueil CI chondrite defined by stepwise leaching. Apart from fraction 3a, all fractions plot off the correlation line defined by inner solar system planets, asteroids, and solids (Fig. 1). **(Inset)** ε^{46}Ti and ε^{50}Ti values plotted as a function of leaching step numbers (table S2). The ε^{46}Ti and ε^{50}Ti scales are different and positioned to the right and left, respectively. Using a different pair of isotopes (^{48}Ti/^{47}Ti or ^{48}Ti/^{49}Ti) to correct for instrumental mass fractionation would not change our conclusion that the anomalous ^{46}Ti and ^{50}Ti reside in different presolar carriers. Error bars represent the external reproducibility or the internal precision, whichever is larger.

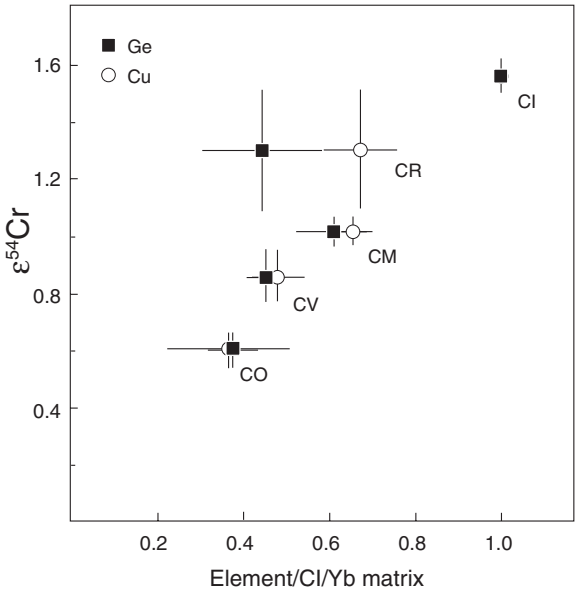

Fig. 4. ^{54}Cr versus Cu and Ge concentrations (ratioed to CI chondrites and ytterbium) in carbonaceous chondrite matrices. Data are from (*3*, *22*). We plot the ^{54}Cr in this diagram because the ^{46}Ti and ^{50}Ti compositions of carbonaceous chondrites are variably affected by the presence of CAIs in these meteorites. Error bars represent the external reproducibility or the internal precision, whichever is larger.

cessing experienced by their precursor material, and not initial disk heterogeneity. Our study demonstrates that Earth and the bulk of the inner solar system's rocky mass did not form from a CI-like precursor but, instead, from appreciably thermally processed material.

The average chemical composition of the protosolar molecular cloud material—and hence that of the Sun—is best approximated by CI chondrites for a refractory element such as titanium. Therefore, mass balance arguments require the existence of a complementary reservoir enriched in ^{46}Ti and ^{50}Ti to account for the widespread depletions observed among the inner solar system bodies. CAIs are the only objects with consistently elevated abundances in ^{46}Ti and ^{50}Ti compared to CI chondrites (Figs. 1 and 2). A possibility is that CAIs represent samples of the complementary gaseous reservoir enriched in ^{46}Ti and ^{50}Ti by thermal processing of pristine molecular cloud material. If correct, this implies that substantive thermal processing and dust-gas fractionation of the inner solar system solids, possibly including moderately volatile-element depletion, occurred before the formation of most CAIs.

References and Notes

1. Isotope anomalies are deviations in the stable-isotope composition of an element compared to that of the Earth.
2. J.-L. Birck, *Rev. Mineral. Geochem.* **55**, 25 (2004).
3. A. Trinquier, J.-L. Birck, C. J. Allègre, *Astrophys. J.* **655**, 1179 (2007).
4. R. Andreasen, M. Sharma, *Astrophys. J.* **655**, 874 (2007).
5. J. N. Goswami, K. K. Marhas, M. Chaussidon, M. Gounelle, B. S. Meyer, in *Chondrites and the Protoplanetary Disk*, A. N. Krot, E. R. D. Scott, B. Reipurth, Eds. (Astrophysical Society of the Pacific, San Francisco, CA, 2005), pp. 485–514.
6. Chondrite meteorites are undifferentiated stony meteorites composed of CAIs, Fe-Mg-silicates spherules called chondrules, and a fine-grained volatile-rich matrix.
7. G. J. MacPherson, A. M. Davis, E. K. Zinner, *Meteoritics* **30**, 365 (1995).
8. M. Bizzarro, J. A. Baker, H. Haack, *Nature* **431**, 275 (2004).
9. K. Thrane, M. Bizzarro, J. A. Baker, *Astrophys. J.* **646**, L159 (2006).
10. J. N. Connelly, Y. Amelin, A. N. Krot, M. Bizzarro, *Astrophys. J.* **675**, L121 (2008).
11. D. D. Clayton, *Handbook of Isotopes in the Cosmos: Hydrogen to Gallium* (Cambridge Univ. Press, Cambridge, UK, 2003).
12. F. R. Niederer, D. A. Papanastassiou, G. J. Wasserburg, *Geochim. Cosmochim. Acta* **45**, 1017 (1981).
13. S. Niemeyer, G. W. Lugmair, *Earth Planet. Sci. Lett.* **53**, 211 (1981).
14. F. R. Niederer, D. A. Papanastassiou, G. J. Wasserburg, *Geochim. Cosmochim. Acta* **49**, 835 (1985).
15. I. Leya, M. Schönbächler, U. Wiechert, U. Krähenbühl, A. N. Halliday, *Earth Planet. Sci. Lett.* **266**, 233 (2008).
16. T. R. Ireland, *Geochim. Cosmochim. Acta* **52**, 2827 (1988).
17. E. Zinner *et al.*, *Geochim. Cosmochim. Acta* **71**, 4786 (2007).
18. Materials and methods are available as supporting online material (SOM) at *Science* Online.
19. H. Palme, A. Jones, in *Treatise on Geochemistry*, H. D. Holland, K. K. Turekian, Eds., Vol. 1, *Meteorites, Comets and Planets*, A. M. Davis, Ed. (Elsevier-Pergamon, Oxford, 2003), pp. 41–61.
20. M. Rotaru, J.-L. Birck, C. J. Allègre, *Nature* **358**, 465 (1992).
21. G. R. Huss, A. P. Meshik, J. B. Smith, C. M. Hohenberg, *Geochim. Cosmochim. Acta* **67**, 4823 (2003).
22. P. A. Bland *et al.*, *Proc. Natl. Acad. Sci. U.S.A.* **102**, 13755 (2005).
23. A. Trinquier, J.-L. Birck, C. J. Allègre, C. Göpel, D. Ulfbeck, *Geochim. Cosmochim. Acta* **72**, 5146 (2008).
24. O. Bogdanovski, D. A. Papanastassiou, G. J. Wasserburg, *Lunar Planet. Sci.* **33**, 1802 (2002).

25. Financial support for this project was provided by the Danish National Research Foundation, the Danish Natural Science Research Council, and the University of Copenhagen's Programme of Excellence. We thank J. Connelly, G. Huss, H. Haack, F. Richter, R. Mendybaev, and B. Meyer for discussion.

Supporting Online Material

www.sciencemag.org/cgi/content/full/324/5925/374/DC1
Methods
SOM Text
Figs. S1 and S2
Tables S1 to S3
References

7 November 2008; accepted 5 March 2009
10.1126/science.1168221

Atlantic Forcing of Persistent Drought in West Africa

T. M. Shanahan,[1,2]* J. T. Overpeck,[1,3] K. J. Anchukaitis,[4] J. W. Beck,[5] J. E. Cole,[1] D. L. Dettman,[1] J. A. Peck,[6] C. A. Scholz,[7] J. W. King[8]

Although persistent drought in West Africa is well documented from the instrumental record and has been primarily attributed to changing Atlantic sea surface temperatures, little is known about the length, severity, and origin of drought before the 20th century. We combined geomorphic, isotopic, and geochemical evidence from the sediments of Lake Bosumtwi, Ghana, to reconstruct natural variability in the African monsoon over the past three millennia. We find that intervals of severe drought lasting for periods ranging from decades to centuries are characteristic of the monsoon and are linked to natural variations in Atlantic temperatures. Thus the severe drought of recent decades is not anomalous in the context of the past three millennia, indicating that the monsoon is capable of longer and more severe future droughts.

Beginning in the late 1960s, much of West Africa experienced severe drought, which peaked in the mid-1970s and lasted for several decades, displacing millions from sub-Saharan Africa (*1*). Since that time, concerted efforts by climatologists, geologists, and modelers have focused on understanding the factors controlling West African monsoon (WAM) variability (*2*–*6*). Much of this research now implicates changing sea surface temperatures (SSTs) in generating long-lasting wet and dry periods, with positive land surface feedbacks exacerbating these changes (*3*–*5*). However, it is uncertain whether recent multidecadal drought is anomalous in the context of late Holocene climate variability, because long instrumental records and high-resolution paleoclimate reconstructions from the African tropics are lacking (*5*).

We generated a near-annual record of West African hydrologic variability, using annually laminated sediment cores from Lake Bosumtwi, Ghana (6°30′N, 1°25′W) (*7*). Lake Bosumtwi is ideally suited to reconstructing variations in the WAM because of its location in humid tropical West Africa and because its sediment laminations provide a high-resolution chronology for the paleoclimatic record (*7*, *8*). Hydrologic changes were reconstructed using oxygen isotopes of authigenic lake carbonate and micro–x-ray fluorescence (μ-XRF) scanning of major element concentrations (*7*). Authigenic carbonate $\delta^{18}O$ reflects that of Bosumtwi lake water, which, because the lake is a closed basin, is linked to the balance between precipitation and evaporation. This interpretation is supported by the correlation (R_{49} = 0.55, P < 0.001) between changes in precipitation measured instrumentally and high-resolution (at 2- to 5-year sampling intervals) carbonate $\delta^{18}O$ variations in the sediment record (Fig. 1). Although the proxy data reproduce variations in local precipitation on decadal time scales, the relationship is weaker on interannual time scales. These differences most likely reflect both the spatially heterogeneous nature of monsoon rainfall on interannual time scales (*8*) and the practical difficulties in precisely subsampling laminae from highly flocculant near-surface sediments. Although differences exist in the magnitude and timing of low-frequency rainfall variability across West Africa, including an apparent delayed onset of late 20th-century drought near the coast and a variable dry period in 1941–1949, quite similar decadal variability is apparent in instrumental records from throughout the monsoon region (fig. S1). This demonstrates that local rainfall reconstructions, such as that from Lake Bosumtwi, may be used to infer regional-scale changes in monsoon precipitation on decadal and longer time scales.

Variations in sediment elemental concentrations are interpreted as reflecting changes in the flux of terrigenous material to the lake during the summer monsoon. This flux is controlled by the size of the erodable catchment area, with higher elemental concentrations occurring during low lake levels, when more of the crater is emergent and the erodable catchment area is larger. High-resolution (20- to 40-μm) XRF scanning of intact sediment cores provides major element concentrations at subannual resolution, allowing the reconstruction of annual to decadal climate variability, which is not possible with $\delta^{18}O$ because of variable carbonate preservation (*7*). Here we focus on the first principal component (PC1) of the full suite of elemental data (Al, Si, K, Ca, Ti, Mn, and Fe) as a proxy for the terrigenous sediment component of the record. The similarities between variations in carbonate $\delta^{18}O$ and PC1 further support our interpretation of the XRF data as an indicator of lake status (supporting online text).

Additional support for our interpretation of the geochemical data comes from geological evidence for past lake levels (*9*, *10*). Low elemental concentrations (more positive PC1) and more negative isotopic signatures in the early part of the record are consistent with evidence for mid-Holocene lake deposits up to 100 m above the modern lake surface (*9*). Stromatolite-encrusted terraces at 20 to 25 m above the modern lake level formed between

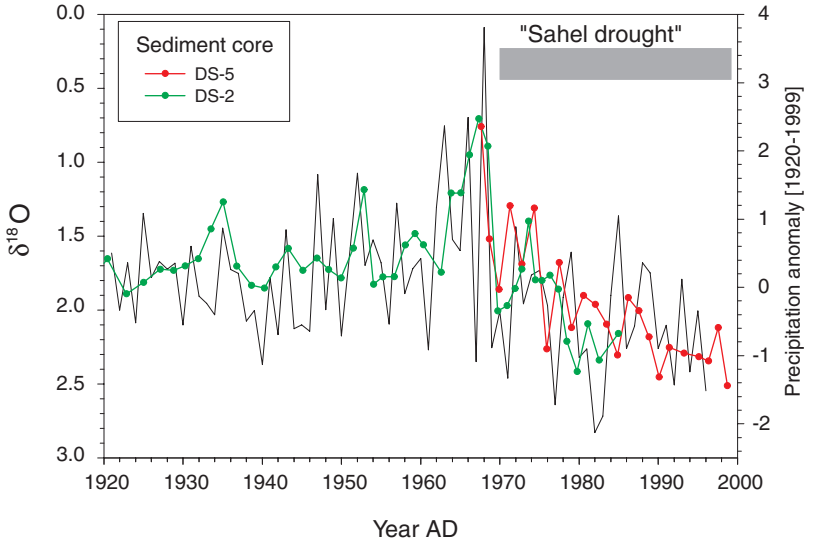

Fig. 1. Proxy instrumental data comparison of rainfall variability in West Africa. Carbonate oxygen isotope data (circles and colored lines) from cores DS-2 and DS-5, placed on a laminae age model plotted with normalized precipitation anomalies from the Kumasi meteorological station (black line), 35 km northwest of the lake, are shown. More negative isotopic values occur during intervals with high precipitation rates (r = 0.55, significant at 95%). Both records show the interval of enhanced precipitation before ~1965 and a dramatic dropoff in precipitation after 1970. This shift in rainfall is synchronous with a well-documented period of extended drought in the Sahel region of North Africa (10° to 20°N, 20°W to 40°E) known as the Sahel drought (gray horizontal bar).

[1]Department of Geosciences, University of Arizona, Tucson, AZ 85721, USA. [2]Jackson School of Geosciences, University of Texas–Austin, Austin, TX 78705, USA. [3]Institute for the Environment and Society and Department of Geosciences, University of Arizona, Tucson, AZ 85721, USA. [4]Lamont Doherty Earth Observatory of Columbia University, Palisades, NY 10964, USA. [5]Department of Physics, University of Arizona, Tucson, AZ 85719, USA. [6]Department of Geology, University of Akron, Akron, OH 44325, USA. [7]Department of Earth Sciences, Syracuse University, Syracuse, NY 13244, USA. [8]Graduate School of Oceanography, University of Rhode Island, Narragansett, RI 02882, USA.

*To whom correspondence should be addressed. E-mail: tshanahan@jsg.utexas.edu

~2200 and ~1650 years before the present (yr B.P.), reflecting a positive water balance at that time, are also consistent with sediment core data (Fig. 2) (*9*). Two late Holocene lowstands are also evident in high-resolution seismic reflection data, suggesting lake level drops of 31 and 24 m at ~700 to 1000 and 250 to 500 calendar yr B.P., respectively (*10*), in agreement with the timing of the largest lowstands in the sediment core data.

Sediment geochemical data indicate that Lake Bosumtwi underwent a progressive drying between 2660 and ~1000 yr B.P., with the most rapid drying occurring after ~1700 to 1800 yr B.P. (Fig. 2A). This long-term trend is consistent with climate simulations (*11*, *12*) and paleoclimate reconstructions (*13*–*17*), which support a weakening of the WAM in response to gradually decreasing summer insolation over the late Holocene. Superimposed on this trend are a series of multicentury droughts. The most recent of these occurred between 1400 and 1750 CE (550 to 200 yr B.P.), similar in timing to the Little Ice Age (LIA, ~1400 to 1850 CE), a well-known interval when Northern Hemisphere temperatures were cooler than at present (*18*). In contrast with earlier studies, which reconstructed wetter conditions in East Africa during this period (*19*), evidence from Lake Bosumtwi supports more recent studies suggesting that this interval was dry (*20*, *21*). Evidence for LIA drought is not restricted to Africa, however. Records from throughout the tropics, including the western Pacific warm pool (*22*), the Arabian Sea (*23*, *24*), continental Asia (*25*), and tropical South America (*26*) all show evidence for dry conditions during this time period. Wet conditions in West Africa during the few centuries preceeding (~1200 to 1400 CE) and following (~1800 CE to the present) this dry interval are also apparent in a number of tropical monsoon records (Fig. 3) (*21*, *23*–*25*), forming a coherent pattern of variability that indicates common large-scale forcing of tropical climate over the past millennium.

These alternating wet and dry conditions form part of a longer pattern of centennial-scale variability in the WAM that spans the late Holocene (Fig. 2A). Multi-taper method (MTM) spectral analysis (*27*) of the XRF data confirms the importance of this mode, with broad areas of significant power centered around 90, 160 to 190, 200 to 240, and >300 years (Fig. 4A). Their statistical significance was confirmed by wavelet spectral analysis (*28*), which displays a maximum in power at century time scales throughout the record (Fig. 2B), and by singular spectrum analysis (SSA), with reconstructed components (RCs) of similar, though not identical, mean periods (RC1 to RC2, 360 to 390 and 500 years; RC3 to RC4, 205 to 220 years) (*29*). Based on similarities with the record of atmospheric $\Delta^{14}C$, a proxy for past solar variability (*30*), previous authors have attributed centennial variability in tropical paleoclimate records to changes in solar irradiance (*23*–*25*). However, there are no clear correlations between centennial variability in the Bosumtwi record and changes in atmospheric $\Delta^{14}C$, indicating that, at least in West Africa, the sun-climate link is weak or indirect. One possibility is that centennial variability in continental West Africa is generated by internal oscillations in the tropical Atlantic ocean-atmosphere system (*31*). Simulations of the Atlantic meridional overturning circulation (AMOC) with the HadCM3 coupled ocean-atmosphere model suggest that interactions between the intertropical convergence zone (ITCZ) and the AMOC can generate centennial-scale climate changes internal to the tropical Atlantic climate system (*32*). Because of the direct effect of ITCZ migrations on the WAM, these changes could dominate rainfall variability over West Africa on these time scales and might overwhelm the influence of any external forcing mechanism such as solar irradiance. The AMOC connection also provides a means of connecting changes in the WAM to changes in the high latitudes and elsewhere in the tropics.

Spectral analysis (*27*) indicates that there is also significant power at annual (3.6-to 4.6-year), decadal (7.1- to 13.8-year), and multidecadal (33- to 42-year) bands (Fig. 4A). Variability at 3- to 5-year periods may be linked to either the remote influence of Pacific El Niño events [typically at 2- to 7-year intervals (*33*)] or zonal SST variations in the tropical Atlantic [Atlantic El Niños, 2- to 2.5-year intervals (*34*)], both of which are known to affect the modern WAM. The decadal variability is similar to that of Atlantic trade wind variations (8.7- to 9.0-year and 12.5- to 13-year) reconstructed from Cariaco

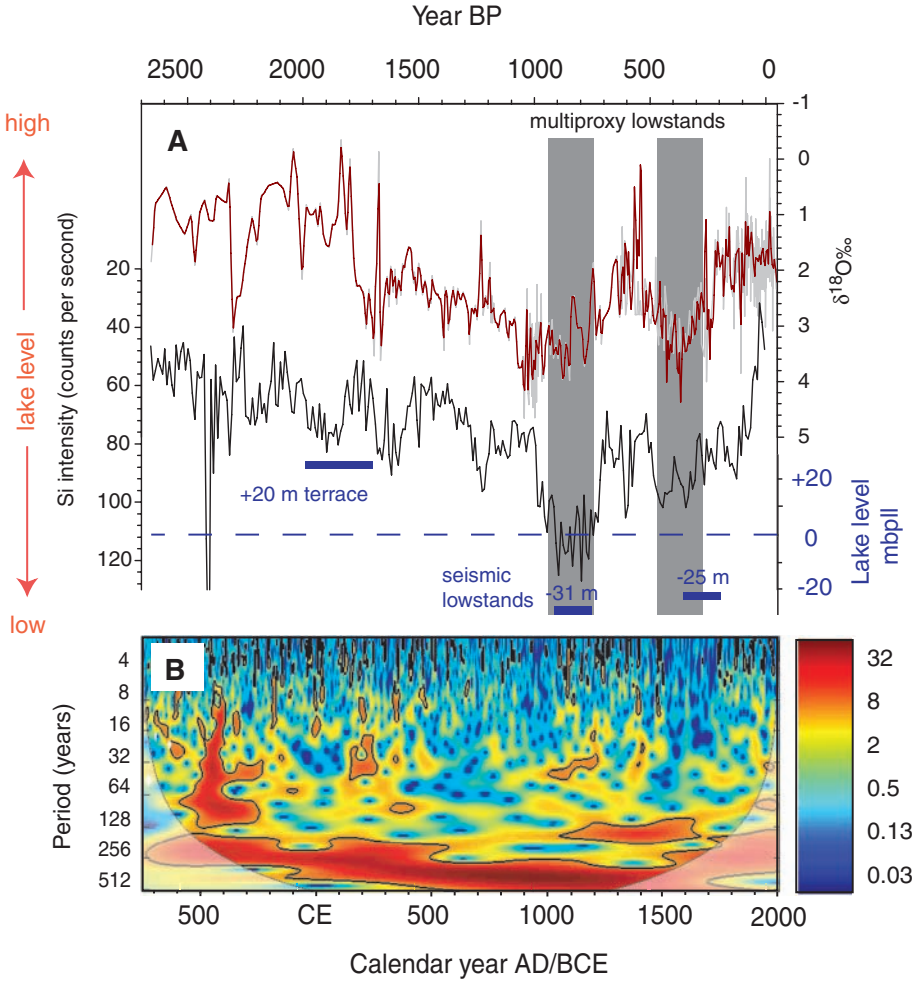

Fig. 2. Paleohydrologic evolution of Lake Bosumtwi. (**A**) Shown are the $\delta^{18}O_{carbonate}$ data (top: red line, 5-year average; gray line, raw data; note the reversed scale), silicon (Si) intensities generated by μ-XRF scanning (middle: black line, note the reversed scale; 10-year averages), and indicators of past lake levels based on emergent terraces and seismic data (bottom: horizontal blue bars). mbpll, meters below present lake level. More positive isotopic values occur during lowstands, which is consistent with a more evaporated lake system. Higher elemental (Si, Al, K, and Ti) concentrations indicate increased transport of terrigenous material to the basin during lowstands, when the base level in the catchment is lowered and more catchment area is exposed to erosion. Vertical gray bars indicate the timing of prominent late Holocene lowstands discussed in the text, as identified in the multiproxy data. (**B**) Evolutive wavelet power spectrum (*28*) computed with a Morlet wavelet (eight octaves, four suboctaves per octave) on the detrended (600-year, 50% spline) PC1 of the XRF data. The black line indicates 95% significance level. Century-scale variability is strong throughout the past approximately three millennia.

Basin (offshore Venezuela) sediments (*35*), suggesting that they may represent an important mode of Atlantic ITCZ variability. The 10.6- and 13.8-year quasi-periodicities are also similar to the dominant meridional mode of SST variability in the tropical Atlantic (11 to 13 years), which is believed to be linked to wind evaporation feedback effects in the tropical Atlantic (*36*).

The strongest frequency component of the sub–century-scale variability is centered on ~40 years (33 to 42 years), suggesting that long-lasting droughts, like those seen in the instrumental record, are a regular feature of the WAM. Because of the potential for producing anomalous narrow-band peaks from noisy data sets using the MTM approach, we confirmed the significance of this multidecadal mode of variability by SSA (*29*), which also produces a curve with an ~40-year period as its fifth and sixth components, and by wavelet analysis, which shows distinct bands of power at multidecadal time scales (*28*) (Fig. 2B). Previous studies have demonstrated that multidecadal drought in West Africa during the instrumental period is primarily driven by changing Atlantic SST patterns (*3*–*5*), and it has been suggested that these patterns may reflect a natural low-frequency mode (65- to 80-year) of SST variability, termed the Atlantic multidecadal oscillation (AMO) (*37*). The relationship between West African rainfall and the AMO is supported by the strong correlations across West Africa over the instrumental period (Fig. 4C). Although the ~40-year mode apparent in the Bosumtwi record is not identical to the instrumental record of the AMO, it is similar to the dominant mode of variability reported from a longer tree-ring–based reconstruction of the AMO (~42.7 years) (*38*) and suggests that the WAM has varied on multidecadal time scales for at least the past 3000 years. To evaluate possible linkages between the AMO and the WAM, we performed a cross-spectral analysis of the Lake Bosumtwi rainfall and tree-ring AMO (*38*) reconstructions. The results suggest that WAM variability and the AMO are coherent and in phase at this 30- to 40-year period over the full 350 years of overlap (Fig. 4B). However, an examination of the power spectra of these records in the time domain (*28*) suggests that this multidecadal variability ranges between ~30 and 65 years (fig. S5). Evolutive cross-wavelet coherence and phase analysis (*39*) demonstrate that despite this nonstationarity, these records remain in phase and coherent, providing additional support for the hypothesized link between multidecadal Atlantic SST variability and the WAM.

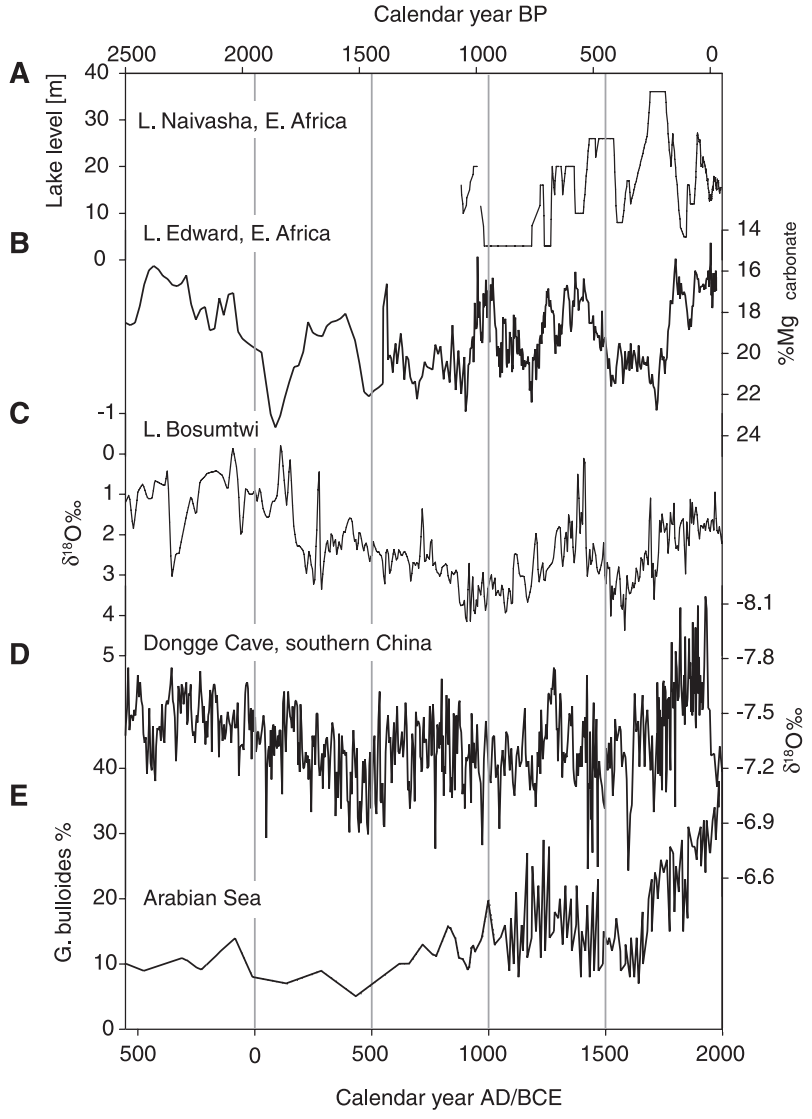

Fig. 3. Records of tropical hydrologic variability. Records are oriented so that a positive water balance is up. (**A**) Lake level variations at Lake Naivasha, East Africa (*19*). (**B**) percent of Mg in carbonate, an indicator of past salinity in Lake Edward, East Africa (*21*). (**C**) $\delta^{18}O$ of carbonate from Lake Bosumtwi. (**D**) $\delta^{18}O$ of speleothem carbonate from Dongge Cave, southern China (*25*). (**E**) *Globigerina bulloides* abundance in sediment cores from the Arabian Sea, an indicator of monsoon wind strength (*23*, *24*). The records show some differences in their evolution before ~1000 yr B.P. but are remarkably similar over the past few centuries, suggesting that these tropical climate systems are linked. An exception is the Lake Naivasha record, which is out of phase with the other records.

These data indicate that long-lasting episodes of alternating wet and dry conditions have been a feature of the WAM over at least the past three millennia and that these modes of variability are linked to changes in the circulation of the Atlantic. There is abundant evidence from both the modern and archaeological record that these hydrologic changes have been important factors in driving the growth and migration of human populations across West Africa (*40*, *41*). Although the most recent multidecadal drought of the 1970s had widespread ecological, political, and socioeconomic impacts, the Lake Bosumtwi reconstruction suggests that the climate system is capable of much more severe and longer droughts, the most recent of which occurred only 200 to 300 years ago. At that time, the level of Lake Bosumtwi dropped by almost four times as much as it did during the drought of the 1970s (*10*). The century-scale pattern of hydrologic changes over the past three millennia suggests that we will eventually shift back into a period of centennial-scale drought conditions much more severe than seen over the past century. The likelihood of such a regime shift may be enhanced by rising global temperatures, which could perturb the system by inducing a slowdown in the MOC with enhanced freshwater inputs into the North Atlantic (*42*), causing the coupled atmosphere-ocean system to switch into a century-long drought mode. Rapidly expanding populations in sub-Saharan Africa depend heavily on monsoon rainfall for agriculture and power generation and are ill prepared to adapt to such a severe drought if it occurred today. Policymakers should move fast to consider concrete strategies and contingency plans for mitigating such unprecedented droughts, which will undoubtedly be exacerbated by rising surface air temperatures in the future (*43*).

References and Notes

1. K. E. Trenberth *et al.*, in *Climate Change: The Physical Science Basis. Contribution of Working Group I to the Fourth Assessment Report of the Intergovernmental Panel*

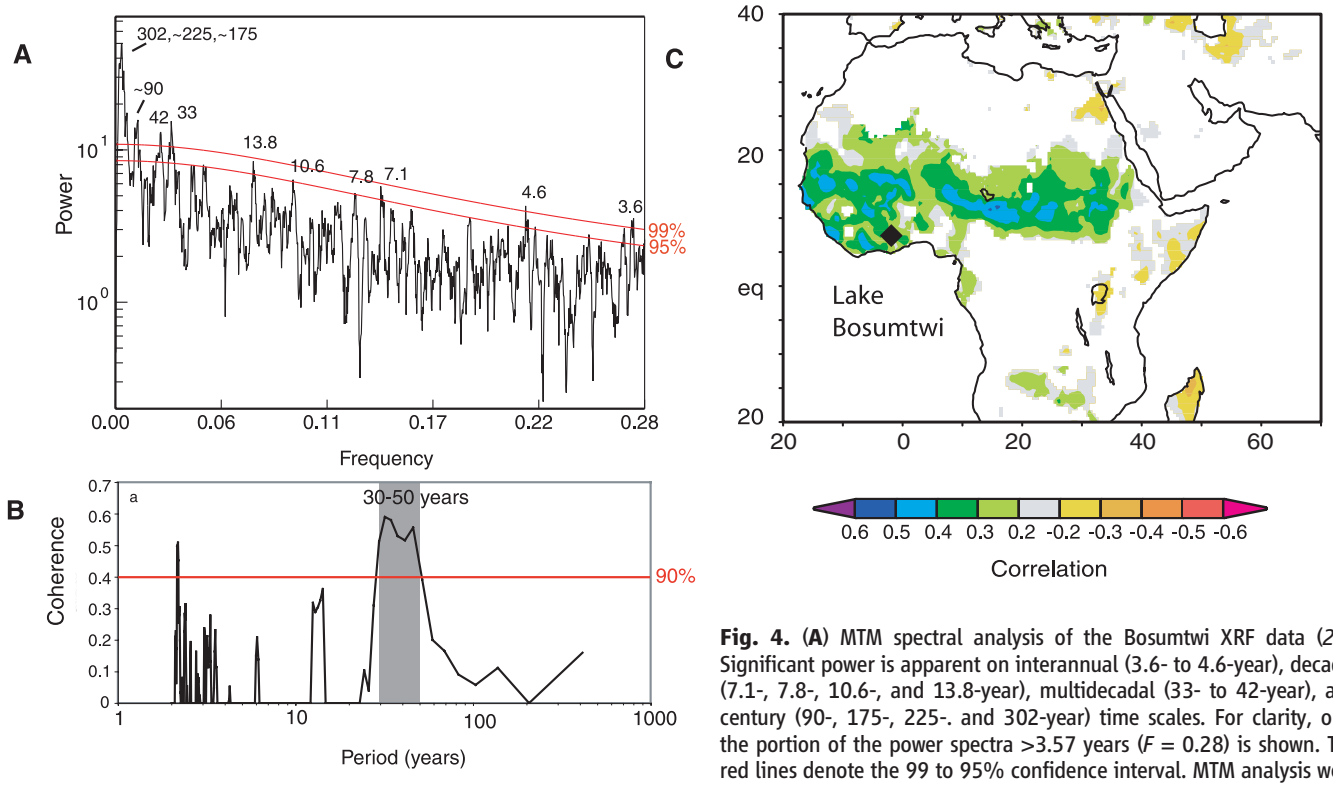

Fig. 4. (**A**) MTM spectral analysis of the Bosumtwi XRF data (*27*). Significant power is apparent on interannual (3.6- to 4.6-year), decadal (7.1-, 7.8-, 10.6-, and 13.8-year), multidecadal (33- to 42-year), and century (90-, 175-, 225-. and 302-year) time scales. For clarity, only the portion of the power spectra >3.57 years (F = 0.28) is shown. The red lines denote the 99 to 95% confidence interval. MTM analysis were performed with the program k-spectra. Parameters p = 3, K = 5, and a null hypothesis of red noise were used in the analysis. Labeled are periods (in years) for peaks that are significant at 95%. (**B**) Cross-spectral coherence computed for Lake Bosumtwi (600-year detrended PC1) and the AMO reconstruction of (*38*). The red horizontal line indicates the 90% confidence interval. The records are in phase and highly coherent at a period of 30 to 50 years (indicated by gray shading). (**C**) Correlations between instrumental records of West African monsoon rainfall (May to October precipitation from the CRU-TS_2.1 data set) (*44*) and the AMO Index [constructed from the HADSST2 dataset (*45*), averaged over the interval from 7° to 75°W and 25° to 60°N for the period 1901–2002], computed with the KMNI Climate Explorer (*46*), suggesting increased precipitation over West Africa (including over Lake Bosumtwi, black diamond) when the AMO is positive (warm anomalies in the North Atlantic).

on Climate Change, S. Solomon *et al.*, Eds. (Cambridge Univ. Press, New York, 2007), pp. 235–336.
2. J. G. Charney, *Q. J. R. Meteorol. Soc.* **101**, 193 (1975).
3. A. Giannini, R. Saravanan, P. Chang, *Science* **302**, 1027 (2003).
4. M. Hoerling, J. Hurrell, J. Eischeid, A. Phillips, *J. Clim.* **19**, 3989 (2006).
5. G. C. Hegerl *et al.*, in *Climate Change: The Physical Science Basis. Contribution of Working Group I to the Fourth Assessment Report of the Intergovernmental Panel on Climate Change* S. Solomon *et al.*, Eds. (Cambridge Univ. Press, New York, 2007) , pp. 663–745.
6. P. K. Swart, K. S. White, D. Enfield, R. E. Dodge, P. Milne, *J. Geophys. Res. -Oceans* **103**, 27885 (1998).
7. Materials and methods are available as supporting material on *Science* Online.
8. T. M. Shanahan *et al.*, *J. Paleolimnol.* **40**, 339 (2008).
9. T. M. Shanahan *et al.*, *Palaeogeogr. Palaeoclimatol. Palaeoecol.* **242**, 287 (2006).
10. T. M. Shanahan *et al.*, *J. Geophys. Res. Atmos.* **113**, D12107 (2008).
11. J. Kutzbach, G. Bonan, J. Foley, S. P. Harrison, *Nature* **384**, 623 (1996).
12. J. E. Kutzbach, Z. Liu, *Science* **278**, 440 (1997).
13. F. Gasse, *Quat. Sci. Rev.* **19**, 189 (2000).
14. D. Jolly, S. P. Harrison, B. Damnati, R. Bonnefille, *Quat. Sci. Rev.* **17**, 629 (1998).
15. S. Weldeab, D. W. Lea, R. R. Schneider, N. Andersen, *Science* **316**, 1303 (2007).
16. S. Weldeab, D. W. Lea, R. R. Schneider, N. Andersen. *Geophys. Res. Lett.* **34**, L24702 (2007).
17. S. Weldeab, R. R. Schneider, M. Kolling, G. Wefer, *Geology* **33**, 981 (2005).
18. E. Jansen *et al.*, in *Climate Change: The Physical Science Basis. Contribution of Working Group I to the Fourth Assessment Report of the Intergovernmental Panel on Climate Change* S. Solomon *et al.*, Eds. (Cambridge Univ. Press, New York, 2007), pp. 433–497.
19. D. Verschuren, K. Laird, B. Cumming, *Nature* **403**, 410 (2000).
20. J. M. Russell, D. Verschuren, H. Eggermont, *Holocene* **17**, 183 (2007).
21. J. M. Russell, T. C. Johnson, *Geology* **35**, 21 (2007).
22. A. Newton, R. Thunell, L. Stott, *Geophys. Res. Lett.* **33**, L19710 (2006).
23. D. M. Anderson, J. T. Overpeck, A. K. Gupta, *Science* **297**, 596 (2002).
24. A. K. Gupta, D. M. Anderson, J. T. Overpeck, *Nature* **421**, 354 (2003).
25. Y. Wang *et al.*, *Science* **308**, 854 (2005).
26. G. H. Haug, K. A. Hughen, D. M. Sigman, L. C. Peterson, U. Rohl, *Science* **293**, 1304 (2001).
27. M. E. Mann, J. Lees, *Clim. Change* **33**, 409 (1996).
28. C. Torrence, G. P. Compo, *Bull. Am. Meteorol. Soc.* **79**, 61 (1998).
29. M. Ghil *et al., Rev. Geophys.* **40**, 3.1 (2002).
30. M. Stuiver *et al.*, *Radiocarbon* **40**, 1041 (1998).
31. D. C. Lund, J. Lynch-Stieglitz, W. B. Curry, *Nature* **444**, 601 (2006).
32. M. Vellinga, P. Wu, *J. Clim.* **17**, 4498 (2004).
33. M. A. Cane, *Annu. Rev. Earth Planet. Sci.* **14**, 43 (1986).
34. P. Chang, Y. Fang, R. Saravanan, L. Ji, H. Seidel, *Nature* **443**, 324 (2006).
35. D. E. Black *et al.*, *Science* **286**, 1709 (1999).
36. P. Chang, L. Ji, H. Li, *Nature* **385**, 516 (1997).
37. C. K. Folland, T. N. Palmer, D. E. Parker, *Nature* **320**, 602 (1986).
38. S. T. Gray, L. J. Graumlich, J. L. Betancourt, G. T. Pederson, *Geophys. Res. Lett.* **31**, L12005 (2004).
39. A. Grinsted, J. C. Moore, S. Jevrejeva, *Nonlinear Process. Geophys.* **11**, 561 (2004).
40. G. E. Brooks, *Landlords and Strangers: Ecology, Society, and Trade in West Africa, 1000-1630* (Westview Press, Boulder, CO, 1993).
41. R. Kuper, S. Kröpelin, *Science* **313**, 803 (2006).
42. R. J. Stouffer *et al.*, *J. Clim.* **19**, 1365 (2006).
43. Intergovernmental Panel on Climate Change, *Climate Change: The Physical Science Basis. Contribution of Working Group I to the Fourth Assessment Report of the Intergovernmental Panel on Climate Change*, S. Solomon *et al.*, Eds. (Cambridge Univ. Press, New York, 2007), pp. 21–91.
44. T. D. Mitchell, P. D. Jones, *Int. J. Climatol.* **25**, 693 (2005).
45. N. A. Rayner *et al.*, *J. Clim.* **19**, 446 (2006).
46. G. J. v. Oldenborgh, G. Burgers, *Geophys. Res. Lett.* **32**, L15701 (2005).

47. This research was funded in part by the following grants from NSF: EAR0601998, ATM0401908, ATM0214525, and ATM0096232. K.J.A. and T.M.S. were partially supported during this research by the NSF Integrative Graduate Education and Research Traineeship Program DGE0221594.

Supporting Online Material

www.sciencemag.org/cgi/content/full/324/5925/377/DC1
Materials and Methods
SOM Text
Figs. S1 to S5
References

24 September 2008; accepted 5 March 2009
10.1126/science.1166352

Protection of *C. elegans* from Anoxia by HYL-2 Ceramide Synthase

Vincent Menuz,[1] Kate S. Howell,[2,3] Sébastien Gentina,[1] Sharon Epstein,[2] Isabelle Riezman,[2] Monique Fornallaz-Mulhauser,[1] Michael O. Hengartner,[4] Marie Gomez,[5]* Howard Riezman,[2]*† Jean-Claude Martinou[1]*†

Oxygen deprivation is rapidly deleterious for most organisms. However, *Caenorhabditis elegans* has developed the ability to survive anoxia for at least 48 hours. Mutations in the DAF-2/DAF-16 insulin-like signaling pathway promote such survival. We describe a pathway involving the HYL-2 ceramide synthase that acts independently of DAF-2. Loss of the ceramide synthase gene *hyl-2* results in increased sensitivity of *C. elegans* to anoxia. *C. elegans* has two ceramide synthases, *hyl-1* and *hyl-2*, that participate in ceramide biogenesis and affect its ability to survive anoxic conditions. In contrast to *hyl-2(lf)* mutants, *hyl-1(lf)* mutants are more resistant to anoxia than normal animals. HYL-1 and HYL-2 have complementary specificities for fatty acyl chains. These data indicate that specific ceramides produced by HYL-2 confer resistance to anoxia.

The molecular pathways underlying resistance of *Caenorhabditis elegans* to oxygen deprivation (*1*–*8*) appear to be conserved, at least in part, between vertebrates and invertebrates. These pathways differ in *C. elegans* according to the developmental stage and oxygen tension. For example, hypoxia-inducing factor 1 (HIF-1) is not required for resistance of either nematode embryos (*2*) or young adults (table S1) to anoxia. However, it stimulates survival of embryos to hypoxia (*9*). On the other hand, mutation of the *daf-2* gene, an insulin and insulin-like growth factor receptor–like gene, promotes survival of *C. elegans* to hypoxia or anoxia (*1*, *5*), an effect that is mediated by the glyceraldehyde-3-phosphate dehydrogenases GPD-2 and GPD-3 (*5*). In *C. elegans*, mutations have not been detected that cause a reduction in viability under anoxia in adult hermaphrodites (*5*). We sought to identify essential components of the pathways regulating the adaptation of *C. elegans* to anoxia.

We tested the ability of young adult wild-type N2 Bristol *C. elegans* (72 hours after the L1 stage grown at 20°C) to survive anoxia at 20°C (0.001% O_2). Survival rates were 99.5% ± 1.5% ($n > 5$), 81% ± 14.5% ($n > 5$), and 8.5% ± 9.5% ($n > 5$) after 24, 48, and 72 hours of anoxia, respectively (Fig. 1A). Animals that failed to survive anoxia became rodlike and showed the presence of propidium iodide–stained necrotic cells throughout their entire body (Fig. 1B).

In order to identify genes required for resistance to anoxia, we screened a library of mutants for animals with increased sensitivity to anoxia (table S1). After eliminating a role for other mutations in the initial mutant line, we characterized a mutation in the homolog of yeast longevity assurance gene 2 (*hyl-2* gene), *hyl-2(gnv1)* (*10*) (fig. S1), that conferred increased sensitivity to anoxia (Fig. 1C and fig. S2). The mutation consists of two consecutive base substitutions at positions 1297 and 1298 (CATCAT → CAATAT) that result in the conversion of $His^{168}His^{169}$ residues into $Gln^{168}Tyr^{169}$ in the Lag motif of HYL-2. Sensitivity to anoxia was also observed in *hyl-2(tm2031)* mutants carrying a deletion of the *hyl-2* gene (Fig. 1C). Both *hyl-2(gnv1)* and *hyl-2(tm2031)* mutants were indistinguishable from N2 animals and had a normal fecundity and life span (fig. S3). *hyl-2(gnv1)* mutants, as *hyl-2(tm2031)*, were also more sensitive to heat shock at 36°C (fig. S4A) but had normal responses to thermal stress at 30°C for 7 days and to hypotonic shock (fig. S4, B and C). Introduction in *hyl-2(gnv1)* animals of a green fluorescent protein (GFP)*::WT hyl-2* transgene under the control of the endogenous *hyl-2* promoter (fig. S5C) showed gene expression from the larval to the adult stage with strong expression in the gut, the posterior bulb of the pharynx, the hypoderm, and unidentified cells of the head and the tail (Fig. 2A). Expression of the transgene partially restored resistance to anoxia and heat shock in *hyl-2(gnv1)* animals (Fig. 2B and fig. S4D). Collectively these experiments indicate that *hyl-2* is required for adaptation of the nematode to anoxia.

hyl-2 belongs to a eukaryotic gene family known as longevity assurance genes (*Lass* genes, fig. S6). Several members encode dihydroceramide synthases for the de novo ceramide pathway (*11*) and are therefore called ceramide synthase (CerS) genes (*12*). These genes have sequence similarity in a domain called the Lag motif that is essential for enzyme activity (fig. S6) (*13*). In *Saccharomyces cerevisiae*, *LAG1* and *LAC1* are required for de novo ceramide synthase activity, and yeast lacking both genes are almost inviable. *C. elegans* has three ceramide synthase genes, *hyl-1*, *hyl-2*, and *lagr-1*. Simultaneous deletion of both *hyl-1* and *hyl-2* is lethal (*10*). Sphingolipids from *C. elegans* are somewhat different from their counterparts in other eukaryotes because they contain exclusively isosphingoid bases (*14*), which are presumably used by the dihydroceramide synthases from worms. Nevertheless, *hyl-1* can complement the loss of function of yeast *LAG1* and *LAC1* (*15*). To test whether HYL-2 is a ceramide synthase, we transformed *lag1Δlac1Δ* yeast with an expression vector carrying the cDNA of either *LAG1*, *hyl-1*, or *hyl-2*. All expression vectors rescued the growth phenotype of *lag1Δlac1Δ* strain (Fig. 2C), indicating that *hyl-2*, like *hyl-1*, is an ortholog of *LAG1*. Expression of *hyl-2(gnv1)*

[1]Department of Cell Biology, University of Geneva, CH-1211 Geneva 4, Switzerland. [2]Department of Biochemistry, University of Geneva, CH-1211 Geneva 4, Switzerland. [3]Faculty of Land and Food Resource, University of Melbourne, Parkville Victoria 3010, Australia. [4]Institute of Molecular Biology, University of Zurich, Winterthurerstrasse, CH-8057 Zurich, Switzerland. [5]Department of Zoology and Animal Biology, University of Geneva, CH-1211 Geneva 4, Switzerland.

*These authors contributed equally to this work.
†To whom correspondence should be addressed. E-mail: Howard.Riezman@unige.ch (H.R.); Jean-Claude.Martinou@unige.ch (J.-C.M.)

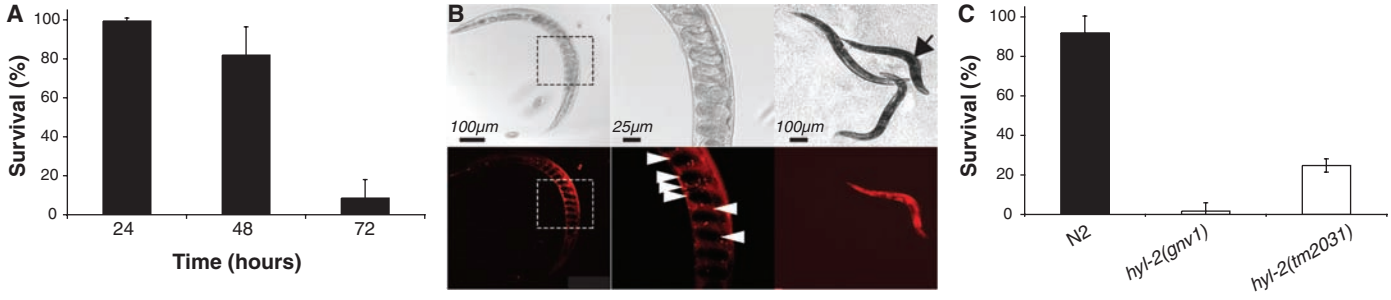

Fig. 1. The *hyl-2(gnv1)* mutation confers hypersensitivity to anoxia in *C. elegans*. (**A**) Survival of wild-type Bristol N2 animals exposed to anoxia for 24, 48, and 72 hours. Results are mean ± SD, $n > 5$. (**B**) Young adults N2 worms were stained with propidium iodide postanoxia and observed with a fluorescent microscope. After 16 hours of anoxia, dead worms displayed stained nuclei (white arrowhead) throughout the cell body (left and middle images). At 48 hours of anoxia, dead animals (top right image, black arrow) were intensively stained as a result of necrosis in all tissues, whereas living animals were unstained (top right image). (**C**) Survival of *hyl-2(gnv1)* and *hyl-2(tm2031)* mutants after 48 hours of anoxia (mean ± SD, $n > 5$).

cDNA in *lag1Δlac1Δ* yeast failed to rescue the lethal phenotype, demonstrating that His^{168}, His^{169}, or both are required for HYL-2 function (Fig. 2C). This result supports previous reports on the essential function of the evolutionarily conserved His residues of the Lag motif (*13*, *16*). Thus, the inability of *hyl-2* mutants to adapt to oxygen deprivation appears to result from a loss of function of the HYL-2 ceramide synthase.

In contrast to *hyl-2* deficient animals, *hyl-1(gk203)* and *hyl-1(ok976)* deletion mutants (fig. S5A) resisted anoxia better than N2 worms (Fig. 3, A and B) (*17*). We therefore tested whether HYL-1 could substitute for HYL-2 in *hyl-2*–deficient worms. We fused *hyl-1* to a sequence encoding GFP and expressed the construct under the control of *hyl-2* promoter. This ensured appropriate temporal and spatial expression of the *GFP::hyl-1* transgene (fig. S5D). Expression of the *GFP::hyl-1* transgene conferred a small protection against anoxia but was significantly less efficient than the *GFP::hyl-2* transgene (Fig. 3C). This finding was confirmed in three different transgenic lines, making it unlikely that suboptimal expression of the *GFP::hyl-1* transgene was responsible for the weak beneficial effect. Thus, although HYL-1 can complement growth defects in yeast as efficiently as does HYL-2, it cannot completely substitute for HYL-2 to confer strong resistance to anoxia. Thus, anoxia tolerance may require one or more ceramide species that are either specifically or preferentially synthesized by HYL-2.

Dihydroceramide synthases combine a sphingoid base with a fatty acyl–coenzyme A (CoA) to form dihydroceramide, which is then desaturated by a dihydroceramide desaturase into ceramide in animals. In many organisms, multiple ceramide synthases are expressed, each displaying fatty acyl-CoA specificity to produce a diversity of ceramides differing in their fatty acyl chains (*18*–*20*). Ceramides are the precursors for sphingolipids, including sphingomyelins, which are present in *C. elegans* (*14*). We quantified the major ceramide (Cer) and sphingomyelin (SM) species of *C. elegans* N2, *hyl-1(ok976)*, and *hyl-2(gnv1)* animals by electrospray ionization mass spectrometry (ESI-MS). *hyl-1(ok976)* and *hyl-2(gnv1)* mutants expressed different types of Cers and SMs than N2 worms did (Fig. 4, fig. S7, and table S2). *hyl-2*–deficient worms [*hyl-2(gnv1)*] had fewer Cers and SMs with C_{20} to C_{22} fatty acyl chains and more with C_{24} to C_{26} fatty acyl chains than did N2 animals. In contrast, *hyl-1*–deficient worms [*hyl-1(ok976)*] expressed more C_{20} to C_{22} Cers and SMs than did N2 worms, but they contained the same or lesser amounts of C_{24} to C_{26} Cers and SMs. These data indicated that efficient synthesis of C_{20} to C_{22} Cers requires HYL-2 whereas that of C_{24} to C_{26} Cers is mainly dependent on HYL-1. To verify this, we measured dihydroceramide synthase activity in microsomes isolated from N2 and mutant worms with ^{3}H-sphinganine and acyl-CoA substrates of various lengths (fig. S8, A and C). Membranes from *hyl-2(tm2031)* mutants catalyzed synthesis of more C_{26} Cers, whereas membranes from *hyl-1(ok976)* mutants catalyzed synthesis of more C_{22} Cers. All membranes were equally active with use of C_{24}-acyl CoA (fig. S8B). These results are consistent with the ESI-MS results and confirm that the two Cer synthases have

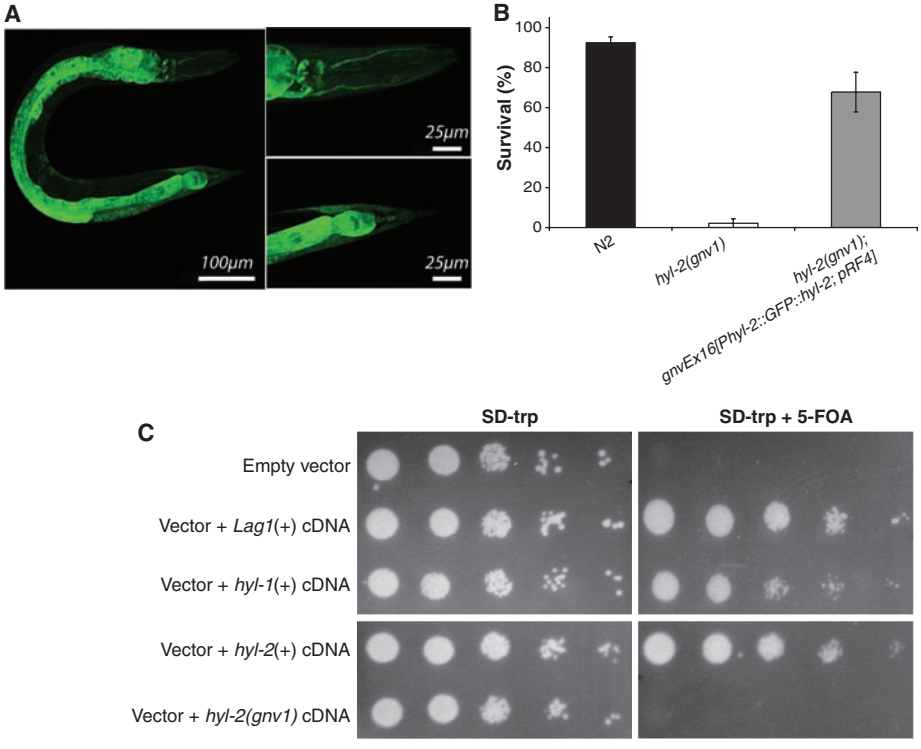

Fig. 2. Sensitivity to anoxia results from loss of function of HYL-2 ceramide synthase. (**A**) GFP staining of *hyl-2(gnv1)* adult animals expressing the transgene *GFP::hyl-2* under the control of the *hyl-2* promoter. (**B**) Survival after 48 hours of anoxia of *hyl-2(gnv1)* animals complemented with the transgene *GFP::hyl-2* under the control of the *hyl-2* promoter (mean ± SD, $n > 5$). (**C**) Functional complementation of mutant yeast cells by *C. elegans hyl-1* and *hyl-2* in *lag1Δlac1Δ S. cerevisiae* transformed with pRS424–*hyl-1*, pRS424–*hyl-2*, and pRS424–*hyl-2(gnv1)* (*TRP1* plasmid). The compound 5-FOA (5-fluorouracil-6-carboxylic acid monohydrate) is a counterselection for cells that carry the *URA3*-based plasmid with yeast *LAG1*. Therefore, only cells that have lost this plasmid can grow, making growth dependent on function of the heterologous ceramide synthase.

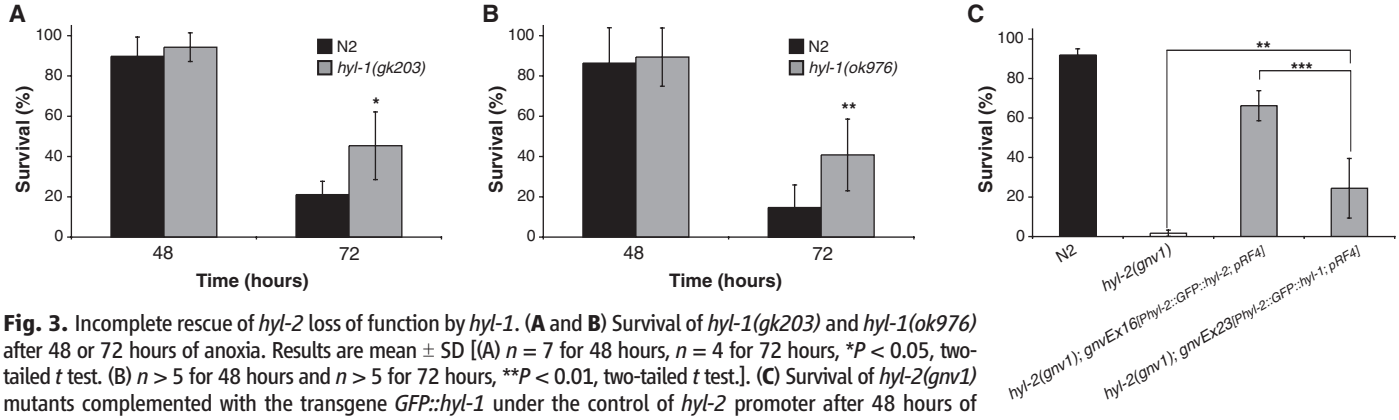

Fig. 3. Incomplete rescue of *hyl-2* loss of function by *hyl-1*. (**A** and **B**) Survival of *hyl-1(gk203)* and *hyl-1(ok976)* after 48 or 72 hours of anoxia. Results are mean ± SD [(A) $n = 7$ for 48 hours, $n = 4$ for 72 hours, $^*P < 0.05$, two-tailed *t* test. (B) $n > 5$ for 48 hours and $n > 5$ for 72 hours, $^{**}P < 0.01$, two-tailed *t* test.]. (**C**) Survival of *hyl-2(gnv1)* mutants complemented with the transgene *GFP::hyl-1* under the control of *hyl-2* promoter after 48 hours of anoxia. Results are mean ± SD, $n > 5$, $^{**}P < 0.01$, $^{***}P < 0.001$, analysis of variance (ANOVA) test.

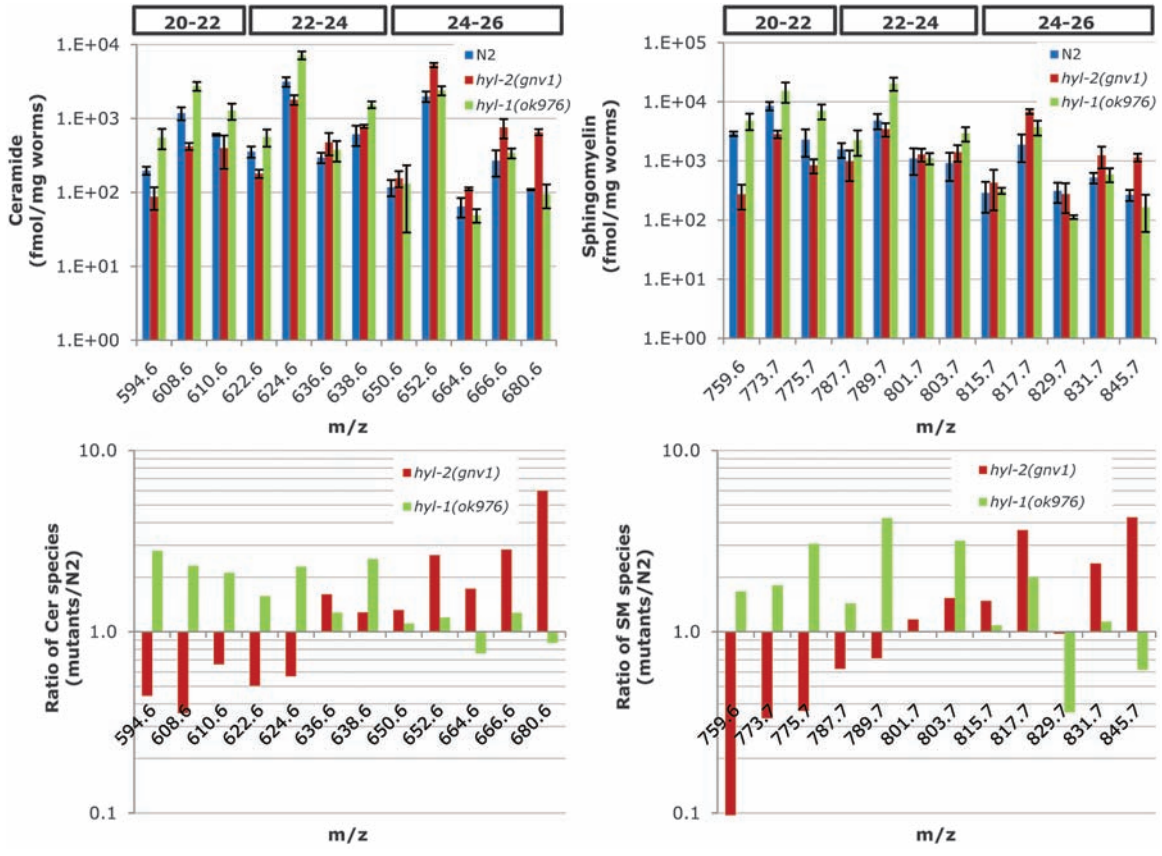

Fig. 4. Ceramide, sphingomyelin, and phosphatidylcholine (PC) quantification in N2, *hyl-2(gnv1)*, and *hyl-1(ok976)* worms. Cers, SMs, and PC species were quantified by ESI-MS (see fig. S7 for quantification of PC species). Cers and SMs were quantified after base hydrolysis of glycerophospholipids (*23*). Graphs of the amounts are shown on a logarithmic scale ± SD (n = 4). The amount of each lipid species found in mutant worms was divided by the amount found in wild-type Bristol N2 worms and shown in a graph below the corresponding graph of the total amounts. Acyl chain lengths corresponding to charge/mass (m/z) values are shown in boxes (see also table S2). The entire profiles of Cer and SM species of N2, *hyl-2(gnv1)*, and *hyl-1(ok976)* animals are different with P = 0.002 for Cers and P = 0.007 for SMs (multivariate ANOVA test).

different specificities for fatty acyl chains. They indicate that HYL-2 may promote survival of animals in anoxic conditions by producing C_{20} to C_{22} Cers and SMs. In support of this hypothesis, the *hyl-1(ok976)* mutant worms produced larger total amounts of Cers and SMs than did N2 and *hyl-2(gnv1)* mutants (fig. S9A). Moreover, expression of the *GFP::hyl-1* transgene under the control of the *hyl-2* promoter in *hyl-2(gnv1)* worms failed to restore normal amounts of C_{20} to C_{22} ceramides (fig. S9B), which could explain why the transgene did not restore normal resistance to anoxia in *hyl-2(gnv1)* animals.

Ceramides function in radiation-induced apoptosis of cells in the germ line (*21*). However, apoptosis appears not to account for the sensitivity of HYL-2–deficient animals to anoxia because lack of CED-3 caspase activity in *ced-3(n717);hyl-2(gnv1)* double mutants did not extend survival of these animals during anoxia (fig. S10). Sphingosine 1-phosphate, an anti-apoptotic derivative of ceramide, also appears not to function in resistance to anoxia because resistance of *sphk-1(ok1097)* animals, in which conversion of isosphingosine to isosphingosine 1-phosphate is prevented by a null allele of sphingosine kinase, was normal and those of *sphk-1(ok1097);hyl-1(ok976)* and *sphk-1(ok1097);hyl-2(tm2031)* double mutants were not modified (fig. S11, A and B). A block in ceramide synthase is expected to lead to an increase in isosphingoid bases, which are ceramide precursors. Therefore, we examined the amounts of isosphingoid bases in the *sphk-1(ok1097)* and *hyl* mutants by MS-ESI. Isosphingoid bases accumulated in *hyl-2* mutants and were less abundant in *hyl-1* mutants (fig. S11C). However, *sphk-1(ok1097)* worms accumulated even more isosphingoid bases than either *hyl* mutant but adapted to anoxia normally (fig. S11, A to C), suggesting that accumulation of isosphingoid bases did not influence survival under anoxic conditions.

The *daf-2/daf-16* insulin-like signaling pathway is involved in oxygen deprivation survival in *C. elegans* (*1*, *5*). We also found that *daf-2(e1370)* mutants survived 72 hours of anoxia better than did N2 worms (fig. S12A). To determine whether *hyl-2* and *daf-2* interact genetically, we generated *daf-2(e1370);hyl-2(gnv1)* double mutants and tested their sensitivity to 48 hours of anoxia. Resistance of the double mutants was significantly improved compared with that of *hyl-2(gnv1)* mutants, whereas it was decreased compared with that of *daf-2(e1370)* mutants (fig. S12B). Thus, it appears that, with respect to anoxia resistance, HYL-2 and DAF-2 are acting in parallel pathways that mutually influence each other.

We have shown that a dihydroceramide synthase, with a distinct substrate specificity, provides an important function in the anoxia response in *C. elegans*. Rather than their quantity, it is the chemical structure of ceramide species that seems to be important for resistance to anoxia. Ceramides have been reported previously to be effectors of kinases or phosphatases in various biological processes (*22*). It is most likely that the activity of key ceramide species during anoxia relies on interaction of ceramides with other molecules integrated in a cell survival pathway.

References and Notes

1. B. A. Scott, M. S. Avidan, C. M. Crowder, *Science* **296**, 2388 (2002); published online 13 June 2002 (10.1126/science.1072302).
2. P. A. Padilla, T. G. Nystul, R. A. Zager, A. C. Johnson, M. B. Roth, *Mol. Biol. Cell* **13**, 1473 (2002).
3. T. G. Nystul, J. P. Goldmark, P. A. Padilla, M. B. Roth, *Science* **302**, 1038 (2003).
4. C. Shen, D. Nettleton, M. Jiang, S. K. Kim, J. A. Powell-Coffman, *J. Biol. Chem.* **280**, 20580 (2005).
5. A. R. Mendenhall, B. LaRue, P. A. Padilla, *Genetics* **174**, 1173 (2006).
6. D. Hoogewijs *et al.*, *BMC Genom.* **8**, 356 (2007).
7. N. Dasgupta, A. M. Patel, B. A. Scott, C. M. Crowder, *Curr. Biol.* **17**, 1954 (2007).
8. V. A. Hajeri, A. M. Stewart, L. L. Moore, P. A. Padilla, *Cell Div.* **3**, 6 (2008).
9. H. Jiang, R. Guo, J. A. Powell-Coffman, *Proc. Natl. Acad. Sci. U.S.A.* **98**, 7916 (2001).
10. Materials and methods are available as supporting material on *Science* Online.
11. B. Vallee, H. Riezman, *EMBO J.* **24**, 730 (2005).
12. Y. Pewzner-Jung, S. Ben-Dor, A. H. Futerman, *J. Biol. Chem.* **281**, 25001 (2006).
13. N. Kageyama-Yahara, H. Riezman, *Biochem. J.* **398**, 585 (2006).
14. D. J. Chitwood, W. R. Lusby, M. J. Thompson, J. P. Kochansky, O. W. Howarth, *Lipids* **30**, 567 (1995).
15. J. C. Jiang, P. A. Kirchman, M. Zagulski, J. Hunt, S. M. Jazwinski, *Genome Res.* **8**, 1259 (1998).
16. S. Spassieva *et al.*, *J. Biol. Chem.* **281**, 33931 (2006).

17. The lifespan of *hyl-1(lf)* mutants is shown in fig. S3.
18. Y. Mizutani, A. Kihara, Y. Igarashi, *Biochem. J.* **390**, 263 (2005).
19. Y. Mizutani, A. Kihara, Y. Igarashi, *Biochem. J.* **398**, 531 (2006).
20. C. Riebeling, J. C. Allegood, E. Wang, A. H. Merrill Jr., A. H. Futerman, *J. Biol. Chem.* **278**, 43452 (2003).
21. X. Deng *et al.*, *Science* **322**, 110 (2008).
22. Y. A. Hannun, L. M. Obeid, *Nat. Rev. Mol. Cell Biol.* **9**, 139 (2008).
23. B. Zanolari *et al.*, *EMBO J.* **19**, 2824 (2000).
24. We thank F. Solary for help with analysis of aging; Y. Mattenberger and D. Courvoisier from the Clinical Research Center University of Geneva and Geneva University Hospitals for statistical support; S. Herzig for artwork; S. Mitani and the Japanese National Bioresource Project for tm strains; and J. Hodgkin for providing strains CB5670, CB6166, CB5439, and CB5430. Some nematodes were provided by the *Caenorhabditis* Genome Center, which is funded by the NIH National Center for Research Resources. This work was funded by the Swiss National Science Foundation [subsidies 3100A0-109419/2 (J.-C.M.), 3100A0-114189 (H.R.), 3100A0-105907/1 (M.G.), and 3100A0-113889 (M.O.H.)], the Human Frontiers Science Program Organization (H.R.), the Swiss SystemsX.ch initiative (H.R.) evaluated by the Swiss National Science Foundation, the Roche Foundation (V.M.), Ernest Boninchi subsidy for the purchase of the anoxic chamber, the Canton of Zurich (M.O.H.), the Ernst Hadorm Foundation (M.O.H.), and the Geneva Department of Education.

Supporting Online Material

www.sciencemag.org/cgi/content/full/324/5925/381/DC1
Materials and Methods
Figs. S1 to S12
Tables S1 and S2
References

14 November 2008; accepted 25 February 2009
10.1126/science.1168532

Sequential Regulation of DOCK2 Dynamics by Two Phospholipids During Neutrophil Chemotaxis

Akihiko Nishikimi,[1,2] Hideo Fukuhara,[1] Wenjuan Su,[3] Tsunaki Hongu,[4] Shunsuke Takasuga,[5] Hisashi Mihara,[6] Qinhong Cao,[1]* Fumiyuki Sanematsu,[1] Motomu Kanai,[6] Hiroshi Hasegawa,[4] Yoshihiko Tanaka,[1,2] Masakatsu Shibasaki,[6] Yasunori Kanaho,[4] Takehiko Sasaki,[5] Michael A. Frohman,[3] Yoshinori Fukui[1,2]†

During chemotaxis, activation of the small guanosine triphosphatase Rac is spatially regulated to organize the extension of membrane protrusions in the direction of migration. In neutrophils, Rac activation is primarily mediated by DOCK2, an atypical guanine nucleotide exchange factor. Upon stimulation, we found that DOCK2 rapidly translocated to the plasma membrane in a phosphatidylinositol 3,4,5-trisphosphate–dependent manner. However, subsequent accumulation of DOCK2 at the leading edge required phospholipase D–mediated synthesis of phosphatidic acid, which stabilized DOCK2 there by means of interaction with a polybasic amino acid cluster, resulting in increased local actin polymerization. When this interaction was blocked, neutrophils failed to form leading edges properly and exhibited defects in chemotaxis. Thus, intracellular DOCK2 dynamics are sequentially regulated by distinct phospholipids to localize Rac activation during neutrophil chemotaxis.

Chemotaxis regulates a wide range of biological functions, including developmental morphogenesis, wound healing, and immune responses (*1*). During chemotaxis, filamentous actin (F-actin) polymerizes asymmetrically at the leading edge of the cell, providing the force necessary to extend membrane protrusions in the direction of migration (*1*, *2*). This morphologic polarity is regulated by Rac, a member of the small guanosine triphosphatases (GTPases) that cycle between inactive guanosine diphosphate (GDP)–bound and active guanosine triphosphate (GTP)–bound states (*3*). Rac is preferentially activated at the leading edge (*1*, *4*, *5*), which is achieved in part by regulating the subcellular localization of guanine nucleotide exchange factors (GEFs) (*1*, *3*). The GEFs contain a variety of localization motifs such as pleckstrin homology (PH) domains and the DOCK homology region (DHR)–1, both of which bind to phosphatidylinositol 3,4,5-trisphosphate (PIP_3) (*3*, *6*), a lipid product of phosphoinositide 3-kinases (PI3Ks). Upon stimulation, PIP_3 transiently accumulates at the plasma membrane edge facing the highest level of chemoattractant (*1*, *2*). However, a functional leading edge is established even in neutrophils lacking PI3Kγ, the major generator of PIP_3 in this cell type (*7*, *8*). Thus, other factors may alternately suffice to localize Rac GEFs at the leading edge during neutrophil chemotaxis.

DOCK2 is a member of the CDM family of proteins (*Caenorhabditis elegans*, CED-5; mammals, DOCK180; and *Drosophila melanogaster*, Myoblast city) and is predominantly expressed in hematopoietic cells (*9*). Although DOCK2 does not contain the PH and Dbl homology domains typically found in GEFs, DOCK2 can bind to PIP_3 through its DHR-1 domain (*10*) and mediates the GTP-GDP exchange reaction for Rac by means of its DHR-2 domain (*11*, *12*). DOCK2 is a major Rac GEF that controls motility and polarity during neutrophil chemotaxis (*10*). In response to chemoattractants, neutrophils polarize and accumulate DOCK2 at the plasma membrane edge (fig. S1). To explore the mechanism controlling intracellular DOCK2 dynamics, we first analyzed the role of PIP_3 by crossing PI3Kγ$^{-/-}$ mice with mice that had been made by a "knock-in" strategy to express endogenous DOCK2 as a fusion protein with green fluorescent protein (GFP) (*10*, *13*). When neutrophils from DOCK2-GFP mice were stimulated in suspension with chemotactic factors such as *N*-formyl-Met-Leu-Phe (fMLP) and C5a, DOCK2 rapidly translocated to the plasma membrane at 15 s in the presence, but not in the absence, of PI3Kγ (fig. S2). Thus, the initial membrane translocation of DOCK2 is mediated by PIP_3. However, despite the absence of PI3Kγ expression, DOCK2 and F-actin nonetheless still accumulated preferentially at the pseudopod at later time points (fig. S2).

Phosphatidic acid (PA) is a negatively charged phospholipid that can function as a lipid anchor by binding directly to positively charged sites on effector proteins (*14*). In response to many types of external stimuli, signaling pools of PA are formed through hydrolysis of phosphatidylcholine (PC) by phospholipase D (PLD) or phosphorylation of diacylglycerol (DAG) by diacylglycerol kinase (DGK) (*14*, *15*). Although PLD has been implicated in migratory responses of *Dictyostelium discoideum*, epithelial cells, and neutrophils (*16*–*18*), the mechanistic basis is largely unknown. To investigate whether subcellular localization of DOCK2 is influenced by PLD, GFP-tagged DOCK2 was expressed in human embryonic kidney (HEK) 293T cells with or without coexpression of PLD2, a PLD isoform that localizes primarily to the plasma membrane (*19*). DOCK2 was localized mainly in the cytosol when expressed alone; however, it readily accumulated at the plasma membrane when PLD2 was coexpressed (Fig. 1, A and B). In contrast, the catalytically inactive PLD2 mutant K758R in which Lys^{758} is replaced by Arg (*20*) failed to alter DOCK2 localization (Fig. 1, A and B). Thus, coexpressing PLD2 induces plasma membrane accumula-

[1]Division of Immunogenetics, Department of Immunobiology and Neuroscience, Medical Institute of Bioregulation, Kyushu University, Fukuoka 812-8582, Japan. [2]Core Research for Evolutional Science and Technology (CREST), Japan Science and Technology Agency, Tokyo 102-0075, Japan. [3]Department of Pharmacology, Center for Developmental Genetics, Stony Brook University, Stony Brook, NY 11794–5140, USA. [4]Graduate School of Comprehensive Human Sciences, Institute of Basic Medical Sciences, University of Tsukuba, Ibaraki 305-8575, Japan. [5]Division of Microbiology, Department of Pathology and Immunology, Akita University School of Medicine, Akita 010-8543, Japan. [6]Graduate School of Pharmaceutical Sciences, The University of Tokyo, Tokyo 113-0033, Japan.

*Present address: College of Biological Sciences, China Agricultural University, Beijing 100193, China.
†To whom correspondence should be addressed. E-mail: fukui@bioreg.kyushu-u.ac.jp

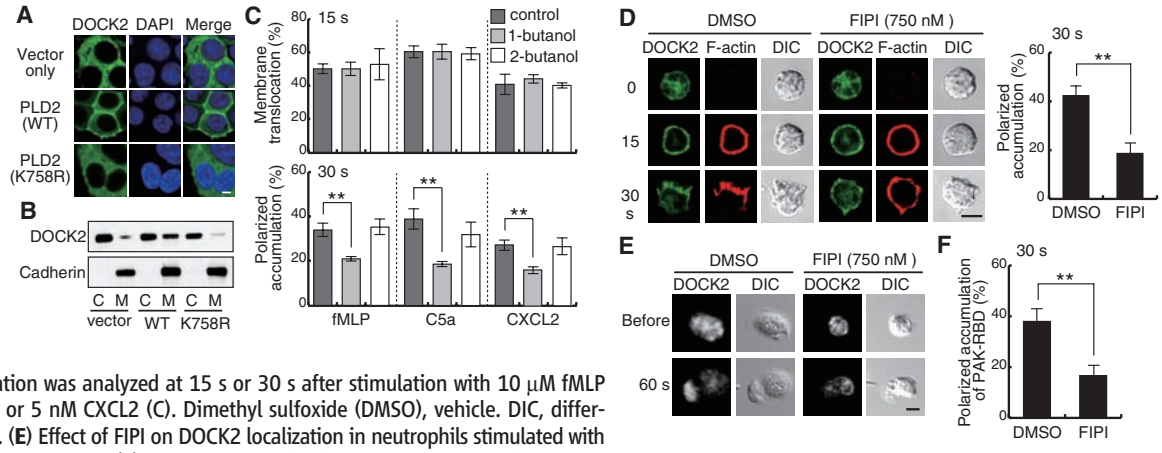

Fig. 1. PA controls DOCK2 localization during neutrophil chemotaxis. (**A** and **B**) Effect of coexpressed PLD2 on localization of GFP-tagged DOCK2 in HEK293T cells. 4′,6′-Diamidino-2-phenylindole (DAPI) was used to stain nuclei. Membrane (M) and cytosol (C) fractions were analyzed by immunoblot. (**C** and **D**) Effect of 0.2% 1-butanol (C) or 750 nM FIPI (D) on DOCK2 localization was analyzed at 15 s or 30 s after stimulation with 10 μM fMLP (C), 25 nM C5a (C and D), or 5 nM CXCL2 (C). Dimethyl sulfoxide (DMSO), vehicle. DIC, differential interference contrast. (**E**) Effect of FIPI on DOCK2 localization in neutrophils stimulated with a micropipette containing 10 μM fMLP. (**F**) Effect of FIPI on localization of GFP-tagged PAK-RBD was analyzed 30 s after stimulation with 25 nM C5a. Data in (C), (D), and (F) are means ± SD of triplicate experiments, in each of which at least 50 cells were analyzed. $^{**}P < 0.01$. Scale bar in (A), (D), and (E), 5 μm.

tion of DOCK2 through a mechanism dependent on its catalytic activity.

Primary alcohols such as 1-butanol compete with water in the hydrolysis of PC by PLD (*15*). To examine whether PLD-generated PA is involved in control of intracellular DOCK2 dynamics, we treated neutrophils of DOCK2-GFP mice with 1-butanol and, as a control, with 2-butanol. In response to fMLP, C5a, and CXCL2, 25 to 35% of neutrophils treated with 2-butanol exhibited polarized morphology with focused distribution of DOCK2. However, treatment with 1-butanol significantly inhibited accumulation of DOCK2 and F-actin at the pseudopods (Fig. 1C and fig. S3). Similar results were obtained when neutrophils were treated with 5-fluoro-2-indolyl des-clorohalopemide (FIPI), a PLD-specific inhibitor (*21*) (Fig. 1D), but not with the DGK inhibitor R59 022 (fig. S4). Although DOCK2 accumulated at the leading edge in control cells in response to a point source of fMLP, the majority of neutrophils treated with 1-butanol or FIPI displayed aberrant morphology with extremely thin lamellae and poorly focused DOCK2 distribution (Fig. 1E and fig. S5). Moreover, treatment with 1-butanol or FIPI impaired localization to the pseudopods of a fluorescent probe that detects activated Rac, the GFP-tagged Rac-binding domain (RBD) of p21-activated kinase (PAK) (*22*) (Fig. 1F and fig. S6). On the other hand, neither 1-butanol nor FIPI inhibited the initial membrane translocation of DOCK2 (Fig. 1, C and D). Thus, PA acts selectively in the late phase to control polarized DOCK2 localization during neutrophil chemotaxis.

Exogenous PA added to culture medium is rapidly incorporated into the plasma membrane and can elicit cellular responses (*23*) (fig. S7). Wild-type (WT) neutrophils treated with PA exhibited polarized morphology with focused distribution of F-actin (Fig. 2A). This morphological change appeared to be mediated by PA itself, because other phospholipids including lysophosphatidic acid (LPA) and DAG, the two major metabolites of PA, failed to induce actin polymerization (Fig. 2B and fig. S8). The effect of PA was insensitive to pertussis toxin, an inhibitor of G_i and G_o proteins (fig. S9), and PA addition did not increase phosphorylation of Akt, a downstream effector of PI3Ks (fig. S10). However, PA-induced DOCK2 accumulation and actin polymerization were attenuated by treating neutrophils with the PI3K inhibitor wortmannin (Fig. 2C and fig. S11), and the ability of PA to stimulate F-actin assembly and morphologic change was almost totally lost for DOCK2$^{-/-}$ neutrophils (Fig. 2A). Thus, PA induces actin polymerization in unstimulated neutrophils and makes "micropolarity" visible in a manner dependent on both basal PI3K activity and DOCK2.

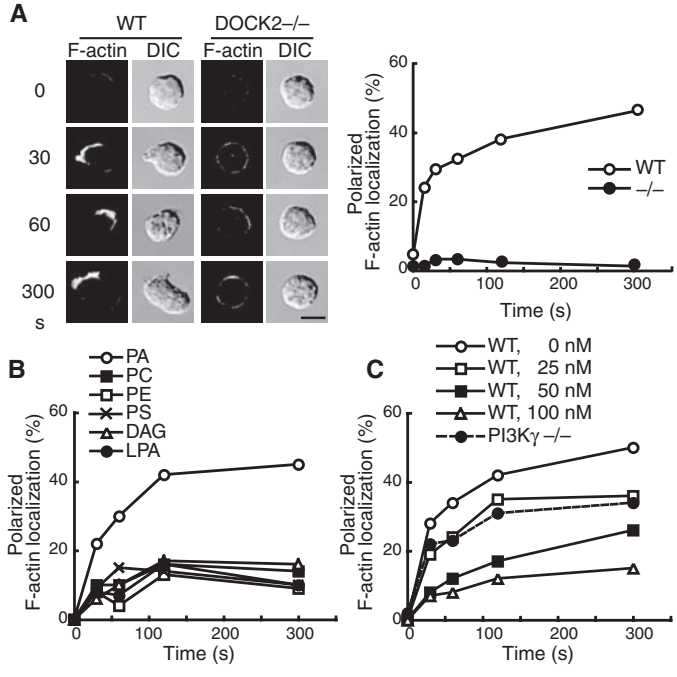

Fig. 2. Exogenous PA induces actin polymerization through a mechanism dependent on DOCK2. (**A**) WT or DOCK2$^{-/-}$ neutrophils were stimulated with PA (10 μg/ml). Scale bar, 5 μm. (**B**) WT neutrophils were stimulated with varied phospholipids (10 μg/ml). (**C**) WT or PI3Kγ$^{-/-}$ neutrophils were stimulated with PA (10 μg/ml) at the indicated concentrations of wortmannin. At least 100 cells were analyzed in each experiment.

This finding led us to examine whether DOCK2 physically interacts with PA. Although no binding was found when HEK293T cell lysates containing DOCK2 were incubated with lipid vesicles composed solely of PC and phosphatidylethanolamine (PE), DOCK2 bound to PA-containing vesicles in a concentration-dependent manner (Fig. 3A). The PA binding was almost totally abolished by deleting the C-terminal 214 amino acid residues (1615 to 1828) (DOCK2-ΔC) (Fig. 3A), and the C-terminal fragment bound in vitro to lipid vesicles containing PA (Fig. 3B) but not to other acidic phospholipids including PIP_3, phosphatidylserine (PS), and phosphatidylinositol 4,5-bisphosphate [$PI(4,5)P_2$] (fig. S12). Thus, the C-terminal region of DOCK2 interacts directly and selectively with PA.

The only motif known for PA-binding proteins is the presence of one or more basic amino acid residues (*14*). Both mouse and human DOCK2 encode the amino acid sequence Ser-Lys-Lys-Arg (residues 1696 to 1699), which mediates PA binding for the yeast protein Opi1p (*24*). When the three basic residues were all mu-

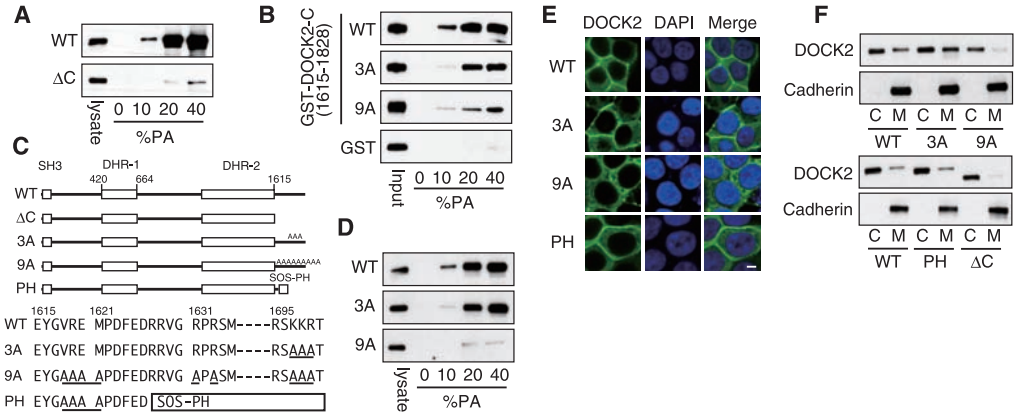

Fig. 3. DOCK2 binds to PA through the C-terminal polybasic amino acid cluster. (**A**) Extracts from HEK293T cells expressing GFP-tagged DOCK2-WT or DOCK2-ΔC were pulled down with PA-containing lipid vesicles. (**B**) Glutathione *S*-transferase (GST) fusion proteins encoding the C-terminal fragment of DOCK2 or its mutants were pulled down with PA-containing lipid vesicles. (**C**) Schematic representation of DOCK2 mutants used in this study (*20*). The mutated amino acid residues are underlined. (**D**) The ability to bind to PA was assayed for DOCK2-WT and its mutants as in (**A**). (**E** and **F**) Localization of DOCK2-WT or its mutants was visualized in HEK293T cells overexpressing PLD2. Scale bar, 5 μm.

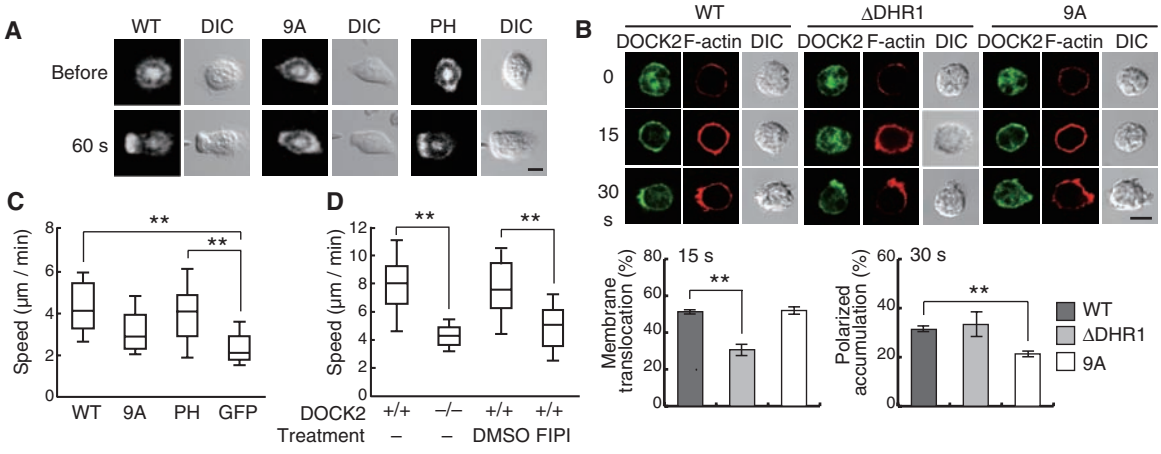

Fig. 4. The DOCK2-PA interaction is required to stabilize the leading edge during neutrophil chemotaxis. (**A**) DOCK2$^{-/-}$ neutrophils expressing GFP-tagged DOCK2 constructs were stimulated with a micropipette containing 10 μM fMLP. (**B**) WT neutrophils expressing GFP-tagged DOCK2 constructs were stimulated with C5a (25 nM). Data are means ± SD of triplicate experiments, in each of which at least 50 cells were analyzed. $^{**}P < 0.01$. (**C**) After expression of GFP-tagged DOCK2 constructs or GFP alone, DOCK2$^{-/-}$ neutrophils were allowed to migrate in an EZ-Taxiscan chamber along an fMLP gradient (0 to 50 μM). The migration speed was analyzed for at least 24 GFP-positive cells that moved more than 20 μm over 15 min. $^{**}P < 0.01$. (**D**) WT or DOCK2$^{-/-}$ neutrophils were allowed to migrate as in (C) in the presence or absence of FIPI (750 nM). The migration speed was analyzed for at least 40 cells. $^{**}P < 0.01$. Scale bar in (A) and (B), 5 μm.

tated to Ala (designated 3A), PA binding was diminished, but only to a modest extent (Fig. 3B). However, by mutating six additional resides to Ala (designated 9A), we found that the binding capacity of the DOCK2 C-terminal fragment to PA decreased to 20% of the WT level (Fig. 3, B and C). Similar results were obtained when full-length DOCK2 protein bearing the 9A mutations (DOCK2-9A) was assayed for PA binding (Fig. 3D). Although the expression of DOCK2-9A in HEK293T cells induced Rac activation fully (fig. S13), the DOCK2-9A failed to localize to the plasma membrane even when PLD2 was coexpressed (Fig. 3, E and F). In contrast, when the C-terminal region of DOCK2 was replaced with a known PA-binding module, the PH domain of Son of sevenless (SOS) (*25*) (Fig. 3C and fig. S14), this chimeric molecule (DOCK2-PH) accumulated effectively at the plasma membrane in the presence of PLD2 (Fig. 3, E and F). Thus, PA controls subcellular localization of DOCK2 by directly binding to the C-terminal polybasic amino acid cluster.

We next examined whether the DOCK2-PA interaction is functionally important by expressing GFP-tagged DOCK2-WT, DOCK2-9A, or DOCK2-PH in DOCK2$^{-/-}$ neutrophils. Although more than 85% of DOCK2$^{-/-}$ neutrophils expressing DOCK2-WT or DOCK2-PH extended lamellipodia containing accumulated DOCK2 toward the fMLP source, the expression of DOCK2-9A only partially restored the leading edge formation (Fig. 4A). Because GFP-tagged SOS-PH localized to the leading edge even in DOCK2$^{-/-}$ neutrophils (fig. S15), this defect appeared to result from the inability of PA to tether DOCK2-9A. Indeed, DOCK2-9A translocated normally to the plasma membrane, but accumulated less effectively at the pseudopods of WT neutrophils than did DOCK2-WT and a DOCK2 mutant lacking DHR-1 domain (DOCK2-ΔDHR1; Fig. 4B). When DOCK2-WT or DOCK2-PH was expressed in DOCK2$^{-/-}$ neutrophils, the migration speed increased by 75% or 65%, respectively, compared with that of the control expressing GFP alone (Fig. 4C). However, the expression of DOCK2-9A failed to significantly increase the motility of DOCK2$^{-/-}$ neutrophils (Fig. 4C). Consistent with this finding, treatment of WT neutrophils with the PLD inhibitor FIPI reduced the migration speed to a level almost comparable to that of the DOCK2$^{-/-}$ neutrophils (Fig. 4D).

We showed here, during neutrophil chemotaxis, that intracellular DOCK2 dynamics were sequentially regulated by two distinct phospholipids: Although the plasma membrane translocation of DOCK2 was initially mediated by PIP_3, PA acted at a late phase to focus DOCK2 localization and to stabilize the leading edge. This two-step regulation fits well with the kinetics of these phospholipids in response to chemoattractants (fig. S16). Lamellipodia formation in epithelial cells is mediated by DOCK180, another GEF, and is inhibited by 1-butanol (*17*, *26*). The C-terminal region of DOCK180 also bound to PA (fig. S17), which suggested a common mechanism for its recruitment. Thus, PA may be involved in spatial regulation for Rac activation in varied biological settings by controlling localization of GEFs.

References and Notes

1. A. J. Ridley *et al.*, *Science* **302**, 1704 (2003).
2. P. Rickert, O. D. Weiner, F. Wang, H. R. Bourne, G. Servant, *Trends Cell Biol.* **10**, 466 (2000).
3. A. Schmidt, A. Hall, *Genes Dev.* **16**, 1587 (2002).

4. V. S. Kraynov *et al.*, *Science* **290**, 333 (2000).
5. E. M. Gardiner *et al.*, *Curr. Biol.* **12**, 2029 (2002).
6. J.-F. Côté, A. B. Motoyama, J. A. Bush, K. Vuori, *Nat. Cell Biol.* **7**, 797 (2005).
7. M. Nishio *et al.*, *Nat. Cell Biol.* **9**, 36 (2007).
8. G. J. Ferguson *et al.*, *Nat. Cell Biol.* **9**, 86 (2007).
9. Y. Fukui *et al.*, *Nature* **412**, 826 (2001).
10. Y. Kunisaki *et al.*, *J. Cell Biol.* **174**, 647 (2006).
11. E. Brugnera *et al.*, *Nat. Cell Biol.* **4**, 574 (2002).
12. J.-F. Côté, K. Vuori, *J. Cell Sci.* **115**, 4901 (2002).
13. Materials and methods are available as supporting material on *Science* Online.
14. C. L. Stace, N. T. Ktistakis, *Biochim. Biophys. Acta* **1761**, 913 (2006).
15. M. McDermott, M. J. O. Wakelam, A. J. Morris, *Biochem. Cell Biol.* **82**, 225 (2004).
16. S. Zouwail *et al.*, *Biochem. J.* **389**, 207 (2005).
17. L. C. Santy, J. E. Casanova, *J. Cell Biol.* **154**, 599 (2001).
18. N. Lehman *et al.*, *Blood* **108**, 3564 (2006).
19. G. Du, P. Huang, B. T. Liang, M. A. Frohman, *Mol. Biol. Cell* **15**, 1024 (2004).
20. Single-letter abbreviations for the amino acid residues are as follows: A, Ala; C, Cys; D, Asp; E, Glu; F, Phe; G, Gly; H, His; I, Ile; K, Lys; L, Leu; M, Met; N, Asn; P, Pro; Q, Gln; R, Arg; S, Ser; T, Thr; V, Val; W, Trp; and Y, Tyr.
21. W. Su *et al.*, *Mol. Pharmacol.* **75**, 437 (2009).
22. S. Srinivasan *et al.*, *J. Cell Biol.* **160**, 375 (2003).
23. Y. Fang, M. Vilella-Bach, R. Bachmann, A. Flanigan, J. Chen, *Science* **294**, 1942 (2001).
24. C. J. R. Loewen *et al.*, *Science* **304**, 1644 (2004).
25. C. Zhao, G. Du, K. Skowronek, M. A. Frohman, D. Bar-Sagi, *Nat. Cell Biol.* **9**, 706 (2007).
26. L. C. Santy, K. S. Ravichandran, J. E. Casanova, *Curr. Biol.* **15**, 1749 (2005).
27. This work was supported by grants for Targeted Proteins Research Project, Genome Network Project, Grants-in-Aid for Scientific Research from the Ministry of Education, Culture, Sports, Science, and Technology of Japan; Toray Science Foundation; CREST program of Japan Science and Technology Agency; the Global Center of Excellence program of the Japan Society for the Promotion of Science; and NIH award R01GM71520.

Supporting Online Material
www.sciencemag.org/cgi/content/full/1170179/DC1
Materials and Methods
Figs. S1 to S17
References

23 December 2008; accepted 10 March 2009
Published online 26 March 2009;
10.1126/science.1170179
Include this information when citing this paper.

Rare Variants of *IFIH1*, a Gene Implicated in Antiviral Responses, Protect Against Type 1 Diabetes

Sergey Nejentsev,[1,2]* Neil Walker,[1] David Riches,[3] Michael Egholm,[3] John A. Todd[1]

Genome-wide association studies (GWASs) are regularly used to map genomic regions contributing to common human diseases, but they often do not identify the precise causative genes and sequence variants. To identify causative type 1 diabetes (T1D) variants, we resequenced exons and splice sites of 10 candidate genes in pools of DNA from 480 patients and 480 controls and tested their disease association in over 30,000 participants. We discovered four rare variants that lowered T1D risk independently of each other (odds ratio = 0.51 to 0.74; $P = 1.3 \times 10^{-3}$ to 2.1×10^{-16}) in *IFIH1* (*interferon induced with helicase C domain 1*), a gene located in a region previously associated with T1D by GWASs. These variants are predicted to alter the expression and structure of IFIH1 [MDA5 (melanoma differentiation-associated protein 5)], a cytoplasmic helicase that mediates induction of interferon response to viral RNA. This finding firmly establishes the role of *IFIH1* in T1D and demonstrates that resequencing studies can pinpoint disease-causing genes in genomic regions initially identified by GWASs.

Genome-wide association studies (GWASs) of common multifactorial diseases have identified dozens of loci harboring disease-causing sequence variants (*1*, *2*). However, because the human genome contains regions of strong linkage disequilibrium, a disease-associated locus sometimes encompasses several genes and multiple tightly associated polymorphisms, making it difficult to pinpoint the causal variant by association mapping. Moreover, in many instances, the single nucleotide polymorphisms (SNPs) showing the most significant disease association map to genomic regions with no obvious function, thus providing few clues as to how causal variants affect the disease gene.

One way to overcome this limitation is to search for sequence variants that are rare in the population (frequency < 3%) but that reside in exons and other genomic regions of known function to identify polymorphisms that alter expression of the gene and/or function of the protein product (*3*). If rare disease-associated variants with obvious functional effects are found in a candidate gene that harbors a common disease-associated variant, then the gene is likely to be causal. Recent technological advances in high-throughput sequencing (*4*) provide an opportunity to resequence multiple genetic regions in hundreds of participants and discover rare sequence variants (*5*–*7*). We used 454 sequencing (*8*) to search for rare variants in 10 candidate genes and to study their association with type 1 diabetes (T1D), previously known as insulin-dependent diabetes mellitus (IDDM). T1D is a common disorder that develops as a result of a complex interaction of genetic and environmental factors leading to the immune-mediated destruction of the insulin-producing pancreatic β cells. To date, 15 loci associated with T1D have been identified in the human genome (*9*–*13*).

Of the 10 genes that we selected, 6 contain common T1D-associated polymorphisms: *PTPN22*, *PTPN2*, *IFIH1*, *SH2B3*, *CLEC16A*, and *IL2RA* (*10*, *11*, *14*–*16*). We also studied two genes that contain rare mutations causing monogenic syndromes that may include immune-mediated diabetes: (i) *FOXP3*, which is responsible for X-linked syndrome of immunodysregulation-polyendocrinopathy-enteropathy [Online Mendelian Inheritance in Man (OMIM) 304790], and (ii) *AIRE*, which is responsible for the autoimmune polyendocrinopathy-candidiasis-ectodermal dystrophy syndrome (OMIM 240300). Finally, we studied *KCNJ11* because mutations in this gene cause permanent neonatal diabetes, an insulin-dependent diabetes of the non-immune etiology that can be misdiagnosed as T1D in young children (*17*). We also studied *IAN4L1* because the ortholog of this gene is associated with immune-mediated diabetes in the rat model of T1D (*18*, *19*).

We resequenced 144 target regions that covered exons and regulatory sequences of the 10 genes, 31 kb in total (table S1 and T1DBase: www.t1dbase.org/page/PosterView/454Resequencing), in DNA of 480 T1D patients and 480 healthy controls from Great Britain arranged in 20 DNA pools (*20*). We generated 9.4 million reads with an average length of 250 bases and identified a total of 212 SNPs (*20*). We classified 33 of them as common because their estimated minor allele frequency (MAF) was >3% (table S2), and we categorized 179 as rare because their estimated MAF was <3%. Of the 179 rare SNPs, 156 were previously unseen (table S3). In the pooled samples, it was impossible to distinguish rare insertion/deletion polymorphisms from sequencing errors; thus, we studied nucleotide substitutions only.

Our goal was not only to discover previously unseen rare variants but also to test their association with T1D in the same experiment, comparing allele frequency in DNA pools of patients and controls. Therefore, it was important that sequence reads generated from the DNA pools estimated accurately allele frequency among individuals that contributed DNA to these pools. To test this, we analyzed eight SNPs from the sequenced regions that had been genotyped previously. We found good correlation between allele frequency in the individual samples and its estimate in the DNA pools (correlation coefficient $r = 0.99$) (fig. S1), demonstrating that high-throughput sequencing of

[1]Juvenile Diabetes Research Foundation/Wellcome Trust Diabetes and Inflammation Laboratory, Cambridge Institute for Medical Research, University of Cambridge, Cambridge, CB2 0XY, UK. [2]Department of Medicine, University of Cambridge, CB2 2QQ, UK. [3]454 Life Sciences, Branford, CT 06405, USA.

*To whom the correspondence should be addressed. E-mail: sn262@cam.ac.uk

Table 1. Association analysis of rare variants in sequenced pools of DNA from T1D patients and controls. Rare SNPs (MAF < 3%) associated with T1D with $P < 0.05$ are shown in this table. Results for all rare SNPs are shown in table S3. *n*, number.

SNP	Location	Alleles	Reads (*n*) | Reads (%) | Estimated chr (*n*)*		*P* value†
			T1D	Controls	
rs35337543	*IFIH1*, intron 8, IVS8+1	G > C	35/9,719 | 0.36 | 3/960	221/8,808 | 2.51 | 24/960	0.000044
rs35667974	*IFIH1*, exon 14, I923V	A > G	261/36,095 | 0.72 | 7/960	906/37,475 | 2.42 | 23/960	0.0049
ss107794688	*CLEC16A*, intron 23	C > T	168/33,712 | 0.50 | 5/960	450/25,138 | 1.79 | 17/960	0.016‡
ss107794687	*CLEC16A*, intron 11	C > T	431/40,186 | 1.07 | 10/960	808/32,947 | 2.45 | 24/960	0.023‡

*Number and proportion of reads and estimated number of chromosomes carrying minor allele. †*P* value was calculated with Fisher's exact test for the estimated number of chromosomes carrying minor alleles in the pools of 960 chromosomes from T1D patients and controls. ‡We genotyped two SNPs located in introns 11 and 23 of the *CLEC16A* (C-type lectin domain family 16, member A) gene in the overall case-control collection but found no association with T1D (table S4).

Table 2. Association analysis of the four rare *IFIH1* polymorphisms in T1D patients and controls and in families that have one or more offspring with T1D and their parents. Results for additional *IFIH1* SNPs are shown in table S5. CI, confidence interval; T/NT, number of alleles transmitted and nontransmitted to the affected offspring.

	Allele* 1 > 2		Case–control study									Family study			
			11	(%)	12	(%)	22	(%)	MAF (%)	OR (95% CI)†	*P* value‡	T/NT	RR (95% CI)†	*P* value§	Combined *P* value‖
rs35667974/I923V Exon 14	A > G	T1D	7853	(97.8)	172	(2.1)	3	(0.04)	1.1	0.51 (0.43 – 0.61)	1.3×10^{-14}	67/111	0.60 (0.45 – 0.82)	5.9×10^{-4}	2.1×10^{-16}
		controls	9166	(95.7)	404	(4.2)	4	(0.04)	2.2						
rs35337543/IVS8+1 Intron 8, splice site	G > C	T1D	7945	(98.0)	163	(2.0)	0	(0.0)	1.0	0.68 (0.56 – 0.83)	1.1×10^{-4}	51/60	0.85 (0.59 – 1.23)	0.20	1.4×10^{-4}
		controls	9330	(97.1)	280	(2.9)	0	(0.0)	1.5						
rs35744605/E627X Exon10	G > T	T1D	8109	(99.1)	76	(0.9)	0	(0.0)	0.46	0.69 (0.52 – 0.91)	9.0×10^{-3}	17/31	0.55 (0.30 – 0.99)	2.8×10^{-2}	1.3×10^{-3}
		controls	9621	(98.7)	131	(1.3)	0	(0.0)	0.67						
rs35732034/IVS14+1 Intron 14, splice site	G > A	T1D	8047	(98.6)	109	(1.3)	2	(0.03)	0.69	0.74 (0.59 – 0.94)	1.2×10^{-2}	35/56	0.63 (0.41 – 0.95)	2.1×10^{-2}	1.1×10^{-3}
		controls	9552	(98.1)	180	(1.9)	1	(0.01)	0.93						

*Major allele is coded 1; minor allele is coded 2. †OR and relative risks (RR) for minor (rarer) alleles are shown. ‡Two-tailed *P* values were calculated with logistic regression. §One-tailed *P* values were calculated with transmission disequilibrium test with robust variance estimates. ‖Combined *P* values for the case-control and family data were calculated with a score test as described previously (*26*).

the DNA pools can be used to accurately measure allele frequencies. We then tested association of all 212 SNPs with T1D, comparing pooled samples of cases and controls. As expected, we confirmed the previously known association of the common SNPs with T1D ($P = 0.02$ to 5×10^{-7}, χ^2 test) (table S2). Among rarer SNPs that had not been previously studied for association with T1D, we noted that the two most associated variants, rs35667974 and rs35337543 ($P = 0.0049$ and 0.000044, exact test) (Table 1), reside within the *interferon induced with helicase C domain 1* (*IFIH1*) gene. We did not find evidence of association for rare variants in other genes, except for potential associations of the two SNPs located in introns of the *CLEC16A* gene (Table 1 and table S3).

We next studied two *IFIH1* and two *CLEC16A* SNPs in individual DNA samples from 8379 T1D patients and 10,575 controls from Great Britain. We also studied *IFIH1* SNPs in 3165 families from Europe and USA that include one or more offspring with T1D and their parents. The two rare intronic *CLEC16A* SNPs were not associated (table S4), whereas both rare *IFIH1* SNPs demonstrated strong statistical evidence of association with T1D, showing consistent effect in the case-control and family collections (combined $P = 2.1 \times 10^{-16}$ for rs35667974 and 1.4×10^{-4} for rs35337543, score test) (Table 2). SNP rs35667974 in exon 14 changes a conserved amino acid from Ile^{923} to Val^{923} (I923V) (fig. S2), whereas SNP rs35337543 resides within a conserved splice donor site at position +1 in intron 8. Apart from these two SNPs, our sequencing study identified other rare *IFIH1* SNPs, including three nonsynonymous SNPs (nsSNPs) (ss107794691/K349R, ss107794690/T702I, and rs10930046/H460R), another SNP in a conserved splice donor site at position +1 in intron 14 (rs35732034), and a nonsense mutation in exon 10 (rs35744605). We genotyped these rare SNPs and found evidence of T1D association for the non-sense mutation rs35744605 and SNP rs35732034 located in the conserved splice site (Table 2), but not for nsSNPs K349R, T702I, or H460R (table S5). We did not genotype *IFIH1* intronic and synonymous SNPs or very rare nsSNP (MAF ≤ 0.2%).

We calculated linkage disequilibrium and found that it is low ($r^2 < 0.04$) between all four associated rare variants, indicating that association of one SNP cannot be explained by any of the other SNPs. We also genotyped two common nsSNPs, rs3747517/R843H and rs1990760/T946A (MAF > 25%), that had been found to be associated with T1D by GWASs (*10*, *12*, *21*), and we confirmed their association (table S5). We also used logistic regression analyses (*22*) and found that all four rare variants (rs35667974, rs35337543, rs35732034, and rs35744605) were associated with T1D, independently of each other and of the common nsSNP rs1990760/T946A (table S6), so these rare variants do not account for association of rs1990760/T946A detected previously by GWASs. Two common nsSNPs were in strong linkage disequilibrium with each other ($r^2 = 0.60$), and association of rs1990760/T946A explained the effect of rs3747517/R843H. Thus, in the *IFIH1* gene, four rare polymorphisms and one common nsSNP (rs1990760/T946A) show independent association with T1D (fig. S3), although we cannot exclude a possibility that additional variants with weaker effects also exist in this gene. Thus, we demonstrated T1D association and measured effects of each of the newly discovered rare variants separately, without grouping them (*5*, *6*).

In the previous GWAS of 12,000 common nsSNPs, we identified a T1D-associated locus on chromosome 2q24 that included *IFIH1*, along with the *FAP* and *GCA* genes and part of the *KCNH7* gene (fig. S4) (*10*). Although *IFIH1* is a biologically plausible candidate gene, there was no evidence to indicate which of these genes is causative for T1D. Discovery of multiple rare T1D-associated variants in *IFIH1* now points to its etiological role in T1D, because it is highly unlikely that multiple untested variants elsewhere in the region could explain association of the rare *IFIH1* variants via linkage disequilibrium. We did not resequence the *FAP*, *GCA*, and *KCNH7* genes, so we cannot formally exclude that they might also contain rare T1D-associated variants. This possibility is unlikely, but if true, it would not negate the role of *IFIH1*; instead, it would imply that *IFIH1* is not the only T1D gene in this region.

All four associated rare *IFIH1* variants have predicted biological effects, either truncating the

protein (non-sense mutation rs35744605) or affecting essential splicing positions (rs35337543 and rs35732034) or a highly conserved amino acid (rs35667974/I923V) (fig. S2). These rare *IFIH1* variants have stronger protective effects on T1D risk [odds ratio (OR) = 0.51 to 0.74] than does the common nsSNP rs1990760/T946A (OR = 0.86) (table S5). For example, rare individuals carrying valine at position 923 of the IFIH1 protein have only ~50% risk of developing T1D compared with those who carry isoleucine. Our results suggest that, in complex diseases such as T1D, there may be no (or very few) low-frequency variants with very strong effects (allele OR > 3), even if such variants have large impacts on a certain molecule's function. This is the case possibly because, in complex multifactorial diseases, such a molecule and its biological pathway are just one of many contributing to the pathogenesis. Nevertheless, the discovery of such rare variants with the use of high-throughput sequencing will help to pinpoint disease genes in the associated loci found by GWASs in various complex diseases.

IFIH1 (interferon induced with helicase C domain 1), also known as MDA5 (melanoma differentiation-associated protein 5), is a 1025–amino acid cytoplasmic protein that recognizes RNA of picornaviruses and mediates immune activation (*23*). Infection with enteroviruses, which belong to the picornavirus family, is more common among newly diagnosed T1D patients and prediabetic subjects than in the general population, and it precedes the appearance of autoantibodies (markers of prediabetes) (*24*). Enteroviruses are small RNA viruses that include coxsackie A and B, polioviruses, and echoviruses and cause common and often asymptomatic infections. Upon infection, IFIH1 senses the presence of viral RNA in the cytoplasm, triggers activation of NF-κB and interferon regulatory factor pathways, and induces antiviral interferon-β response (*25*). Although the mechanisms by which *IFIH1* polymorphisms contribute to T1D pathogenesis remain to be explored, we note that one of the protective variants is a non-sense mutation leading to a truncated 626–amino acid protein lacking the C-terminal helicase domain (fig. S3), whereas two other protective variants localize to the conserved splice donor sites and probably disrupt normal splicing of the IFIH1 transcript. This suggests that variants, which are predicted to reduce function of the IFIH1 protein, would decrease the risk of T1D, whereas normal IFIH1 function is associated with T1D. To elucidate a biological mechanism linking enterovirus infection with T1D, future functional experiments should test whether normal immune activation caused by enterovirus infection and mediated by IFIH1 protein may stimulate autoreactive T cells leading to T1D and whether blocking IFIH1 can disrupt this pathogenic mechanism.

We have found that rare alleles of all associated *IFIH1* polymorphisms consistently protect from T1D, whereas *IFIH1* alleles carried by the majority of the population predispose to the disease. This observation suggests that variants that disrupt IFIH1 function in the host antiviral response have been negatively selected, rather than positively selected because they confer protection from T1D.

References and Notes

1. M. I. McCarthy *et al.*, *Nat. Rev. Genet.* **9**, 356 (2008).
2. D. Altshuler, M. J. Daly, E. S. Lander, *Science* **322**, 881 (2008).
3. W. Bodmer, C. Bonilla, *Nat. Genet.* **40**, 695 (2008).
4. E. R. Mardis, *Trends Genet.* **24**, 133 (2008).
5. J. C. Cohen *et al.*, *Science* **305**, 869 (2004).
6. W. Ji *et al.*, *Nat. Genet.* **40**, 592 (2008).
7. S. Romeo *et al.*, *Nat. Genet.* **39**, 513 (2007).
8. M. Margulies *et al.*, *Nature* **437**, 376 (2005).
9. S. Nejentsev *et al.*, *Nature* **450**, 887 (2007).
10. D. J. Smyth *et al.*, *Nat. Genet.* **38**, 617 (2006).
11. J. A. Todd *et al.*, *Nat. Genet.* **39**, 857 (2007).
12. P. Concannon *et al.*, *Diabetes* **57**, 2858 (2008).
13. J. D. Cooper *et al.*, *Nat. Genet.* **40**, 1399 (2008).
14. Wellcome Trust Case Control Consortium, *Nature* **447**, 661 (2007).
15. N. Bottini *et al.*, *Nat. Genet.* **36**, 337 (2004).
16. C. E. Lowe *et al.*, *Nat. Genet.* **39**, 1074 (2007).
17. R. Murphy, S. Ellard, A. T. Hattersley, *Nat. Clin. Pract. Endocrinol. Metab.* **4**, 200 (2008).
18. L. Hornum, J. Romer, H. Markholst, *Diabetes* **51**, 1972 (2002).
19. A. J. MacMurray *et al.*, *Genome Res.* **12**, 1029 (2002).
20. Materials and methods are available as supporting material on *Science* Online.
21. S. Liu *et al.*, *Hum. Mol. Genet.* **18**, 358 (2009).
22. H. J. Cordell, D. G. Clayton, *Am. J. Hum. Genet.* **70**, 124 (2002).
23. H. Kato *et al.*, *Nature* **441**, 101 (2006).
24. H. Hyöty, K. W. Taylor, *Diabetologia* **45**, 1353 (2002).
25. E. Meylan, J. Tschopp, M. Karin, *Nature* **442**, 39 (2006).
26. D. Smyth *et al.*, *Diabetes* **53**, 3020 (2004).

27. We thank the patients, control participants, and family members for participating in the study. S.N. held the Diabetes Research and Wellness Foundation Non-Clinical Fellowship at the early stages of the project and now holds the Royal Society University Research Fellowship. The Juvenile Diabetes Research Foundation/Wellcome Trust Diabetes and Inflammation Laboratory is funded by the Juvenile Diabetes Research Foundation, the Wellcome Trust, and the National Institute for Health Research Biomedical Research Centre. The Cambridge Institute for Medical Research is in receipt of a Wellcome Trust Strategic Award (079895). Full acknowledgements are in the supporting online material. Previously unseen SNPs were submitted to dbSNP database (www.ncbi.nlm.nih.gov/SNP/); their submission numbers are in table S3.

Supporting Online Material

www.sciencemag.org/cgi/content/full/1167728/DC1
Materials and Methods
SOM Text
Figs. S1 to S5
Tables S1 to S6
References

27 October 2008; accepted 19 February 2009
Published online 5 March 2009;
10.1126/science.1167728
Include this information when citing this paper.

Local DNA Topography Correlates with Functional Noncoding Regions of the Human Genome

Stephen C. J. Parker,[1] Loren Hansen,[1,2] Hatice Ozel Abaan,[3] Thomas D. Tullius,[1,4]* Elliott H. Margulies[3]*

The three-dimensional molecular structure of DNA, specifically the shape of the backbone and grooves of genomic DNA, can be dramatically affected by nucleotide changes, which can cause differences in protein-binding affinity and phenotype. We developed an algorithm to measure constraint on the basis of similarity of DNA topography among multiple species, using hydroxyl radical cleavage patterns to interrogate the solvent-accessible surface area of DNA. This algorithm found that 12% of bases in the human genome are evolutionarily constrained—double the number detected by nucleotide sequence–based algorithms. Topography-informed constrained regions correlated with functional noncoding elements, including enhancers, better than did regions identified solely on the basis of nucleotide sequence. These results support the idea that the molecular shape of DNA is under selection and can identify evolutionary history.

Genomic sequences that code for proteins are relatively well understood but make up only ~2% of the human genome (*1*). Many functions are encoded in the remaining ~98% noncoding portion of the genome, but little is known about how functional noncoding information is specified (*2*). It has been hypothesized that functional regions are likely to be evolutionarily constrained because of their importance to the organism (*3*–*11*). Nonetheless, evolutionary sequence-constraint algorithms fail to identify many noncoding functional elements (*12*–*15*). This may be because these methods analyze only the primary nucleotide sequence of a genome (that is, the order of A's, C's, G's, and T's). However, DNA is a molecule with a three-dimensional structure that varies according to the nucleotide sequence (*16*–*18*).

[1]Bioinformatics Program, Boston University, Boston, MA 02215, USA. [2]National Center for Biotechnology Information, National Institutes of Health, Bethesda, MD 20892, USA. [3]Genome Technology Branch, National Human Genome Research Institute, National Institutes of Health, Bethesda, MD 20892, USA. [4]Department of Chemistry, Boston University, Boston, MA 02215, USA.

*To whom correspondence should be addressed. E-mail: elliott@nhgri.nih.gov (E.H.M.); tullius@bu.edu (T.D.T.)

We used a previously developed method based on the hydroxyl radical cleavage pattern of DNA (*19*) to quantitatively evaluate how the structure of DNA varies throughout a genome. This approach can be used to predict the shape of the DNA backbone and grooves of genomic DNA at single-nucleotide resolution (*20*). We call this pattern the structural profile of a DNA region. Structural profiles reveal that the relationship of DNA structure to the corresponding DNA sequence is not always simple. Although similar sequences often adopt similar structures (Fig. 1A), divergent nucleotide sequences can have similar local structures (Fig. 1B) (*20*). Conversely (albeit less frequently), similar sequences can adopt very different structures (Fig. 1C). These observations indicate that DNA regions that differ on the basis of the order of nucleotides may be similar in structure, which suggests that they may perform similar biological functions.

We quantified the effect of single-base substitutions on DNA structure by computing the structural profiles of all possible 11–base pair (bp) sequences (4,194,304 in total), measuring the similarity between profiles for all pairs of 11-bp sequences that differ only by a single substitution at the central nucleotide (*21*). A histogram of structural differences for all 11-bp sequences reveals a range of effects from minor to drastic (Fig. 1, D to G). In some cases, the one-base change in an 11-bp sequence has a minor effect, but the sequence may have a dramatically different structure if another base is substituted.

Because current sequence-constraint algorithms do not compute the effect of a base change on DNA structure, we developed a computer program, Chai, that incorporates structural information. This method works in a manner analogous to the DNA sequence–based binomial conservation (binCons) algorithm (*8*), but instead of computing the binomial probability of observed base substitutions between species, Chai calculates the difference between DNA structural profiles as a measure of similarity (*21*). We used the binCons and Chai algorithms to analyze 30 Mb of high-quality comparative sequence data for 36 different species [the ENCODE pilot project regions (*15*, *22*)]. We defined a false discovery rate (FDR) on the basis of a neutral (or null) alignment (*10*, *22*) in an identical manner for assessing both sequence- and structure-informed conservation, so that each type of conserved region was identified with equal statistical confidence. We found that at any given FDR, the structure-informed Chai algorithm identified more evolutionarily constrained bases than did binCons (Fig. 2A and table S1). For example, at a 5% FDR, binCons identified 6.7% of bases as constrained, corresponding with previous findings of sequence-based mammalian constraint (*8*–*11*, *15*, *22*, *23*). Chai identified nearly twice as many bases as constrained (12%) (Fig. 2B), while identifying 89% of the regions identified with the binCons method.

We next determined the extent to which evolutionarily constrained regions identified by Chai and binCons harbor functional elements. We examined deoxyribonuclease I (DNase I)–hypersensitive sites (*15*) and predicted transcriptional enhancers identified using chromatin modification patterns (*24*) from published studies (*21*) as examples of noncoding functional elements that frequently exhibit little sequence similarity. Compared to binCons regions, we found that Chai-detected regions overlapped a higher proportion of DNase I–hypersensitive sites (78% for Chai versus 50% for binCons) and predicted enhancers (84% for Chai versus 59% for binCons) (Fig. 2C). To test whether the increased correlation with functional sequences was due to the additional territory identified by Chai relative to binCons, we tuned each algorithm for equal base coverage as opposed to equal statistical confidence and found that Chai-detected regions still overlapped a significantly greater number of functional noncoding elements as compared to binCons-detected regions ($P < 10^{-12}$, Fisher's exact test) (figs. S1 and 2A and table S1).

Focusing our analysis on regions identified only by Chai and not by binCons (Chai-only

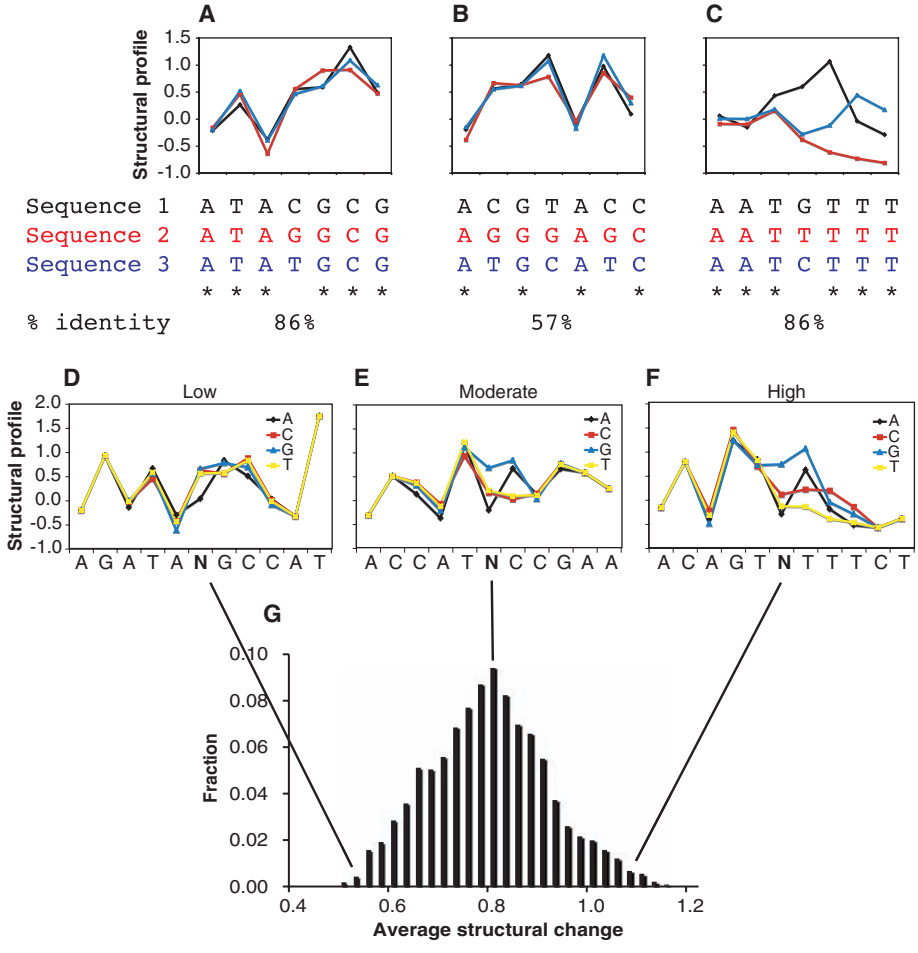

Fig. 1. DNA topography versus nucleotide sequence. (**A** to **C**) Hydroxyl radical cleavage patterns (referred to here as the structural profile) and corresponding color-matched sequence alignments (below each panel). Asterisks indicate identical columns in the sequence alignment. (**D** to **G**) Single-base substitutions have a range of effects on local DNA structure. For all possible 11-bp nucleotide sequences, we computationally changed the middle position to each possible base and measured its effect on the structural profile. These changes were quantitatively measured by calculating the mean Euclidean distance (referred to here as the average structural change) (*21*), where low values indicate similar structure profiles and high values indicate different structure profiles. (G) The distribution of average structure changes observed for all 11-bp sequences. Arrows indicate what we classify as low, moderate, or high average structure changes, with representative 11-bp sequences for each shown in (D), (E), and (F), respectively. For (D) to (F), the *y* axis indicates the structural profile at each nucleotide position in the 11-bp sequence (*x* axis). The structural profile for each sequence containing a different base in the middle position (noted by an "N") is plotted in a different color. The structural profiles are increasingly different in changing from low to high structural change [(E) to (G)].

regions) resulted in a statistically significant overrepresentation of noncoding functional sequences [$P < 0.01$, genome structure correction (GSC) statistic] [see (*21*) for a description of the GSC statistic] in the Chai-only regions and a statistically significant underrepresentation ($P < 10^{-9}$, GSC statistic) of coding regions (Fig. 2C). This suggests that some of the functional information in the noncoding portion of the genome is conferred by DNA structure as well as by the nucleotide sequence.

We thus examined whether noncoding nucleotide substitutions inducing changes in DNA structure affect the biological function of a sequence. We focused on the DNA binding properties of the Zif268 protein, a mammalian transcription factor that consists of three zinc fingers that wrap around DNA in the major groove (*25*). Binding affinity data (*26*) were compared with structural profiles for the 15 sites identified to bind wild-type Zif268 and the Zif268 REDV mutant (*21*). For both proteins, the structural profiles of the high-affinity sequence motifs were similar, whereas low-affinity motifs had a different structural profile (figs. S2A and S3A).

We ranked each Zif268 REDV motif by the extent of DNA structural difference relative to the best binding site and found that binding affinity correlated with this ranking ($r = 0.75$, $P = 6.9 \times 10^{-4}$; *t* test; fig. S2B). In other words, low-affinity binding sites differed dramatically in structure from high-affinity sites, whereas sites with intermediate affinity showed less structural difference. We observed a similarly high correlation for the wild-type protein, which has different binding preferences ($r = 0.74$, $P = 7.5 \times 10^{-4}$; *t* test; fig. S3B). Analysis of DNA binding site structural profiles and binding affinity for the archaeal transcriptional regulator Ss-LrpB revealed trends similar to those found for Zif268 (fig. S4).

We next tested whether mutations that change the molecular topography of noncoding genomic regions have phenotypic consequences, using data from the PhenCode Project (*27*), which organizes information from several locus-specific mutation databases. We gathered 734 noncoding single-nucleotide variants in the human genome associated with a phenotype. For each variant, we calculated the difference in the structural profile between the mutant and nonmutant sequence over an 11-bp window centered on the variant nucleotide (similar to the analysis above). For comparison, a distribution of baseline variation in DNA topography was computed for 16,832 neutrally evolving single-nucleotide polymorphisms (SNPs) (*21*). The phenotype-associated distribution was significantly correlated with larger changes in structure ($P < 3 \times 10^{-4}$, Wilcoxon rank sum test) relative to the baseline distribution and contained an additional high structure-change peak (Fig. 3). These results indicate that phenotype-associated mutations tend to induce larger changes in the structural profile of noncoding DNA than does baseline neutral variation.

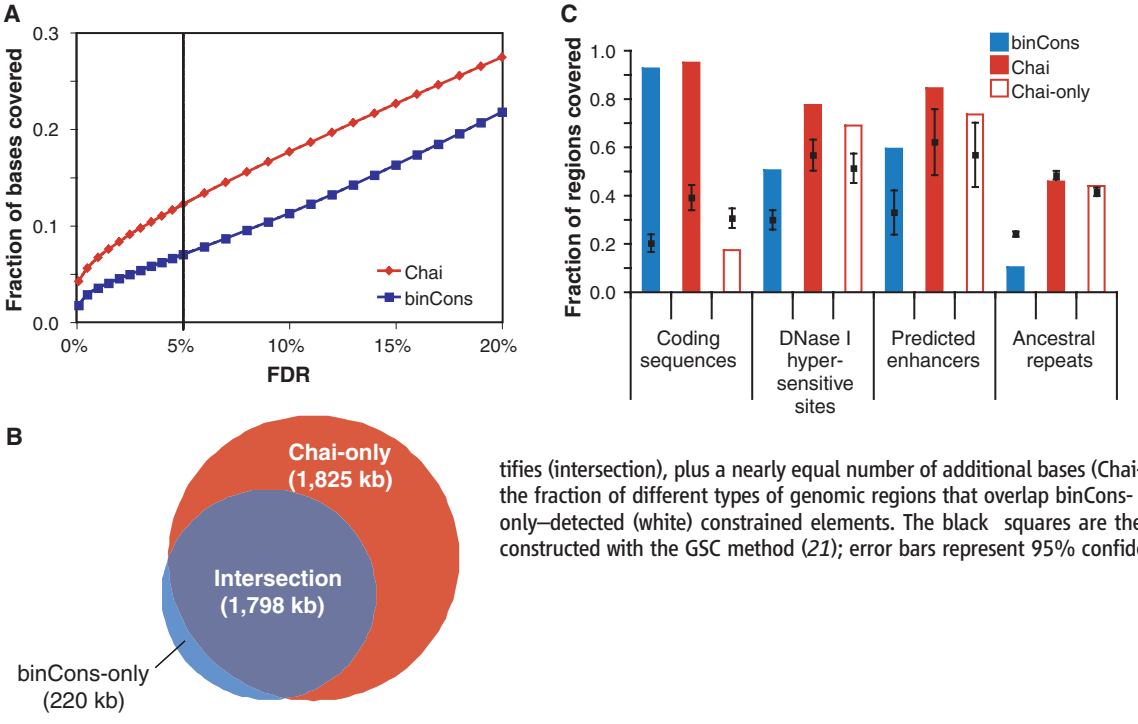

Fig. 2. Structure-informed evolutionarily constrained regions. (**A**) Plot showing the fraction of bases identified as evolutionarily constrained at various FDRs (*21*) by the DNA sequence–based algorithm binCons (blue line) and the structure-informed algorithm Chai (red line). (**B**) Venn diagram showing nucleotides identified by each algorithm (Chai, red; binCons, blue) at a 5% FDR [gray vertical line in (A)]. Chai detects nearly the same set of bases as binCons identifies (intersection), plus a nearly equal number of additional bases (Chai-only). (**C**) Bar graph showing the fraction of different types of genomic regions that overlap binCons- (blue), Chai- (red), and Chai-only–detected (white) constrained elements. The black squares are the mean of a null distribution constructed with the GSC method (*21*); error bars represent 95% confidence intervals.

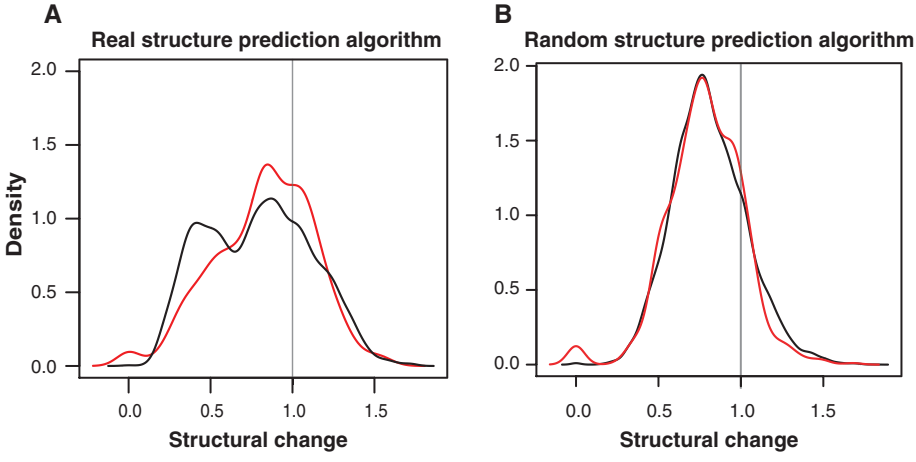

Fig. 3. The distribution of DNA structural changes for phenotype-associated variants (red line) and neutral variants (black line) (*21*) with the real structure prediction algorithm (**A**) and a randomized version (**B**). (A) The phenotype-associated distribution was shifted significantly to the right ($P < 3 \times 10^{-4}$, Wilcoxon rank sum test) and contains an additional high structure-change peak relative to the neutral distribution. (B) No significant shift ($P > 0.05$, Wilcoxon rank sum test) was observed with a randomized version of the structure prediction algorithm.

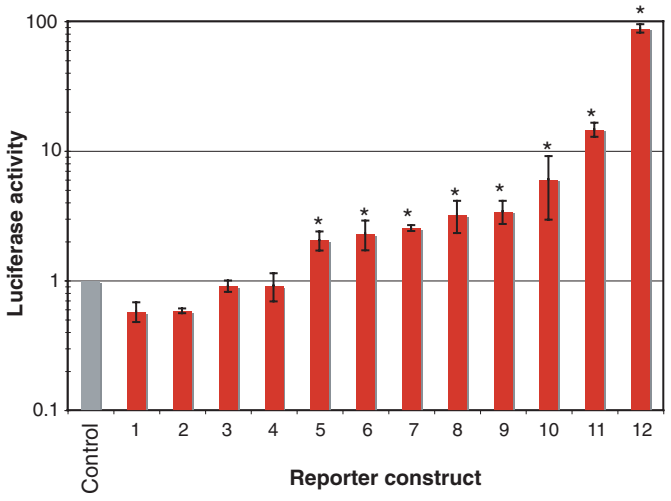

Fig. 4. Luciferase-based reporter activity of 12 regions containing Chai-detected elements (*21*). These regions overlapped predicted enhancer regions. Plotted for each element is the luciferase activity relative to the median activity from 100 random control constructs (*y* axis; see fig. S5). Error bars represent 1 SD from the mean of four experimental replicates, and asterisks denote $P \leq 0.05$ (Wilcoxon rank sum test).

We also identified phenotype-associated SNPs causing the top 10% of structural changes and the lowest 10%. The phenotype-associated mutations with the greatest changes in DNA structure occurred significantly more often ($P < 10^{-2}$, Fisher's exact test) in evolutionarily constrained regions of the genome (56% for high structure-change regions versus 29% for low structure-change regions) (*21*). This suggests that noncoding DNA may be under selective constraint, which may prevent changes in DNA structure. Because the severity of structural change might help identify functional SNPs, we constructed a database of changes in the structural profile for all known SNPs in the human genome (*21*).

Finally, we demonstrated that structural changes affect biological function in noncoding evolutionarily constrained regions identified by the Chai algorithm. We chose 12 predicted enhancer-containing regions (*24*): 5 regions overlap elements detected only by the Chai algorithm; 7 regions overlap a combination of Chai- and binCons-detected elements (table S2). We cloned the 300 bp surrounding each of these genomic regions in a luciferase reporter construct and transfected them into 293T cells. Eight of the 12 constructs displayed luciferase activity that was significantly greater ($P \leq 0.05$, Wilcoxon rank sum test) than that of random control sequences (Fig. 4). Three of the five constructs overlapping only Chai-detected elements were positive (table S2).

Given the plethora of regulatory functions that a genome encodes and the three-dimensional genomic architecture required to orchestrate these events (*28*), it may not be surprising that there is widespread conservation of local DNA topography. Perhaps only a subset of local structural configurations can accommodate the functional requirements of a genomic locus [for example, see (*29*)]. Once the molecular topography of a locus is permissive to a regulatory function, this structure may be maintained within the genome. Our high-resolution topography-based constraint-detection method reveals that structure-informed constraint is widespread in the human genome and that these regions overlap known noncoding functional sites. Because different DNA sequences can have similar local structures (*20*), these regions might escape detection with sequence-based conservation–identification methods.

References and Notes

1. International Human Genome Sequencing Consortium, *Nature* **431**, 931 (2004).
2. M. D. Wilson *et al.*, *Science* **322**, 434 (2008).
3. L. Elnitski *et al.*, *Genome Res.* **13**, 64 (2003).
4. M. Kellis, N. Patterson, M. Endrizzi, B. Birren, E. S. Lander, *Nature* **423**, 241 (2003).
5. G. G. Loots *et al.*, *Science* **288**, 136 (2000).
6. L. A. Pennacchio, E. M. Rubin, *Nat. Rev. Genet.* **2**, 100 (2001).
7. W. W. Wasserman, M. Palumbo, W. Thompson, J. W. Fickett, C. E. Lawrence, *Nat. Genet.* **26**, 225 (2000).
8. E. H. Margulies, M. Blanchette, NISC Comparative Sequencing Program, D. Haussler, E. D. Green, *Genome Res.* **13**, 2507 (2003).
9. A. Siepel *et al.*, *Genome Res.* **15**, 1034 (2005).
10. G. M. Cooper *et al.*, *Genome Res.* **15**, 901 (2005).
11. S. Asthana, M. Roytberg, J. Stamatoyannopoulos, S. Sunyaev, *PLoS Comp. Biol.* **3**, e254 (2007).
12. S. Fisher, E. A. Grice, R. M. Vinton, S. L. Bessling, A. S. McCallion, *Science* **312**, 276 (2006).
13. D. M. McGaughey *et al.*, *Genome Res.* **18**, 252 (2008).
14. H. M. Petrykowska, C. M. Vockley, L. Elnitski, *Genome Res.* **18**, 1238 (2008).
15. The ENCODE Project Consortium, *Nature* **447**, 799 (2007).
16. T. Ohyama, Ed., *DNA Conformation and Transcription* (Landes Bioscience/Eurekah.com, Georgetown, TX, 2005).
17. W. K. Olson, A. A. Gorin, X. J. Lu, L. M. Hock, V. B. Zhurkin, *Proc. Natl. Acad. Sci. U.S.A.* **95**, 11163 (1998).
18. R. E. Dickerson, *Methods Enzymol.* **211**, 67 (1992).
19. M. A. Price, T. D. Tullius, *Methods Enzymol.* **212**, 194 (1992).
20. J. A. Greenbaum, B. Pang, T. D. Tullius, *Genome Res.* **17**, 947 (2007).
21. Materials and methods are available as supporting material on *Science* Online.
22. E. H. Margulies *et al.*, *Genome Res.* **17**, 760 (2007).
23. Mouse Genome Sequencing Consortium, *Nature* **420**, 520 (2002).
24. N. D. Heintzman *et al.*, *Nat. Genet.* **39**, 311 (2007).
25. N. P. Pavletich, C. O. Pabo, *Science* **252**, 809 (1991).
26. M. L. Bulyk, P. L. F. Johnson, G. M. Church, *Nucleic Acids Res.* **30**, 1255 (2002).
27. B. Giardine *et al.*, *Hum. Mutat.* **28**, 554 (2007).
28. T. Misteli, *Bioessays* **27**, 477 (2005).
29. R. Joshi *et al.*, *Cell* **131**, 530 (2007).

30. We thank E. D. Green and L. C. Brody for feedback on the manuscript, E. Bishop and D. Landsman for discussion, and G. K. McEwen for assistance with experimental steps. Funded by the National Human Genome Research Institute (NHGRI) of the NIH (grant R01 HG003541) to T.D.T. and by the Research Corporation for Science Advancement. E.H.M. was supported by the Intramural Research Program of the NHGRI, NIH. S.C.J.P. was supported by a National Academies Ford Foundation Dissertation Fellowship.

Supporting Online Material

www.sciencemag.org/cgi/content/full/1169050/DC1
Materials and Methods
Figs. S1 to S5
Tables S1 and S2
References

26 November 2008; accepted 23 February 2009
Published online 12 March 2009;
10.1126/science.1169050
Include this information when citing this paper.

In Vivo Analysis of Dendritic Cell Development and Homeostasis

Kang Liu,[1]* Gabriel D. Victora,[1]† Tanja A. Schwickert,[1]† Pierre Guermonprez,[1] Matthew M. Meredith,[1] Kaihui Yao,[1] Fei-Fan Chu,[1] Gwendalyn J. Randolph,[2] Alexander Y. Rudensky,[3,4] Michel Nussenzweig[1,4]*

Dendritic cells (DCs) in lymphoid tissue arise from precursors that also produce monocytes and plasmacytoid DCs (pDCs). Where DC and monocyte lineage commitment occurs and the nature of the DC precursor that migrates from the bone marrow to peripheral lymphoid organs are unknown. We show that DC development progresses from the macrophage and DC precursor to common DC precursors that give rise to pDCs and classical spleen DCs (cDCs), but not monocytes, and finally to committed precursors of cDCs (pre-cDCs). Pre-cDCs enter lymph nodes through and migrate along high endothelial venules and later disperse and integrate into the DC network. Further cDC development involves cell division, which is controlled in part by regulatory T cells and fms-like tyrosine kinase receptor-3.

Dendritic cells (DCs) are immune cells that are specialized to capture, process, and present antigens to T lymphocytes in order to induce immunity or tolerance (*1*). Where commitment to DC development takes place, at what stage the monocyte lineage diverges from DCs, and the precise nature of the migrating DC precursor that moves from the bone marrow to

the peripheral lymphoid organs are not known. These questions have been difficult to resolve in part because DC subsets are functionally and phenotypically diverse (*2*). For example, classical spleen DCs (cDCs) include two major functionally distinct subsets that are distinguished by the expression of a variety of C-type lectins and CD8 (*2*–*4*). Spleen and other tissues also contain plasmacytoid DCs (pDCs) that primarily initiate immune responses to nucleic acids (*5*, *6*).

Lymphoid tissue cDCs, pDCs, and monocytes share a common progenitor called the macrophage and DC precursor (MDP) that is identified by its surface phenotype (Lin^- $cKit^{hi}$ $CD115^+$ CX_3CR1^+ $Flt3^+$) (*7*, *8*), whereas a distinct progenitor called the common DC precursor (CDP) (Lin^- $cKit^{lo}$ $CD115^+$ $Flt3^+$) is restricted to producing cDCs and pDCs (*9*, *10*). Although monocytes can develop many of the phenotypic features of DCs under inflammatory conditions (*11*–*13*), the cDC, pDC, and monocyte lineages separate by the time they reach tissues, and neither monocytes nor pDCs develop into cDCs under steady-state conditions (*8*, *14*). Unlike monocytes and pDCs, cDCs in lymphoid tissues are thought to emerge from the bone marrow as immature cells that must further differentiate and divide in lymphoid organs (*15*, *16*). Consistent with this idea, pre-cDCs that are restricted to the cDC lineage were isolated from the spleen and bone-marrow cultures containing fms-like tyrosine kinase receptor-3–ligand (Flt3-L) (*17*, *18*). However, the relationship between MDP, CDP, and pre-cDC in vivo and the question of where the monocyte, pDC, and cDC lineages split have not been addressed (*10*, *14*, *18*).

We searched for MDPs and CDPs in the blood and spleen by means of flow cytometry but could only detect them in the bone marrow (Fig. 1A and fig. S1). Although pre-cDCs can be identified in the spleen by combining density centrifugation and flow cytometry (*18*), we speculated that these cells could be identified directly by expression of Flt3 and the chemokine receptor CX_3CR1, which are expressed on other DC progenitors and also on mature cDCs (*7*, *10*, *19*). Indeed, we found a small but distinct population of lineage-negative $CD11c^+$

[1]Laboratory of Molecular Immunology, Rockefeller University, New York, NY 10065, USA. [2]Department of Gene and Cell Medicine, Mount Sinai School of Medicine, New York, NY 10029, USA. [3]Department of Immunology and Howard Hughes Medical Institute (HHMI), University of Washington, Seattle, WA 98195, USA. [4]HHMI, Rockefeller University, New York, NY 10021, USA.

*To whom correspondence should be addressed. E-mail: liuk@rockefeller.edu (L.K.); nussen@rockefeller.edu (M.N.)
†These authors contributed equally to this work.

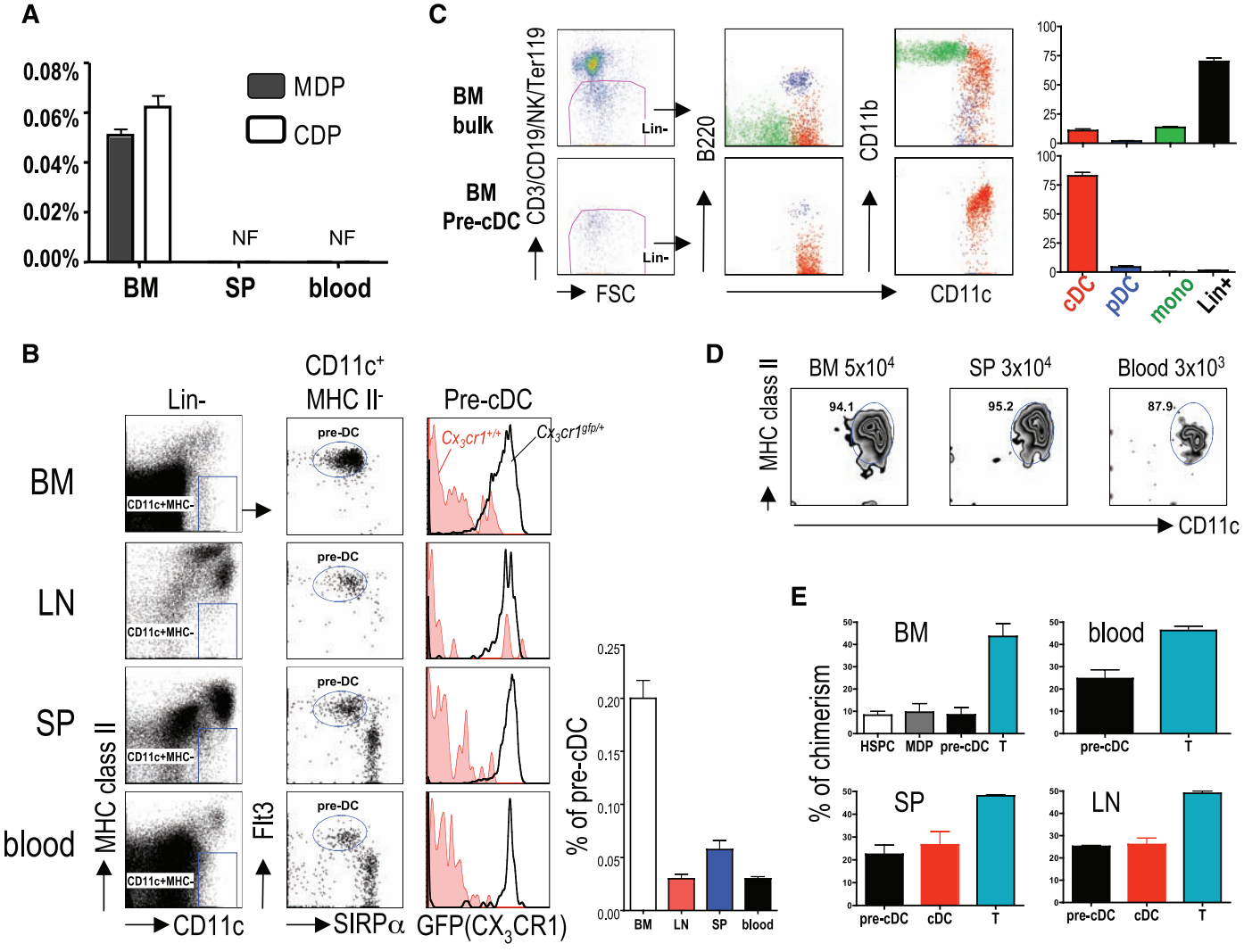

Fig. 1. Isolation of pre-cDCs. (**A**) Presence of MDPs and CDPs in the bone marrow (BM), blood, or spleen (SP). NF, not found. (**B**) Identification of pre-cDCs in bone marrow, LNs, spleen, and blood. The bar graph shows the percentage of pre-cDC in each organ. 1×10^6 cells were acquired per sample. Lin- indicates cells that do not express CD3, CD19, Ter119, NK 1.1, or B220 antigens. (**C**) Donor-derived spleen cells ($CD45.2^+$) were analyzed for cDC ($CD11c^+$ MHC class II^+), pDC ($CD11c^{int}$ $B220^+$), and monocytes ($CD11b^+$ $CD11c^{lo/-}$) 7 days after intravenous injection of 2×10^6 bone marrow cells or 1×10^5 pre-cDCs. (**D**) Analysis of donor-derived splenocytes after transfer with the indicated number of pre-cDCs from bone marrow, spleen, and blood. (**E**) Chimerism in parabiotic mice. In (B) and (C), the left side shows representative dot plots. The bar graphs summarize 2 to 4 independent experiments with 3 to 4 mice each. Error bars represent the mean ± SEM.

major histocompatability complex (MHC) class II$^-$ SIRP-α^{int} Flt3$^+$ cells (pre-cDCs) in the bone marrow (0.2%), blood (0.03%), spleen (0.05%), and lymph nodes (LNs) (0.03%) (Fig. 1B).

To determine whether pre-cDCs develop into cDCs in vivo, we compared them with unfractionated bone marrow cells in adoptive transfer experiments. After 7 days, unfractionated bone marrow gave rise to cDCs (10.2 ±1.2%), pDCs (1.9± 0.7%), and monocytes (13.5 ± 2.1%); in contrast, pre-cDCs from bone marrow, blood, or spleen yielded predominantly cDCs (88 to 95%) (Fig. 1, C and D, and fig. S2). These data indicate that pre-cDCs are indeed precursors to cDCs that arise in the bone marrow. They are restricted to the cDC lineage and have a reduced potential to produce monocytes or other lymphoid cells, including B, T, and natural killer (NK) cells (fig. S3). Pre-cDCs give rise to CD8$^-$ and CD8$^+$ DCs but at slightly different ratios than are present in the unperturbed steady state (fig. S3).

Although the circulating pre-cDC had not been identified, parabiosis experiments suggested that they should be unequally exchanged between mice that share blood circulation because of their short half-life in the blood (*15*). To test this idea, we measured the exchange of cDCs and pre-cDCs in the bone marrow, blood, spleen, and LNs 50 weeks after parabiosis. We found incomplete (24%) chimerism of pre-cDCs in the blood and peripheral lymphoid organs even after prolonged parabiosis (Fig. 1E). We conclude that pre-cDCs arise from progenitors in the bone marrow and travel through the blood to peripheral lymphoid organs, where they further differentiate into cDCs.

To determine the relationship between pre-cDCs and other reported DC progenitors, we fractionated bone marrow cells from *Cx$_3$cr1$^{gfp/+}$* reporter mice. In addition to MDPs (*7*) and CDPs (*9*, *10*), we included an earlier developmental stage, myeloid progenitors (MPs) (Fig. 2A and fig. S2) (*19*). To determine the precursor-progeny relationship between MPs, MDPs, CDPs, and pre-cDCs, we performed adoptive transfer experiments in which purified progenitors were injected into the bone marrow of unirradiated 3- to 4-week-old recipient mice (*8*, *10*). Two days after the transfer, MPs gave rise to MDPs, CDPs, and pre-cDCs, whereas MDPs only generated CDPs and pre-cDCs (Fig. 2B). Furthermore, at this early time point, CDPs produced only pre-cDCs (Fig. 2B). As previously reported, 7 days after transfer MDPs produced cDCs, pDCs, and monocytes, whereas CDPs gave rise to pDCs and cDCs but not monocytes (Fig. 2C and figs. S4 and S5) (*8*–*10*). Thus, MPs give rise to MDPs, which produce monocytes and CDPs. CDPs are further restricted in order to generate pre-cDCs and pDCs.

Monocytes and pre-cDCs shared features with MDPs, but they diverged phenotypically from MDP in the bone marrow (figs. S6 and S7). To confirm the point of divergence between monocytes and cDCs, we made use of *LysM-CrexRosa26-StopfloxEGFP* mice (*20*). In these mice, monocytes and their progeny are irreversibly marked with enhanced green fluorescent protein (EGFP) expression because lysozyme promoter–driven Cre expression leads to deletion of the Stop sequence from *Rosa26-StopfloxEGFP* (Fig. 2D and fig. S8) (*20*). In contrast to bone marrow and blood monocytes and their progeny, MDP, CDP, pDCs, pre-cDCs, and cDCs did not express EGFP and therefore never went through a monocyte intermediate (Fig. 2D). We conclude that monocytes separate from the cDC lineage during the transition from MDP to CDP in the bone marrow, but our data do not rule out the possibility of an alternative monocyte-independent pathway of cDC development.

Similar to MDPs, monocytes and pre-cDCs in the bone marrow actively divided as measured

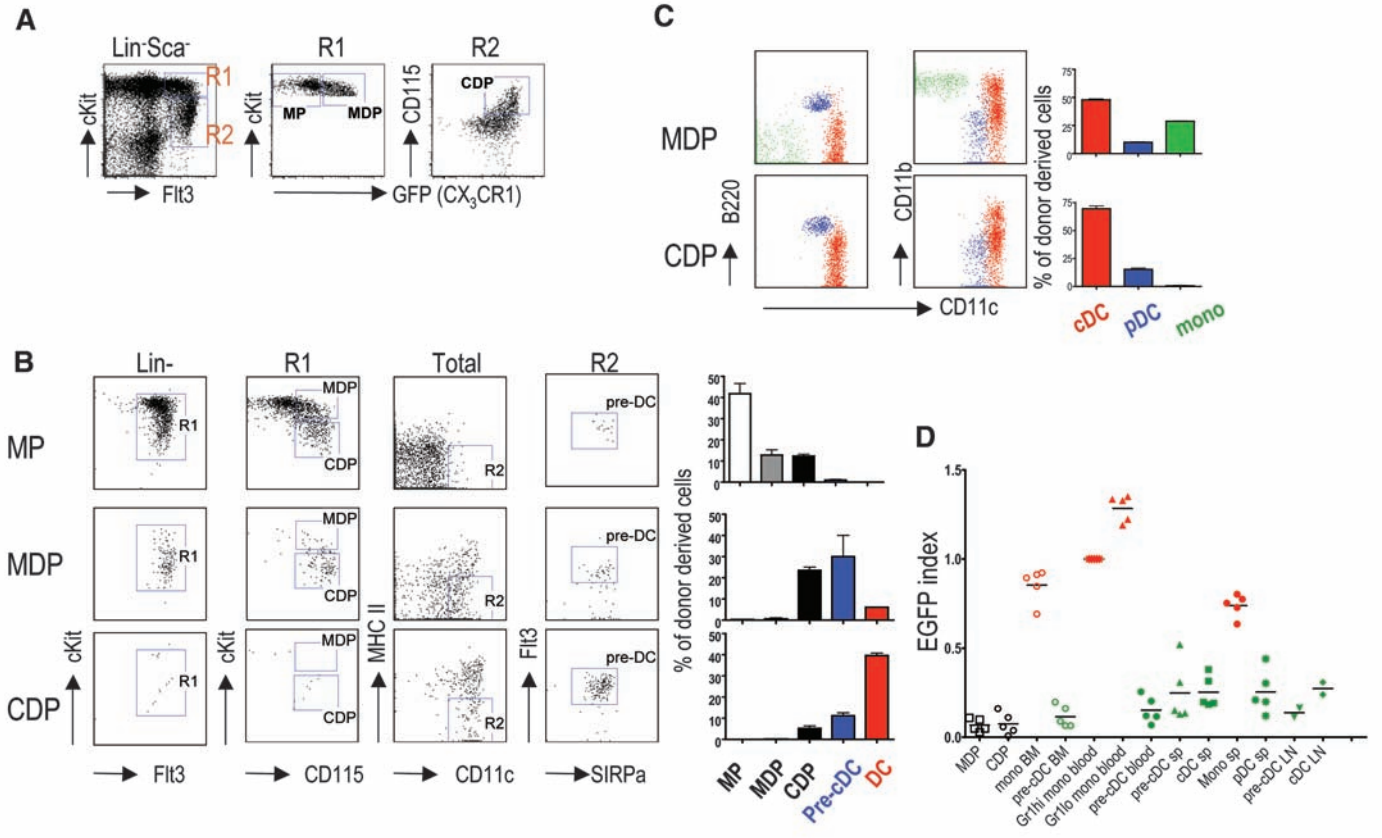

Fig. 2. Progenitor-product relationship among MDP, CDP, and pre-cDC. (**A**) Phenotype of MP (Lin$^-$ Sca-1$^-$ c-Kit^{high} CX$_3$CR1$^-$), MDP (CX$_3$CR1$^+$ c-Kit^{hi}), and CDP (CD115$^+$CX$_3$CR1$^+$c-Kit^{lo}) in *Cx$_3$cr1$^{gfp/+}$* mice. (**B**) Donor-derived bone marrow cells analyzed with flow cytometry for presence of MDPs, CDPs, and pre-cDCs 2 days after intra–bone marrow transfer of 5 × 10^4 MPs, MDPs, or CDPs. (**C**) Donor-derived splenocytes analyzed for the presence of cDCs, pDCs, and monocytes 7 days after transfer of MDPs or CDPs. (**D**) EGFP expression in indicated cell populations in *LysM-CrexRosa26-StopfloxEGFP* reporter mice (fig. S8). EGFP index is the percentage of EGFP$^+$ cells divided by the percentage of EGFP$^+$ Gr1^{high} blood monocytes (*20*). In (B) and (C), the left side shows representative dot plots. The bar graphs summarize 2 to 4 independent experiments with 3 to 4 mice. Error bars represent the mean ± SEM.

by 4′,6′-diamidino-2-phenylindole staining and 5-bromo-2′-deoxyuridine incorporation; however, this was not observed in the spleen or in the blood (fig. S9). We conclude that pre-cDC expansion takes place primarily in the bone marrow and that upon differentiation into cDCs in lymphoid tissues, the latter undergo cell division (fig. S9) (*17*).

To examine the fate and distribution of pre-cDCs in lymphoid organs, we visualized them by means of two-photon laser scanning microscopy. Up to 5 hours after adoptive transfer, pre-cDCs were detected in close proximity to major blood vessels, primarily in the medullary side of the node and at the interface between the T cell zone and B cell follicles (Fig. 3A and movies S1 to S3; ratio of cortical to medullary pre-cDC = 0.41 at 2 to 5 hours after injection; $n = 3$ nodes). These vessels showed a cobblestone morphology and a distribution that is typical of high endothelial venules (HEVs) (movies S2 and S3). Consistent with the observation that pre-cDCs were frequently found near HEVs, pre-cDCs expressed CD62L, and antibody-mediated inhibition of CD62L prevented cDC accumulation in the LNs but not the spleen, in which pre-cDCs may enter the white pulp through the marginal sinuses (Fig. 3B and fig. S10) (*21*). Between 1 and 5 hours after injection, transferred pre-cDCs were sessile (average speed = 1.9 μm/min; SD = 1.0) and remained in contact with HEVs, exhibiting very little displacement (Fig. 3, C and D, and movies S2 and S3). After 16 to 18 hours, pre-cDCs and their progeny continued to localize to vessel-rich areas; however, they were no longer attached to blood vessels and displayed a more migratory behavior (average speed = 5.6 μm/min; SD = 3.0) (Fig. 3, C and D, and movies S4 and S5). In contrast, after 6 days the progeny of pre-cDCs were distributed throughout the LN paracortex and integrated into the endogenous DC network (Fig. 3A and movies S6 and S7; ratio of cortical to medullary pre-cDC = 1.95 at 6 days after injection; $n = 3$ nodes). These cells displayed dendritic morphology (Fig. 3A) and active probing behavior with very restricted displacement and

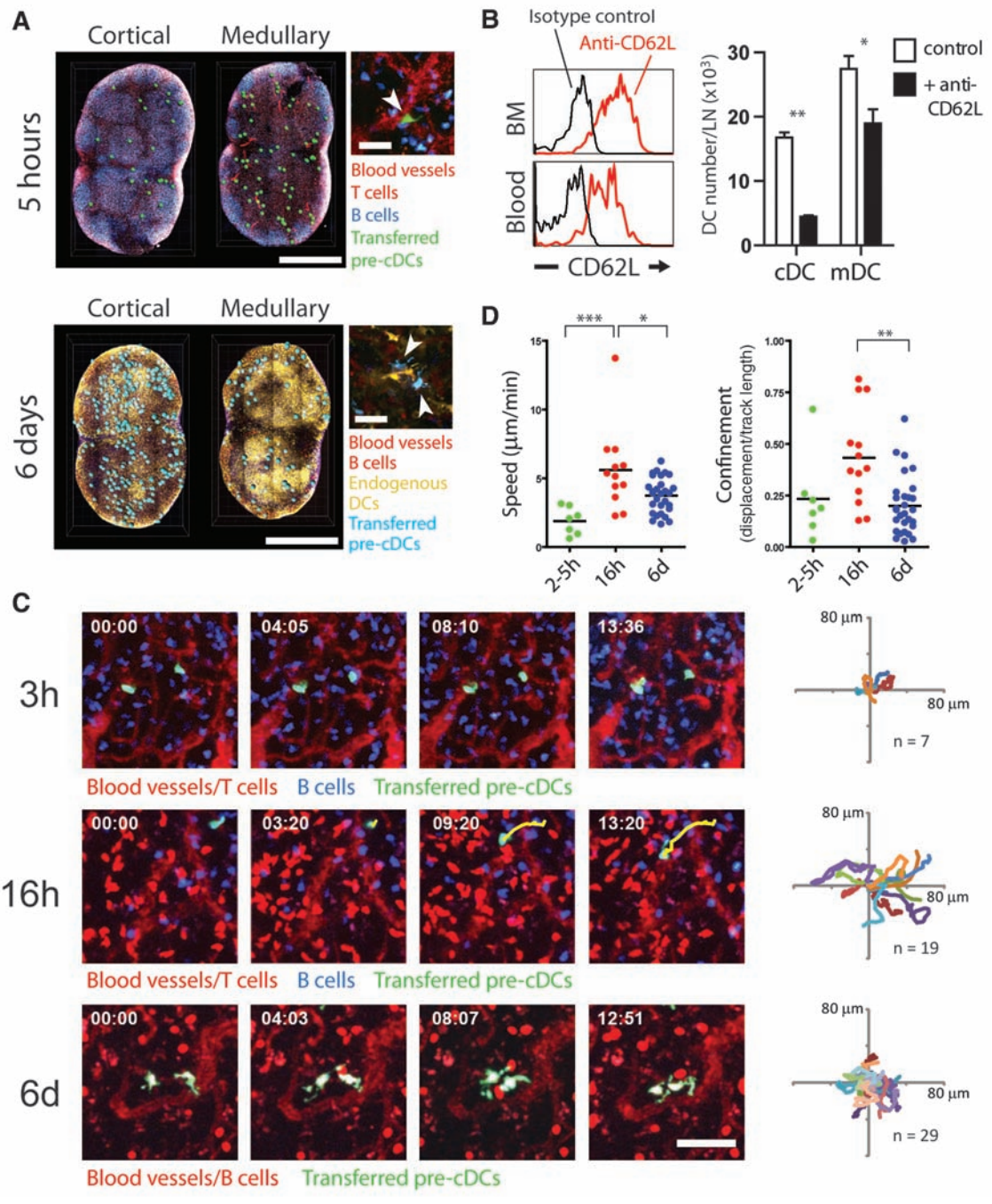

Fig. 3. Multi-photon imaging of pre-cDCs. (**A**) Transferred cells in inguinal LNs 5 hours (top, green) and 6 days (bottom, blue) after pre-cDC transfer. Panels at right show morphology of transferred pre-cDCs (arrowheads). Scale bars, 1 mm (left) and 30 μm (right). (**B**) (Left) CD62L expression on pre-cDCs. (Right) Graph showing the number of LN cDCs or migratory DCs (mDCs) after treatment with antibody to CD62L. The graph represents the mean ± SD ($n = 4$ mice per group in 3 experiments). *$P = 0.0286$; **$P < 0.0001$; Student's t test. (**C**) Dynamic behavior, morphology, and position of pre-cDCs at indicated times. A cell track (yellow) is superimposed to visualize displacement. Scale bar, 50 μm. Far right shows superimposed two-dimensional (XY) tracks with starting coordinates set to the origin. The number of cells analyzed (n) is indicated. (**D**) Graphs show velocity and confinement of pre-cDCs at indicated times. Differences between columns are significant according to a Kruskal-Wallis test (a heterogeneity of speed, $P = 0.0006$; and meandering, $P = 0.0055$). *$P < 0.05$; **$P < 0.01$; ***$P < 0.001$; Dunn's multiple comparison test. All multi-photon data represent at least two independent experiments.

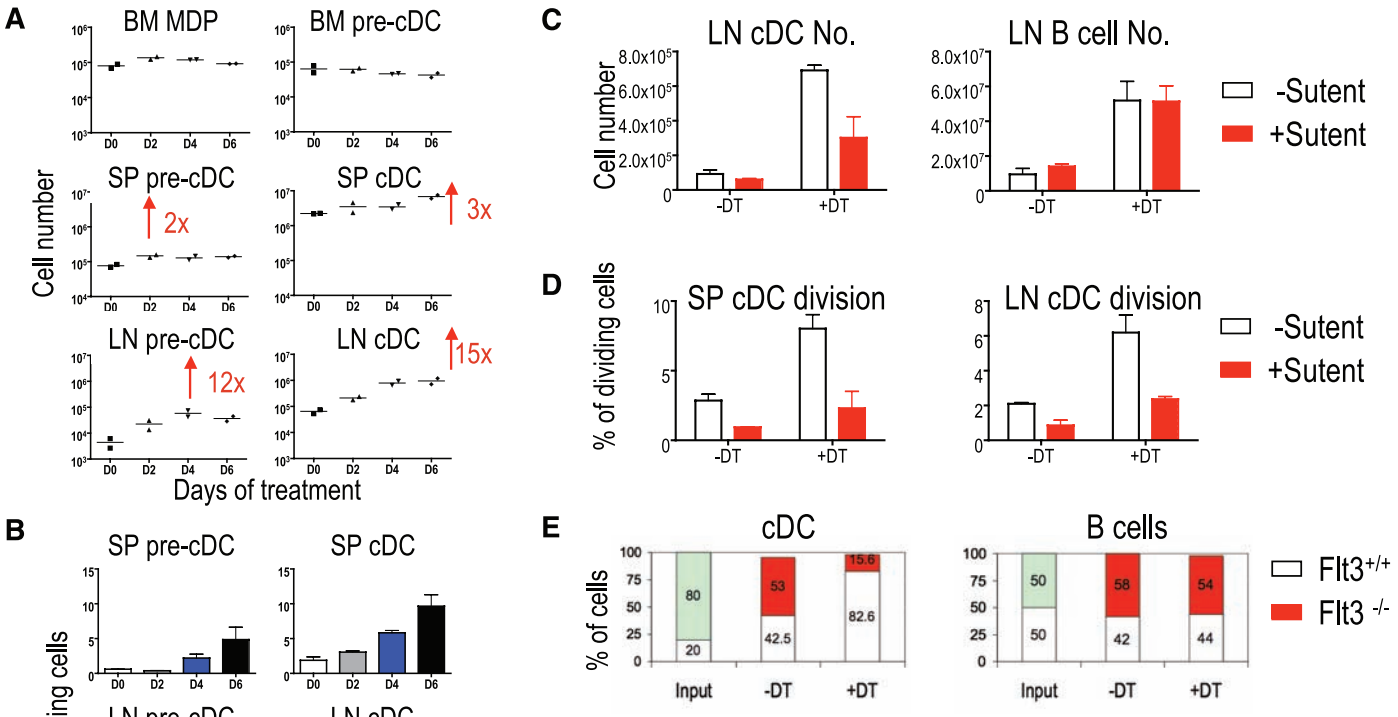

Fig. 4. T_{reg}s control DC expansion in the peripheral lymphoid organs. (**A**) Numbers of MDP, pre-cDCs, and cDCs in the indicated organs after T_{reg} depletion in *Foxp3*^{DTR} mice. (**B**) Pre-cDC and cDC division in spleen and LNs at indicated time after T_{reg} depletion. (**C** and **D**) Effect of the Flt3 inhibitor, Sutent, on T_{reg}-depletion–induced cDC and B cell expansion. (**E**) Bar graph shows the relative percentage of Flt3$^{-/-}$ CD45.1 and Flt3$^{+/+}$ CD45.2 DCs and B cells after a mixed bone-marrow transfer into *FoxP3*^{DTR} CD45.1XCD45.2 mice after DT treatment. The panels represent two to four independent experiments. The bar graph represents the mean ± SEM (n = 3 to 4 mice).

reduced average speeds (3.7 μm/min; SD = 1.3) (Fig. 3, C and D, and movies S7 and S8) (*22*). We conclude that pre-cDCs enter the LNs through HEVs and then distribute themselves throughout the LN and assume typical DC behavior.

Depletion of CD4$^+$Foxp3$^+$ regulatory T cells (T_{reg}s) leads to DC expansion, but how or where T_{reg}s affect the DC developmental pathway has not been determined (*23*). To examine this, we investigated the effect of T_{reg} depletion on DC development with the use of *Foxp3*^{DTR} mice. These mice express the diphtheria toxin receptor (DTR) under the control of the Foxp3 promoter, and treatment of these mice with diphtheria toxin (DT) results in the specific deletion of Foxp3$^+$ cells (*23*). We found no change in MDPs or bone-marrow pre-cDCs after T_{reg} depletion. In contrast, spleen and LN pre-cDCs and cDCs increased by 2- and 12-fold, respectively (Fig. 4A) (*23*). In addition, the percentage of dividing cDCs in both spleen and LNs increased from 5 to 10%, which suggests that T_{reg} depletion results in augmented pre-cDC and cDC division specifically in lymphoid organs (Fig. 4B).

Under steady-state conditions, the rate of cDC division in lymphoid organs is regulated in part by Flt3 receptor signaling (*16*). To determine whether the Flt3 pathway is required for T_{reg} control of cDC expansion, we used Sutent (Pfizer, New York), a multi-targeted tyrosine kinase inhibitor with affinity for Flt3 (*24*). We found that Sutent treatment inhibited cDC expansion but not B cell expansion in T_{reg}-depleted mice (Fig. 4, C and D). To further confirm the role of the Flt3 pathway in cDC expansion in response to T_{reg} depletion, we adoptively transferred mixtures of bone marrow–derived DC progenitors from wild-type *Flt3*$^{+/+}$ and *Flt3*$^{-/-}$ mice into *Foxp3*^{DTR} recipients and measured their response to DT treatment. Whereas wild-type cDCs expanded, *Flt3*$^{-/-}$ cDCs did not (Fig. 4E). We conclude that increased local production of Flt3-L by a yet-to-be-determined cell type is required for DC division in response to T_{reg} depletion.

The precursor-progeny relationship of monocytes, cDCs, and pDCs has been debated since the discovery of DCs 35 years ago (*1*). Resolving this issue has been particularly difficult because monocytes can develop many of the phenotypic characteristics of DCs under conditions of inflammation in vivo or in the presence of certain cytokines in vitro (*11*–*13*, *20*). Furthermore, cDCs, pDCs, and monocytes share a common progenitor, the MDP (Fig. 2C). Several studies have shown that monocytes do not develop into cDCs, however, and that they make only a minor contribution to the lymphoid-organ DC network in the steady state (*8*, *25*). We have defined the point of divergence between multipotential precursors and cDC restricted progenitors in the bone marrow and shown that the latter migrate through the blood to lymphoid tissues, where they and their progeny divide to fill the DC compartment. We further revealed that T_{reg}s control DC development in the peripheral lymphoid organs in a Flt3-dependent manner (fig. S11). These newly recognized features of DC development in vivo open up the possibility of expanding or reducing DC numbers in vaccines and other clinical settings.

References and Notes

1. R. M. Steinman, *Nat. Med.* **13**, 1155 (2007).
2. K. Shortman, Y. J. Liu, *Nat. Rev. Immunol.* **2**, 151 (2002).
3. T. Iyoda *et al.*, *J. Exp. Med.* **195**, 1289 (2002).
4. D. Dudziak *et al.*, *Science* **315**, 107 (2007).
5. T. Di Pucchio *et al.*, *Nat. Immunol.* **9**, 551 (2008).
6. M. Gilliet, W. Cao, Y. J. Liu, *Nat. Rev. Immunol.* **8**, 594 (2008).
7. D. K. Fogg *et al.*, *Science* **311**, 83 (2006).
8. C. Varol *et al.*, *J. Exp. Med.* **204**, 171 (2006).
9. S. H. Naik *et al.*, *Nat. Immunol.* **8**, 1217 (2007).
10. N. Onai *et al.*, *Nat. Immunol.* **8**, 1207 (2007).
11. G. J. Randolph, S. Beaulieu, S. Lebecque, R. M. Steinman, W. A. Muller, *Science* **282**, 480 (1998).
12. G. J. Randolph, K. Inaba, D. F. Robbiani, R. M. Steinman, W. A. Muller, *Immunity* **11**, 753 (1999).
13. F. Geissmann, S. Jung, D. R. Littman, *Immunity* **19**, 71 (2003).
14. C. Auffray, M. H. Sieweke, F. Geissmann, *Annu. Rev. Immunol.* 10.1146/annurev.immunol.021908.132557 (2009).
15. K. Liu *et al.*, *Nat. Immunol.* **8**, 578 (2007).
16. C. Waskow *et al.*, *Nat. Immunol.* **9**, 676 (2008).
17. J. Diao *et al.*, *J. Immunol.* **176**, 7196 (2006).

18. S. H. Naik *et al.*, *Nat. Immunol.* **7**, 663 (2006).
19. H. Karsunky, M. Merad, A. Cozzio, I. L. Weissman, M. G. Manz, *J. Exp. Med.* **198**, 305 (2003).
20. C. B. M. Jakubzick, A. J. Bonito, E. L. Kuan, M. Merad, G. J. Randolph, *J. Exp. Med.* **205**, 2839 (2008).
21. M. D. Catalina *et al.*, *J. Exp. Med.* **184**, 2341 (1996).
22. R. L. Lindquist *et al.*, *Nat. Immunol.* **5**, 1243 (2004).
23. J. M. Kim, J. P. Rasmussen, A. Y. Rudensky, *Nat. Immunol.* **8**, 191 (2007).
24. R. Tussiwand, N. Onai, L. Mazzucchelli, M. G. Manz, *J. Immunol.* **175**, 3674 (2005).
25. C. Jakubzick *et al.*, *J. Immunol.* **180**, 3019 (2008).
26. The authors thank S. Bhuvanendran for two-photon microscopy, K. Velinzon and T. Shengelia for cell sorting, and R. Steinman and A. Silva for discussions and critical reading of the manuscript. K.L. was supported by a C. H. Li Memorial Scholarship Award from the Rockefeller University. T.A.S. was supported by the Schering Foundation. This work was supported in part by grants from the NIH to M.C.N. M.C.N. is an HHMI investigator.

Supporting Online Material
www.sciencemag.org/cgi/content/full/1170540/DC1
Materials and Methods
Figs. S1 to S11
References
Movies S1 to S8

6 January 2009; accepted 4 March 2009
Published online 12 March 2009;
10.1126/science.1170540
Include this information when citing this paper.

A Contemporary Microbially Maintained Subglacial Ferrous "Ocean"

Jill A. Mikucki,[1]* Ann Pearson,[1] David T. Johnston,[2] Alexandra V. Turchyn,[3] James Farquhar,[4] Daniel P. Schrag,[1] Ariel D. Anbar,[5] John C. Priscu,[6] Peter A. Lee[7]

An active microbial assemblage cycles sulfur in a sulfate-rich, ancient marine brine beneath Taylor Glacier, an outlet glacier of the East Antarctic Ice Sheet, with Fe(III) serving as the terminal electron acceptor. Isotopic measurements of sulfate, water, carbonate, and ferrous iron and functional gene analyses of adenosine 5′-phosphosulfate reductase imply that a microbial consortium facilitates a catalytic sulfur cycle. These metabolic pathways result from a limited organic carbon supply because of the absence of contemporary photosynthesis, yielding a subglacial ferrous brine that is anoxic but not sulfidic. Coupled biogeochemical processes below the glacier enable subglacial microbes to grow in extended isolation, demonstrating how analogous organic-starved systems, such as Neoproterozoic oceans, accumulated Fe(II) despite the presence of an active sulfur cycle.

Subglacial environments represent a largely unexplored component of Earth's biosphere (*1*). In the McMurdo Dry Valleys, Antarctica, an iron-rich subglacial outflow (Blood Falls) flows from the Taylor Glacier (Fig. 1A), providing unique access to a subglacial ecosystem. The likely fluid source to Blood Falls is a pool of marine brine of unknown depth trapped underneath the glacier ~4 km from the glacier snout where the overlying ice is ~400 m thick (*2*). Pliocene surface uplift of the Taylor Valley floor, and the associated recession of the Ross Sea Embayment, isolated this pocket of brine (*3*). Before isolation from direct contact with the atmosphere, the brine was cryoconcentrated (*4*, *5*), resulting in hypersalinity (~1375 mM Cl^-). This brine has been isolated for at least 1.5 million years (My), when the Taylor Glacier last advanced over the area (*6*). Although the brine at present is anoxic and highly ferrous and the pH is circumneutral (Table 1), activity and DNA sequence data reveal that it supports a metabolically active, largely marine microbial assemblage (*7*).

Taylor Glacier is frozen to its bed, and surface-derived water does not penetrate to the base (*8*). Poorly understood hydrologic controls result in episodic release of brine. The data in this study are from one of these active discharge events. Salts and the iron mineral goethite rapidly precipitate upon contact of the outflow with the oxidizing atmosphere (*5*). Although regelation as the glacier slides over the bedrock and brine may add trace amounts of meteoric gases including O_2 (*9*), multiple geochemical measurements reveal no quantitatively significant contributions. Radiocarbon data confirm that dissolved inorganic carbon (DIC) is old [$\Delta^{14}C_{DIC}$ = –993 ± 1 (SE) per mil (‰) (*10*)]. Presumably, interactions with air at the point of outflow collection are responsible for the small amount of $^{14}C_{DIC}$ in our samples (^{14}C-free would be –1000‰). No dissolved O_2 was detected in the brine [reduction potential (E_h) = 90 mV], and iron was 97% Fe(II), indicating that inputs from ice-bound atmospheric O_2 are minimal.

Heterotrophic activity was measured by using ^{3}H-thymidine incorporation (Table 1) (*10*). Although the most abundant electron acceptor in the brine is SO_4^{2-}, isotope data suggest that SO_4^{2-} is not terminally reduced in quantities sufficient to affect isotopes of sulfur. Values of $\delta^{34}S_{SO4}$ and $\Delta^{33}S_{SO4}$ in the brine (21.0‰ and range = 20.8 to 21.7‰ for $^{34}S_{SO4}$; 0.08‰ and range = 0.06 to 0.09‰ for $^{33}S_{SO4}$; n = 6) were similar to measurements of seawater SO_4^{2-} from the past 15 My measured in marine barites (*11*). In contrast, values of $\delta^{18}O_{SO4}$ (3.3‰; range = 2.7 to 4.9‰; n = 6) were up to 7‰ depleted compared with that of seawater $\delta^{18}O_{SO4}$ from marine barites over the Pliocene [10.4 ± 1.6‰ (*12*)]. Because values of both $\delta^{34}S$ and $\delta^{18}O$ in SO_4^{2-} are influenced independently by microbial sulfur metabolism, including sulfate reduction, disproportionation, and reoxidation reactions (*13*, *14*), we expect that both oxygen and sulfur isotopes would be affected. For example, dissimilatory sulfate reduction to sulfide would cause preferential enrichment of ^{34}S ($SO_4^{2-} \rightarrow H_2S$, fractionation factor (ε) = 20 to 40‰ for natural populations) (*15*) because ^{34}S-depleted S^{2-} is sequestered in iron sulfides. This would increase the $\delta^{34}S_{SO4}$ value of the remaining sulfate pool.

Our isotope data indicate that incorporation of ^{18}O-depleted brine water oxygen into sulfate has occurred (Fig. 1B and table S3). During glacial advancement, meltwater mixing with the remaining seawater decreased the $\delta^{18}O$ value of the brine from a marine value to its current composition ($\delta^{18}H_2O_{Brine}$ = –39.5‰; Table 1). The depleted value of $\delta^{18}O_{SO4}$ cannot be explained by abiotic oxygen isotope exchange between SO_4^{2-} and water. Such equilibration would take tens of millions of years at subglacial temperatures and pH (*16*) (Table 1). However, oxygen isotope exchange between sulfite (SO_3^{2-}) and water occurs rapidly [50% exchange in <5 min (*17*)], and the reduction of SO_4^{2-} to SO_3^{2-} is biologically mediated (*7*). Complete equilibration of SO_4^{2-} via cycling through SO_3^{2-} and exchanging all oxygen atoms with water would result in a 30.9‰ offset from brine water or a value for $\delta^{18}O_{SO4}$ of –8.6‰ (Fig. 1B). This offset represents the temperature-adjusted equilibrium fractionation factor of ^{18}O in SO_3^{2-} relative to brine H_2O (ε = 30.9‰ at –5.2°C). Given the measured values of $\delta^{18}O_{SO4}$ (2.7‰ to 4.9‰), isotopic mass balance requires that 30 to 40% of the SO_4^{2-} pool has exchanged its O atoms with water, likely through equilibration with SO_3^{2-}.

Characterization of the Blood Falls microbial assemblage has revealed taxa that could participate in active sulfur cycling, including autotrophs and heterotrophs (table S1). Sulfate is biologically reduced to SO_3^{2-} by using (phospho-)adenosine 5′-phosphosulfate–reductase by assimilatory [3′-phosphoadenosine 5′-phosphosulfate (PAPS)]

[1]Department of Earth and Planetary Sciences, Harvard University, Cambridge, MA 02138 USA. [2]Department of Organismic and Evolutionary Biology, Harvard University, Cambridge MA, 02138 USA. [3]Department of Earth Sciences, University of Cambridge, Cambridge CB2 3EQ, UK. [4]Department of Geology, University of Maryland, College Park, MD 20742, USA. [5]School of Earth and Space Exploration and Department of Chemistry and Biochemistry, Arizona State University, Tempe, AZ 85287, USA. [6]Department of Land Resources and Environmental Sciences, Montana State University, Bozeman, MT 59717, USA. [7]Hollings Marine Laboratory, College of Charleston, Charleston, SC 29412, USA.

*Present address: Department of Earth Sciences, Dartmouth College, Hanover, NH 03755, USA. To whom correspondence should be addressed. E-mail: jill.a.mikucki@dartmouth.edu

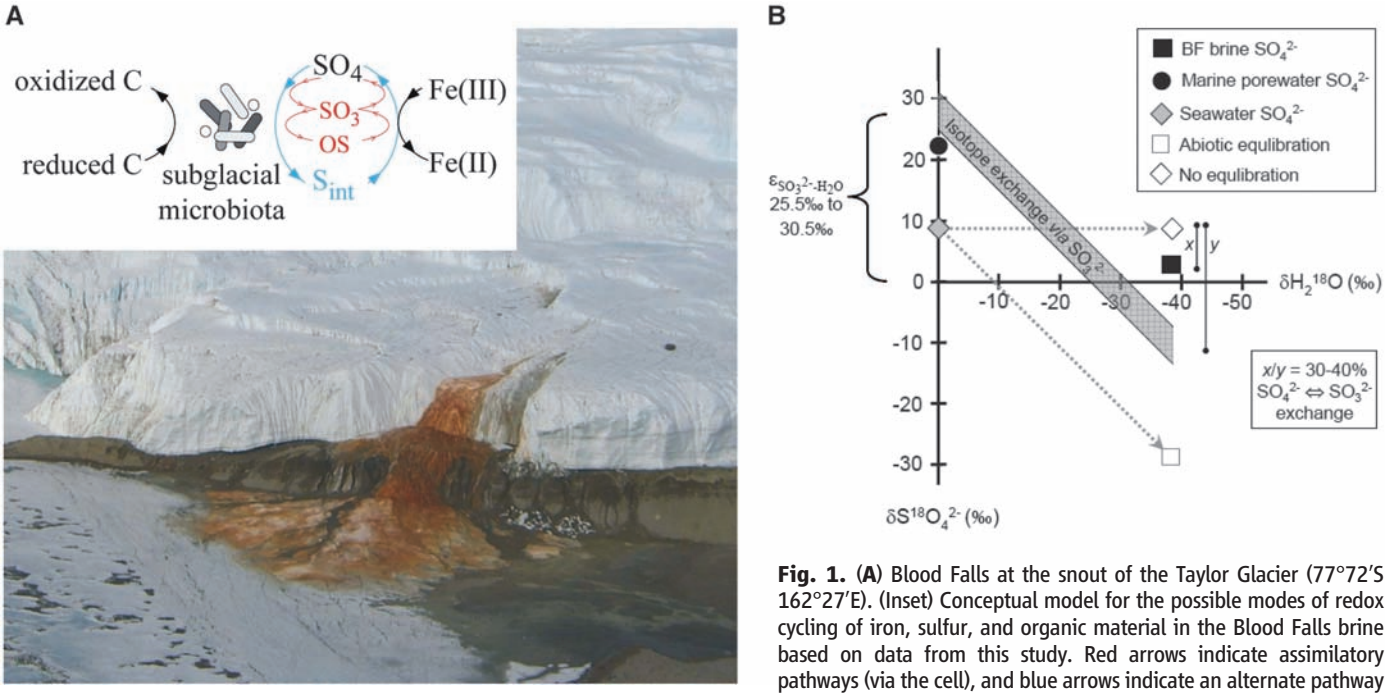

Fig. 1. (**A**) Blood Falls at the snout of the Taylor Glacier (77°72′S 162°27′E). (Inset) Conceptual model for the possible modes of redox cycling of iron, sulfur, and organic material in the Blood Falls brine based on data from this study. Red arrows indicate assimilatory pathways (via the cell), and blue arrows indicate an alternate pathway via catalytic sulfur cycling mediated by APS reductase. (**B**) Values of $\delta^{18}O_{SO4}$ relative to $\delta H_2{}^{18}O$, given different reaction scenarios. Sulfate and water will have equilibrated by no more than 1‰ within 50 My, therefore no net change would be expected in the $\delta^{18}O_{SO4}$ of a seawater brine mixed with ^{18}O-depleted glacier water (gray diamond). Where $SO_4{}^{2-}$ reduction occurs, $SO_3{}^{2-}$ equilibrates with the in situ water, ε = 25 to 30.5‰, resulting in $\delta^{18}O_{SO4}$ predicted by the shaded gray line (*15*, *24*). In marine sediments (*32*) (black diamond), complete equilibration of $SO_3{}^{2-}$ with in situ water is observed, indicating quantitative reduction of $SO_4{}^{2-}$. If $SO_4{}^{2-}$ reduction occurred to completion in Blood Falls, values of $\delta^{18}O_{SO4}$ between −8 and −10‰ (25 to 30.5‰ isotopically heavier than the in situ water) would be expected. Because the data (3.3‰, black circle) plot above this line of complete equilibration, only a portion (30 to 40%) of the total $SO_4{}^{2-}$ pool has equilibrated.

or dissimilatory (APS) metabolisms, although APS also has been identified in sulfur oxidizers and certain organisms that only assimilate sulfate (*18*). The majority of APS genes detected in Blood Falls brine (Fig. 2) clustered with APS sequences of known dissimilatory and sulfur-disproportionating species (group 1). Sequences closely related to the APS gene from *Desulfocapsa sulfexigens* are consistent with the presence of a relative of this species among the 16*S* ribosomal RNA clones (*7*). Clone APS_20 (group 2) shares relations with sulfur-oxidizing isolates and *Thermacetogenium phaeum*, a syntrophic acetate-oxidizing bacterium that can also reduce sulfate (*19*). We cannot eliminate the possibility of trace production of H_2S because one sequence (clone B_11) showed distant relation to groups known to mediate complete sulfate reduction (e.g., *Desulfovibrio* spp.). However, we were unable to detect dissimilatory sulfite reductase (*dsrA*) genes across several methods and attempts, and the sulfur isotope data are inconsistent with measureable quantities of sulfide formation.

Table 1. Biogeochemical parameters of Blood Falls outflow during a brine discharge event. Outflow samples collected in December 2004. nd indicates none detected. The first six parameters and sulfate and chloride concentrations are from (*33*); total iron is from (*7*).

Temperature	−5.2°C
pH	6.2
E_h	90 mV
Dissolved oxygen	nd
DIC	55 mM
Dissolved organic carbon (DOC)	420 μM
Dissolved inorganic nitrogen (DIN)	94 μM (100% as $NH_4{}^+$)
Total iron	3.45 mM [>97% as Fe(II)]
Sulfate	50 mM
Chloride	1375 mM
Total cells	6×10^4 ml^{-1}
Thymidine (Tdr) incorporation rate	1.9×10^{-4} nM Tdr day^{-1} ($\pm 2 \times 10^{-5}$)
$\Delta^{14}C_{DIC}$	−993 ± 1‰
$\delta^{34}S_{Sulfate}$	21.0 ± 0.4‰
$\Delta^{33}S_{Sulfate}$	0.08‰ (range = 0.06 to 0.09‰)
$\delta^{18}O_{Sulfate}$	3.3 ± 0.8‰
$\delta^{18}O_{H2O}$	−39.5 ± 0.1‰
$\delta^{56}Fe$	−2.60 ± 0.5‰

The presence of metabolically active cells requires a small supply of assimilated sulfur because sulfur composes ~0.1% of cell biomass (*15*). We estimated a doubling time for heterotrophs of ~300 days (Table 1) (*10*) equaling ~10^6 generations over 1.5 My of isolation. If all cellular organic sulfur requirements were derived each generation by de novo assimilatory reduction, an upper limit of ~35% of the $SO_4{}^{2-}$ pool would have been used. This result is consistent with our estimate of 30 to 40% $SO_4{}^{2-}$ turnover but is unlikely to provide the full explanation for sulfur cycling in the brine. Initially the system would have included reduced organic nutrients (N, S, and P), including S-containing amino acids, in stoichiometric proportion to the initial supply of organic matter. Availability of this additional pool of biological metabolites could decrease the effective assimilatory $SO_4{}^{2-}$ demand substantially. Additionally, the presence of diverse sulfur-cycling microbes (*7*) and several groups of APS genes indicate the presence of metabolic processes beyond assimilation strictly for biomass.

How then is the additional sulfate cycled? The unchanged values of $\delta^{34}S_{SO4}$ indicate that there is insignificant loss of sulfur to sedimentary pyrite. This implies that the reduction of $SO_4{}^{2-}$ to

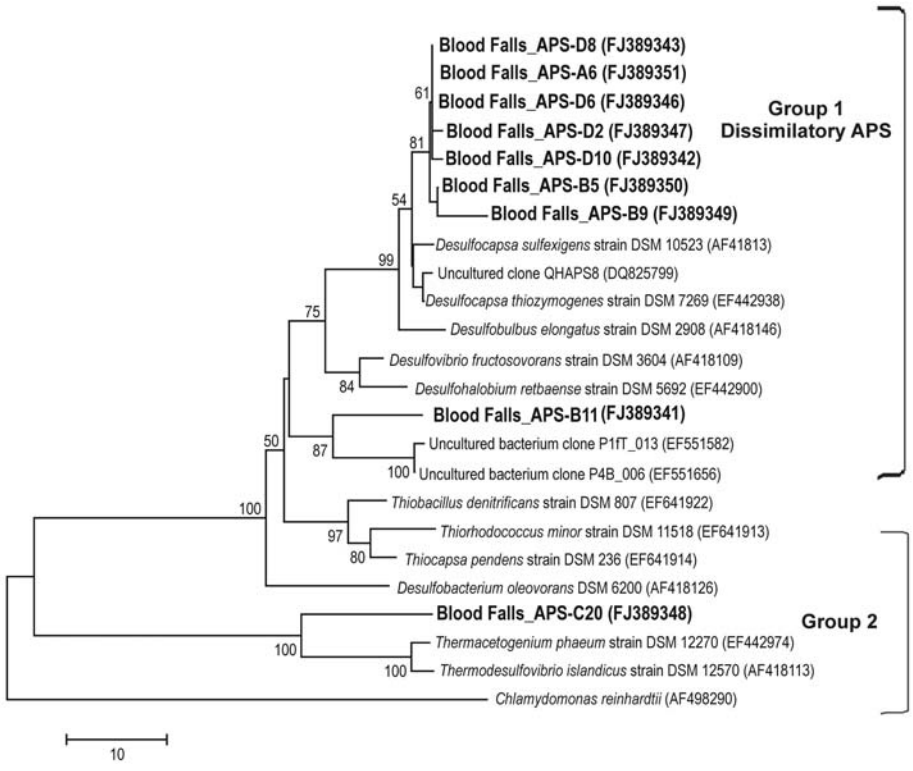

Fig. 2. Neighbor-joining phylogenetic tree of APS-reductase genes cloned from Blood Falls genomic DNA. Results of bootstrap analysis with 1000 replications are noted. The scale bar represents 10 nucleotide substitutions per sequence position. Clones from Blood Falls are in bold. GenBank accession numbers are listed in parentheses.

SO_3^{2-} does not proceed all the way to H_2S, which is consistent with the observation of ferruginous and not euxinic conditions (no detectable H_2S). To achieve these isotopic values, the net metabolism in the brine requires two remarkable properties: (i) SO_4^{2-} must recycle through sulfur intermediates, and (ii) these sulfur intermediates must be quantitatively reoxidized to SO_4^{2-}.

We advocate that sulfur is catalytically cycled to facilitate the oxidation of organic matter in a system in which Fe(III) is the terminal acceptor. Both assimilatory and dissimilatory reduction of SO_4^{2-} proceed enzymatically through intermediate species (*15*). To date, no cultured dissimilatory organism has been described in which SO_4^{2-} reduction does not ultimately terminate in H_2S. The initial steps of $SO_4^{2-} \rightarrow SO_3^{2-} \rightarrow S_2O_3^{2-}$ are endergonic, but progression to S^0 when coupled to common electron donors [e.g., acetate and lactate (*10*)] does yield free energy (table S2). Coupling of any of the subsequent reoxidation reactions to the reduction of Fe(III) would also yield free energy (table S2). Additionally, numerous examples suggest that microbes use carrier molecules, including sulfur compounds, as electron shuttles between cells and iron oxides (*20*–*22*). Cycling sulfur as an electron shuttle to catalyze iron reduction would also be a feasible route to reduced sulfur species in this system.

Such a catalytic cycle would preserve the total dissolved sulfur concentration (Fig. 1, inset) while progressively accumulating Fe(II) to a level controlled by the solubility product constant of siderite. Although the mechanism by which recycling of sulfur species mediates Fe(III) reduction is not fully understood (*23*), in contemporary marine pore waters at depths below O_2 penetration values of $\delta^{18}O_{SO4}$ show SO_4^{2-} regeneration perhaps in association with Fe and Mn oxides (*24*). The net thermodynamics of such a system are favorable and could be described as syntrophic.

Ferric iron likely is mobilized by the scouring action of the glacier over the basement complex of metamorphic rocks intruded by granodioritic and granitic plutons (*25*). The redox state of these rocks is minimally $Fe^{2.4+}$ in the contacts and $Fe^{2.2+}$ in the basement sills and diabase sheets (*26*). A nonzero $\delta^{56}Fe$ signature in Fe(II) dissolved in the brine indicates iron redox cycling, and the strong negative fractionation (–2.6‰; Table 1) implies dissimilatory iron reduction (*27*). Given the elemental abundance of iron in Earth's crust, Fe(III) may be an important electron acceptor for many subglacial microbial ecosystems. Most subglacial environments do not contain entrapped marine salts, but all subglacial biomes interact with their underlying bedrock (*28*), and many contain low concentrations of dissolved organic carbon (*29*). Consequently, glaciers may be important in delivery of soluble Fe(II). Below Taylor Glacier, the subglacial supply of Fe(III) appears to exceed the supply of electron donors such as reduced sulfur and organic matter. Thus, the system is paradoxically rich in electron acceptors relative to electron donors, despite being anaerobic; the result is the absence of euxinia.

During periods of diminished net photosynthesis, such as Neoproterozoic Snowball Earth episodes (*30*, *31*), a decrease in organic flux from reduced photosynthetic production would drive the ocean away from SO_4^{2-} reduction, analogous to the Blood Falls system. When organic matter became sufficiently limited, euxinia would cease and Fe(II) would accumulate. This respiratory source of Fe(II) would add to the flux of hydrothermal Fe to the deep ocean (*13*), and both could lead to an episodically ferruginous ocean (*32*). Importantly, our model is independent of the size of the marine SO_4^{2-} reservoir because it depends only on the ratio of Fe(III) to labile organic matter. The brine below the Taylor Glacier provides a contemporary, natural example of an active, catalytic sulfur cycle, and it uniquely allows for the study of the long-term persistence of life and associated bioenergetics under ice.

References and Notes

1. J. C. Priscu *et al.*, in *Polar Lakes and Rivers*, W. F. Vincent, J. Laybourn-Parry, Eds. (Oxford Univ. Press, New York, 2008), pp. 119–135.
2. A. Hubbard, W. Lawson, B. Anderson, B. Hubbard, H. Blatter, *Ann. Glaciol.* **39**, 79 (2004).
3. D. P. Elston, S. L. Bressler, *Antarct. Res. Ser.* **33**, 413 (1981).
4. W. B. Lyons *et al.*, *Geochim. Cosmochim. Acta* **69**, 305 (2005).
5. R. F. Black, M. L. Jackson, T. E. Berg, *J. Geol.* **73**, 175 (1965).
6. T. I. Wilch, G. H. Denton, D. R. Lux, W. C. McIntosh, *Geogr. Ann.* **75**, 331 (1993).
7. J. A. Mikucki, J. C. Priscu, *Appl. Environ. Microbiol.* **73**, 4029 (2007).
8. A. G. Fountain *et al.*, *Bioscience* **49**, 961 (1999).
9. S. M. Aciego, K. M. Cuffey, J. L. Kavanaugh, D. L. Morse, J. P. Severinghaus, *Quat. Res.* **68**, 303 (2007).
10. Material and methods are available as supporting material on *Science* Online.
11. J. Farquhar *et al.*, *Science* **298**, 2369 (2002).
12. A. V. Turchyn, D. P. Schrag, *Science* **303**, 2004 (2004).
13. D. E. Canfield, *Nature* **396**, 450 (1998).
14. B. Brunner, S. M. Bernasconi, J. Kleikemper, M. H. Schroth, *Geochim. Cosmochim. Acta* **69**, 4773 (2005).
15. D. E. Canfield, in *Stable Isotope Geochemistry*, vol. 43 of *Reviews in Mineralogy and Geochemistry*, J. W. Valley, D. R. Cole, Eds. (Mineralogical Society of America, Washington, DC, 2001), pp. 607–636.
16. H. Chiba, H. Sakai, *Geochim. Cosmochim. Acta* **49**, 993 (1985).
17. R. H. Betts, R. H. Voss, *Can. J. Chem.* **48**, 2035 (1970).
18. J. A. Bick, J. J. Dennis, G. J. Zylstra, J. Nowack, T. Leustek, *J. Bacteriol.* **182**, 135 (2000).
19. S. Hattori, Y. Kamagata, S. Hanada, H. Shoun, *Int. J. Syst. Evol. Microbiol.* **50**, 1601 (2000).
20. D. R. Lovley, J. D. Coates, E. L. Blunt-Harris, E. J. P. Phillips, J. C. Woodward, *Nature* **382**, 445 (1996).
21. D. K. Newman, R. Kolter, *Nature* **405**, 94 (2000).
22. K. L. Straub, B. Schink, *Appl. Environ. Microbiol.* **70**, 5744 (2004).
23. B. Schink, *Eng. Life Sci.* **6**, 228 (2006).
24. A. V. Turchyn, O. Sivan, D. P. Schrag, *Geobiology* **4**, 191 (2006).
25. S. C. Cox, A. H. Allibone, *Antarct. Sci.* **3**, 405 (1991).
26. W. Hamilton, "Diabase sheets of the Taylor Glacier Region Victoria Land, Antarctica with sections on petrography and sections on chemistry" (Geological Survey Professional Paper 456-B, 1965).
27. C. M. Johnson, B. L. Beard, E. E. Roden, *Annu. Rev. Earth Planet. Sci.* **36**, 457 (2008).

28. M. Tranter, M. Skidmore, J. Wadham, *Hydrol. Process.* **19**, 995 (2005).
29. J. C. Priscu *et al.*, *Science* **286**, 2141 (1999).
30. J. L. Kirschvink, in *The Proterozoic Biosphere*, J. W. Schopf, C. Klein, Eds. (Cambridge Univ. Press, Cambridge, 1992), pp. 51–52.
31. P. F. Hoffman, D. P. Schrag, *Terra Nova* **14**, 129 (2002).
32. D. E. Canfield *et al.*, *Science* **321**, 949 (2008); published online 16 July 2008 (10.1126/science.1154499).
33. J. A. Mikucki, thesis, Montana State University (2005).
34. G. Eischeld and S. Fawcett assisted with oxygen isotope measurements, A. Masterson assisted with sulfur isotope measurements, and G. Gordon assisted with iron isotope measurements. We are grateful for assistance from the Crary Laboratory, Petroleum Helicopters Incorporated, and S. Carter. We would like to extend a special thanks to McMurdo personnel B. Peace and W. Hayworth. Discussions with H. Keys, M. Tranter, K. Welch, W. B. Lyons, W. Hamilton, F. MacDonald, S. Shah, and A. Knoll were helpful in formulating the ideas presented. The comments of three anonymous reviewers and A. J. Kaufman greatly improved the manuscript. This research was funded by an NSF Polar postdoctoral fellowship (OPP-0528710) to J.A.M. Additional support was provided by NSF grants EAR-0311937 (A.P.), OPP-432595 and OPP-0631494 (J.C.P.), and OPP-0338097 and OCE-0728683 (awarded to G. R. DiTullio) (P.A.L.); Canadian Institute for Advanced Research (A.V.T.); Harvard–Microbial Sciences Initiative; and NASA (NNX07AV51G) (D.T.J.). DNA sequences have been submitted to GenBank with accession numbers FJ389341 to FJ389351.

Supporting Online Material
www.sciencemag.org/cgi/content/full/324/5925/397/DC1
Materials and Methods
Fig. S1
Tables S1 to S4

17 October 2008; accepted 5 March 2009
10.1126/science.1167350

Recursive Processes in Self-Affirmation: Intervening to Close the Minority Achievement Gap

Geoffrey L. Cohen,[1]* Julio Garcia,[1] Valerie Purdie-Vaughns,[2] Nancy Apfel,[3] Patricia Brzustoski[3]

A 2-year follow-up of a randomized field experiment previously reported in *Science* is presented. A subtle intervention to lessen minority students' psychological threat related to being negatively stereotyped in school was tested in an experiment conducted three times with three independent cohorts (N = 133, 149, and 134). The intervention, a series of brief but structured writing assignments focusing students on a self-affirming value, reduced the racial achievement gap. Over 2 years, the grade point average (GPA) of African Americans was, on average, raised by 0.24 grade points. Low-achieving African Americans were particularly benefited. Their GPA improved, on average, 0.41 points, and their rate of remediation or grade repetition was less (5% versus 18%). Additionally, treated students' self-perceptions showed long-term benefits. Findings suggest that because initial psychological states and performance determine later outcomes by providing a baseline and initial trajectory for a recursive process, apparently small but early alterations in trajectory can have long-term effects. Implications for psychological theory and educational practice are discussed.

Whether and how psychological interventions produce lasting positive consequences are critical questions for scientists and policy-makers. This report presents evidence of how interventions, even brief or subtle, can produce lasting benefit when targeted at important psychological processes. It does so by focusing on the long-term impact of a psychological intervention designed to reduce the racial achievement gap through the lessening of academic underperformance.

The achievement gap between academically at-risk minority students and European American students has long concerned the educational community (*1*). In a society where economic success depends heavily on scholastic accomplishment, even partial remediation of this gap would be consequential. This is especially true for low-achieving students, given the societal, institutional, and personal costs of academic failure.

Research shows the importance of psychological factors in intellectual achievement (*2*–*4*). Situations where one could be judged or treated in light of a negative stereotype can be stressful and thus undermine performance (*5*–*7*). For African Americans in school, the concern that they or another African American could be seen as confirming a negative stereotype about their group's intelligence can give rise to stress and depress performance (*5*–*8*).

Findings of two randomized field experiments addressing this psychological threat in the classroom were reported in *Science* (*8*). These tested a values-affirmation intervention. Beginning early in seventh grade, students reflected on an important personal value, such as relationships with friends and family or musical interests, in a series of structured writing assignments. Such self-affirmations reduce psychological threat and stress (*9*–*11*) and can thus improve performance. The intervention should benefit students from groups subjected to threat pervasive enough to undermine their average performance—in this case, negatively stereotyped minority students. As predicted, relative both to a control group and to historical norms, one or two administrations of the intervention improved the fall-term grades of African Americans and lowered the psychological availability of the stereotype. European Americans were unaffected (*8*).

A 2-year follow-up is now reported. We assess whether the affirmation buffers minority students from the effects of psychological threat over the long term, leading to academic benefits beyond the short-term ones of a single academic term previously found. Generally, psychological processes and their consequences are examined for relatively brief periods, often in experimental studies lasting 30 min or an hour. By contrast, because the present study spans 2 years, its findings speak to how an apparently brief psychological intervention triggers processes that affect performance and psychological outcomes over considerable periods of time. Given the multitude of factors that could mute the effects of such processes in the classroom, the findings address the longevity and real-world significance of these processes. This is particularly important given that the effects of interventions and psychological manipulations often decay and may even reverse over time for reasons that are little understood (*12*, *13*).

Because chronic evaluation is a key aspect of school and work environments, performance in these settings can be self-reinforcing. A recursive cycle, where psychological threat lowers performance, increasing threat and lowering performance further, in a repeating process, can magnify early performance differences among students (*14*). Early outcomes set the starting point and initial trajectory of a recursive cycle and so can have disproportional influence. For instance, the low self-confidence of students who experience early failure, even by chance, is surprisingly difficult to undo (*15*). A well-timed intervention could provide appreciable long-term performance benefits through early interruption of a recursive cycle.

Results encompass the original two student cohorts and a third cohort run after the original two experiments. The cohorts were observed for a period running from the first term of seventh grade to the end of eighth grade, typically covering ages 12 to 14. Although the period involves the last 2 years of middle school, for clarity these will henceforth be referred to as Year 1 and 2, respectively. Individual students were randomly assigned to the affirmation condition or the control condition. The former completed affirmation exercises, the latter neutral exercises. The treatment consisted of variations on the original affirmation exercise in which students wrote about the personal importance of a self-defining value (*16*). The control exercises consisted of variations on the original control exercise in which students wrote about an unimportant value or a similarly

[1]Department of Psychology, University of Colorado, Muenzinger Psychology Building, Boulder, CO 80309–0345, USA. [2]Department of Psychology, Columbia University, 405 Schermerhorn Hall, New York, NY 10027, USA. [3]Department of Psychology, Yale University, 2 Hillhouse Avenue, New Haven, CT 06520, USA.

*To whom correspondence should be addressed. E-mail: cohen.geoff@gmail.com

neutral topic like their morning routine. The experimental manipulation, given three to five times in the seventh grade, occurred at roughly equal intervals throughout the year.

With the exception of a treatment dosage manipulation introduced at the beginning of Year 2, all original condition assignments were preserved (*16*). At the start of Year 2, 50% of the affirmed students were randomly assigned to a booster condition. These students received between two and four additional affirmations in Year 2. All remaining participants completed control exercises. This would determine whether long-term intervention effects, if present, rested on the treatment's continued administration or were triggered by its early effects.

The key outcome was grade point average (GPA) in core academic courses (science, social studies, math, and English), as the intervention was administered in different courses over 2 years and its effect was found across core courses in the original studies (*8*). To increase statistical power, we combined data from the three cohorts, because the intervention's effect, if found, was expected to be small and was found to be consistent across cohorts (*16*).

Complete GPA data for 2 years were obtained for 93% of the original participants (N = 385). Attrition did not vary by experimental condition either overall or within racial group (*16*). Degrees of freedom are greater for earlier outcomes because of attrition. Multiple regression tested treatment effects (*16*). A positive effect of affirmation on average 2-year GPA emerged for African Americans but not for European Americans. As with short-term grades, a group × experimental condition interaction emerged for the new long-term data [B = 0.33, $t(321)$ = 3.59, $P < 0.001$] (table S1). African Americans earned a higher 2-year GPA in the affirmation condition than in the control condition [B = 0.24, $t(144)$ = 3.45, P = 0.001]. No treatment effect was found for European Americans [B = −0.07, $t(170)$ = −1.19, P = 0.236]. The treatment effect for African Americans emerged for GPA in both outcome years. The group × treatment interaction and treatment effect for African Americans was significant for each year [Year 1: interaction B = 0.25, $t(344)$ = 2.73, P = 0.007, treatment B = 0.18, $t(162)$ = 2.69, P = 0.008; Year 2: interaction B = 0.39, $t(321)$ = 3.25, P = 0.001, treatment B = 0.27, $t(144)$ = 3.03, P = 0.003].

If the intervention interrupts a recursive process, its effects should be larger for initially low-achieving African Americans, because low performance should trigger worsening performance. Affirmation should make their prior performance less predictive of subsequent achievement. A three-way interaction between racial group, condition, and a continuous measure of pre-intervention performance on average 2-year GPA shows this [B = −0.32, $t(319)$ = −2.59, P = 0.010] (*16*). A two-way interaction between condition and pre-intervention performance emerged for African Americans [B = −0.21, $t(144)$ = −2.49, P = 0.014], not European Americans [B = 0.10, $t(170)$ = 1.10, P = 0.274]. Regardless of previous performance level, European Americans were unaffected by the intervention. However, the affirmation effect was significant for low-performing African Americans, those at the 25th percentile of pre-intervention performance for their racial group [B = 0.41, $t(144)$ = 4.41, $P < 0.001$]. Although the affirmation effect was present in the first term for high-performing African Americans, those at the 75th percentile of pre-intervention performance for their group [Fig. 1; B = 0.19, $t(160)$ = 2.30, P = 0.019], it decayed and did not reach significance on 2-year GPA for them [B = 0.15, $t(144)$ = 1.67, P = 0.096]. At mean or moderate pre-intervention performance, treatment effects were virtually identical to those in the overall analysis (*16*).

Affirmed African Americans should be more likely to maintain their performance over time if the intervention interrupted a recursive process of worsening performance. Indeed, the downward trend in performance commonly found in middle school (*17*) was less steep for these students than for African Americans in the control condition, not just for one term but across 2 years. Although all children performed progressively worse with time (Fig. 1), the linear decline in annual GPA was smaller among affirmed than nonaffirmed African Americans [$F(1,146)$ = 7.36, P = 0.007] (*16*). The decline among European Americans did not vary by condition [$F(1,172)$ = 1.37, P = 0.24; group × condition × measure interaction, $F(1,323)$ = 7.41, P = 0.007]. Figure 2 illustrates how the performance trajectory of low-achieving African Americans angles upward after the intervention, keeping the gap between them and European Americans from widening with time.

Although the initial treatment had long-term performance effects, the dosage manipulation did not moderate the treatment effect on Year 2 GPA for either racial group or for any pre-intervention performance subgroup [| t's | < 1.3, P's > 0.20]. This further supports the presence of a recursive process, as the intervention's early effects suffice to explain its long-term effects (*16*). All students, including African Americans, tended to perform relatively worse in Year 2 if they had performed poorly in Year 1, even controlling for pre-intervention performance (*16*). That the treatment effect on Year 2 GPA was significantly mediated by Year 1 GPA suggests that this natural performance cycle could have carried forward the intervention's early impact (SOM Text).

The intervention's impact on students' psychological environment is indicated by data suggesting that it buffered African Americans against the impact of early poor performance on their long-term perceptions of adequacy. A survey assessed students' self-perceived ability to fit in and succeed in school—their adaptive adequacy in the academic environment (*16*). These data indicate

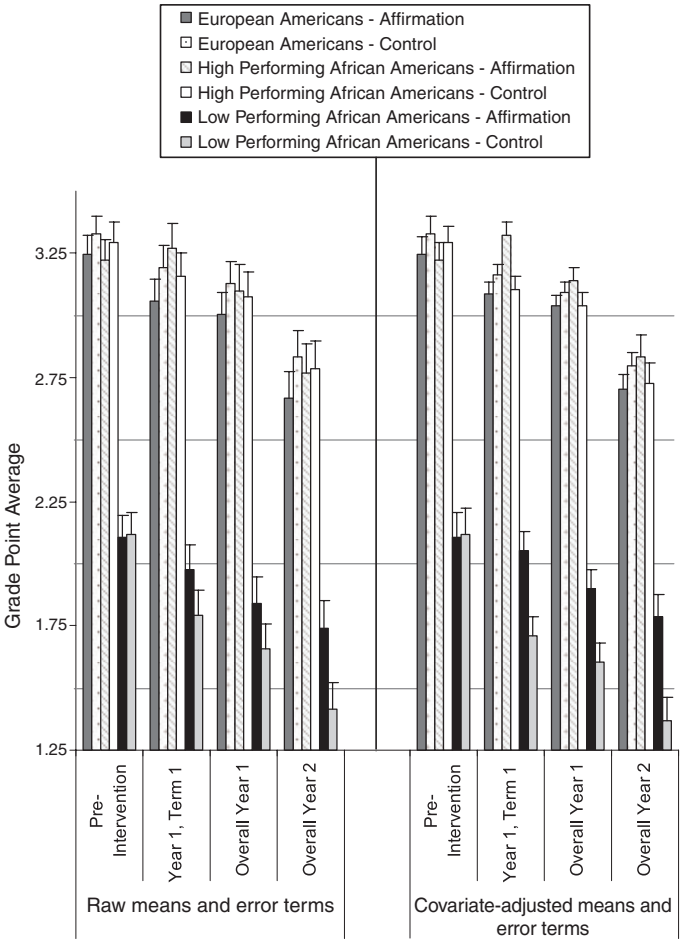

Fig. 1. Mean GPA in core courses, as a function of student group (African American versus European American), experimental condition, and pre-intervention level of performance of African Americans (an average of the prior year's GPA and pre-intervention seventh-grade performance). Data from participants with complete data are presented. Error bars represent standard errors. African Americans were categorized into low and high performers based on a median split within their racial group, reflecting their relative standing within their group. Year 1, Term 1 represents the first term after the initiation of the intervention. **(Left)** Raw means and error terms. **(Right)** Means and error terms adjusted for baseline covariates and students' assigned teacher team. The scale reflects the grade metric, ranging from 0 (= F) to 4.33 (= A+).

that the intervention uncoupled African Americans' long-term perceptions of adequacy from early poor performance. African Americans who had performed poorly early in the school year, and then received the affirmation, maintained a sense of their ability to fit and succeed in school over time. They had similar levels of self-perceived adequacy at the beginning and end of the year [paired $|\ t\ | < 0.2$]. For them, as for European Americans, early poor performance bore little relationship to their perceptions of adequacy at year's end, controlling for baseline perceptions [B's < 0.04, $|\ t$'s $|\ < 1$]. By contrast, for African Americans in the control condition, performing poorly before the manipulation predicted more negative perceptions of adequacy later [$B = 0.23$, $t(155) = 3.79$, $P < 0.001$]. They had lower self-perceived adequacy at the end of the year than they had had at the beginning [paired $t(40) = -2.45$, $P = 0.019$]. Low-performing African Americans thus ended the year with a lower sense of personal adequacy in the control condition than in the affirmation condition [$B = 0.31$, $t(155) = 3.30$, $P = 0.001$], with the latter not differing from European Americans [$|\ t\ | < 1$]. A mid-year assessment, which due to pragmatic constraints involved a shorter scale and only the first two cohorts, yielded the same results. Without intervention, early poor performance for minority students appeared to deliver a lasting blow to their sense of adequacy (*18*).

Although end-of-year adequacy correlated with higher GPA [$R = 0.23$, $P < 0.001$], statistical evidence that it mediated the treatment effect on GPA was not found (*16*). This suggests that the intervention might have discrete effects on a host of education-relevant psychological and behavioral outcomes. Here the intervention weakened the relationship not only between past and future performance, but also between past performance and later psychological state.

We also explored the effect of the intervention on students' assignment by their school to two major performance tracks—whether students were placed in remediation (assigned to a remedial program or held back in their grade), and whether they received advanced placement in math (*16*). Of the 13 students in the sample placed in remediation after the intervention, 11 were in the control condition (6%, versus 1% in the affirmation condition). Because counts for European Americans receiving the intervention were zero, we tested main effects of affirmation and racial group separately (*16*) (fig. S1). Logistic regression yielded a condition effect, with fewer affirmation-treated students placed in remediation [$\Delta\chi^2\ (1) = 14.06$, $P < 0.001$]. Additionally, fewer European Americans (2%) were placed in remediation than African Americans (6%) [$\chi^2\ (1) = 4.03$, $P = 0.045$]. However, fewer affirmed African Americans were so classified than nonaffirmed African Americans [3% versus 9%; $\Delta\chi^2\ (1) = 9.31$, $P = 0.002$]. This condition effect was confined to previously low-performing African Americans [5% versus 18%] (*16*). Condition effects were virtually identical in a rare events logistic regression (*19*).

Evidence of a positive treatment effect regarding assignment to advanced placement in math was found for African Americans (SOM Text) (*16*).

A values-affirmation intervention closed the achievement gap not only over one school term, but throughout African Americans' tenure in middle school. It also decreased the number of African Americans identified as at-risk and enrolled in remediation. Moreover, the intervention benefited those most in need and often least affected by traditional intervention—low-achieving students (*20*).

In chronically evaluative settings such as school, performance issues from self-reinforcing or recursive processes. A feedback loop, with psychological threat and poor performance reinforcing one another, can create worsening performance over time. Students' poor performance may also cause them to be seen as less able by their teachers and less worthy of attention and mentoring, increasing the likelihood of lower performance (*21*). The ability of the intervention to interact with recursive processes lies at the heart of how its effects persisted for 2 years. Because initial psychological states and early performance establish the starting point and initial trajectory of a recursive cycle, they can have disproportionate influence on long-term outcomes. When such recursive cycles are interrupted early, baseline outcomes and the long-term performance trajectories following from them can be changed. That a new starting point and trajectory for the recursive cycle was introduced by the affirmation is suggested by its weakening of the relationship between early poor performance and later performance and felt adequacy.

The following findings provide evidence for the intervention's interruption of a recursive cycle. First, early poor performance was less predictive of later performance and psychological state for affirmed African Americans than for nonaffirmed ones, suggesting that the intervention reset the starting point of a recursive cycle. Second, the affirmation not only benefited GPA, but also lifted the angle of the performance trajectory and thus lessened the degree of downward trend in performance characteristic of a recursive cycle. Third, the affirmation's benefits were most evident among low-achieving African Americans. These are the children most undermined by the standard recursive cycle with its worsening of performance and magnifying of initial differences in performance. Fourth, the affirmation prevented the achievement gap from widening with time. Fifth, treatment boosters were not needed to sustain its impact into Year 2. This indicates that processes triggered by the intervention in Year 1 suffice to explain its effect in Year 2. That the intervention's first-year

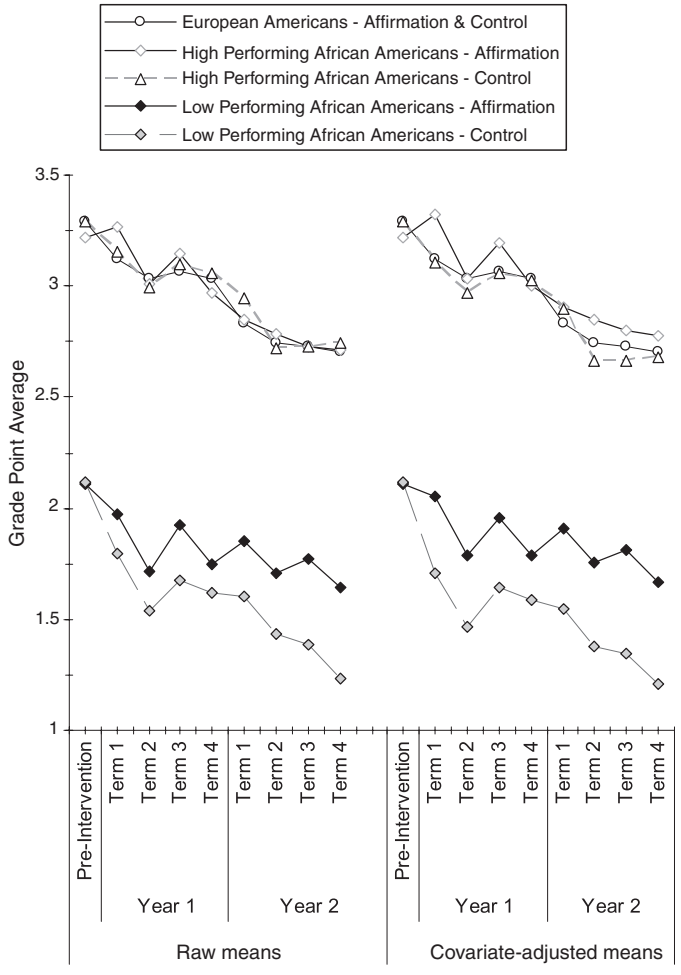

Fig. 2. Mean GPA in core courses for each term over 2 years, as a function of student group (African American versus European American), experimental condition, and pre-intervention level of performance of African Americans (an average of the prior year's GPA and pre-intervention seventh-grade performance). Data from participants with complete data are presented. African Americans were categorized into low and high performers based on a median split within their racial group, reflecting their relative standing within their group. Because European Americans in the two conditions did not differ significantly, their data were combined. **(Left)** Raw means. **(Right)** Means adjusted for baseline covariates and students' assigned teacher team.

impact mediated much of this effect further supports this notion.

Finally, students' psychological state sheds light on how affirmation processes interact with the recursive cycle. African Americans, a stereotyped group, displayed greater psychological vulnerability to early failure. For them, early failure may have confirmed that the stereotype was in play as a stable global indicator of their ability to thrive in school. By shoring up self-integrity at this time, the affirmation helped maintain their sense of adequacy and interrupted the cycle in which early poor performance influenced later performance and psychological state. Students' performance and psychological trajectory can be strongly influenced by timely actions, even when apparently small, that alter or reset the trajectory's starting point.

Other factors, such as teachers' expectancies of their students, could contribute to the longevity of the treatment's effect (*21*). For instance, that fewer affirmed children were assigned to remediation suggests that the intervention's effects were not only noted by the academic system, but acted upon by it.

The findings demonstrate how initial psychological processes, triggered by an apparently subtle intervention, can have psychological and pragmatic effects that perpetuate themselves over extended time spans, in the present case 2 years (*6*, *13*). They demonstrate the role of such processes in long-term intellectual achievement and also suggest a practical strategy for addressing the achievement gap. Effective psychological interventions depend on the presence of positive and sufficient structural, material, and human resources. Together with such resources and other educational programs, psychological interventions can help individuals perform to their potential and produce lasting positive changes in equity and opportunity.

References and Notes

1. C. Jencks, M. Phillips, *The Black-White Test Score Gap* (Brookings Institution, Washington, DC, 1998).
2. A. Bandura, *Social Foundations of Thought and Action: A Social Cognitive Theory* (Prentice Hall, Englewood Cliffs, NJ, 1986).
3. C. S. Dweck, C. Chiu, Y. Hong, *Psychol. Inq.* **6**, 267 (1995).
4. E. Zigler, E. C. Butterfield, *Child Dev.* **39**, 1 (1968).
5. C. M. Steele, S. J. Spencer, J. Aronson, in *Advances in Experimental Social Psychology,* M. P. Zanna, Ed. (Academic Press, San Diego, CA, 2002), pp. 379–440.
6. J. Aronson, C. B. Fried, C. Good, *J. Exp. Soc. Psychol.* **38**, 113 (2002).
7. G. L. Cohen, J. Garcia, *J. Pers. Soc. Psychol.* **89**, 566 (2005).
8. G. L. Cohen, J. Garcia, N. Apfel, A. Master, *Science* **313**, 1307 (2006).
9. J. D. Creswell *et al.*, *Psychol. Sci.* **16**, 846 (2005).
10. C. M. Steele, in *Advances in Experimental Social Psychology*, L. Berkowitz, Ed. (Academic Press, New York, 1988), pp. 261–302.
11. D. K. Sherman, G. L. Cohen, in *Advances in Experimental Social Psychology*, M. P. Zanna, Ed. (Academic Press, San Diego, CA, 2006), pp. 183–242.
12. R. Schulz, B. H. Hanusa, *J. Pers. Soc. Psychol.* **36**, 1194 (1978).
13. L. Ross, R. Nisbett, *The Person and the Situation* (McGraw-Hill, New York, 1991).
14. T. D. Wilson, P. W. Linville, *J. Pers. Soc. Psychol.* **49**, 287 (1985).
15. M. R. Lepper, L. Ross, R. Lau, *J. Pers. Soc. Psychol.* **50**, 482 (1986).
16. Materials and methods are available as supporting material on *Science* Online.
17. J. S. Eccles, S. Lord, C. Midgley, *Am. J. Educ.* **8**, 520 (1991).
18. For the adequacy outcome, the racial group × condition × prior performance interaction was significant [$B = -0.31$, $t(328) = -2.54$, $P = 0.011$], indicating that while there was no condition × prior performance interaction among European Americans [$B = 0.11$, [$|t| < 1.1$], there was such an interaction among African Americans [$B = -0.20$, $t(155) = -2.75$, $P = 0.007$].
19. M. Tomz, G. King, L. Zeng, RELOGIT: Rare events logistic regression, v. 1.1; Harvard Univ., Cambridge, MA, 1 October 1999, http://gking.harvard.edu/.
20. S. J. Ceci, P. B. Papierno, *Am. Psychol.* **60**, 149 (2005).
21. R. Rosenthal, *Curr. Dir. Psychol. Sci.* **3**, 176 (1994).

22. We thank the student participants and their parents, the teachers, staff, and administrators of the school district for their involvement in the project. We also thank E. Zigler, D. Green, C. Steele, E. Pronin, D. Sherman, G. Walton, J. Correll, C. Judd, J. Cook, E. Paluck, S. Taborsky-Barba, S. Tomassetti, and S. Wert for their help and feedback. This research was supported primarily by grants from the William T. Grant Foundation and the Russell Sage Foundation. Additional support was provided by the Nellie Mae Education Foundation and the Institute for Social and Policy Studies of Yale University.

Supporting Online Material

www.sciencemag.org/cgi/content/full/324/5925/400/DC1
SOM Text
Fig. S1
Table S1
References

12 January 2009; accepted 26 February 2009
10.1126/science.1170769

Mirror Neurons Differentially Encode the Peripersonal and Extrapersonal Space of Monkeys

Vittorio Caggiano,[1] Leonardo Fogassi,[2,3] Giacomo Rizzolatti,[3] Peter Thier,[1] Antonino Casile[1]*

Actions performed by others may have different relevance for the observer, and thus lead to different behavioral responses, depending on the regions of space in which they are executed. We found that in rhesus monkeys, the premotor cortex neurons activated by both the execution and the observation of motor acts (mirror neurons) are differentially modulated by the location in space of the observed motor acts relative to the monkey, with about half of them preferring either the monkey's peripersonal or extrapersonal space. A portion of these spatially selective mirror neurons encode space according to a metric representation, whereas other neurons encode space in operational terms, changing their properties according to the possibility that the monkey will interact with the object. These results suggest that a set of mirror neurons encodes the observed motor acts not only for action understanding, but also to analyze such acts in terms of features that are relevant to generating appropriate behaviors.

Mirror neurons are a set of neurons, first described in the monkey premotor area F5, that respond both when the monkey performs an active goal-directed motor act and when he observes the same motor act performed by others (*1*, *2*). The most accepted interpretation of the function of mirror neurons is that they are involved in action understanding. Here, we investigated whether mirror neurons, besides playing a role in this function, also encode aspects of the observed actions that are relevant to subsequent interacting behaviors. A way to test this hypothesis is to examine the effect of relative distance between observer and actor on mirror neuron responses. Although completely irrelevant for "understanding" what the actor is doing, a precise knowledge of the distance at which the observed action is performed is crucial for selecting the most appropriate behavioral reaction.

To investigate quantitatively the possible degree of spatial modulation of the visual responses of mirror neurons, we first isolated hand movement–related neurons in area F5 of two rhesus monkeys by measuring the neurons' discharge while each monkey was executing hand goal-directed motor acts. The visual properties of these neurons were then assessed by having the experimenter perform the same motor acts in the monkey's peripersonal and extrapersonal (*3*–*7*) space, respectively (Fig. 1, A and B). The position of the experimenter's body was the same in all conditions, and actions were performed in the middle sagittal plane of the monkey's body. The selectivity for one of the two regions of space was then assessed by means of quantitative statistical analysis of the response patterns of 105 mirror neurons recorded from two monkeys (*8*).

Figure 2A shows the visual responses of three mirror neurons to motor acts executed in the peri- or extrapersonal space of the monkey. All three neurons responded during active movements of the monkey. However, their visual responses exhibited different types of tuning depending on whether the observed actions were executed in the monkey's peri- or extrapersonal space. Of all F5 mirror neurons tested, 26% ($n = 27$) exhibited a

[1]Department of Cognitive Neurology, Hertie Institute for Clinical Brain Research, University of Tübingen, 72076 Tübingen, Germany. [2]Dipartimento di Psicologia, Università di Parma, 43100 Parma, Italy. [3]Dipartimento di Neuroscienze e Istituto Italiano di Tecnologia, Università di Parma, 43100 Parma, Italy.

*To whom correspondence should be addressed. E-mail: antonino.casile@uni-tuebingen.de

selective visual response when the motor acts were performed in the monkey's extrapersonal space and 27% (n = 28) showed instead a selectivity for the monkey's peripersonal space. The remaining 47% (n = 50) responded to the visual presentation of actions independent of the spatial location at which they were performed (Fig. 2, B and C, and fig. S1). These results indicate that in monkey area F5, the visual responses of mirror neurons were modulated by the location in space at which observed actions were performed. In particular, a subgroup of these neurons exhibited significantly different responses during observation of actions performed in the monkey's peri- and extrapersonal space, respectively.

We performed an additional experiment in which motor acts were executed at five different distances, with the middle one marking the border between the peri- and extrapersonal regions of the monkey (Fig. 3A). Figure 3B shows the average responses of 27 space-selective mirror neurons as a function of distance. In this figure, distances shorter than 37 cm (corresponding to the length of the monkey's extended arm) lie inside the monkey's peripersonal space, and distances longer than 37 cm are in the monkey's extrapersonal space. As the curves show, the population activity varied in a quasi-monotonic manner with the distance from the monkey's body. That is, it decreased with the distance from the monkey's body for mirror neurons exhibiting selectivity for the peripersonal space and conversely increased for mirror neurons exhibiting selectivity for the extrapersonal space.

We next investigated whether space-selective neurons encode the peri- and extrapersonal regions in a metric format (i.e., the boundary between the two regions is fixed and only depends on the distance from the monkey's body) or in an operational format [i.e., the boundary between the two regions is dynamic and depends on the workspace of the monkey (*3*, *9*–*11*)]. In this experiment, visual responses of mirror neurons to motor acts performed in the peripersonal space were measured, in one monkey, under one additional condition in which the frontal panel of the primate chair was closed, thus preventing the monkey from reaching for objects close to his body. Nine (43%) of the 21 tested space-selective mirror neurons changed their tuning as a result of this experimental manipulation. More specifically, after closure of the frontal panel, neurons selective for the extrapersonal space started to respond also in the peripersonal space (similarly to neuron 1 in Fig. 4), while neurons selective for the peripersonal space ceased to respond (similarly to neuron 2 in Fig. 4). This experiment suggests that mirror neurons sensitive to a specific part of space fall into two categories: One encodes peri- and extrapersonal space in a purely metric format; the other parcellates space in an operational manner and changes its properties according to the possibility that the monkey will act.

Taken together, our results seem to suggest that mirror neurons, in addition to their basic properties of encoding observed motor acts, also encode the distance at which they are performed with respect to the observer. However, there is a possible caveat to this conclusion, namely the possibility that the responses of those neurons that we interpret as responding only to actions in peripersonal space might actually reflect the mere presence of an object close to the monkey's body. Such responses are present in adjacent area F4 (*3*–*5*). However, this interpretation can be rejected for two reasons. First, neurons in the ventral premotor cortex visually responding to objects close to the monkey's body also exhibit somatosensory responses. In our experiments, when tested for somatosensory responses, none of the mirror neurons responding to motor acts performed in the monkey's peripersonal space discharged during tactile stimulation of body parts. Second, no discharge was observed when three-dimensional objects were presented in isolation in the monkey's peripersonal space.

Another possible interpretation of the selective neuronal responses to the observation of motor acts performed in the monkey's peripersonal space is that the presence of an object close to the monkey's body induced a motor preparation to grasp the object. This interpretation can also be refuted for two reasons. First, as the monkeys received no reward, the number of attempts to grasp the object quickly decayed to virtually zero. Second, as mentioned earlier, the mere presentation of an object elicited no neuronal response. Such responses also during object presentation—and not only during action observation—would have been expected if they were related solely to motor preparation. Finally, we can also exclude the possibility that differential responses in the monkey's peri- or extrapersonal space are due to differences in the amount of attention allocated during these two experimental conditions, as only those trials in which the monkey was fixating the observed action were considered for further analysis. Furthermore, off-line analysis of eye position records revealed no significant difference in the duration of fixations in the two experimental conditions (*8*).

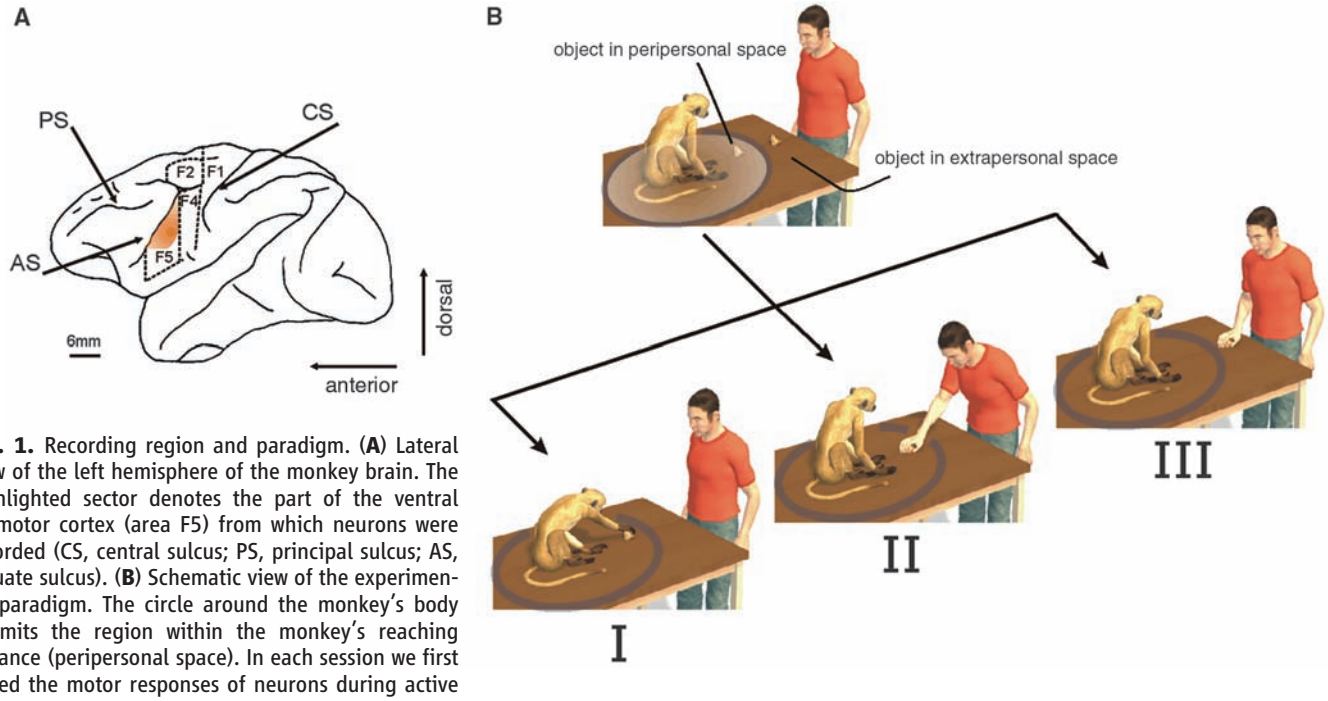

Fig. 1. Recording region and paradigm. (**A**) Lateral view of the left hemisphere of the monkey brain. The highlighted sector denotes the part of the ventral premotor cortex (area F5) from which neurons were recorded (CS, central sulcus; PS, principal sulcus; AS, arcuate sulcus). (**B**) Schematic view of the experimental paradigm. The circle around the monkey's body delimits the region within the monkey's reaching distance (peripersonal space). In each session we first tested the motor responses of neurons during active movements of the monkey (I). The visual responses of these neurons were further tested with the experimenter executing goal-directed motor acts in the peripersonal (II) and extrapersonal (III) space of the monkey. The order of conditions II and III was counterbalanced across sessions.

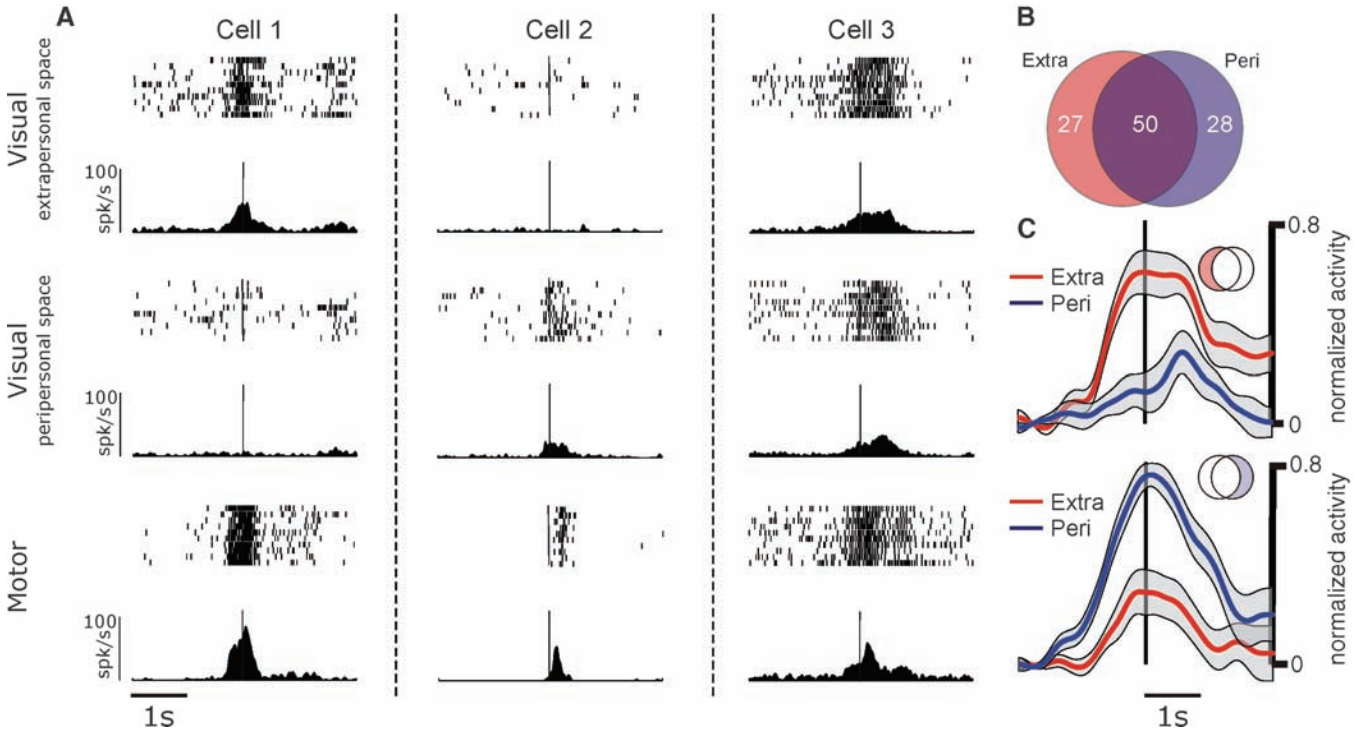

Fig. 2. Single-unit responses and population activity of mirror neurons during observation of actions executed in the monkey's peri- and extrapersonal space. (**A**) Responses of three mirror neurons during observation of motor acts performed in the monkey's extrapersonal (top row) and peripersonal (middle row) space, respectively, and during execution of motor acts (bottom row). Each panel shows a raster plot (top) and a peristimulus spike density function (bottom) of the cells' responses. Raster plots and spike density functions are aligned with the time of contact of the experimenter's or monkey's hand with the object. Cells 1 and 2 exhibited a visual preference for motor acts performed in the monkey's extrapersonal and peripersonal regions, respectively. Cell 3 instead responded to the visual presentation of motor acts independent of the spatial region in which they were performed. (**B**) Venn diagram illustrating the number of mirror neurons showing a preference for the monkey's peri- or extrapersonal space. The intersection of the two circles represents neurons whose discharges exhibited no statistically significant difference in the two experimental conditions. Neurons not contained in the intersection responded with a significantly stronger discharge during one of the two experimental conditions. (**C**) Population responses to the preferred and nonpreferred conditions of mirror neurons exhibiting a spatial selectivity. The upper and lower panels show the average visual response of mirror neurons selectively discharging during observation of motor acts performed in the monkey's extrapersonal and peripersonal space, respectively. The shaded regions around each curve represent standard error. Vertical lines represent the time of contact between the experimenter's hand and the object. See fig. S1 for an analysis of visual selectivity for specific motor acts.

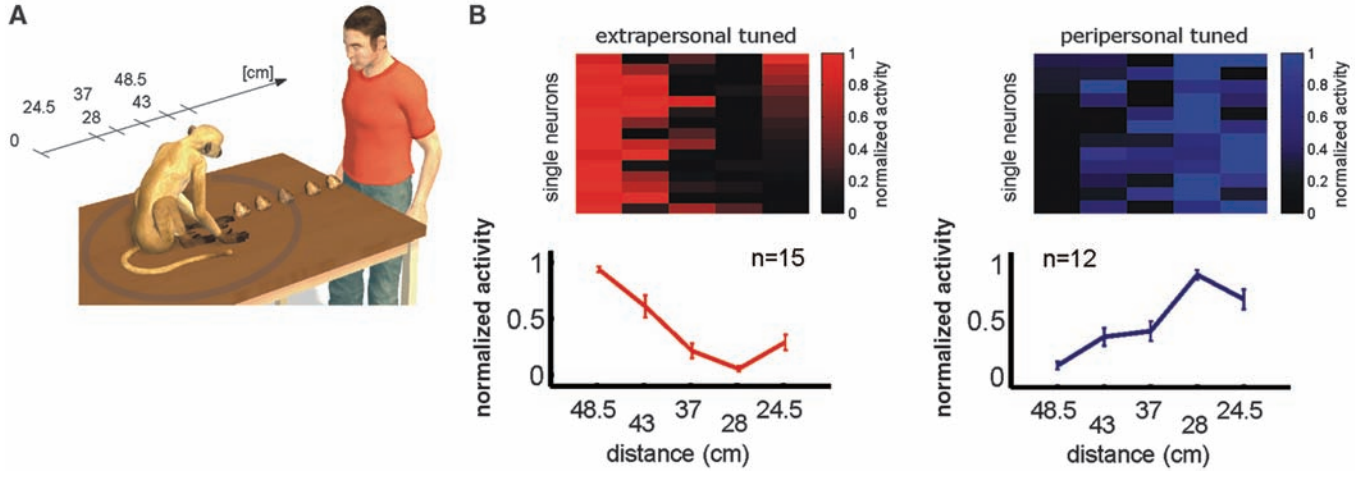

Fig. 3. Experiment in which actions were executed at five different distances, thus more finely sampling the monkey's peri- and extrapersonal space. (**A**) Schematic view of the experimental setup. (**B**) Population responses of mirror neurons as a function of the distance between the monkey and the observed action. The curves represent the normalized population activity of mirror neurons selectively responding to motor acts performed in the monkey's extrapersonal (left panel, n = 15 units) or peripersonal (right panel, n = 12 units) space, respectively, tested in this experiment. The horizontal axis signifies the distance between the object and the monkey's body. A distance of 37 cm represents the maximum extension of the monkey's arm and thus marks the border between the monkey's peri- and extrapersonal regions. Vertical lines represent standard errors. The panels above each curve show the normalized activities of the single neurons.

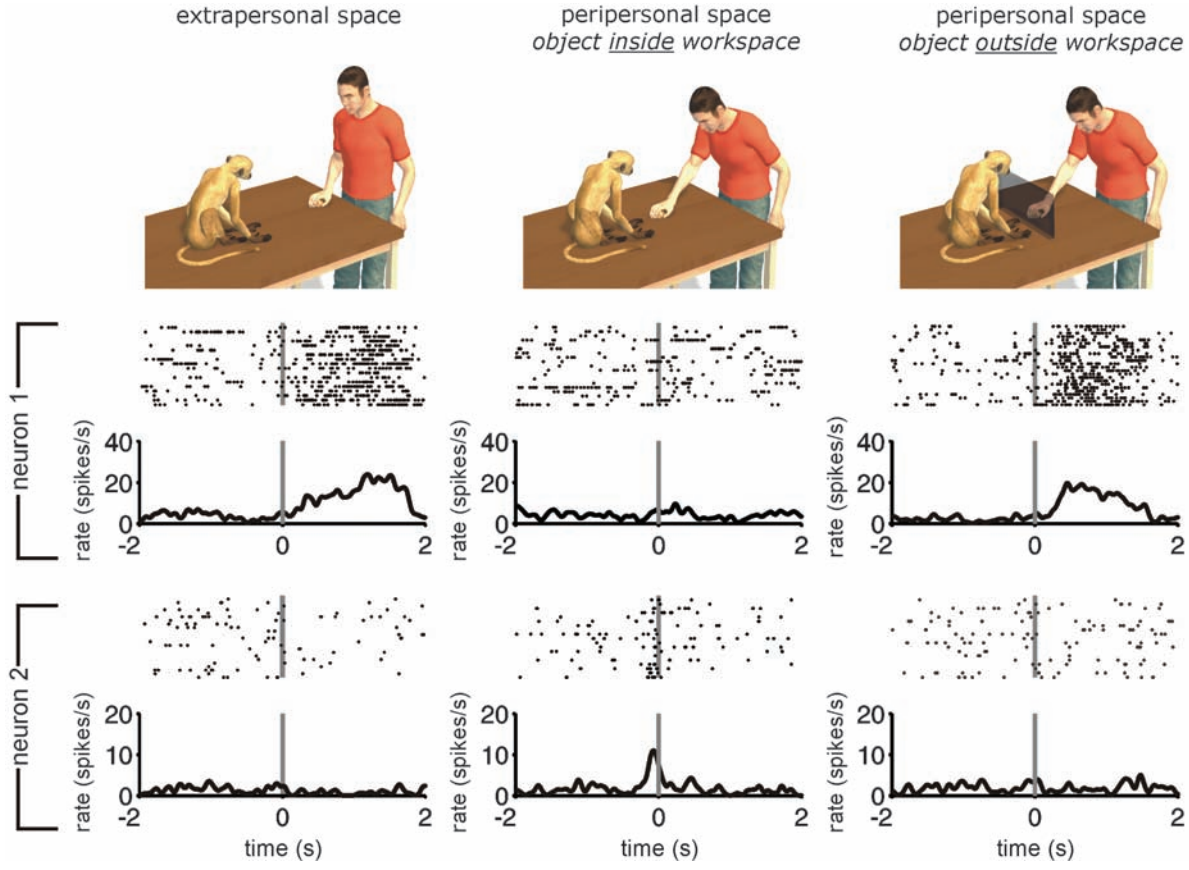

Fig. 4. Dynamical encoding of the monkey's peri- and extrapersonal space. The three columns show the responses of two mirror neurons (neuron 1 and neuron 2) to actions performed in the extrapersonal space (left column) and in the peripersonal space under two different experimental conditions: (i) The monkey is free to perform actions close to his body (central column), and (ii) the frontal panel of the primate chair is closed, thus preventing the monkey from reaching toward objects close to his body (right column). The vertical lines mark the time of contact of the experimenter's hand with the object. The two mirror neurons in the figure encoded space in an operational manner and showed complementary responses. Before closure of the frontal panel (left), neuron 1 exhibited visual responses only during observation of motor acts executed in the monkey's extrapersonal space; it did not respond when motor acts were executed close to the monkey's body (center). However, after closure of the frontal panel of the primate chair, this neuron discharged also during observation of motor acts performed close to the monkey's body for which it was previously unresponsive (right panel). Neuron 2, before closure of the frontal panel, exhibited visual responses only for motor acts executed in the monkey's peripersonal space (left and center). After closure of the frontal panel, this neuron no longer visually responded to motor acts performed close to the monkey's body (right). See also fig. S3.

These considerations suggest that we are indeed dealing with mirror neurons differentially responding to motor acts performed in different regions of space. What is the possible functional meaning of the different types of mirror neurons described in this study?

The distance between observer and actor is a feature that plays virtually no role in "understanding" the meaning of an observed motor act; nonetheless it is important for evaluating adequate subsequent interacting behaviors. Although an observer can immediately interact with an individual acting in the observer's peripersonal space, interactions in the observer's extrapersonal space are possible only through intermediate steps (e.g., approaching the observed agent or removing an obstacle). The fact that the responses of a subpopulation of mirror neurons exhibit spatial selectivity suggests that these neurons might encode observed actions for subsequent different types of behavioral responses—for example, an approaching behavior in the case of motor acts performed in the extrapersonal space, or a competitive behavior in the case of motor acts performed in the peripersonal space. The presence of mirror neurons that encode space not in metric but in operational terms, and that modify their properties according to behavioral contingencies (such as the possibility or impossibility of reaching the observed agent), further supports this interpretation.

Our results suggest a cognitive role for mirror neurons as a system that not only encodes the meaning of observed actions but also contributes to choosing appropriate behavioral responses to those actions. In particular, a stimulating (although admittedly speculative) interpretation of our results is that mirror neurons not only may represent a neuronal substrate for understanding "what others are doing," but also may contribute toward selecting "how I might interact with them."

References and Notes

1. V. Gallese, L. Fadiga, L. Fogassi, G. Rizzolatti, *Brain* **119**, 593 (1996).
2. G. Rizzolatti, L. Fadiga, V. Gallese, L. Fogassi, *Brain Res. Cogn. Brain Res.* **3**, 131 (1996).
3. L. Fogassi *et al.*, *J. Neurophysiol.* **76**, 141 (1996).
4. M. Gentilucci, C. Scandolara, I. N. Pigarev, G. Rizzolatti, *Exp. Brain Res.* **50**, 464 (1983).
5. M. S. Graziano, X. T. Hu, C. G. Gross, *J. Neurophysiol.* **77**, 2268 (1997).
6. G. Rizzolatti, M. Matelli, G. Pavesi, *Brain* **106**, 655 (1983).
7. M. S. Graziano, G. S. Yap, C. G. Gross, *Science* **266**, 1054 (1994).
8. See supporting material on *Science* Online.
9. A. Iriki, M. Tanaka, Y. Iwamura, *Neuroreport* **7**, 2325 (1996).
10. G. Rizzolatti, L. Fadiga, L. Fogassi, V. Gallese, *Science* **277**, 190 (1997).
11. A. Maravita, A. Iriki, *Trends Cogn. Sci.* **8**, 79 (2004).
12. We thank P. Dicke for many decisive technical contributions, two anonymous reviewers for helpful comments, and M. Giese for stimulating discussions. Supported by Deutsche Forschungsgemeinschaft grant SFB550-C10 and by the Hermann and Lilly Schilling Foundation.

Supporting Online Material

www.sciencemag.org/cgi/content/full/324/5925/403/DC1
Materials and Methods
Figs. S1 to S3
References

6 October 2008; accepted 27 February 2009
10.1126/science.1166818

DNA Binding Site Sequence Directs Glucocorticoid Receptor Structure and Activity

Sebastiaan H. Meijsing,[1]* Miles A. Pufall,[1]* Alex Y. So,[1,2] Darren L. Bates,[3] Lin Chen,[3] Keith R. Yamamoto[1,2]†

Genes are not simply turned on or off, but instead their expression is fine-tuned to meet the needs of a cell. How genes are modulated so precisely is not well understood. The glucocorticoid receptor (GR) regulates target genes by associating with specific DNA binding sites, the sequences of which differ between genes. Traditionally, these binding sites have been viewed only as docking sites. Using structural, biochemical, and cell-based assays, we show that GR binding sequences, differing by as little as a single base pair, differentially affect GR conformation and regulatory activity. We therefore propose that DNA is a sequence-specific allosteric ligand of GR that tailors the activity of the receptor toward specific target genes.

Allosteric mechanisms have evolved to modulate protein function. Allostery can enable a protein to integrate and respond to multiple signals. For example, nuclear hormone receptors, such as the glucocorticoid receptor (GR), use hormones as allosteric effectors of their transcriptional regulatory activity (*1*); additional inputs, such as phosphorylation, also affect GR function (*2*).

Upon hormone binding, GR associates with high affinity to genomic GR binding sequences (GBSs), typically imperfect palindromic, hexameric half sites separated by 3–base pair (bp) spacers (*3*). Within these 15-bp GBSs, five positions are nearly invariant, whereas the remainder can be altered with little effect on GR binding (*4*) and vary substantially among all functional GBSs (*5*). In contrast, certain GBSs linked to target genes are highly conserved across species (*5*). Similarly, single nucleotide differences in NF-κB binding sequences determine cofactor specificity for NF-κB dimers (*6*). Thus, the precise nucleotide sequence of a regulatory factor binding site, in addition to guiding the factor to specific genomic loci, may also specify the mode of transcriptional regulation.

To examine GBS effects on GR activity, we constructed luciferase reporters, each containing a single 15-bp core GBS (Fig. 1A). The GBSs,

[1]Department of Cellular and Molecular Pharmacology, University of California, San Francisco, CA 94158, USA. [2]Chemistry and Chemical Biology Program, University of California, San Francisco, CA 94107, USA. [3]Department of Molecular and Computational Biology, University of Southern California, Los Angeles, CA 90089, USA.

*These authors contributed equally to this work.
†To whom correspondence should be addressed. E-mail: yamamoto@cmp.ucsf.edu

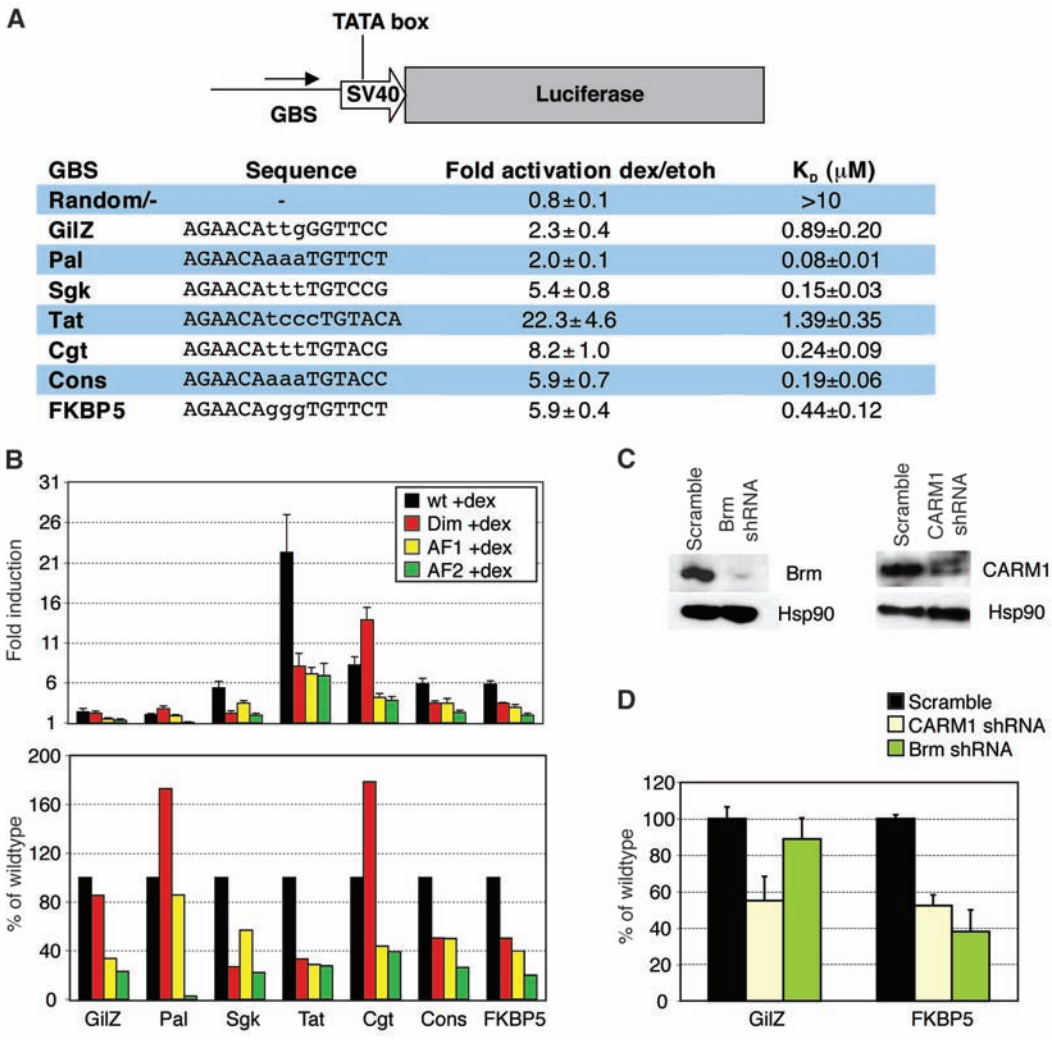

GBS	Sequence	Fold activation dex/etoh	K_D (μM)
Random/-	-	0.8±0.1	>10
GilZ	AGAACAttgGGTTCC	2.3±0.4	0.89±0.20
Pal	AGAACAaaaTGTTCT	2.0±0.1	0.08±0.01
Sgk	AGAACAtttTGTCCG	5.4±0.8	0.15±0.03
Tat	AGAACAtcccTGTACA	22.3±4.6	1.39±0.35
Cgt	AGAACAtttTGTACG	8.2±1.0	0.24±0.09
Cons	AGAACAaaaTGTACC	5.9±0.7	0.19±0.06
FKBP5	AGAACAgggTGTTCT	5.9±0.4	0.44±0.12

Fig. 1. GBSs differentially direct GR activity. (**A**) GBSs were cloned upstream of a minimal SV40 promoter driving luciferase. Transcriptional activities and binding affinities (humanGR-DBD 380 to 540) for each GBSs ± SEM are shown [number of independent experiments (n) ≥ 3]. K_D, dissociation constant. (**B**) GBS-specific patterns of domain utilization. GBS reporters respond differentially to mutations in Dim (red, A477T), AF1 (yellow, E219K/F220L/W234R), and AF2 (green, E773R) domains. Fold induction by dex ± SEM (top) and percent induction by mutant GR relative to wild type (bottom) are shown (n ≥ 3). (**C**) Immunoblots demonstrating short hairpin–mediated RNA (shRNA) knock-down of Brm and CARM1. (**D**) GBS inductions after CARM1 or Brm knock-down, relative to scrambled shRNA ± SEM, are shown (n = 3).

differing by as little as 1 bp, were derived from endogenous target genes, matched the GR consensus motif (*5*), or were reportedly responsive (*7*). The reporters displayed comparable basal activities (fig. S1A), whereas induction by dexamethasone (dex), a synthetic glucocorticoid, varied from ~twofold (Pal, GilZ) to ~20-fold (TAT) (Fig. 1A).

However, gel shift assays revealed no correlation between in vitro GBS affinities and in vivo transcriptional activities (Fig. 1A and fig. S1C) for a GR fragment with DNA binding affinities comparable to that of full-length GR (*8*, *9*). For example, TAT was 2- to 10-fold more active than the other GBSs but bound comparably to those with lower activities, whereas GBSs with similar transcriptional activities (Pal, GilZ) displayed different affinities. Moreover, merely reversing the orientation of asymmetric GBSs relative to the transcription start site, which presumably does not alter their affinities, altered their regulatory activities (fig. S2). These data suggest that GBS half sites confer unique function to the associated monomer.

Next, we tested the effects of mutating each of three GR surfaces implicated in transcriptional activation: (i) activation function 1 (AF1), (ii) AF2, and (iii) the dimerization region (Dim) (*10*). Wild-type GR or point mutants that abrogate each activity were cotransfected with GBS reporter plasmids into U2OS cells, which lack endogenous GR expression. Similar to endogenous target genes (*10*), we found a GBS-specific usage of GR surfaces (Fig. 1B). For example, GBSs that differed by 1 bp (Cgt, Sgk) differed in their dependence on the Dim domain, and GBSs with identical half sites but different spacer sequences (FKBP5, Pal) used all three surfaces differently. Pal and GilZ used different patterns of GR surfaces to arrive at their final indistinguishable activities. Furthermore, for a ~1-kb genomic fragment that recapitulated the domain utilization of endogenous GilZ [see supporting online material (SOM) text] (*10*, *11*), changing only GBS sequences changed domain utilization, suggesting that GBSs direct GR activity, even in the context of large composite elements found at endogenous genes (fig. S3).

To assess GBS specific actions of GR cofactors, we knocked down expression of SWI/SNF subunit Brahma (Brm) (*12*) and coactivator-associated arginine methyltransferase 1 (CARM1) (*13*). Knock-down of CARM1 reduced activation for each GBS tested (Fig. 1, C and D), whereas Brm knock-down had effects ranging from only ~10% reduction on the GilZ GBS to ~60% at FKBP5 (Fig. 1, C and D). Thus, the influence of GBS sequences on GR, in turn, alters the composition or function of cognate regulatory complexes.

To test the structural basis for these sequence specific changes, we examined the GR–DNA binding domain (GR-DBD) (Fig. 2A) in complex with various GBSs by x-ray crystallography. Each GBS was bound asymmetrically by a GR-DBD dimer, with crystal packing contacts between dimerization domain residues on both monomers and a surface of one monomer, denoted here as chain A (fig. S4). By convention, we place chain A in contact with the conserved AGAACA half site and chain B in contact with the variable half site. The chain A crystal packing surface included parts of the DNA recognition helix, the Dim domain, and the "lever arm" (residues 469 to 474) (*9*, *14*) loop connecting these two motifs (Fig. 2B). In contrast to a described structure (a palindrome with a noncanonical 4-bp spacer) (*15*), the 3-bp spacer allowed both recognition helices to make specific major groove contacts (figs. S4 and S5). The contact made by R466 (*16*) was invariant, whereas V462, and more profoundly K461, were GBS-specific (fig. S5). However, the lack of fixed DNA orientation (*17*) precluded definitive attribution of side chain contacts to individual bases.

We also observed a C-terminal helix (H3; residues 509 to 515) that, as with progesterone receptor (PR) (*18*), made a nonspecific minor groove backbone contact 3 bp upstream of the GBS motif mediated by R510 (fig. S6). Distinct from PR, H3 of GR laid across the minor groove, presenting five lysines following R510 as potential sources of interaction. The R510A mutation reduced GR-DBD affinity for DNA (~threefold) and K514A (~twofold), whereas transcriptional activation was unaffected by the K514A mutation and increased by R510A, reaffirming that regulatory activity is not determined solely by affinity (fig. S6).

A comparison of 13 GR-DBD:GBS structures revealed that they were virtually super-

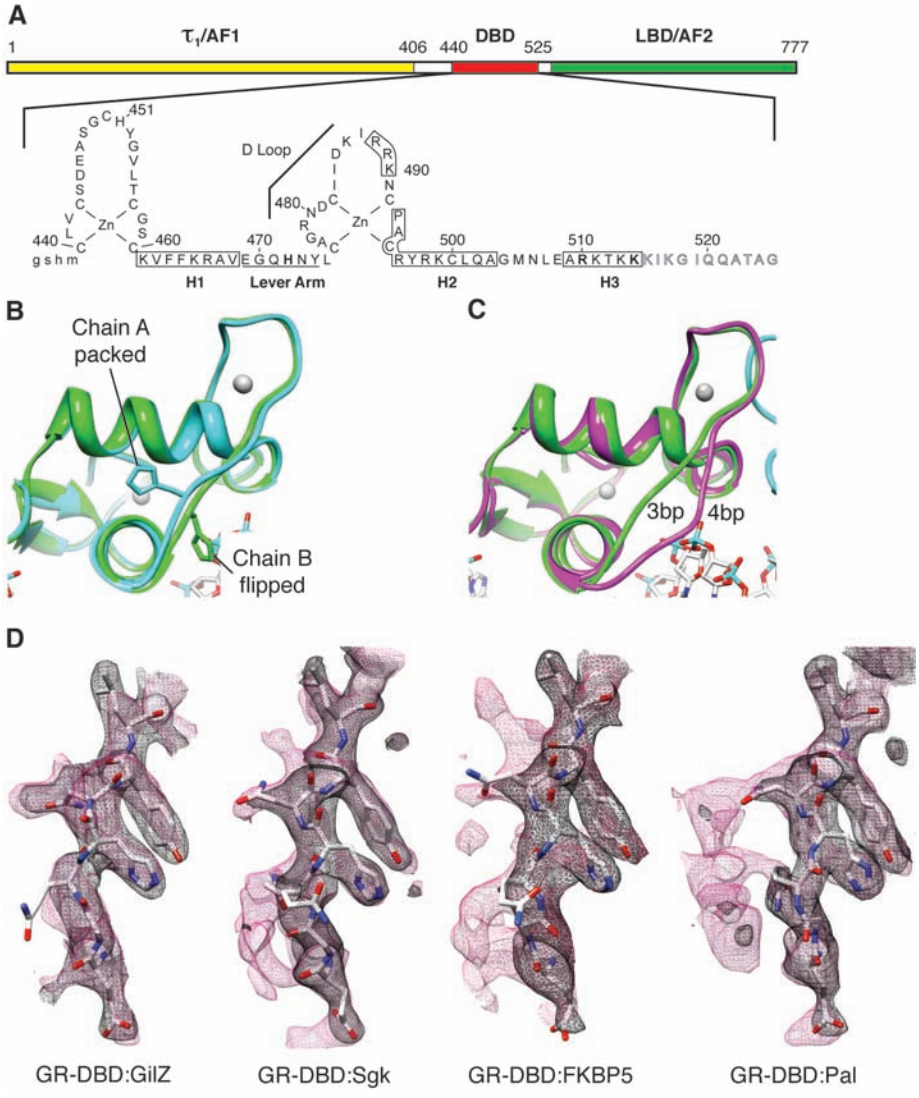

Fig. 2. DNA sequence-mediated structural differences in GR-DBD. (**A**) Domain structure of GR. τ_1, tau1. (**B**) Overlay of chains A and B from GR-DBD:Pal complex shows packed and flipped conformations. (**C**) Overlay of chain B from GR-DBD complexed with 4-bp spacer (*15*) (magenta) and 3-bp spacer GBS (green). (**D**) Composite omit maps of GR-DBD complexed with different GBSs (GilZ, FKBP5, Sgk, and Pal) under the same conditions. Lever arm peptide is shown with 2Fo-Fc (black mesh) and composite omit map (red mesh) overlaid.

imposable, except for the lever arm. In every complex, H472 within the lever arm adopted one of two distinct orientations (Fig. 2B and fig. S7, A and B). In chain A of each structure, H472 packed identically in the core of the protein fold; in chain B, H472 was flipped out, and the lever arm conformation was more heterogeneous, particularly between complexes with a different spacer length (Fig. 2C). The chain B lever arm of four different GR-DBD:GBS complexes crystallized under the same conditions refined to a similar predominant conformation, albeit with higher B factors, indicating less well-defined structure. Composite omit maps (for an explanation, see SOM text) revealed additional electron density specifically at the lever arm, indicating discrete alternate conformations (Fig. 2D). The densities were distinct for each complex, suggesting that DNA sequence directs distinct changes in the lever arm.

The conformation of the lever arm appeared to be influenced by DNA backbone contacts at one or both ends. At one end, Y474 formed a weak hydrogen bond to the DNA backbone at GilZ but not the other GBSs (fig. S8). At the other end, E469 contacted the DNA backbone through K465. GilZ displayed the strongest interactions at these two sites and no alternate conformations, whereas for the other GBSs, the anchoring was weaker and exhibited alternate conformations (Fig. 2D). Thus, the conformation of the lever arm is specified by DNA topology, which, in turn, is determined by sequence. Crystallization of GR-DBD:GilZ complexes under a range of conditions revealed substantial lever arm heterogeneity, whereas GR-DBD:Sgk complexes were invariant under the crystallization conditions tested (fig. S7, C and D). Together, these structures reveal that the lever arm is conformationally sensitive, responding to small environmental shifts, including DNA sequence.

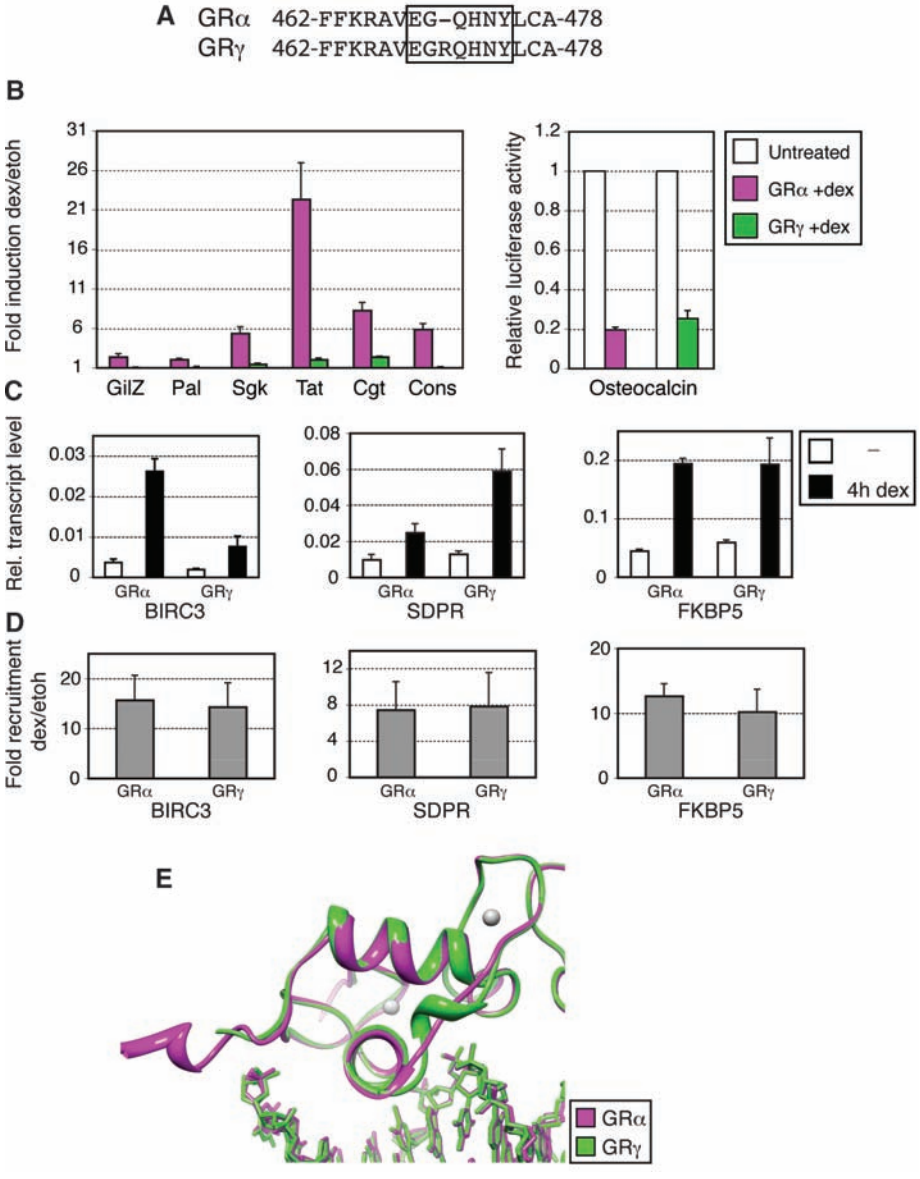

Fig. 3. Activities and structure of GRγ. (**A**) GRγ amino acid sequence, showing Arg insertion in the lever arm. (**B**) U2OS cells were cotransfected with GRα or GRγ, together with GBS reporters (left) or with an osteocalcin reporter (right). Fold induction (left) and luciferase activity relative to untreated cells (right) ± SEM are shown (n = 3). (**C**) Regulation of endogenous target genes in U2OS cells stably expressing GRα or GRγ, measured by quantitative real-time fluorescence polymerase chain reaction. (**D**) Chromatin immunoprecipitation of GR at GBSs of isoform-specific target genes; GR recruitment upon dex treatment ± SEM is shown (n = 3). (**E**) Overlay of structures for GRα:FKBP5 and GRγ:FKBP5 complexes.

To assess the role of the lever arm in modulating GR activity, we studied GRγ, a splice variant that inserts an arginine in the lever arm (Fig. 3A) (*19*). Consistent with the initial description of GRγ (*19*), reporter assays revealed reduced activity for each GBS (Fig. 3B). Relative to the predominant GRα isoform, GRγ displayed normal DNA binding affinity (fig. S9) and near-normal repression of osteocalcin (*20*), suggesting that the lever arm selectively affects transcriptional activation. We then tested the role of the lever arm on activity at endogenous genes by comparing U2OS cells stably expressing GRα (*21*) or GRγ. The two isoforms were generally similar, but transcriptional regulation was distinct at a subset of target genes (Fig. 3C and fig. S10). Transcriptional activation of FKBP5 by GRγ was equivalent to GRα, whereas SDPR was elevated and BIRC3 was decreased by GRγ. Chromatin immunoprecipitation showed comparable GRα and GRγ occupancy (Fig. 3D) at these genes (*5*), indicating that the lever arm modulates events subsequent to GR:GBS binding to produce gene-specific, probably GBS-specific, regulation.

We crystallized GRγ-DBD:GBS complexes and found that the structures were similar to those with GRα, except within the lever arm (Fig. 3E). Base-specific and DNA backbone contacts were maintained (fig. S11), reflecting the similar affinities of GRα and GRγ. Thus, the conformational differences in the lever arm have functional consequences.

Mutational analysis of the lever arm revealed that E469 was an important residue for mediating activation (Fig. 4A) and that the H472A mutation produced increased activity, whereas H472R impaired GR activation. Several lever arm mutations had GBS-specific effects (Fig. 4A): N473A selectively reduced activation at Pal, whereas G470A reduced activation at Pal and Tat. Thus, different lever arm conformations may produce multiple functionally distinct interaction surfaces.

In chain A, the packing of H472 occurred through interactions with residues within the DBD core that are GR-specific within the nuclear hormone receptor family (Fig. 4C): Y497, L501, and the carbonyl adjacent to V468 (Fig. 4B). GRα complexes with 16- and 18-bp GBSs displayed different crystal packing, yet all exhibited the packed chain A and flipped out chain B (fig. S12).

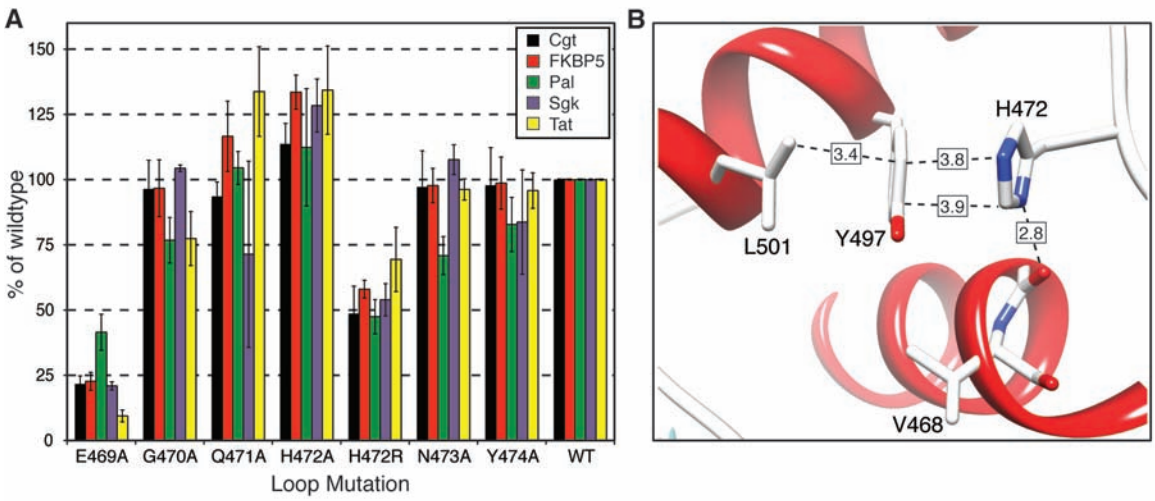

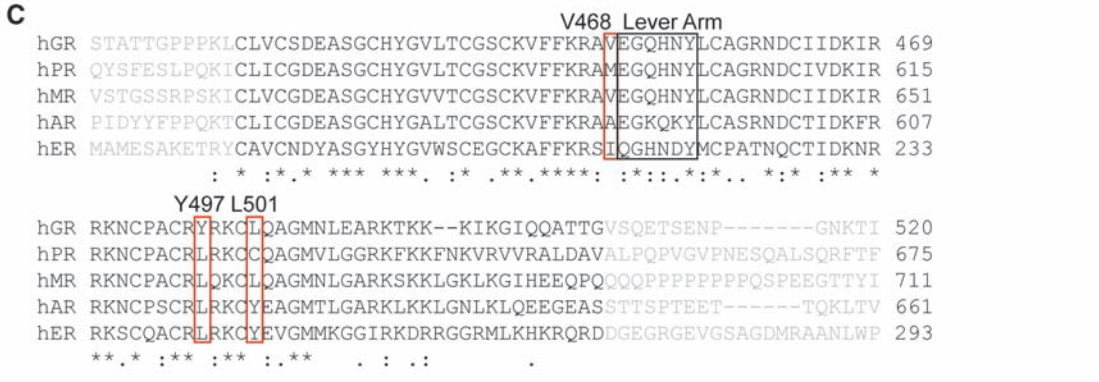

Fig. 4. Receptor activity is modulated by lever arm residues. (**A**) H472 is critical for tuning activity. Effects of mutating lever arm residues were assayed using GBS reporters; activities are plotted as percentage of wild type ± SEM ($n \geq 3$). (**B**) H472 resides in the DBD pocket formed by the carbonyl adjacent to V468, Y497, and L501. (**C**) Human DBD sequence alignments reveal variation at V468, Y497, and L501.

Disruption of chain A packing by a Y497L mutation (*22*) or by the R insertion in GRγ affected receptor activity in certain contexts, suggesting that packing of GRα chain A confers functional consequences quite distinct from those seen if both chains are flipped, as in GRγ and perhaps in other nuclear hormone receptors.

Protein functions have evolved commonly to be modulated by cellular signals. Based on our results, we propose that DNA sequences serve as one such signal, functioning as allosteric ligands that direct the activity of GR and probably other transcriptional regulators (*23*). Evidence for transduction of structural changes from DNA to other nuclear receptor domains has been described: DNA binding by GR induces secondary structure in its AF1 domain (*24*), and the estrogen receptor (ER) AF2 domain interacts with different cofactor peptides when ER is bound to different sequences (*25*, *26*). We propose that conformational changes in the lever arm amplify signals at the reading head and transmit them to other domains. Our studies with the GR-DBD are an important first step establishing that distinct binding site sequences induce subtle structural differences that are propagated and functionally amplified in the context of the full-length receptor. Studies of other transcriptional regulatory factors imply that interpretation of sequence may be a general property of DNA binding proteins (*6*, *23*, *27*).

References and Notes

1. L. Nagy, J. W. Schwabe, *Trends Biochem. Sci.* **29**, 317 (2004).
2. N. Ismaili, M. J. Garabedian, *Ann. N.Y. Acad. Sci.* **1024**, 86 (2004).
3. U. Strahle, G. Klock, G. Schutz, *Proc. Natl. Acad. Sci. U.S.A.* **84**, 7871 (1987).
4. J. La Baer, K. R. Yamamoto, *J. Mol. Biol.* **239**, 664 (1994).
5. A. Y. So, C. Chaivorapol, E. C. Bolton, H. Li, K. R. Yamamoto, *PLoS Genet.* **3**, e94 (2007).
6. T. H. Leung, A. Hoffmann, D. Baltimore, *Cell* **118**, 453 (2004).
7. J. A. Iniguez-Lluhi, D. Pearce, *Mol. Cell. Biol.* **20**, 6040 (2000).
8. P. J. Godowski, S. Rusconi, R. Miesfeld, K. R. Yamamoto, *Nature* **325**, 365 (1987).
9. Amino acid numbering refers to rat GR. We conducted affinity assays with the use of human GR-DBD 380 to 540 (rat 401 to 558).
10. I. Rogatsky *et al.*, *Proc. Natl. Acad. Sci. U.S.A.* **100**, 13845 (2003).
11. J. C. Wang *et al.*, *Proc. Natl. Acad. Sci. U.S.A.* **101**, 15603 (2004).
12. C. Muchardt, M. Yaniv, *EMBO J.* **12**, 4279 (1993).
13. H. Ma *et al.*, *Curr. Biol.* **11**, 1981 (2001).
14. M. A. van Tilborg *et al.*, *J. Mol. Biol.* **301**, 947 (2000).
15. B. F. Luisi *et al.*, *Nature* **352**, 497 (1991).
16. Single-letter abbreviations for the amino acid residues are as follows: A, Ala; C, Cys; D, Asp; E, Glu; F, Phe; G, Gly; H, His; I, Ile; K, Lys; L, Leu; M, Met; N, Asn; P, Pro; Q, Gln; R, Arg; S, Ser; T, Thr; V, Val; W, Trp; and Y, Tyr.
17. Materials and methods are available as supporting material on *Science* Online.
18. S. C. Roemer *et al.*, *Mol. Endocrinol.* **20**, 3042 (2006).
19. Y. Kasai, *FEBS Lett.* **274**, 99 (1990).
20. T. Meyer, J. A. Gustafsson, J. Carlstedt-Duke, *DNA Cell Biol.* **16**, 919 (1997).
21. I. Rogatsky, J. M. Trowbridge, M. J. Garabedian, *Mol. Cell. Biol.* **17**, 3181 (1997).
22. S. Heck *et al.*, *EMBO J.* **13**, 4087 (1994).
23. J. A. Lefstin, K. R. Yamamoto, *Nature* **392**, 885 (1998).
24. R. Kumar *et al.*, *J. Biol. Chem.* **274**, 24737 (1999).
25. D. M. Heery, E. Kalkhoven, S. Hoare, M. G. Parker, *Nature* **387**, 733 (1997).
26. J. M. Hall, D. P. McDonnell, K. S. Korach, *Mol. Endocrinol.* **16**, 469 (2002).
27. K. M. Scully *et al.*, *Science* **290**, 1127 (2000).

28. We thank E.C. Bolton, A. Kroch, J. J. Miranda, and A. Frankel for reviewing the manuscript. Work by M.A.P. was performed under NIH grant GM08537 and by M.A.P. and S.H.M. as fellows of the Leukemia and Lymphoma Society. We received research support from NIH grants (to K.R.Y., D.L.B., and L.C.). Coordinates and structure factors have been deposited in the Protein Data Bank with accession codes 3FYL, 3G6P, 3G6Q, 3G6R, 3G6T, 3G6U, 3G8U, 3G97, 3G8X, 3G99, 3G9I, 3G9J, 3G9M, 3G9O, and 3G9P. K.R.Y. is a paid consultant with Merck and Company.

Supporting Online Material

www.sciencemag.org/cgi/content/full/324/5925/407/DC1
Material and Methods
SOM Text
Figs. S1 to S12
Tables S1 and S2
References

6 August 2008; accepted 24 February 2009
10.1126/science.1164265

Nanoscale Liquid Chromatography

Designed to bring improved reproducibility and ease of use to proteomics research, the cHiPLC-nanoflex System is a docking station for up to three microfluidic chips that contain NanoLC columns or trap columns. The proprietary EksPort microconnector system ensures consistent fluidic connections to facilitate column changes. Chips can be interchanged in seconds, even by inexperienced users, with minimal dead volume to compromise resolution. The proprietary microfabrication process used for both the trap chips and analytical column chips delivers exceptional column-to-column reproducibility. Superior quality separations and reproducibility are critical to the success of biomarker validation studies. In these applications, in which peptides are measured by multiple reaction monitoring, the improved column-to-column reproducibility delivered by the cHiPLC-nanoflex helps in obtaining consistent data from large numbers of samples.

Eksigent
For information 925-560-2600
www.eksigent.com

Dry Blotting System

The iBlot Dry Blotting System for protein immunoblotting offers complete protein transfer in 7 minutes or less. It offers reduced variability in blot preparation and running and high-quality transfer without bubbles or distortions. It features the convenience of a self-contained unit, with no need for added buffers or an external power supply.

Invitrogen
For information 800-955-6288
www.invitrogen.com

Protein Detection Kits

The Kodak X-Sight Western Kits offer an analytical technique to detect proteins. The kits are built on X-Sight Nanosphere Conjugates, which are available in four distinct wavelengths, including three in the near-infrared range. The kits are offered in several different wavelength combinations that include up to three conjugates, making them suitable for multiplex applications. Each kit includes membranes and buffers to achieve high signal-to-noise ratios.

Carestream Health
For information 877-747-4357
www.carestreamhealth.com

Microwave Peptide Cleavage System

The Accent Cleavage System is a microwave peptide cleavage system that enables chemists to perform a full peptide cleavage in less than 30 minutes and microcleavages in as little as 2 minutes. The rapid microcleavage enables chemists to get a liquid chromatography/mass spectrometry analysis of their peptide in as little as 15 minutes, so they can quickly determine how their synthesis is progressing. The system is fast, improves peptide purities and yields, and enables chemists to use less noisome reagents than other cleavage systems. The system accepts 4-ml, 25-ml, and 35-ml vessels and a cleavage scale of microcleavage to 0.25 mmol.

CEM Corp.
For information 704-821-7015
www.cem.com

Protein Interaction System

The DUALhunter System is a flexible assay system designed to find novel protein interaction partners for transcriptionally active and self-activating proteins. The system quickly screens full-length soluble nuclear proteins in vivo and can also be used to screen protein domains or fragments for novel protein interactions. It also permits easy subcloning of full-length complementary DNA (cDNA) inserts; the protein of interest is screened against a cDNA library of choice, which can be very large, and cell-type specific interactions can be detected. The system detects protein interactions based on the split-ubiquitin system, giving researchers the ability to screen classes of proteins such as transcription factors or strongly acid proteins that cannot be screened using classic yeast two-hybrid systems.

Dualsystems Biotech
For information +41-(0)1-738-50-00
www.dualsystems.com

IgG Antibody Purification

BioVyon Protein A microplates and columns offer a simple and rapid method for antibody purification. The new products give a consistent recovery of immunoglobulin G (IgG) antibody that is independent of the flow rate during loading. Unlike existing bead-based technologies, there are no time-consuming slurries to equilibrate and pour into columns. BioVyon Protein A Mini Columns and Micro Columns give consistent recoveries of purified IgG. The high purity is consistent in multiple extractions using the same column or from column to column. The columns can be reused several times. The minicolumns have a capacity of 2.5 mg IgG, and the microcolumns have a 10 µg capacity.

Porvair Filtration Group
For information +44-1489-864330
www.biovyon.com

Protein Extraction Buffers

The Mammalian Protein Extraction Buffer and Yeast Protein Extraction Buffer Kit are mild, nondenaturing buffer compositions that deliver high-quality protein lysate compatible with most downstream applications without the need for mechanical cell lysis. Both products give highly reproducible, consistent results that maintain biological activity. The mammalian buffer is designed for use in cultured cells, and can be used for both cell suspensions and adherent cells. The yeast kit is suitable for preparation of approximately 10 ml of yeast cell pellet suspension and eliminates the need for glass beads. The buffers are compatible with downstream applications such as chromatography, enzyme assays, and electrophoresis.

GE Healthcare
For information 262-501-0777
www.gelifesciences.com

Electronically submit your new product description or product literature information! Go to **www.sciencemag.org/products/newproducts.dtl** for more information.

Newly offered instrumentation, apparatus, and laboratory materials of interest to researchers in all disciplines in academic, industrial, and governmental organizations are featured in this space. Emphasis is given to purpose, chief characteristics, and availabilty of products and materials. Endorsement by *Science* or AAAS of any products or materials mentioned is not implied. Additional information may be obtained from the manufacturer or supplier.

Science Careers
Classified Advertising

For full advertising details, go to **ScienceCareers.org** and click **For Advertisers**, or call one of our representatives.

UNITED STATES & CANADA
E-mail: advertise@sciencecareers.org
Fax: 202-289-6742

Joribah Able
Industry – US & Canada
Phone: 202-326-6572

Alexis Fleming
Northeast Academic
Phone: 202-326-6578

Tina Burks
Southeast Academic
Phone: 202-326-6577

Daryl Anderson
Midwest/Canada Academic
Phone: 202-326-6543

Nicholas Hintibidze
West Academic
Phone: 202-326-6533

EUROPE & INTERNATIONAL
E-mail: ads@science-int.co.uk
Fax: +44 (0) 1223 326532

Tracy Holmes
Associate Director, *Science* Careers
Phone: +44 (0) 1223 326525

Alex Palmer
Phone: +44 (0) 1223 326527

Dan Pennington
Phone: +44 (0) 1223 326517

Susanne Kharraz Tavakol
Phone: +44 (0) 1223 326529

Louise Moore
Phone: +44 (0) 1223 326528

JAPAN
Mashy Yoshikawa
Phone: +81 (0) 3 3235 5961
E-mail: myoshikawa@aaas.org

To subscribe to *Science*:
In US/Canada call 202-326-6417 or 1-800-731-4939.
In the rest of the world call +44 (0) 1223 326515.

Science makes every effort to screen its ads for offensive and/or discriminatory language in accordance with US and non-US law. Since we are an international journal, you may see ads from non-US countries that request applications from specific demographic groups. Since US law does not apply to other countries we try to accommodate recruiting practices of other countries. However, we encourage our readers to alert us to any ads that they feel are discriminatory or offensive.

Science Careers
From the journal *Science* AAAS

POSITIONS OPEN

吉林大学生命科学学院

COLLEGE OF LIFE SCIENCE
Jilin University, Changchun, China

The College of Life Science at Jilin University has multiple open **FACULTY POSITIONS** in the following fields: microbiology (preferably virus and HIV vaccine research, six positions), biochemistry and molecular biology (three positions), cell biology (three positions), and biophysics (three positions).

Candidates should be interested in graduate/undergraduate education and should be dedicated to scientific research with collaborative spirit and scientific integrity. Jilin University offers highly competitive salaries and startup packages. Applicants with extensive research experience as a senior postdoctoral fellow, assistant professor, or higher are welcome to send their curriculum vitae plus a statement of research interests, a copy of doctoral degree diploma, and copies of representative publications or other accomplishments electronically to: **Prof. Desheng Yang, e-mail: yds@jlu.edu.cn. Telephone: 86-431-85168372; fax: 86-431-85168175.**

FACULTY POSITION
AT THE UNIVERSITY OF VIRGINIA

The Department of Pharmacology (**website: http://www.healthsystem.virginia.edu/internet/pharmacology/**) is seeking to fill a position at the **ASSISTANT/ASSOCIATE/FULL PROFESSOR** level. The Department has current strengths in endocrinology and in mammalian cellular and integrative neurobiology. To complement and broaden these areas of interest, we are looking for individuals who will develop a research program that utilizes any combination of modern molecular, cellular biological, and mouse genetic approaches. The position offers newly renovated space and access to state-of-the-art departmental and core facilities. A doctoral degree in pharmacology, physiology, chemistry, biochemistry, medicine, or related discipline with at least two years postdoctoral training and evidence of significant research productivity is required. To apply send curriculum vitae, a two-page document delineating significant research accomplishments and future research plans, and a list of three references (including e-mail addresses and telephone numbers) to: **Pharmacology Search Committee, Department of Pharmacology, University of Virginia, P.O. Box 800735, Charlottesville, VA 22908-0735. E-mail: pharmsearch@virginia.edu.** The position will remain open until filled. *The University of Virginia is an Equal Opportunity/Affirmative Action Employer.*

ASSISTANT SCIENTIST

In this role, you will be in charge of a process to study the immune regulation of atherosclerosis and mechanism of cardiovascular disease.

Bachelor's degree in related field of science with at least one to three years of experience in cardiovascular science, molecular biology, or immunology required. Ph.D. in cardiovascular science and experience in atherosclerosis research preferred.

To apply online, visit our **website: http://www.temple.edu** and click on **Jobs@temple.** Please reference **TU-12217.** *Temple University is an Affirmative Action/Equal Opportunity Employer with a strong commitment to cultural diversity.*

TWO POSITIONS available immediately at the University of Michigan, Ann Arbor, to study the molecular mechanism of action of human microsomal cytochrome P450 with its flavin and heme redox partners. One position is for a highly motivated, experienced individual while the second position can be at a more minor level, although prior postdoctoral experience is preferred. Ph.D. in chemistry/biochemistry essential. Salary commensurate with experience. Knowledge of biophysical techniques employing pre-steady-state kinetics, electron paramagnetic resonance, mass spectrometry, and/or experience with site-directed mutagenesis, membrane protein purification, crystallography is desirable. Send resume and names of three references to **email: waskell@umich.edu.**

POSITIONS OPEN

DEPARTMENT OF MEDICINE
University of California, San Francisco

The Department of Medicine at the University of California, San Francisco (UCSF) is searching for an outstanding **PHYSICIAN-SCIENTIST.** Candidates must have demonstrated potential to lead an independent research program in an area broadly relevant to pulmonary biology. Candidates must be Board-certified in internal medicine and competent to practice and teach in one of the divisions of the Department of Medicine. The recruited faculty member will be a member of the UCSF interdisciplinary Program in Biological Sciences and the Biomedical Sciences graduate programs and will be a member of the UCSF Lung Biology Center. Outstanding laboratory space will be provided in Genentech Hall on the new UCSF Mission Bay campus. Long-term base salary support and a generous startup package will be provided. Appointments will be at the **ASSISTANT** or **ASSOCIATE PROFESSOR** level depending on seniority and experience of the successful candidate.

Send curriculum vitae, a brief statement of your research plans, and three letters of reference to: **Dean Sheppard, M.D., Chair, Search Committee, Director, Lung Biology Center.** Send materials electronically to **e-mail: dean.sheppard@ucsf.edu** and/or by mail to: **UCSF Box 2922, San Francisco, CA 94143-2922.** *UCSF seeks candidates whose experience, teaching, research, or community service has prepared them to contribute to our commitment to diversity and excellence. The University is an Equal Opportunity/Affirmative Action Employer. All qualified applicants are encouraged to apply, including minorities and women.*

FACULTY POSITIONS
in Science Teacher Education

The University of Nebraska-Lincoln seeks to fill up to three tenured/tenure-track positions to support a major commitment to enhancing science teacher education. Individuals with a Ph.D. or Ed.D. in a field of science (physical, earth, life, agricultural, or natural resources sciences) and/or education and a demonstrated record of scholarly achievement are urged to submit their applications. Visit **website: http://nuteach.unl.edu** for complete job description.

To apply, go to **website: http://employment.unl.edu (requisition 090148)** and complete the faculty academic administrative information form. Attach a letter of application, curriculum vitae, and a personal statement describing your research and teaching interests and experience. Arrange for three letters of reference to be submitted electronically to **e-mail: bwest1@unl.edu.** Review of applications will begin May 15, 2009, and continue until all positions have been filled or the search is closed.

The University of Nebraska has an active National Science Foundation ADVANCE gender equity program, and is committed to a pluralistic campus community through affirmative action, equal opportunity, work-life balance, and dual careers.

The University of Chicago/Department of Radiation and Cellular Oncology is seeking applicants for full-time **RESEARCH ASSOCIATE** (**ASSISTANT PROFESSOR/PROFESSOR**) all-rank position. Candidates are required to possess a doctorate degree with experience in studying the molecular mechanisms of metastasis. Applicants must have experience with molecular and cell biology approaches, in vitro systems, and animal tumor models. As the laboratory also focuses on understanding pathways that control how metastasis responds to treatment, applicants with experience in mechanisms of chemotherapy/radiation resistance are favored.

Interested candidates should submit curriculum vitae, bibliography, a statement of research, and contact information for three professional references to: **Dr. Andy J. Minn, Department of Radiation and Cellular Oncology, 5758 S. Maryland Avenue MC9006, Chicago, IL 60637, or by e-mail: aminn@radonc.uchicago.edu.** For information about the University of Chicago, please consult **website: http://uchicago.edu.**

The University of Chicago is an Affirmative Action/Equal Opportunity Employer.

EMBL

The European Molecular Biology Laboratory is searching for a Group Leader. EMBL offers a highly collaborative, uniquely international culture. It fosters top quality, interdisciplinary research by promoting a vibrant environment consisting of young, independent researchers with access to outstanding graduate students and post-doctoral fellows.

Group Leader
Mouse Biology Unit
at EMBL Monterotondo (near Rome), Italy

We seek a dynamic, independent scientist with an excellent track record and demonstrated experience or interest in mouse genetics and physiology, and a desire to work in a multidisciplinary environment. We encourage applicants addressing fundamental questions in organismal biology with a focus on models of human disease, using modern genetic and genomic approaches.

EMBL's Scientific Programme emphasises experimental analysis at multiple levels of biological organisation, incorporating Systems Biology, Computational Biology and Bioinformatics. Within this structure, the Mouse Biology Unit applies a wide range of modern technologies to diverse problems of whole organism biology. In addition to exciting colleagues, EMBL Monterotondo offers state-of-the-art recombineering, transgenic and knockout mouse core services, automated monoclonal antibody production, confocal microscopy, histology and flow cytometry core facilities and a broad range of in vivo systems for conditional mutagenesis.

We benefit from close interactions with EMBL Heidelberg, the European Bioinformatics Institute in Hinxton, near Cambridge and our Outstations in Hamburg and Grenoble. The Mouse Biology Unit is part of several pan-European initiatives to coordinate the generation, screening and characterisation of novel mouse strains and mutants.

An initial contract of 5 years will be offered to the successful candidate. This can be renewed, depending on circumstances at the time of review.

Further information on the position can be obtained from the Head of Outstation Nadia Rosenthal (**nadia.rosenthal@embl.it**).

To apply, please email by June 6, 2008 a CV, three reference letters and a concise description of research interests and future plans, quoting ref. no. S/09/035 in the subject line, to: **application@embl.de**

EMBL is an inclusive, equal opportunity employer offering attractive conditions and benefits appropriate to an international research organisation.

www.embl.org/jobs

Are you conducting research into the sustainable use of renewable natural resources? Do you want to contribute to the solution of urgent environmental problems, especially in developing and emerging countries?

If yes, then we would like to invite you to apply for the

Robert Bosch Junior Professorship Research into the Sustainable Use of Renewable Natural Resources

together with a German university or research institution of your choice. Applicants of all nationalities are welcome.

Areas addressed
We are looking for an outstanding young scientist whose research areas concern the sustainable use of renewable natural resources relating to agriculture, forestry, fisheries, use of biodiversity (animal and plant genomic resources) and water. Research approaches may be based in the natural sciences as well as in the social, economic, political, medical and public health sciences. The research should focus on developing and emerging countries. We welcome applications from all areas of research. For this year's call for applications, we would especially like to encourage applications in the following area of research:

Global Environmental Change and Health
Increased environmental change caused by drivers such as climate or land use change, environmental pollution or urbanization has consequences for human health that are poorly understood. Studies should focus on the effect of such a change on the epidemiology of (a) human disease(s) and the potential for adaptation. Applicants must show that their planned research is a confident and genuinely innovative step into new areas in their field. It should be obvious from your application that you are developing your own scientific profile. Research concepts should be interdisciplinary and integrate research methods that explore interconnections between global and regional environmental problems.

Scope
The successful applicant will be awarded a grant worth up to 1 million euros for a five year period, in order to set up a research group in a German research institution or university. The funds can be allocated flexibly towards covering the candidate's and personnel salaries as well as towards meeting research costs (working lab space, access to resources, equipment, travelling, consumables). If the successful applicant is interested in a tenure track position, the host institution is expected to guarantee the post. This means that it assumes the obligation to install a regular professorship ad personam after expiry of the grant and after a successful evaluation of the performance of the Junior Professor.

Candidate profile
:: excellent doctorate degree, completed no more than 5 years prior to the application deadline of 10 June 2009 (adjusted for documented parental leave)
:: compelling independent past scientific achievements and publications in peer-reviewed journals
:: international research experience
:: excellent proficiency in English
:: potential to obtain a leading position in his/her research field
:: non-German applicants should be prepared to learn German.

How can I apply?
The application deadline is **10 June 2009.** The earliest possible date for a successful applicant to take up the position is 1 February 2010.

For application guidelines, please visit our website at **www.bosch-stiftung.de/juniorprofessorship**

Robert Bosch Stiftung

The University of Montana, College of Health Professions and Biomedical Sciences, Skaggs School of Pharmacy, has been awarded an Endowment Program grant for increasing research and training capacity from the NIH-NCMHD (National Center for Minority Health and Health Disparities).

The four major aims of this program are:

1) creation of a more substantial health disparities research emphasis particularly relevant to the American Indian population,
2) addition of American Indian faculty,
3) enhancement of the recruitment, education, and training of minorities at both the professional and graduate levels, and
4) formation of partnerships that foster both minority recruitment and health disparities research.

The current position opening is for a talented biomedical/pharmaceutical scientist who can help to address these aims. The position is open at a tenure track position at Assistant or Associate Professor level. The appointment will be in the Department of Biomedical & Pharmaceutical Sciences (**www.umt.edu/pharmsci**) or the Department of Pharmacy Practice (**www.health.umt.edu/schools/practice**).

For a complete description and application instructions, visit **http://www.health.umt.edu/**. **American Indian, Alaska Native, and Pacific Islander candidates are strongly encouraged to apply.**

AA/EOE/ADA/Veterans Preference Employer


DFG Graduiertenkolleg 1026


BMBF ZIK HALOmem


Martin- Luther-University Halle-Wittenberg

Postdoc and Ph.D. positions available
Biochemistry/Biology/Chemistry/Physics

A number of Postdoc and Ph. D. positions will be available from July 1st 2009 within the DFG Graduate College 1026 "Conformational transitions in macromolecular interactions" (**www.biochemtech.uni-halle.de/grk1026/**) as well as the recently established BMBF 'Zentrum für Innovationskompetenz' HALOmem (**www.halomem.de**).

The interdisciplinary GRK 1026 studies the causes and effects of protein folding transitions on biological macromolecular complex formation in a collaborative environment, using a wide variety of biophysical, biochemical and cell biological approaches. HALOmem focuses on the structure and dynamics of integral membrane proteins and their lipid membranes.

Successful candidates should be highly motivated, of above average ability and good team workers. They should hold a degree in a relevant subject, and have a keen interest in acquiring the broad range of available techniques necessary to tackle the experimental problems and questions involved.

Applications to be made by **May 15th 2009** by E-mail (incl. PDF of CV and diploma testimony) to the following E-mail address: grk1026@biochemtech.uni-halle.de

GRK 1026, Institut für Biochemie und Biotechnologie
Martin-Luther-Universität Halle-Wittenberg
Kurt-Mothes-Str. 3, 06120 Halle (Saale)
Speaker: Prof. Milton T. Stubbs, Coordinator: Mechtild Wahle
Tel:++49/(0)345/5524809 Fax:++49/(0)345/5527360
E-mail:grk1026@biochemtech.uni-halle.de

UW Medicine
SCHOOL OF MEDICINE

The University of Washington School of Medicine seeks a Professor and Chair of the Department of Immunology. Candidates should have a PhD degree in Immunology or a related biomedical discipline and/or an MD degree, an internationally recognized research program in Immunology, and well-demonstrated academic leadership skills. The Department of Immunology at the University of Washington has outstanding research and graduate training programs in Immunology, and it participates actively in teaching in the medical curriculum and in interdisciplinary training of MD and PhD students through multi-departmental graduate programs in Molecular and Cellular Biology and Molecular Medicine. UW faculty engage in teaching, research and service.

Please submit applications (including a CV and names of reference) or nominations to:

William A. Catterall, PhD, Chair
Immunology Search Committee
Department of Pharmacology
University of Washington
Box 357280, Seattle
WA 98195-7280

THE UNIVERSITY OF WASHINGTON IS AN AFFIRMATIVE ACTION/EQUAL OPPORTUNITY EMPLOYER.

UT HEALTH SCIENCE CENTER
DEPARTMENT OF CELLULAR AND STRUCTURAL BIOLOGY

ENDOWED CHAIR IN STEM CELL AGING

The **EWING HALSELL FOUNDATION DISTINGUISHED CHAIR IN AGING RESEARCH** is available for an eminent **stem cell biologist** with an interest in aging research to **lead the development** of a new initiative in stem cell biology. The primary academic appointment will be held in the Department of Cellular and Structural Biology as an **Associate Professor or Professor**, with membership in the Barshop Institute for Longevity and Aging Studies. Applicants should have demonstrated academic scholarship in terms of publications in major peer-reviewed journals, a strong record of sustained extramural research support and the ability and willingness to build multidisciplinary research programs. The successful applicant will be expected to establish and maintain a premier multidisciplinary program in **aging stem cell biology**. Opportunities are available to interact with established and emerging researchers and to mentor predoctoral PhD, MD/PhD, and DDS/Ph.D. students. The Department is highly active in research, teaching and service throughout the UT Health Science Center at San Antonio and is the primary academic home to over 30 tenured or tenure-track faculty. Departmental faculty oversee three research core facilities: an optical imaging facility, a genomics core and a bone core. In efforts to support and enhance research activities in stem cell biology and regenerative medicine, a stem cell core is under development. Access to institutional core facilities (**http://cores.uthscsa.edu/**) is readily available. The Department of Laboratory Animal Resources, and a number of other service departments are available to support research activities. Investigators seeking to promote collaborative multidisciplinary opportunities and to lead in the development of stem cell research at the UT Health Science Center at San Antonio are encouraged to apply. The UT Health Science Center at San Antonio is home to one of five Nathan Shock Centers for Excellence in Biology of Aging, an NCI-designated Cancer Center, an NIH-funded Clinical Translational Science Award, and the Greehey Children's Cancer Research Institute. An attractive startup package will be offered to the successful candidate. A highly competitive candidate may be eligible for additional startup funds from the UT System STARS program (**http://www.utsystem.edu/Aca/initiatives/STARS_Program.htm**).

Interested applicants should submit a curriculum vitae, a summary of research accomplishments, future goals (2-3 pages) and contact information for five references to (**ENDCHCSB@UTHSCSA.EDU**) directed to the attention of **Christi A. Walter, Ph.D., Professor and Chair, Department of Cellular and Structural Biology, The University of Texas Health Science Center at San Antonio, 7703 Floyd Curl Drive, San Antonio, TX 78229-3900**.

The University of Texas Health Science Center at San Antonio is an Equal Employment Opportunity/Affirmative Action Employer. All faculty appointments are designated as security sensitive positions.

EUROPEAN SCIENCE FOUNDATION
SETTING SCIENCE AGENDAS FOR EUROPE

Invites applications for a

Head of the Life, Earth and Environmental Sciences (LESC) Unit

The European Science Foundation (ESF) provides a platform for its Member Organisations to advance European research and explore new directions for research at the European level. Established in 1974 as an independent non-governmental organisation, the ESF currently serves 80 Member Organisations, including Research Funding Agencies, Research Performing Organisations and Academies, across 30 countries.
The Standing Committee for Life, Earth and Environmental Sciences (LESC) aims at a better understanding of biological, environmental and Earth systems across time and space.

Mission of the position
In order to mobilise high-quality researcher-led co-operation in science in Europe and to provide a natural multi-national arena for such cooperation through its relations with Member Organisations, the Head of Unit is in charge of developing and implementing the ESF Strategic Plan in his/her domain.
This position will involve:

- Developing and implementing strategies to catalyse and support researchers and ESF Member Organisations;
- Overseeing and contributing to the development of policy and its implementation within the overall ESF Strategy, taking responsibility, as the Secretary of the Life, Earth and Environmental Sciences Standing Committee, for the mobilisation and motivation of the Science Committee and for the development of strategic activities within the overall ESF Strategy;
- Overseeing and participating in the impartial implementation of scientific quality control through the peer review process of proposals;
- Liaising on behalf of the LESC Standing Committee with ESF Member Organisations and external scientific bodies;
- Publicising and informing the LESC Community through publication, the Web…
- Taking responsibility for the management and achievement of budgets of specific activities;
- Ensuring compliance with external contract obligations, including European Commission contracts;
- Managing the performance of the LESC team in a professional manner.

The post is based at ESF in Strasbourg, France.
Profile and working conditions are described in the complete position announcement available at www.esf.org/vacancy-leschou
Please send your application by **4 May 2009** to **jobs@esf.org** quoting the following reference identifier **LESC-HOU**.
Interviews will be held in Strasbourg on **20 May 2009**.
Further details at **www.esf.org**

University of Massachusetts Medical School
UMASS

Brudnick Neuropsychiatric Research Institute
bnri

TENURE-TRACK NEUROSCIENCE POSITION

The Brudnick Neuropsychiatric Research Institute (BNRI), established as part of the unprecedented research expansion at the University of Massachusetts Medical School, invites applications for a tenure-track position at the level of Assistant, Associate or Full Professor. The BNRI, a division of the Department of Psychiatry, is committed to broad-based research investigating basic neurobiological principles related to psychiatric disorders. While we invite applications from all areas of neuroscience, we are particularly interested in applicants using electrophysiological approaches in mammalian systems to investigate mechanisms underlying neuronal plasticity. The BNRI, situated in a state-of-the-art laboratory facility, is an integral part of the campus-wide Program in Neuroscience, which consists of over 55 basic neuroscientists. The successful candidate will establish and/or maintain an independent research program and play an integral role in new Program initiatives. The position is highly competitive with regard to salary, start-up funds and laboratory space.

Applicants should send a CV, statement of research interests, and names and addresses of three references by **June 1, 2009** to:

Dr. Paul D. Gardner, Search Committee Chair
Brudnick Neuropsychiatric Research Institute
University of Massachusetts Medical School
303 Belmont Street
Worcester, MA 01604
E-mail: bnri@umassmed.edu
www.umassmed.edu/bnri

An Equal Opportunity/Affirmative Action Employer.

National Oceanic and Atmospheric Administration (NOAA)

DIRECTOR, GREAT LAKES ENVIRONMENTAL RESEARCH LABORATORY

(A Senior Executive Service Position in the Federal Government)
Vacancy Announcement: TBD

Department of Commerce (DOC)
National Oceanic and Atmospheric Administration (NOAA)
Ann Arbor, MI • ES-1301-00/00
$117,787.00 - 177,000.00 annually

This position is that of Director, Great Lakes Environmental Research Laboratory (GLERL), Office of Oceanic and Atmospheric Research (OAR), National Oceanic and Atmospheric Administration (NOAA). GLERL conducts high-quality research and provides scientific leadership on important issues in both Great Lakes and marine coastal environments leading to new knowledge, tools, approaches, awareness and services. The research focuses on investigations to improve our understanding and prediction of biological, chemical, physical and hydrological processes occurring in natural systems. Special emphasis is placed on a system approach to problem-oriented environmental research to develop environmental service tools. Assistance is provided to resource managers and others in obtaining and applying the information and services developed by the Laboratory.

The incumbent is required to have the following:

1. Expert knowledge of current and state-of-the-art theories in a combination of the following disciplines: limnology; fisheries ecology; hydrology; climate; and biological, physical, or chemical oceanography. Demonstrated ability to conceive, design, direct, and evaluate theoretical and experimental atmospheric, oceanographic, and climate studies of a complex and large-scale nature.

2. Demonstrated knowledge of and high-level competence in physical or biological sciences sufficient to perceive complex problems in broad perspective, to coach and infuse ideas, and to participate in critical discussions and assessment of the scientific leadership in order to make determinations on sound scientific projects, in support of NOAA's research mission.

3. Demonstrated ability to communicate research and assessment results to a broad range of constituents (e.g., scientists, the public, the agency, Congress, etc.) through the media, speeches, testimony, service in professional or technical societies, briefings, and/or presentations.

Please contact Norma Hughes at 301/713-6307 for announcement information (Internet address: **norma.j.hughes@noaa.gov**), including mailing instructions—referring to the announcement number -OR- you may access the entire full-text vacancy **USAJOBS.OPM.GOV.** Incomplete applications will be returned.
This vacancy will close on TBD.
*NOAA Values a Diverse Workforce and is an Equal Opportunity Employer"

Chair, Department of Neuroscience and Cell Biology

The University of Medicine and Dentistry of New Jersey - Robert Wood Johnson Medical School invites applications and nominations for the position of Professor and Chair of the Department of Neuroscience and Cell Biology. As an internationally recognized academic leader, the Chair will have a strong track record of scientific accomplishment and be engaged in an active research program that complements the department's strengths in cell biology and molecular, cellular, developmental and behavioral neuroscience. This is an exceptional opportunity to lead and further build a distinguished department with a strong history of research accomplishments and an excellent graduate training program.

The Department of Neuroscience and Cell Biology faculty research covers diverse areas in the fields of neuroscience, stem cell biology and molecular cell biology. The department is noted for extensive collaborations with faculty in the strong research and clinical environment at RWJMS, including the clinical departments, The Cancer Institute of New Jersey, the Child Health Institute of New Jersey, and the joint institutes, including the Center for Advanced Biotechnology and Medicine and the Environmental and Occupational Health Sciences Institute, and departments of Rutgers University, located on the same campus.

Letters of interest, including a current CV, should be sent before May 15, 2009 to: **Aaron J. Shatkin, Ph.D., Email: shatkin@cabm.rutgers.edu, Chair, Search Committee, Center for Advanced Biotechnology and Medicine, 679 Hoes Lane, Piscataway, New Jersey 08854**. UMDNJ is an Affirmative Action/Equal Opportunity Employer. For more information, visit www.umdnj.edu/hrweb.

UMDNJ
ROBERT WOOD JOHNSON MEDICAL SCHOOL
University of Medicine & Dentistry of New Jersey

POSITIONS OPEN

INSTRUCTOR OF MEDICINE POSITION
School of Medicine
Department of Medicine
Division of Cardiovascular Disease

The University of Alabama at Birmingham, Department of Medicine, Division of Cardiovascular Disease is seeking applicants with a Ph.D. for the position of Instructor. This is a nontenure-track faculty position. Candidates must have an expertise in cardiomyocyte cell biology with at least three years of experience in in vivo animal models of heart failure and ischemia/reperfusion injury. Candidates should also be proficient in echocardiographic analysis of heart function, immunohistochemistry, and ingenuity pathway analysis. Interested candidates should send curriculum vitae with three letters of recommendation to: **Louis J. Dell'Italia, M.D., 901 19th Street South, BMR2 432, Birmingham, AL 35294-2180.** *The University is committed to building a culturally diverse educational environment. Women, minorities, individuals with disabilities, and veterans are encouraged to apply. The University of Alabama at Birmingham is an Equal Opportunity/Affirmative Action Employer.*

DIRECTOR, DIVISION OF UNDERGRADUATE EDUCATION
National Science Foundation, Arlington, Virginia

National Science Foundation's Directorate for Education and Human Resources seeks candidates for the position of Director, Division of Undergraduate Education (DUE). The Division serves as a focal point for NSF's agencywide commitment in promoting excellence in undergraduate science, technology, engineering, and mathematics (STEM) education for all students. Information about the Division's activities may be found at **website: http://www.nsf.gov/div/index.jsp?org=DUE.**

Appointment to this Senior Executive Service position may be on a career basis, on a one- to three-year limited term basis, or by assignment under the Intergovernmental Personnel Act (IPA) provisions.

Announcement S20090055 and position requirements and application procedures are posted on NSF's Home page at **website: http://www.nsf.gov/about/career_opps/.** Applicants may also obtain the announcements by contacting Executive Personnel Staff at **telephone: 703-292-4376** (hearing impaired individuals may call **TDD 703-292-8044**). Applications must be received by May 26, 2009.

NSF is an Equal Opportunity Employer.

The Henry M. Jackson Foundation for the Advancement of Military Medicine, Inc. (HMJF), is seeking a **POSTDOCTORAL FELLOW** to support the Division of Retrovirology in Rockville, Maryland, U.S.A. to work on characterizing the structure-function relationships in HIV-1 using surface plasmon technology. Research involves protein biochemistry and tissue culture. Candidate should have Ph.D. in biological sciences and a strong background in biochemistry. Experience in using a Biacore is desirable. Please send resumes to **e-mail: careers@hjf.org or to fax: 240-314-7334. Job No: 204193.** The Foundation is a nonprofit medical research organization that provides support services to the military medical community and offers a competitive salary and generous benefits package. *HMJF is an Affirmative Action/Equal Employment Opportunity Employer.*

The McGill Group for Suicide Studies (MGSS) is seeking a **POSTDOCTORAL FELLOW** to lead a project investigating the role of microRNA on mood disorders. The MGSS (**website: http://www.douglasrecherche.qc.ca**) is a multidisciplinary center investigating biomedical risk factors for major depression and suicide. Successful candidates should have outstanding research credentials and extensive experience in molecular and cell biology. Interested individuals should submit curriculum vitae and contact information for three academic professional references to: **Dr. Gustavo Turecki, e-mail: gustavo.turecki@mcgill.ca.**

POSITIONS OPEN

POSTDOCTORAL FELLOWSHIP
Biomedical Sciences Program
Oklahoma State University
Center for Health Sciences

Oklahoma State University Center for Health Sciences, College of Osteopathic Medicine is seeking to fill a Postdoctoral Researcher position to participate within our multidisciplinary group studying autism spectrum disorders using the prairie vole as a model system through the Biomedical Sciences Program. Experience with whole animal research and basic neuroscience techniques is a plus, but a strong desire to adopt neuroethological methods will suffice. Requires a Ph.D, D.O./Ph.D, or M.D./Ph.D. degree. Salary will be no less than stated in the most recent NIH guidelines. The Center for Health Sciences is located in Tulsa, Oklahoma, and is experiencing a period of growth and development with construction beginning on 78,000 square feet of new research space scheduled for completion in 2010. Applications will be reviewed as received; open until filled. Must apply online at **website: https://jobs.okstate.edu, job #05279.** *OSU is an Affirmative Action/Equal Opportunity Employer/E-Verify employer committed to diversity.*

POSTDOCTORAL RESEARCH FELLOWSHIPS

Sanford Research/USD is seeking two Postdoctoral Fellows. Sanford Research/USD was established by the Sanford School of Medicine of the University of South Dakota and Sanford Health and is dedicated to research excellence. Successful candidates should have a recent Ph.D., M.D./Ph.D., or D.V.M./Ph.D. with a record of scientific productivity.

One position is available in **Dr. Gregory Shearer's** laboratory within the Cardiovascular Health Research Center at Sanford Research/USD. The Fellow will perform analyses of lipoprotein structure and function in dyslipidemias with an emphasis on cellular binding and analytical chemistry. A strong background in physiology or biochemistry is preferred. Experience with clinical trials a plus.

The other position is available in **Dr. Da-Qing Yang's** laboratory. The Fellow will study signal transduction of the ATM protein kinase in response to insulin or translational regulation of the expression of p53 tumor suppressor in tumorigenesis. Experience in type 1 diabetes research and/or animal models of cancer desired.

For more information and to apply for either of these positions, please visit our **website: http://www.sanfordhealth.org.** Refer to **job #206126-046** for **Dr. Shearer's** position and **job #205654-046** for **Dr. Yang's** position. Please include a cover letter addressing your interest in the position along with your resume, summary of your research experience, and contact information of three professional references.

Sanford Research/USD
1305 W. 18th Street
Sioux Falls, SD 57117
Telephone: 605-333-7000
Website: http://www.sanfordhealth.org

Equal Opportunity Employer.

MARKETPLACE

NF-κB signaling analysis simplified

Luciferase Glo Reporter Assays Accurately Quantify Changes in Cell Signaling Pathways

Understanding how RNA transcription is controlled is crucial to discovery in cancer research, developmental biology, and drug development. Luciferase reporter gene assays provide the simplest and most sensitive method for monitoring transcriptional regulation. By providing optimized vectors, cell lines, engineered luciferase genes, and add-mix-read assay reagents, Promega simplifies cell signaling analysis.

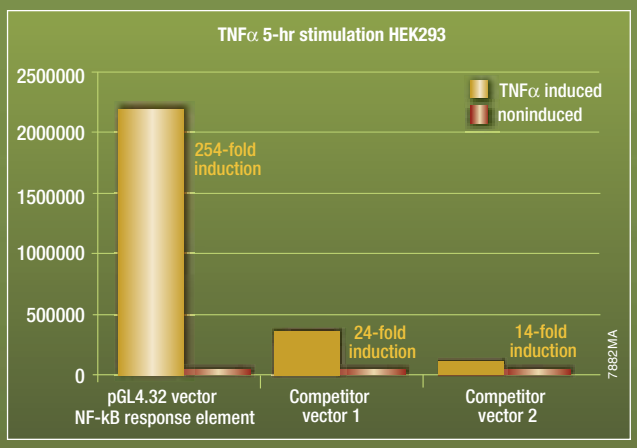

To learn about more applications using luciferase reporters, including our new NF-κB vector and qualify for a FREE SAMPLE visit:
www.promega.com/lucapps

TODAY COULD BE THE DAY.

Promega

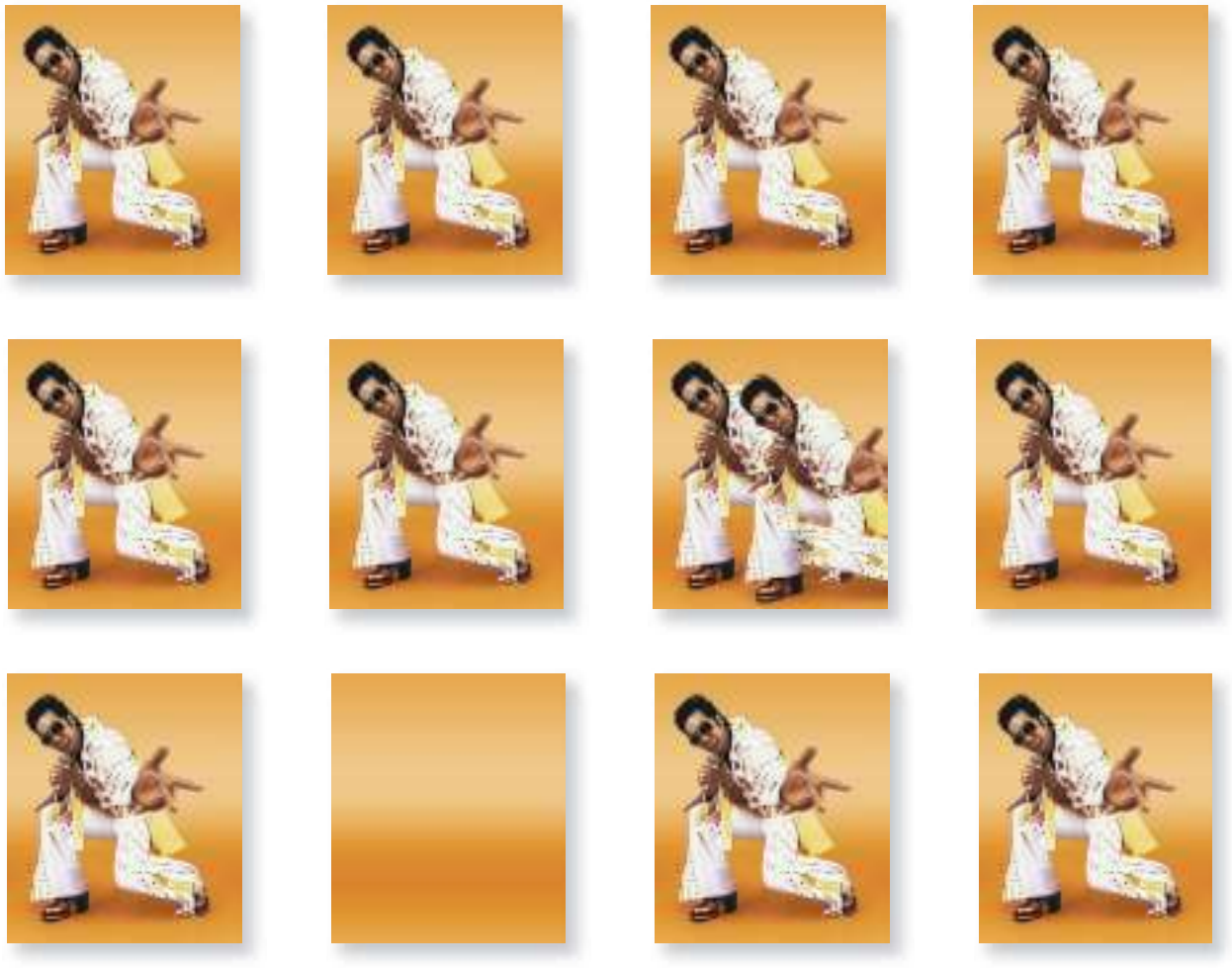

Introducing TaqMan® Copy Number Assays.

Accurate quantitation for copy number confidence.

Meet the new king of detecting deletions and duplications.

New pre-designed and custom TaqMan® Copy Number Assays enable you to accurately validate and screen specific targets. Combining Applied Biosystems real-time PCR instruments with gold standard TaqMan® Assay chemistry allows you to get results that are specific, reproducible, and easy to interpret. With an automated workflow and CopyCaller™ Software, you can streamline data analysis and process thousands of samples in hours—not days. Get quantitation you can count on with TaqMan® Copy Number Assays.

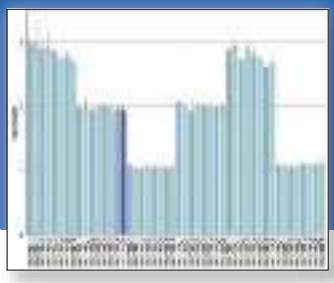

Analysis made easy
with CopyCaller™ Software

Over 1.6 Million TaqMan® Copy Number Assays for Genome-Wide Coverage.

For more information, and to view our online video brochure,
visit **www.appliedbiosystems.com/cnv**

Applied Biosystems